Photophysical properties and photodynamic therapy activities of symmetrical and asymmetrical porphyrins embedded into Pluronic polymer micelles and nonlinear optical properties of an asymmetrical phthalocyanine

A thesis submitted in fulfilment of the requirements for the degree of

DOCTOR OF PHILOSOPHY

Of

RHODES UNIVERSITY

By

Muthumuni Elizabeth Managa

May 2018

Dedication

Mother

(Angelina Avhurengwi Managa)

May your soul continue resting in peace.

Vhovha vha zwothe kha nne mme anga

Father

(Nthatheni Mackson Managa)

Khosi Vho Luvhaivhai

Acknowledgments

First and foremost, I humbly acknowledge my supervisor: Distinguished Professor T. Nyokong, Thank you for your patience, guidance and support that you gave me throughout this work. Thank you for opening new avenues by sending me to United Kingdom (UCL - London's Global University) and Russia (Institute of Physical chemistry and electrochemistry. Russian Academy of science). My gratitude also goes to Dr Britton and Dr Edith K. Amuhaya for guidance and support. To Biotechnology Innovation Centre I'm thankful for hosting me in doing cell studies. To my Father, Mr N.M. Managa, No words can ever express my gratitude. You have always been my pillar of strength and my reason to keep going regardless of obstacles. To my siblings Tshinanne, Khumbudzo, Tshifhiwa, Halatedzi, Mikovhe, Zwivhuya thank you for always walking along side me. Your encouragement kept me going throughout this work. Hlayisani Valoyi, ndzi khense ngopfu. To my friends thank you so much for all your encouragements and love throughout this work. You are all highly appreciated. It was a privilege and an honor to have worked with the Rhodes University Chemistry Department S22 Nanotechnology Research Group. You guys are indeed a family away from home. Chemistry department technical stuff; I'm thankful for making my work easier with all technical support. The E.M.U. Shirley and Marvin I'm thankful. Financial support from Pearson Young foundation is gratefully acknowledged

Abstract

This work reports on the synthesis of symmetrical and asymmetrical novel porphyrins that have been incorporated into Pluronic polymers, as well as the synthesis of asymmetrical phthalocyanine. The new compounds were characterized by elemental analysis, Fourier-transform infrared spectroscopy (FT-IR), proton nuclear magnetic resonance (^{1}H NMR), mass spectrometry and UV–Visible spectroscopy. The porphyrins that are synthesised were not water soluble but upon incorporating into Pluronic polymer micelles, they became water soluble. The polymer was also modified and linked to folic acid, to enhance selectivity for photodynamic therapy application, where MCF7 breast cancer cells were used.

The singlet oxygen quantum yields were lower for the metal free porphyrins as compared to metalled ones due to the heavy atom effect of ClGa, Zn and Cl_2Si in the latter which encourages intersystem crossing to the triplet state. Singlet oxygen quantum yields for water soluble derivatives increased upon being encapsulated into the micelles for all. The Stern-Volmer constant (K_{sv}), binding constant (K_b) and number of binding sites (n) were investigated in order to understand the interaction between the polymer micelles and the porphyrins, and it was showed that the central metals play a role in the manner which the porphyrin interacts with the micelles.

The dark toxicity and photodynamic activity of the novel porphyrins upon encapsulating to Pluronic polymer micelles is also reported. There was minimal dark toxicity for all complexes with > 90% cell survival. The photodynamic activity of water insoluble porphyrins improved when

encapsulated into the micelles. Novel asymmetrical phthalocyanines were also synthesised for nonlinear optics (NLO) studies in solution and thin films.

Legend page

Title Page

Dedication

Acknowledgements

Abstract

Contents

List of Abbreviations

List of Symbols

Table of Contents

List of Abbreviations

A/abs	Absorbance
ADMA	Tetrasodiuma,a-(anthracene-9,10-diyl)dimethylmalonate
DBU	1,8-diazabicyclo[5.4.0]undec-7-ene
DMSO	Dimethyl sulfoxide
EDS	Energy dispersive spectroscopy
F	Fluorescence
H_2Pc	Free base phthalocyanine
^1H NMR	Proton nuclear magnetic resonance
HOMO	Highest Occupied Molecular Orbital
IC	Internal conversion
IR	Infrared
ISC	Intersystem crossing
LUMO	Lowest Unoccupied Molecular Orbital
MPc	Metallophthalocyanine
NPs	Nanoparticles
Pc	Phthalocyanine
PDT	Photodynamic therapy

ROS	Reactive Oxygen Species
PluS NPs	Pluronic nanoparticles
SEM	Scanning electron microscope
TEM	Transmission electron microscope
TEOS	Tetraethyl orthosilicate
THF	Tetrahydrofuran
TPP	Tetrakis-5,10,15,20-(4-phenyl) porphyrin
UV/Vis	Ultraviolet/visible
XRD	X-ray diffractometer

List of Symbols

α	non-peripheral position
β	peripheral position
τ	lifetime
τ_0	fluorescence radiative lifetime
τ_F	fluorescence lifetime
τ_T	triplet state lifetime
$t_{1/2}$	half-life
Φ_F	fluorescence quantum yield
Φ_T	triplet state quantum yield
Φ_Δ	singlet oxygen quantum yield
F	area under fluorescence emission curve
$O_2(^1\Delta_g)$	singlet molecular oxygen
t	time
T_1	triplet excited state

Chapter 1

Introduction

Preface: This chapter provides an overview on the effect of Pluronic micelles as drug delivering agents of porphyrins. The photophysical properties of these nano-conjugates will also be introduced. The possible applications of these conjugates being in photodynamic therapy. This chapter will also provide brief insight on nonlinear optics as an application for molecules closely related to porphyrins known as phthalocyanines as a side study.

---

1. Introduction

1.1 Background on Porphyrins

Applications of porphyrins are extensive mainly as molecules of life **[1-4]**. Synthetic porphyrins have been employed in different areas such as in analytical sensors, molecular electronics and as photosensitizers in photodynamic therapy (PDT) **[5-7]**. Of interest in this work is the application of porphyrins in PDT when embedded in Pluronic micelles, as well as molecules closely related to porphyrins called phthalocyanines for application in optical limiting (OL), as a side study.

1.1.1. Structure of porphyrins and phthalocyanines

Porphyrins are aromatic tetrapyrrolic macrocycles (**Fig. 1.1**) which follow Hückel's rule. The structure of porphyrin was first proposed by Küster **[8]** in 1912, however it was never believed that such a molecule with large ring could be stable. Fischer and Zeile later on proposed the same structure when they succeeded in synthesizing heme from pyrrolic starting materials **[9]**.

The unsubstituted porphyrin macrocycle consists of four pyrrole type residues, linked together by four methine bridging groups. The carbons on the pyrrole fragments are the α and β-positions while the carbon atoms that are bridging the pyrroles are on the *meso*-positions **[10]**, (**Fig. 1.1**).

Phthalocyanines (Pcs) are a class of synthetic tetrapyrrolic compounds, similar in structure the of porphyrins [**11**]. The structural differences between porphyrins and Pcs macrocycles are the four extended benzo subunits and

four nitrogen atoms at the meso position on the macrocycle of Pcs (**Fig. 1.1**). Pcs are often referred to as tetra-benzotetraazaporphyrins and are a unique set of organic pigments that are stable with a strong blue and green colours [**12**].

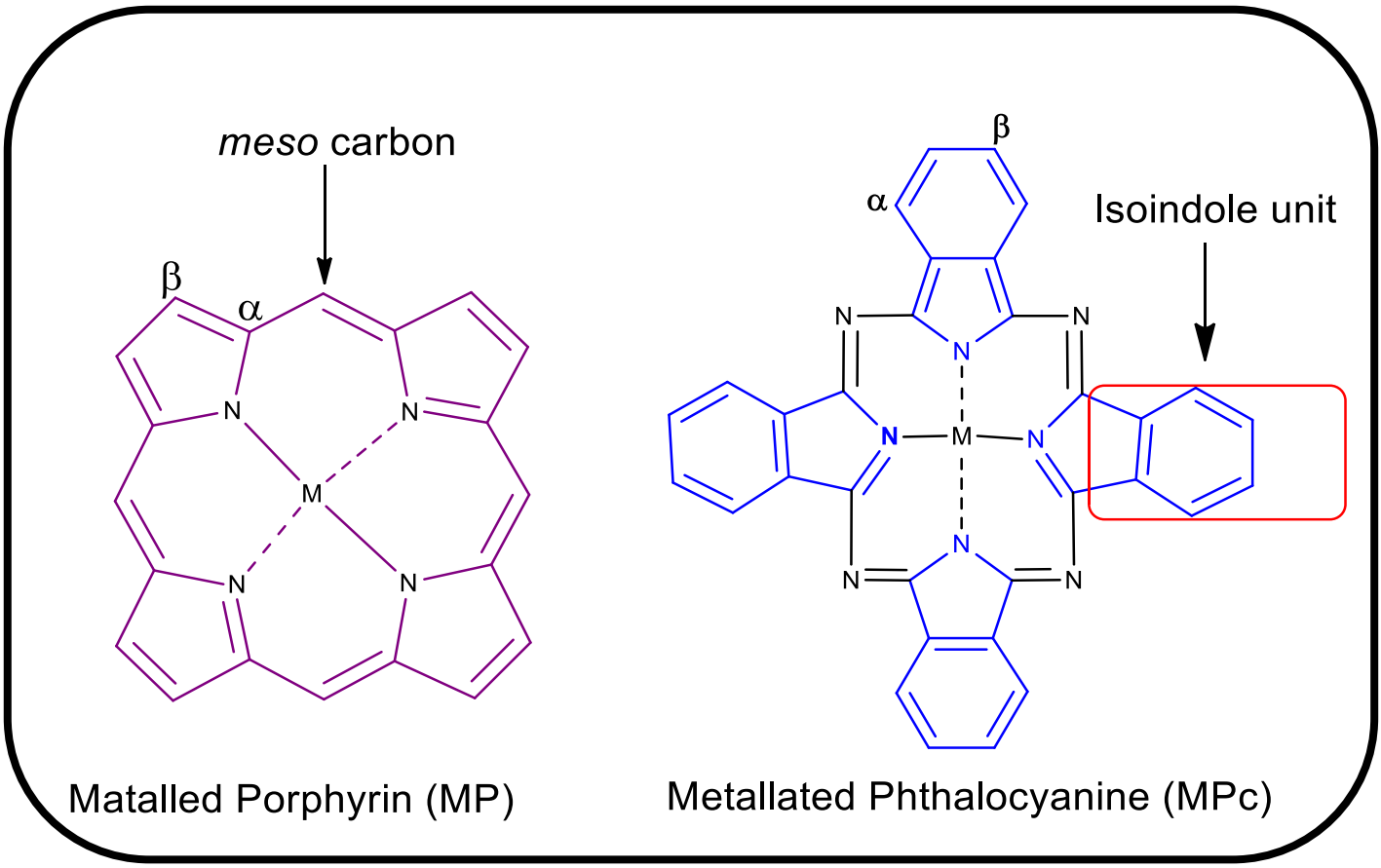

Figure 1.1: The structure of freebase (unmetallated) porphyrin and metalloporphyrin

1.1.2. Synthesis of porphyrins and phthalocyanines

The synthetic world of porphyrins is extremely rich, and its history began in the middle of 1930s **[13]**. In principle, there are many different chemical strategies for the synthesis of porphyrins, involving different building blocks, such as pyrroles, aldehydes, dipyrromethanes, dipyrromethenes, tripyrranes

and linear tetrapyrroles. *Meso*-tetraphenyl porphyrins are synthetic porphyrins employed as a model for the naturally occurring porphyrins **[14]** and are generally synthesised as shown in **Scheme 1.1**.

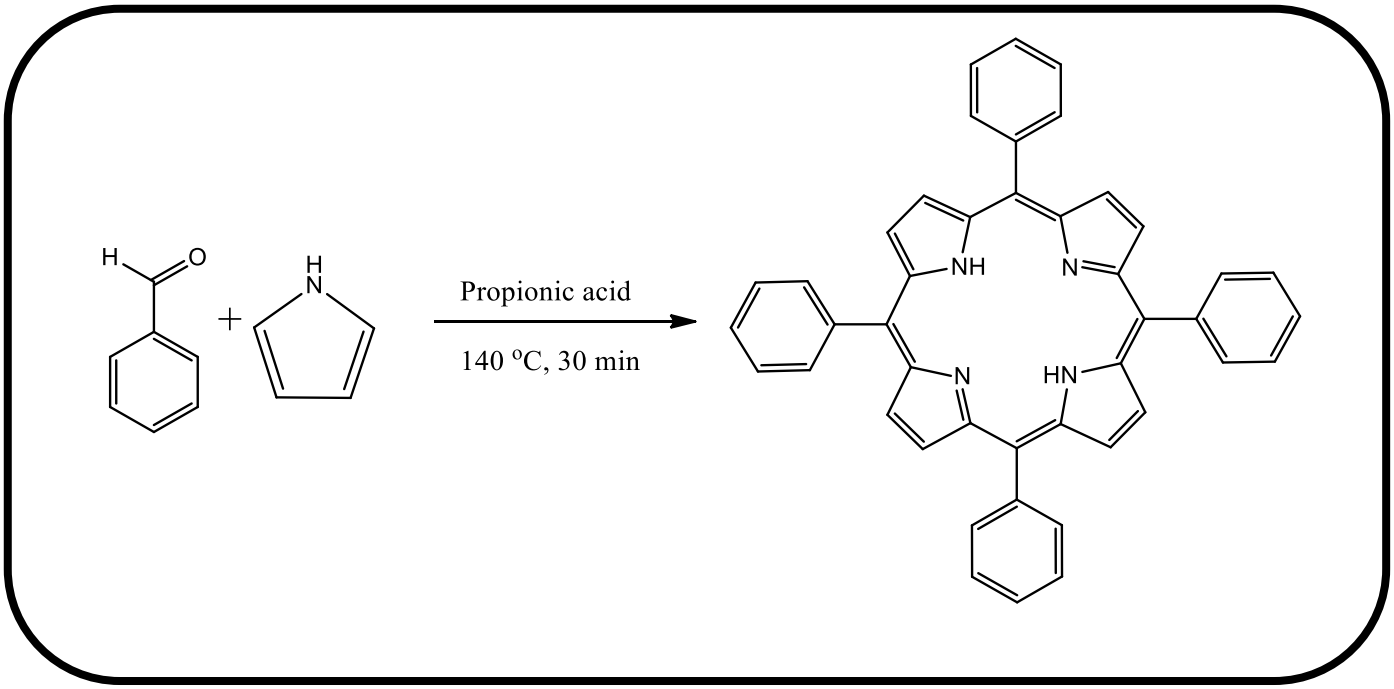

Scheme 1.1: Alder et al synthetic route of substituted porphyrins

The Adler *et al* synthetic route [**15**] was used in the synthesis of porphyrins that will be reported in this work.

Unsymmetric porphyrins can also be made in this way by using two or three different benzaldehydes; however, this requires extensive column chromatography to separate the products. If acid sensitive functional groups on the benzaldehyde are present, it is not possible to synthesise porphyrins following this method, however the problem was addressed by Lindsey *et al* in 1987 **[16]**.

The reaction is performed under inert conditions with an acid catalyst such as boron trifluoride etherate (BF_3OEt_2) or trifluoroacetic acid (TFA), to produce a high concentration of the porphyrinogen intermediate **[16]**. To ensure that high concentrations of the cyclic porphyrinogen are produced, the reaction is performed with low concentrations (10^{-2}) of the pyrrole and desired benzaldehyde. Following completion of the formation of porphyrinogen a chemical oxidant, 2,3,dichloro-5-6-dicyanobenzoquinone (DDQ), which is hydrogenated in situ to form 2,3,dichloro-5-6-dihydroxyphthalonotrile is added to convert the porphyrinogen to the corresponding porphyrin **[16]**, (**Scheme 1.2**).

The advantages of this method are that it allows functional groups that are acid sensitive to be introduced, as well as allowing more facile purification and higher yields, hence this method was employed in this work.

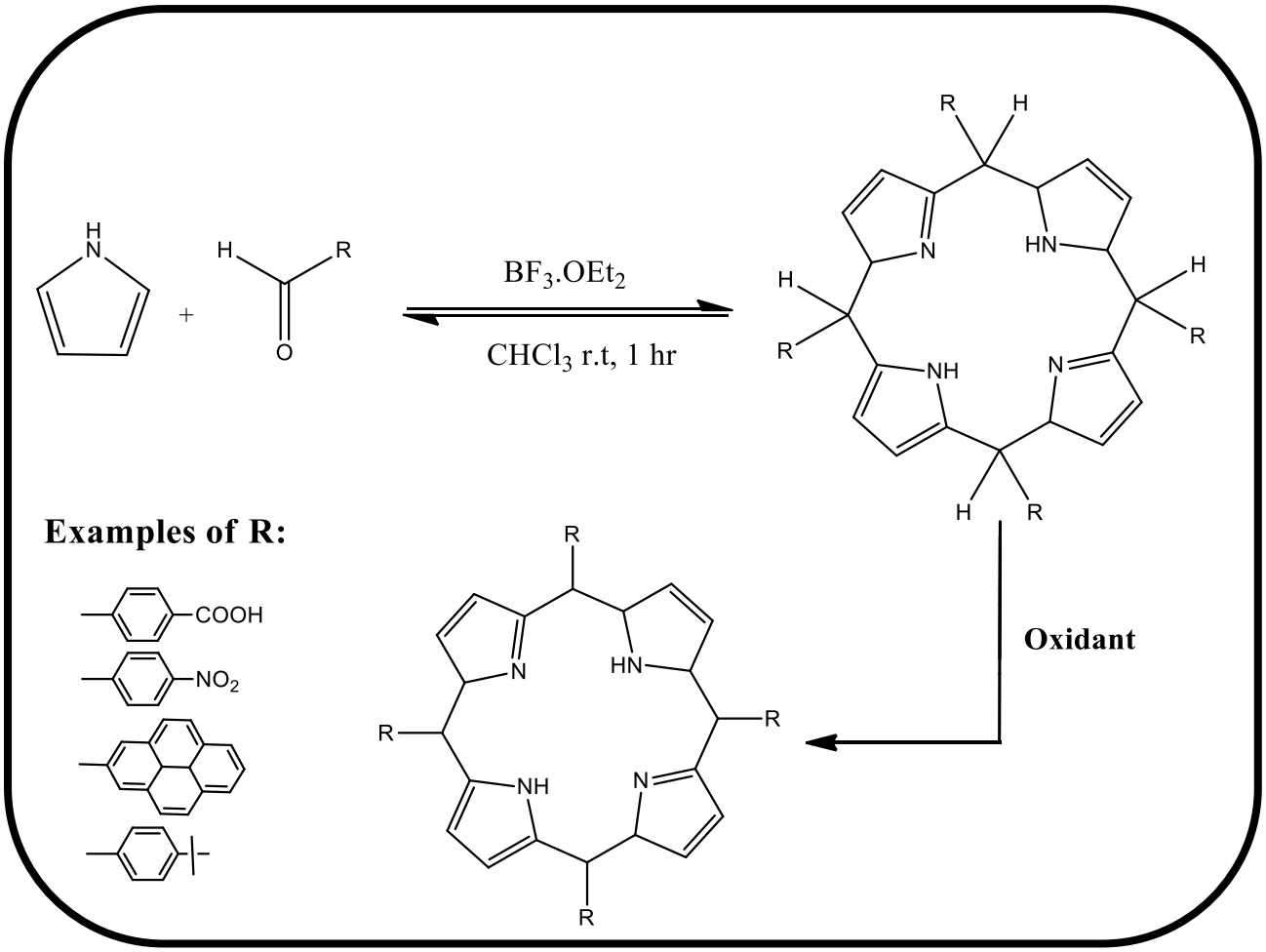

Scheme 1.2: Lindsey synthetic route.

The synthesis of asymmetric Pcs can be achieved by using different methods namely statistical mixed condensation route [**17,18**], subphthalocyanine ring expansion route [**17,19**] and polymeric-support based route [**17,20**]. Statistical mixed condensation has been the most utilized protocol for the synthesis of asymmetrical Pcs (**Scheme 1.3**) with three identical and one non-identical isoindole subunits (A_3B, B_3A) due to simplicity and high yields which are usually obtained from this approach, but mixtures are obtained, and extensive chromatography is required. This synthetic route was used in this work.

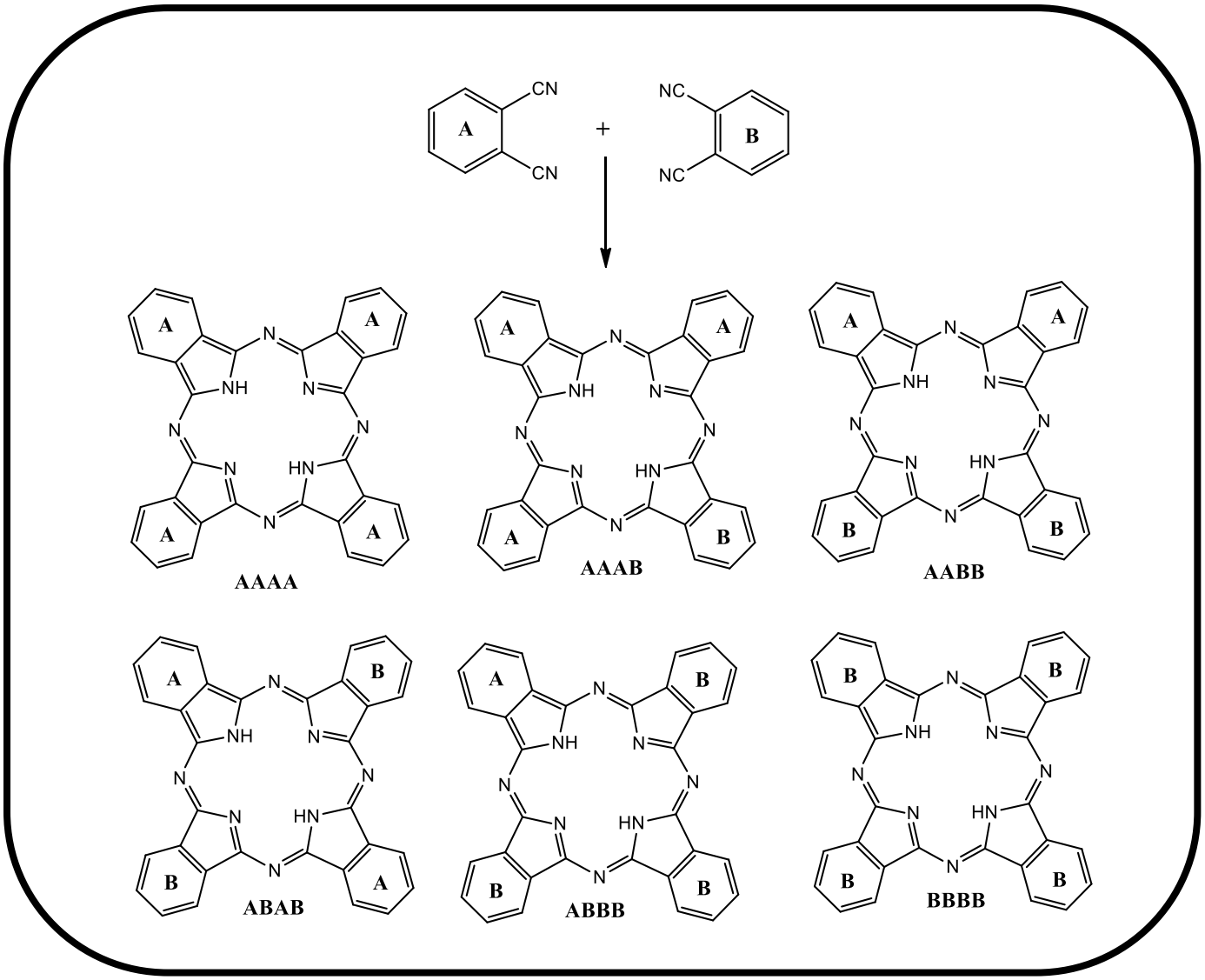

Scheme 1.3: Synthetic route for asymmetrical Pcs through statistical mixed condensation approach.

1.1.3. Electronic absorption spectra of porphyrins and phthalocyanines

The absorption spectra of porphyrins and phthalocyanines has long been understood in terms of the Gouterman's four-orbital model **[21]**. In this model, the two highest occupied molecular orbitals (HOMO), the a_{1u} and a_{2u} and lowest unoccupied molecular orbitals (LUMO), the degenerate e_g are taken into account **[22]**, **Fig. 1.2**.

Orbital mixing of the HOMO and LUMO splits the energy states and therefore gives rise to 2 distinct spectral regions of porphyrins. A high energy state is formed that creates the dominating porphyrin Soret or B band between 380-420 nm and the low energy state gives rise to the less intense Q bands. The Q bands are observed between 500-600 nm **[22,23]**, four Q bands are observed for metal free porphyrin (**Fig. 1.3A**). In the presence of a central metal which adds symmetry to the macrocycle, the Q bands are reduced to two **[23-25].**

While the Q band of Pcs occurs as a result of the $\pi \rightarrow \pi^*$ transitions from the a_{1u} of the HOMO) to the e_g of the LUMO of the MPc ring **Fig. 1.2**. The Q band is observed between 670-1000 nm in Pcs [**26**]. The Soret or B band which arises from the transition from a_{2u} and b_{2u} to the e_g level is usually broad compared to the Q band. This is due to the superimposition of the B_1 and B_2 bands [**26**].

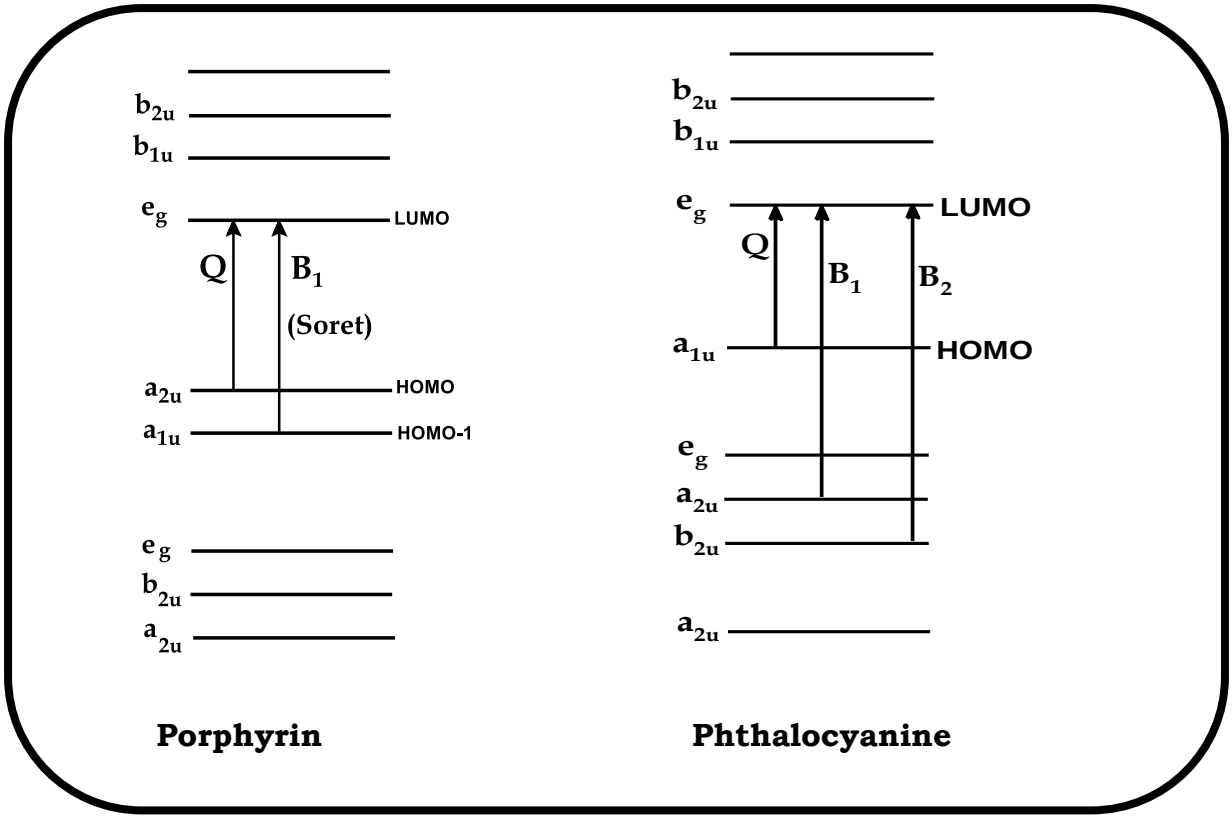

Figure 1.2: Electronic transitions in porphyrins and phthalocyanines showing the origin of Q and B (Soret) absorption bands

For H_2Pc, the Q band splits into a two (**Fig. 1.3A**), due to the low symmetry compared with metallophthalocyanine **[27]**. The energy transitions between the HOMO and LUMO can be affected not only by metal centre, but also substituents on the porphyrin or phthalocyanine core which in turn alters the electronic absorption spectra.

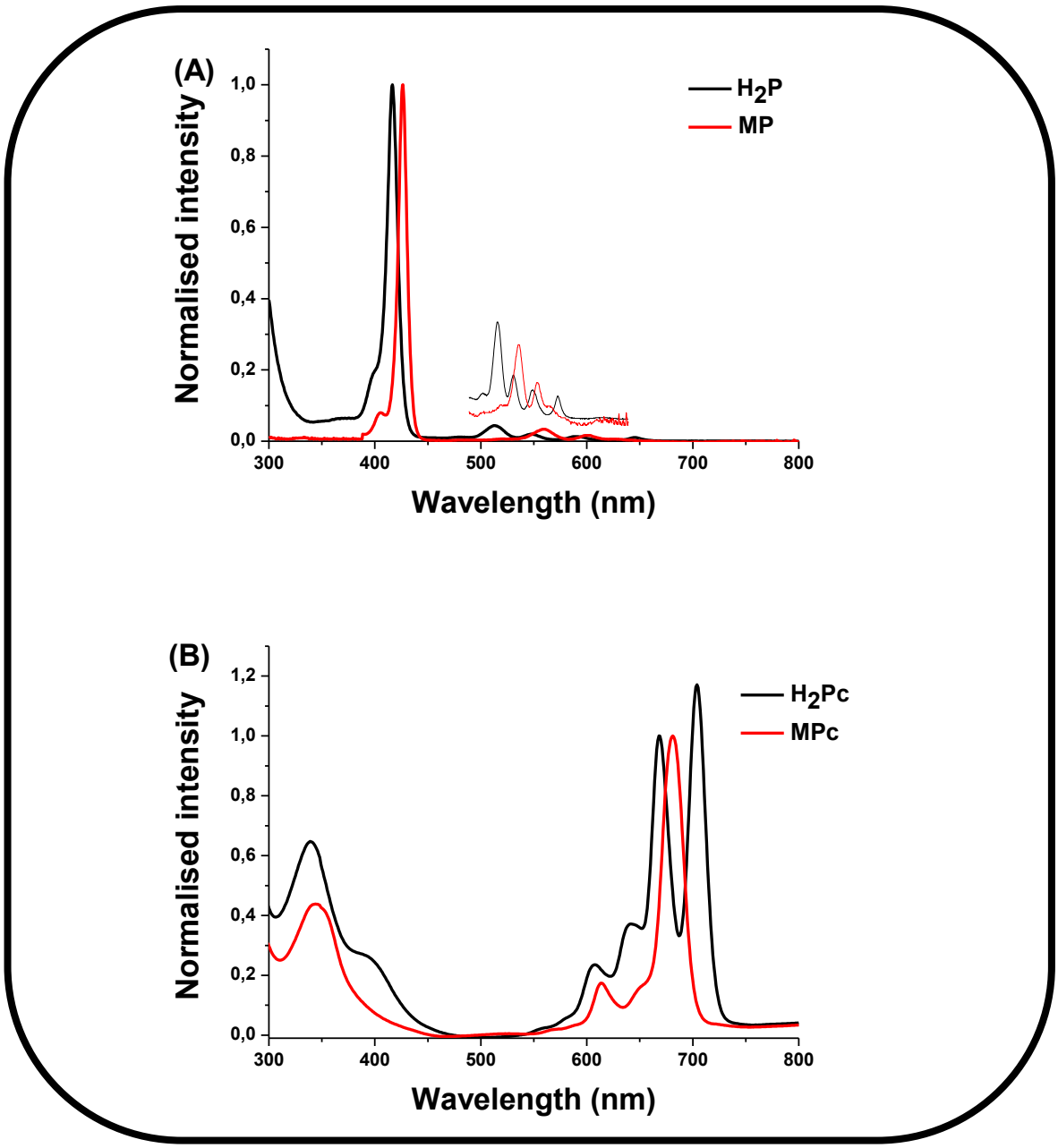

Figure 1.3: Ground state electronic absorption spectra of unmetallated and metallated porphyrin (A) and phthalocyanine (B) [Unpublished work].

1.1.4. Porphyrins and phthalocyanines that were synthesized in this work.

Porphyrins that were synthesized in this work are shown in **Table 1.1** (**complexes 1-8**) and phthalocyanines are shown in (**Fig. 1.4**). The central metals (Zn, Ga, Si, In) were chosen due to their diamagnetic nature. Ga, In and Zn as central metals have been shown to improve triplet and singlet oxygen of porphyrins and phthalocyanines due to the heavy atom effect which encourages intersystem crossing to the triplet state due to their size, therefore singlet oxygen production will be increased **[28]**. Metal free porphyrins were also prepared. Porphyrins in this work are new except for metal free derivatives of **complexes 1**-H_2**, 3**-H_2, **4**-H_2, **5**-H_2, **6**-H_2 and **8**-H_2 **[29-34]** and **complex 8** metalled with Zn **[34]**. For **complex 2**, the COOH substituent was employed for amide bond as to link to Pluronic Silica (PLuS) nanoparticles (NPS)

Table 1.1: Structures of porphyrins synthesised in this work[a]

Structure	Substituents	Abbreviation
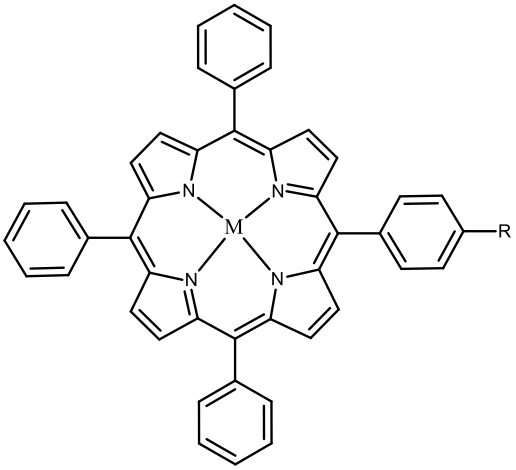	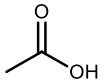 **1**	M=H_2 (**1**-H2) [**29**] ClGa (**1**-ClGa)
	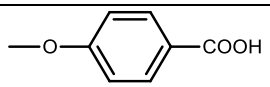 **2**	M=H_2 (**2**-H_2) ClGa (**2**-ClGa) Zn (**2**-Zn) Cl_2Si (**2**- Cl_2Si)
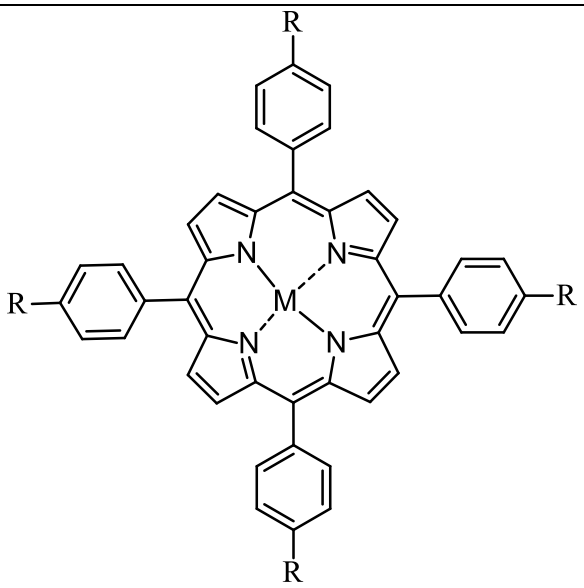	NO_2 **3**	M = H_2 (**3**-H_2) [**30**] ClGa (**3**-ClGa)
	SO_3H **4**	M=H_2 (**4**-H_2) [**31**] ClGa (**4**-ClGa)
	Br **5**	M = H_2 (**5**-H_2) [**32**] ClGa (**5**-ClGa)
	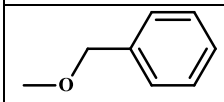 **6**	M = H_2 (**6**-H_2) [**33**] Zn (**6**-Zn)

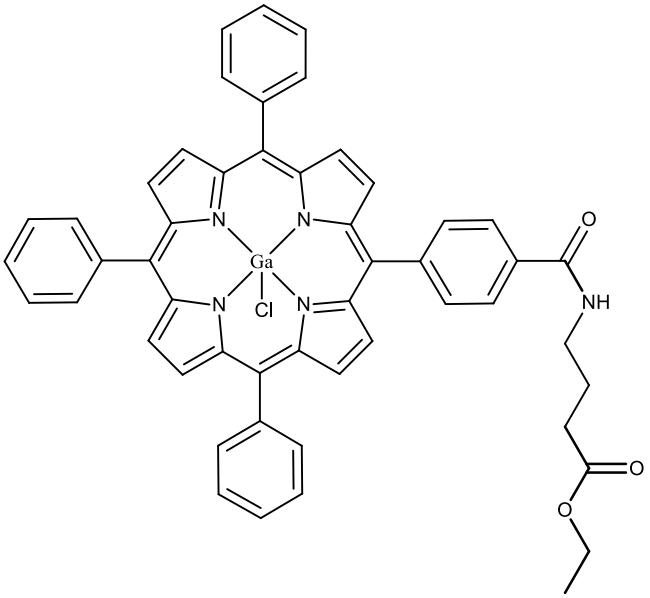	- **7**	**7**-ClGa
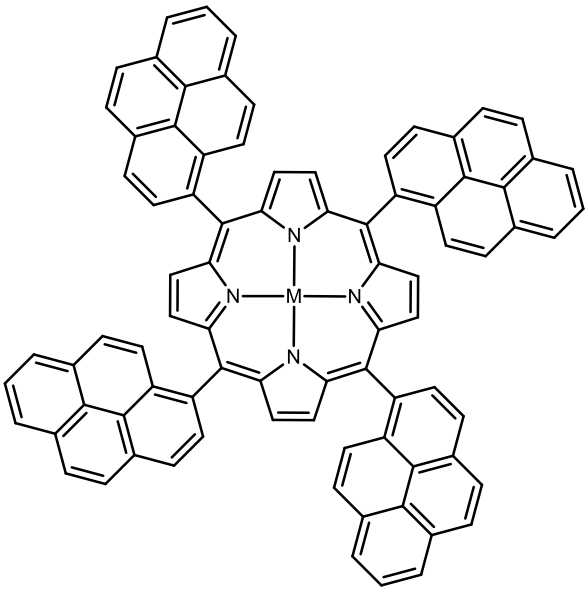	- **8**	M=H_2 (**8**-H_2) [**34**] Zn (**8**-Zn) [**34**] ClGa (**8**-ClGa)

[a]**Names of the complexes in Table 1.1:** [**1**-H_2] = 5-(4-carboxyphenyl)-10,15,20-tris(phenyl)porphyrin and metalled derivative = [**1**-ClGa]. [**2**-H_2] = 5-(4-(4-carboxyphenoxy) phenyl)-10,15,20-tris(phenyl)-porphyrin and metallated derivatives = [**2**-ClGa], [**2**-Zn] and [**2**-Si]. [**3**-H_2] = 5,10,15,20-tetra(4-nitrophenyl) porphyrin and metalled derivative = [**3**-ClGa]. [**4**-H_2] = 5,10,15,20-tetra(4-sulfophenyl) porphyrin and metalled derivative = [**4**-ClGa]. [**5**-H_2] = 5, 10, 15, 20-tetra(4-bromophenyl) porphyrin and metalled derivative= [**5**-ClGa]. [**6**-H_2] =H_2 5,10,15,20-tetra[4-(benzyloxy) phenyl] porphyrin and metalled derivative = [**6**-Zn]. [**7**-ClGa] = **2**-ClaGa (ALA linked). [**8**-H_2] = 5,10,15,20-tetra(1-pyrenyl) porphyrin and metalled derivatives = [**8**-ClGa] and [**8**-Zn].

Phthalocyanines that have been synthesised in this work are asymmetrical and were metalled with indium and gallium (**complexes 9**).

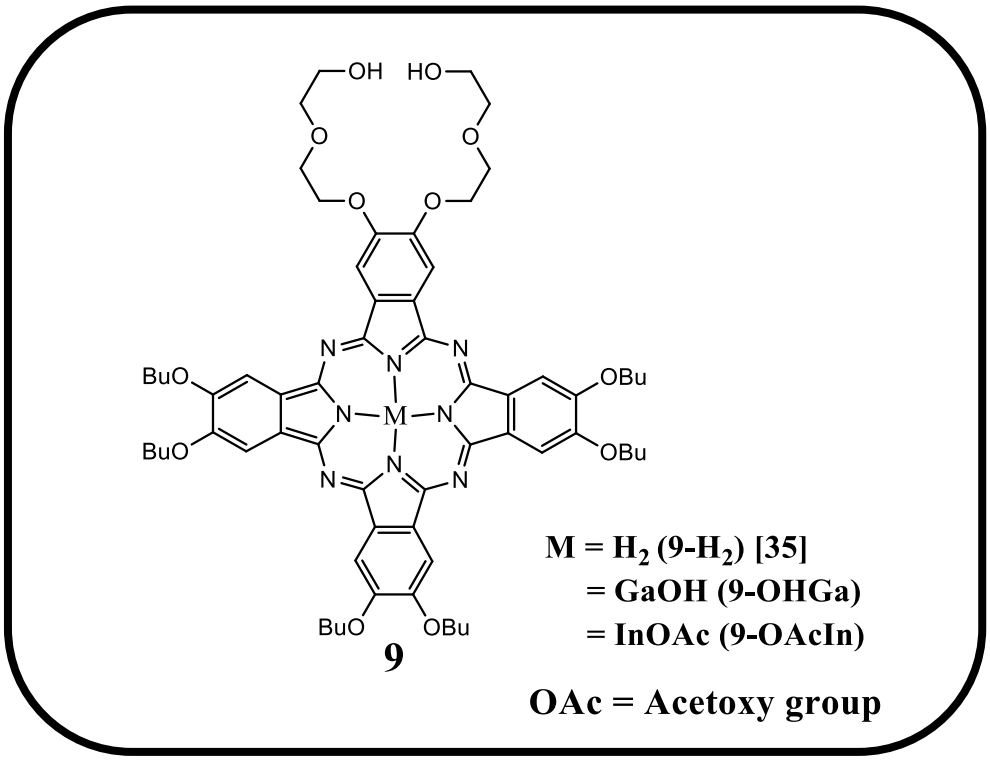

Figure 1.4: Structures of phthalocyanines synthesised in this work

Names of the complexes in Figure 1.4: [**9**-H_2] = 2,3-bis [2'-(2''-hydroxy ethoxy) ethoxy] -9,10,16,17,23,24- hexa-n-butoxyphthalocyanine [**35**] and metalled derivatives = [**9**-OHGa] and [**9**-OAcIn] which are new.

1.2. Pluronic polymer micelles

Pluronic™ block copolymers (also known under their non-proprietary name 'poloxamers') are nonionic polymers comprised of two blocks of poly(ethylene oxide) (PEO) separated by a central block of poly(propylene oxide) (PPO) arranged in A-B-A triblock structure as illustrated (**Fig. 1.5**). The PEO and

PPO segments on the micelles act as hydrophilic corona and hydrophobic core, respectively **[36-39]**.

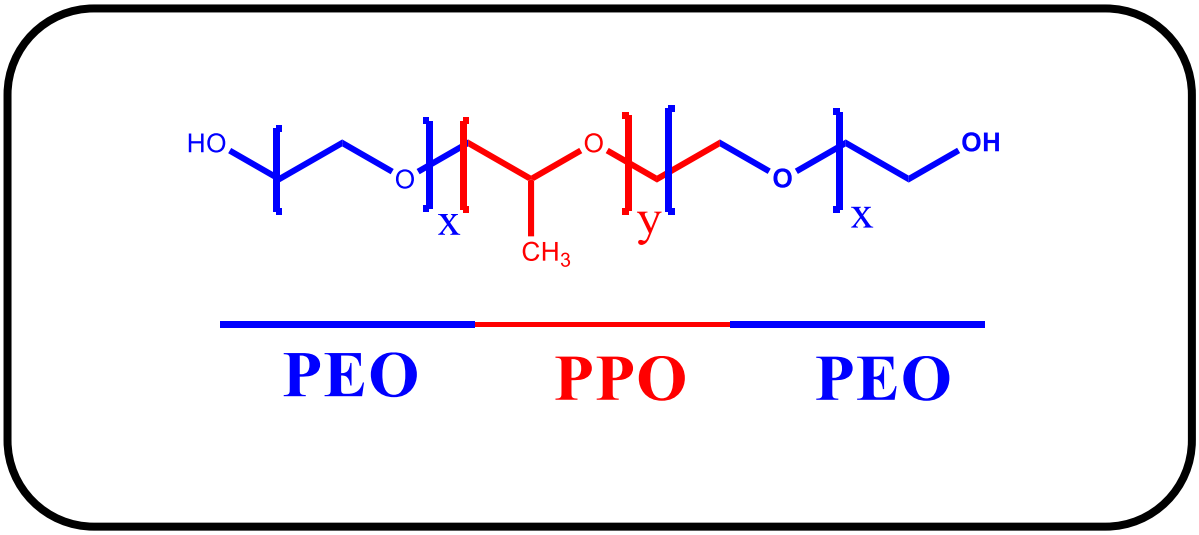

Figure 1.5: Schematic representation of the arrangement of Pluronic polymer

Pluronic™ block copolymers are appealing because their physicochemical properties are much tuneable. The advantages of Pluronic block copolymers are that they are available commercially in very broad compositions and they are regarded as being cost effective.

A defining property of amphiphilic block copolymers is the ability of individual block copolymer termed 'unimers', to self-assemble into micelles in aqueous solutions. The formed micelles can have an estimated diameter of 30–50 nm at concentrations equal to or above the critical micelle concentration (CMC) **[40-43]**. The CMC is very important because it determines the stability of micelles against possible dilution of the drug delivery system and also specifies the maximal achievable concentration of Pluronic unimers to the targeted cells **[41,43]**.

The micelles can be spherical, rod-like, or lamellar depending on the length of the ethylene oxide (EO) and propylene oxide (PO) blocks, concentration of the block copolymers, and the temperature **[44]**.

Polymer micelles are fast becoming a powerful nanomedicine platform for cancer therapeutic applications because of their biocompatibility and relatively small size, which help to prevent them from being recognized by proteins and macrophages therefore allowing a greater circulation time **[45]**. Polymer micelles also can solubilize water insoluble drugs **[46]**. Several Pluronics have been approved by Food and Drug Administration (FDA) for oral or intravenous administration because they are widely employed as solubilizers, emulsifiers or coating agents due to their biocompatibility and high drug loading ability **[45, 47-49]**

1.2.1. Incorporation of porphyrins into Pluronic polymers

There are different methods that can be used to incorporate drugs into polymer micelles such as dialysis, emulsion and evaporation methods [**50**]

Under the evaporation methods there is solid dispersion and film formation **[51]**. Solid dispersion method involves cosolubilization of copolymer with the porphyrin (**Fig. 1.6**), followed by rotative evaporation. The mixtures are then placed on a sonicator at room temperature and solvent is removed **[52]**. The achieved solid products are left in a vacuum desiccator, followed by hydration and vigorous stirring. The solutions are transferred onto test tubes and left undisturbed for precipitation of porphyrins which were not bound onto the polymer, which are then filtered **[52, 53]**.

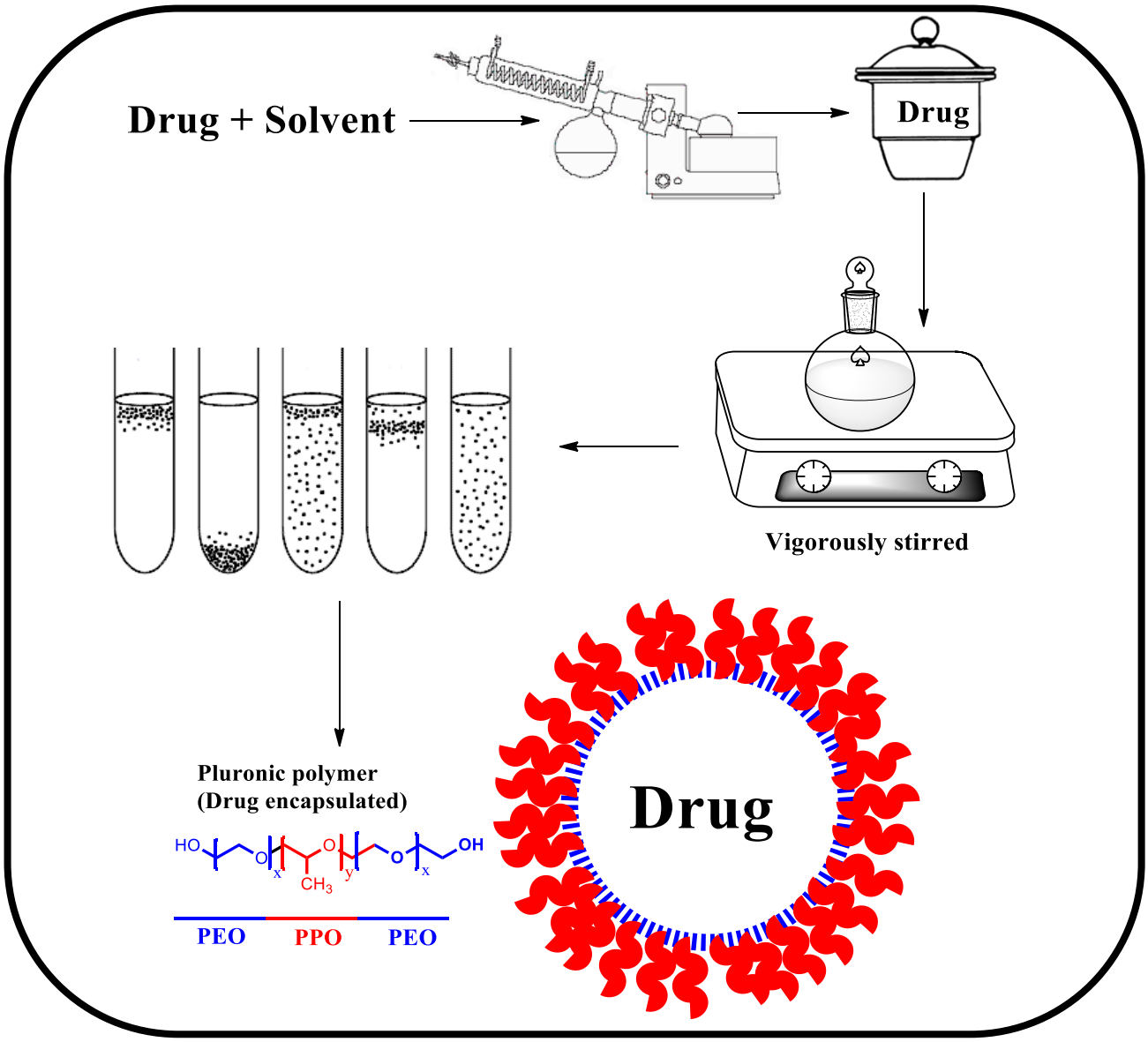

Figure 1.6: Schematic representation of incorporation of drugs into Pluronic polymers.

Film formation method involves the addition of the drug into a polymer solution. The organic solvents are removed under vacuum and a drug–polymer film is obtained. Micelles are formed by extensive vortexing of this film in Hepes buffer solution (HBS), pH 7.4. Non-incorporated drug are separated by filtration of micelle suspension **[51]**. The solid dispersion method was employed in this work. There have been drugs (porphyrins) that have

been embedded into different Pluronic polymers reported in literature [**54-61**] as shown in **Table 1.2**.

Table 1.2: Porphyrins, which have been embedded in individual Pluronic polymers.

Compound	Pluronic polymer	Photophysical studies	Reference
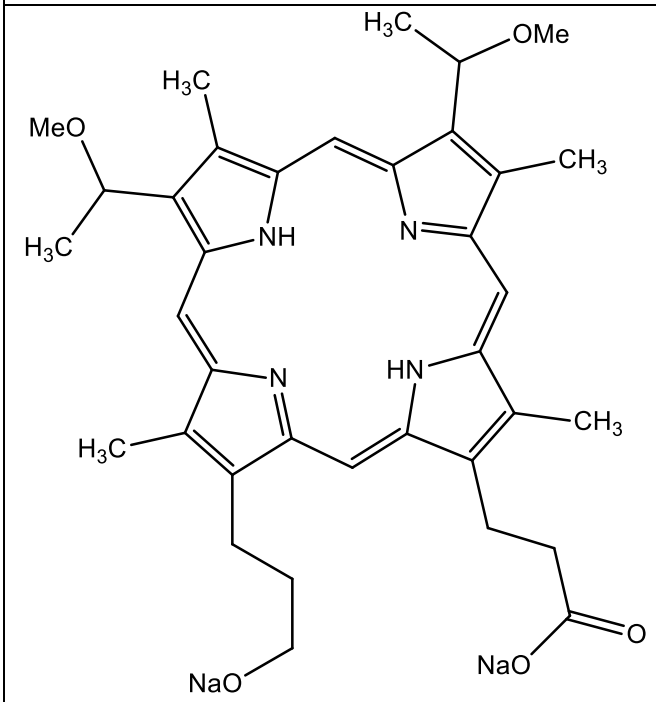	F108, F127, P85, P123, L61 and L64	Singlet oxygen quantum yields	**[54, 55]**
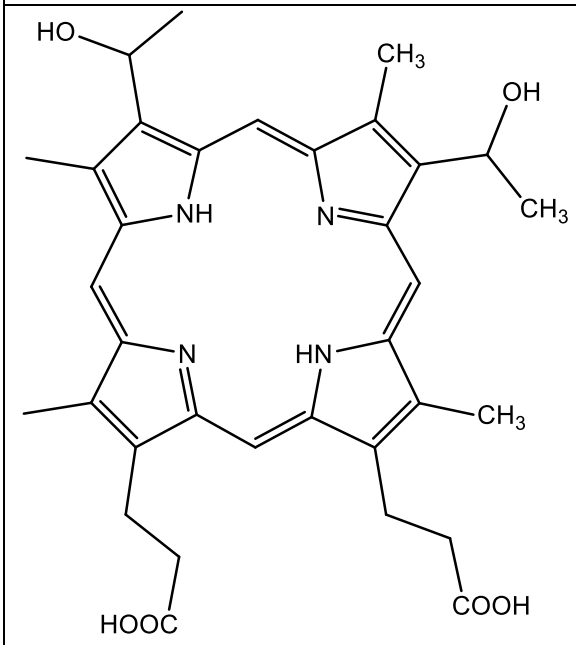	F127, P108 and L122	Fluorescence quantum yields and Singlet oxygen quantum yields	**[56]**

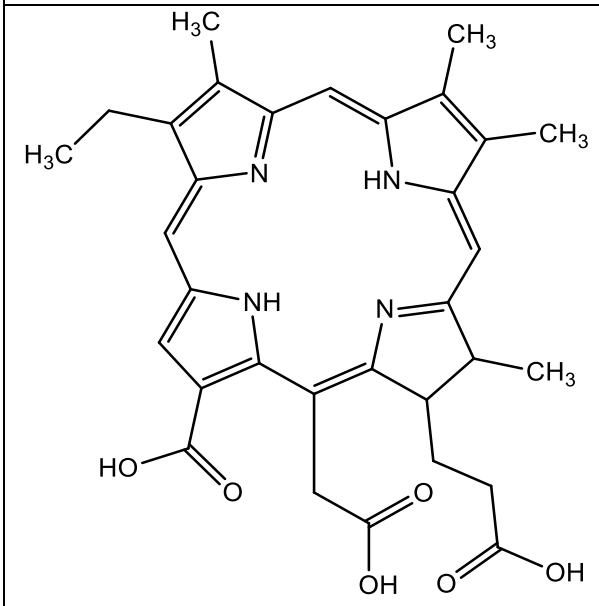	F127	Singlet oxygen quantum yields	**[57]**

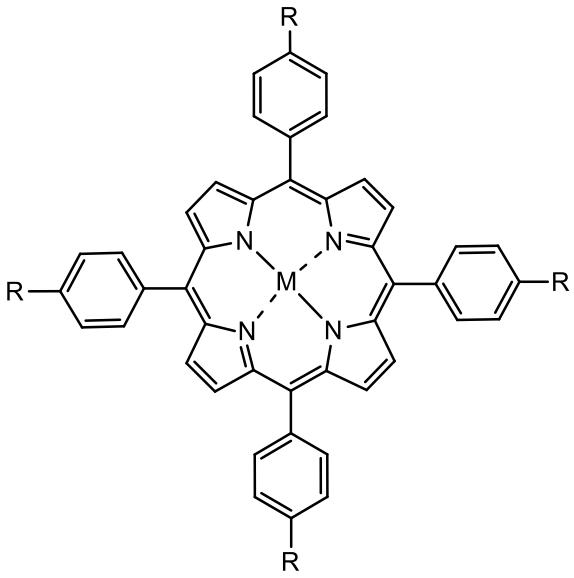 **M =H_2** **R = H**	F127	Singlet oxygen quantum yields	**[54,58]**
M =H_2 **R = OH**	F127, P108 and L122	Fluorescence quantum yields	**[57]**
M =H_2 **R = $N(CH_3)^+$)** **= OH** **= SO_3H** **= COOH**	F68, F127, P123 and L44	-	**[59]**
M =H_2 **R =** 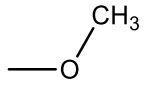	F127 and P123	-	**[60]**
M =H_2 **=Zn** **R =** 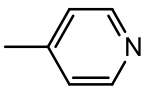 **=** 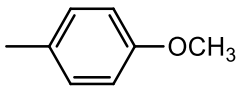	F127 and P123	Fluorescence quantum yields	**[61]**

As **Table 1.2** shows that are very few asymmetrical porphyrins [**56-58**] embedded into Pluronic polymers, and there are no phenyl substituted asymmetrical porphyrin embedded into Pluronic polymer hence **complexes 1-2** are synthesised in this work. Asymmetric porphyrins show a better efficacy in PDT, since the cellular affinity depends on amphiphilic character, that is, on the structural arrangement of hydrophilic (phenolic −OH or carboxylic −COOH) and hydrophobic (alkyl or aryl chains) meso-substituents on the macrocycle **[62]**. **Complexes 1-8** that contain heavy central metals are embedded into Pluronic polymers for the first time.

It has been demonstrated that binary mixture of Pluronics may compensate for drawbacks of a single Pluronic system **[63]**. The encapsulation of porphyrin derivatives into binary mixture system micelles resulted in monomerization and enhanced photophysical properties and stability **[64]**. Binary mixtures allow higher loading capacity than mono systems **[63]**. **Table 1.3.** shows porphyrins that have been embedded into binary mixture of Pluronic polymers [**64-66**].

Table 1.3: Porphyrins embedded into Binary mixture of Pluronic polymers.

Compound	Pluronic polymer	Photophysicochemical studies	Reference
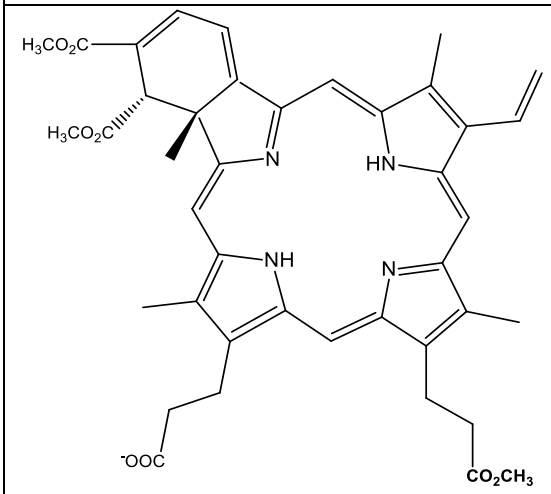 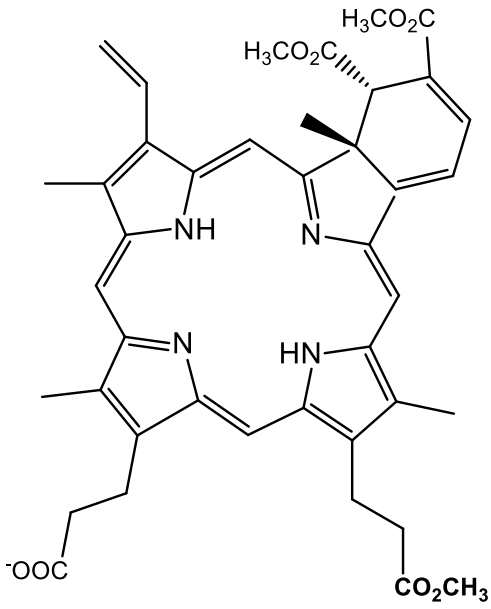	P123/F127	Fluorescence quantum yields and Singlet oxygen quantum yields	**[64,65]**

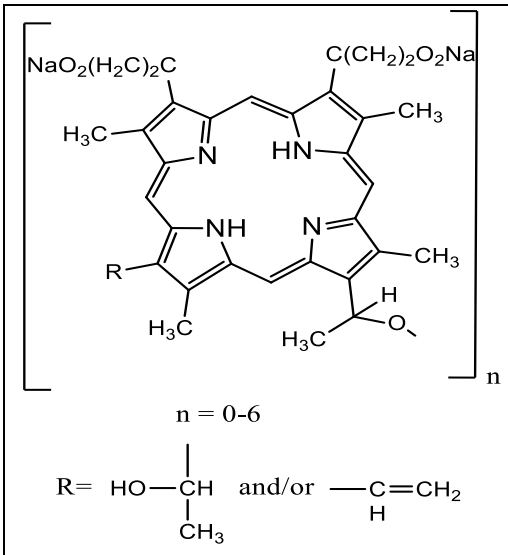	P123/F127	Singlet oxygen quantum yields	**[66]**

Table 1.3 shows that there are no metallated porphyrins or porphyrins that have substituted with phenyl groups that have been embedded into binary mixtures hence this is reported for the first time in this work using **complex 6** as an example.

Table 1.4. shows the complexes that are studied in this thesis indicating the Pluronic polymers that they have been imbedded in as well as the photophysical studies that were carried out for the nanoconjugates.

Table 1.4: Pluronic-Porphyrin conjugates studied in this work.

Complex	**Pluronic polymer**	**Studies**
1-H_2 and **1**-ClGa	F127	**Photophysics:** Fluorescence quantum yields, life-times and singlet oxygen quantum yields Fluorescence quenching **Cell studies:** Cytotoxicity effect on MCF-7 breast cancer cells
2-H_2, **2**-ClGa, **2**-Zn and **2**-Cl_2Si **2**-H_2, **2**-ClGa, **2**-Zn and **2**-Cl_2Si	Linked to PLuS NPs F127	**Photophysics:** Fluorescence quantum yields, life-times and singlet oxygen quantum yields Fluorescence quenching **Cell studies:** Cytotoxicity and PDT effect on MCF-7 breast cancer cells

3-H_2, **3**-ClGa, **4**-H_2, **4**-ClGa, **5**-H_2 and **5**-ClGa	F127 F127 F127 linked to Folic acid	**Photophysics:** Fluorescence quantum yields, life-times and singlet oxygen quantum yields Fluorescence quenching
6-H_2, **6**-Zn	F127/P123	**Photophysics:** Fluorescence quantum yields, life-times and singlet oxygen quantum yields Fluorescence quenching
7-ClGa	-	**Photophysics:** Fluorescence quantum yields, life-times and singlet oxygen quantum yields Fluorescence quenching **Cell studies:** Cytotoxicity effect on MCF-7 breast cancer cells
8-H_2, **8**-ClGa and **8**-Zn	F127	**Photophysics:** Fluorescence quantum yields, life-times and singlet oxygen quantum yields

		Fluorescence quenching **Cell studies:** Cytotoxicity and PDT effect on MCF-7 breast cancer cells

1.2.2. Pluronic Silica nanoparticles (Plus NPs)

The linking of these nanoparticles to porphyrins does not allow for the formation of micelles. These studies were done to compare with Pluronic micelles for **Complexes 2**. Polymers on the surface of nanoparticles are of great scientific and technological importance since they dictate many important properties and functions of dispersed systems **[67].** As previously mentioned Pluronic polymers can be used as surfactants hence they were used in the synthesis of silica nanoparticles (SiNPs) in this work.

The advantage of using Pluronic polymer for the synthesis of nanoparticles is that the pore size can be regulated by using different temperatures therefore one can obtain nanoparticles with small size. Plus NPs have low toxicity, show photophysical inertness, have high surface to volume ratio which allows linking to photosensitizers such as porphyrins which was done in this work.

Porphyrins have been encapsulated into mesoporous SiNPs for drug delivery **[68,69]**. Porphyrins have also been covalently grafted onto mesomeric SiNPs **[70]**. The formation of nanoparticle–Pluronic–porphyrin conjugate where Pluronic moiety (not as nanoparticles) acts as a bridge has been reported **[71]**. This work reports for the first time on a more controlled grafting of porphyrins

onto PluS NPs. **Complexes 2** were linked to Plus NPs making use of COOH group of the porphyrin and OH of the NPs

The synthesis of Plus NPs is highly depended on the interaction between the silica and PEO (**Fig. 1.7**). It has been said that generally hydrogen bonding is responsible for the attraction. The synthesis is comprised of two steps. The tetraethyl orthosilicate (TEOS) is first hydrolysed and the Pluronic is subsequently added at different times after the hydrolysis. The variation of the time between the hydrolysis and the addition of Pluronic is used to vary the degree of condensation of the silica source **[72,73]**.

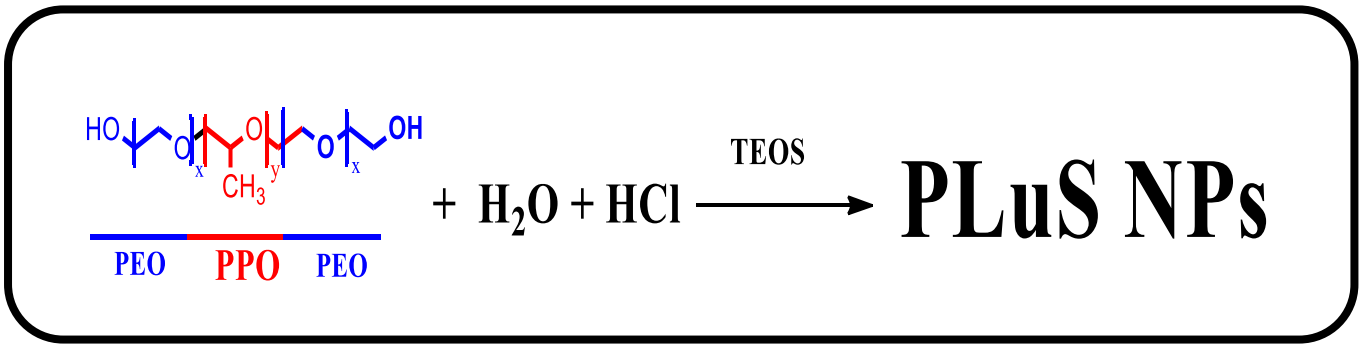

Figure 1.7: Synthetic route of PLuS NPs.

1.2.3. Pluronic polymer linked to Folic acid

The terminal hydroxyl groups of Pluronic polymer are easy to modify in order to enhance tumor targeting ability and improve the stability of polymeric micelles. Pluronic triblock-copolymer has been conjugated to folic acid (FA) **[74]**. FA (structure shown in **Fig. 1.8**) is essential for cell replication and cell growth. Folic acid is acquired by cells through the presence of folate receptors (FRs) **[75]**. Tumor cells grow rapidly as their vasculature tends to be different

from normal cells. During the rapid cell proliferation, the majority of malignant cells overexpress folate receptors and other antigens that help them multiply more quickly **[75]**. Thus, cancer cells that are most difficult to treat with classical methods can be easily targeted with folate linked therapeutics **[76,77]**. There are no reports of porphyrin that have been embedded into Pluronic-FA micelles system, hence this is the subject of this work, such system will act as the transport and targeting moiety. **Complex 5** was used as an example and embedded in Pluronic-FA

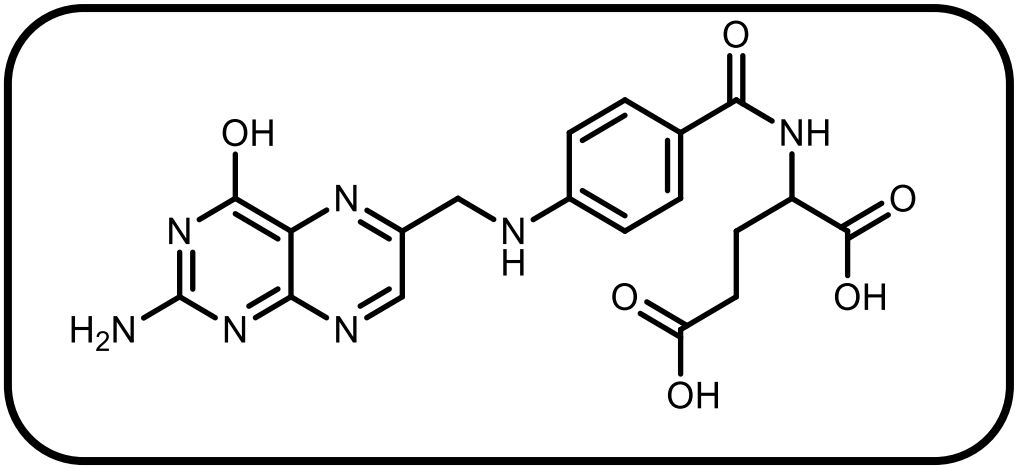

Figure 1.8: Structure of Folic acid (FA).

1.2.4. Porphyrins linked to ALA

In this work porphyrin was linked a to ethyl ester functionalised δ-aminolevulinic acid (ALA) (**Complex 7**). ALA is a prodrug and a precursor for the biosynthesis of porphyrin IX for photodynamic therapy (PDT) [**78-80**]. ALA and its esters have been an approved treatment of several malignant and premalignant conditions including actinic keratosis, basal cell carcinoma,

Bowen's disease and bladder cancer **[81]**. Even though ALA has been used for the biosynthesis of porphyrins, the conjugates of the two have not been reported in literature, hence are reported in this work.

1.3. Use of porphyrins loaded into Pluronic micelles in Photodynamic therapy (PDT).

Photodynamic therapy (PDT) has continued to gain attention as an effective treatment approach for some cancers. PDT involves administration of a tumor localizing photosensitizing agent, followed by activation of the photosensitizer by light of a specific wavelength **[82,83]**. The electronically excited photosensitizer (porphyrin) transfers its energy to ground state molecular oxygen to produce excited singlet oxygen, which acts as the chief cytotoxic species and thus, results in irreversible photo-damage of the tumor cells **[83,84]** (**Fig. 1.9**). Even though porphyrins are well-known photosensitizers for PDT **[83]**, their drawback is that they are known to aggregate **[85]**, which affects their photophysical behaviour. The driving forces behind the aggregation of porphyrins are the cooperative formation of hydrogen bonds, van-der-Waals forces and the hydrophobic effects **[86-88]**.

Pluronic triblock copolymers reduce the self-aggregation and increase solubility of porphyrins in aqueous media **[58,88]**. Encapsulation of porphyrins into Pluronic micelles results in water solubility of the conjugate for porphyrins that are not water soluble **[58,89]**. **Complexes 1-3, 5,6** and **8** became water soluble upon encapsulating into Pluronic polymer.

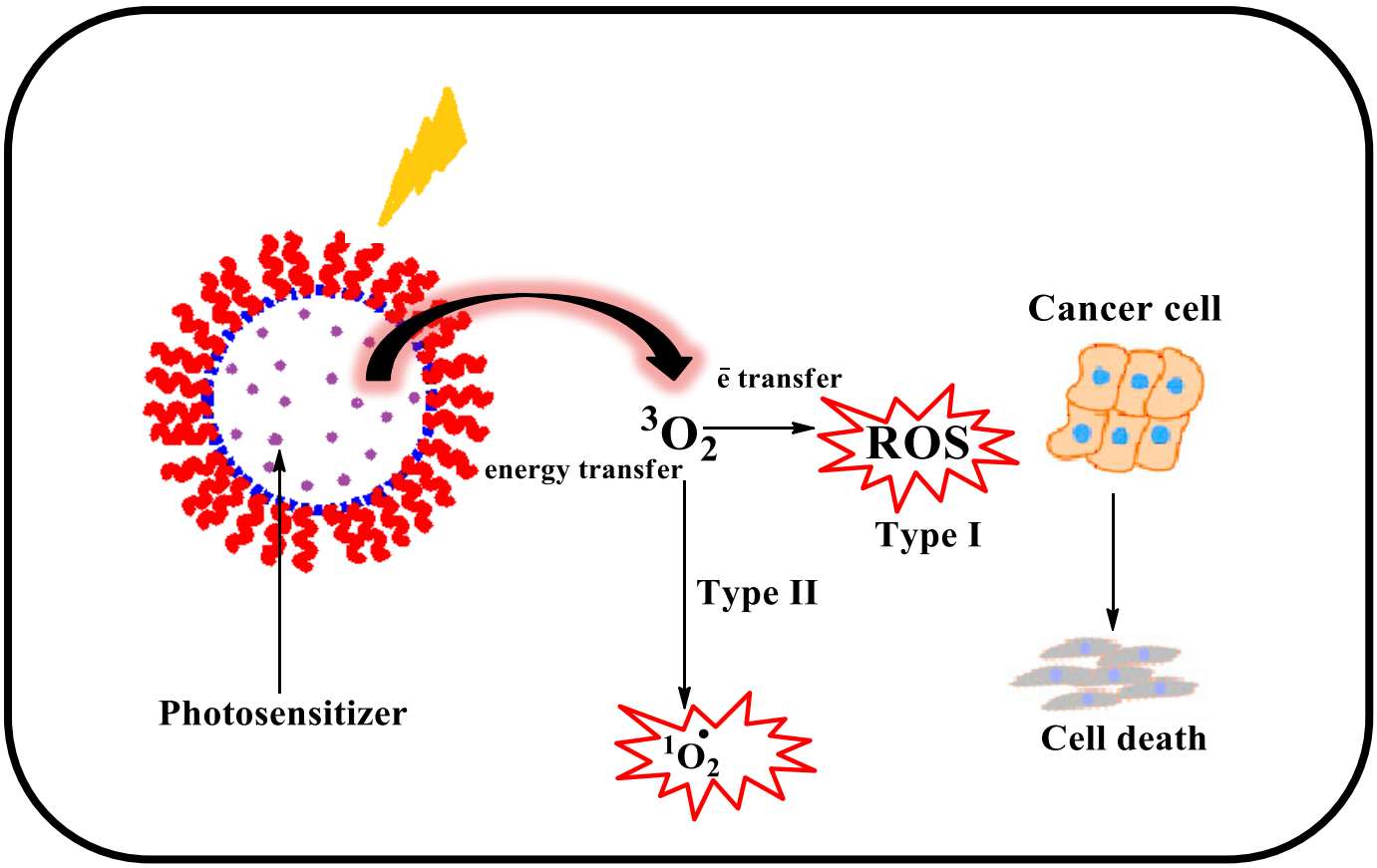

Figure 1.9: Schematic illustration of PDT

This work is based on synthesis of porphyrins and encapsulating/linking them to Pluronic polymers for PDT. A few porphyrins are already in clinical trials such as Photofrin®, Levulan®, Metvix® and Visudyne® **[90]**. None of the porphyrins in clinical trials have been metalled with heavy elements or embedded into Pluronic polymers, this is for the first time being reported in this work

1.4. Phthalocyanines as nonlinear optics (NLO) materials.

The field of nonlinear optics has been developing in the last decades with important applications including optical limiting (OL), optoelectronics and photonics [**91-93**]. Nonlinear optical (NLO) materials such as phthalocyanines can be used to manipulate optical signals in telecommunication systems and other optical signal processing applications [**94**]. Phthalocyanines are regarded as a good NLO material because of the high delocalized π- electron system [**95-97**], ease of structural modification, good optical properties, high molar absorptivity, chemical and thermal stability [**98-101**].

Metallophthalocyanines (MPcs) having heavy central metals such as indium or gallium exhibit better optical limiting due to the heavy metal effect, which enhances the intersystem crossing through spin orbit coupling, leading to a higher triplet state population [**102**]. Hence these central metals are used in this work.

Asymmetric MPcs (**Fig. 1.4**) are desired due to the presence of permanent dipole moment which encourages NLO response [**90,102**]. This asymmetry can be a result of different substituents being used on the Pc ring or large central metals being used in the cavity. Hence this work reports on asymmetrical Pcs metallated with heavy elements and embedded into thin films for NLO application.

Most of the work regarding Pcs as NLO that has been reported in literature is done in solution. This is good for understanding trends in NLO behaviour of materials but however it is also important to study these properties in the

solid state for real life application. This can be achieved by the formation of films. There are variety of ways in forming films for example polymer thin films and Langmuir-Blodgett films [**103**].

In this work poly(bisphenol A carbonate) (PBC) was used to embed Pcs. PBC is a common polymer that is used for the manufacturing of optical eyewear, protective sportswear and other safety products [**104-106**]. **Table 1.5 [107-109]** shows substituted phthalocyanines either metal free and metallated that have been embedded into PBC, this work reports for the first time an asymmetrical Pc containing heavy In and Ga as central metals.

Table 1.5: Known phthalocyanines used in NLO embedded in PBC

Complex	**References**
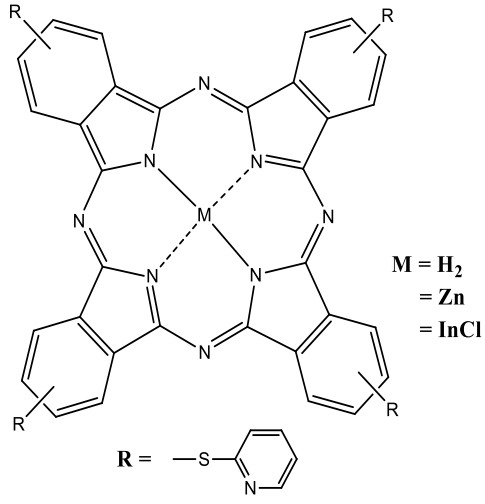	**[107]**

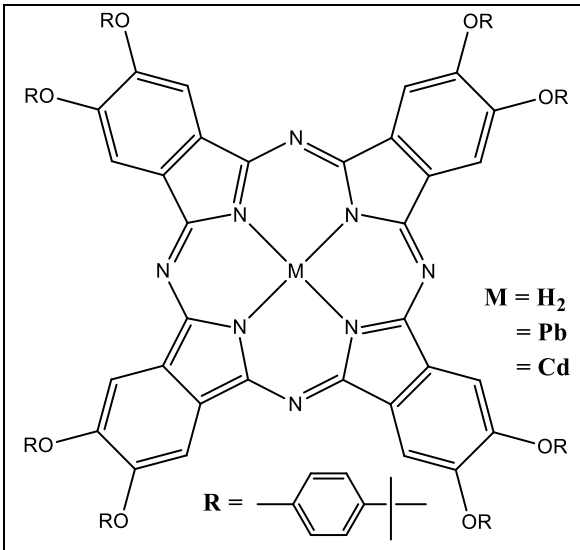	**[108]**
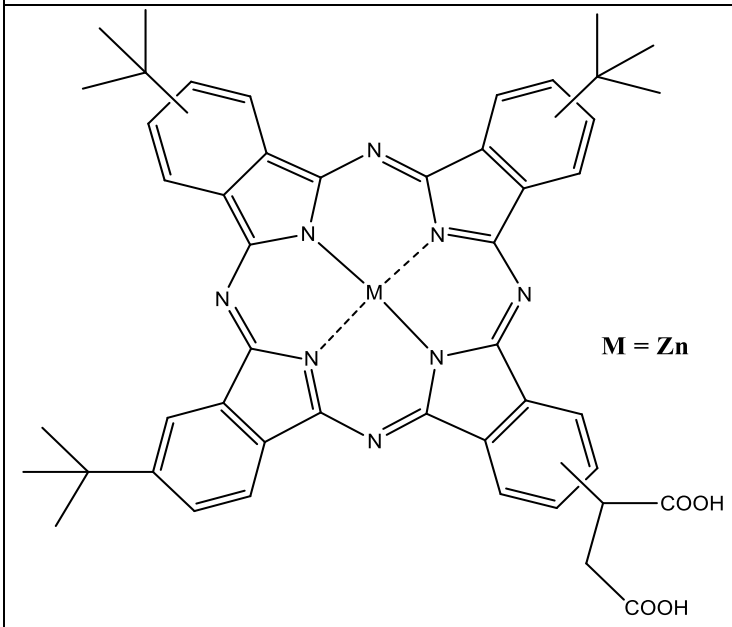	**[109]**

In this work, open aperture Z-scan technique was employed to show the strength of the nonlinear absorption [**110**]. A sample is allowed to pass through from one point to the other along the path (Z) of a focused Gaussian beam and the transmittance is measured as a function of the sample's position relative to the focus (**Fig. 1.10.**)

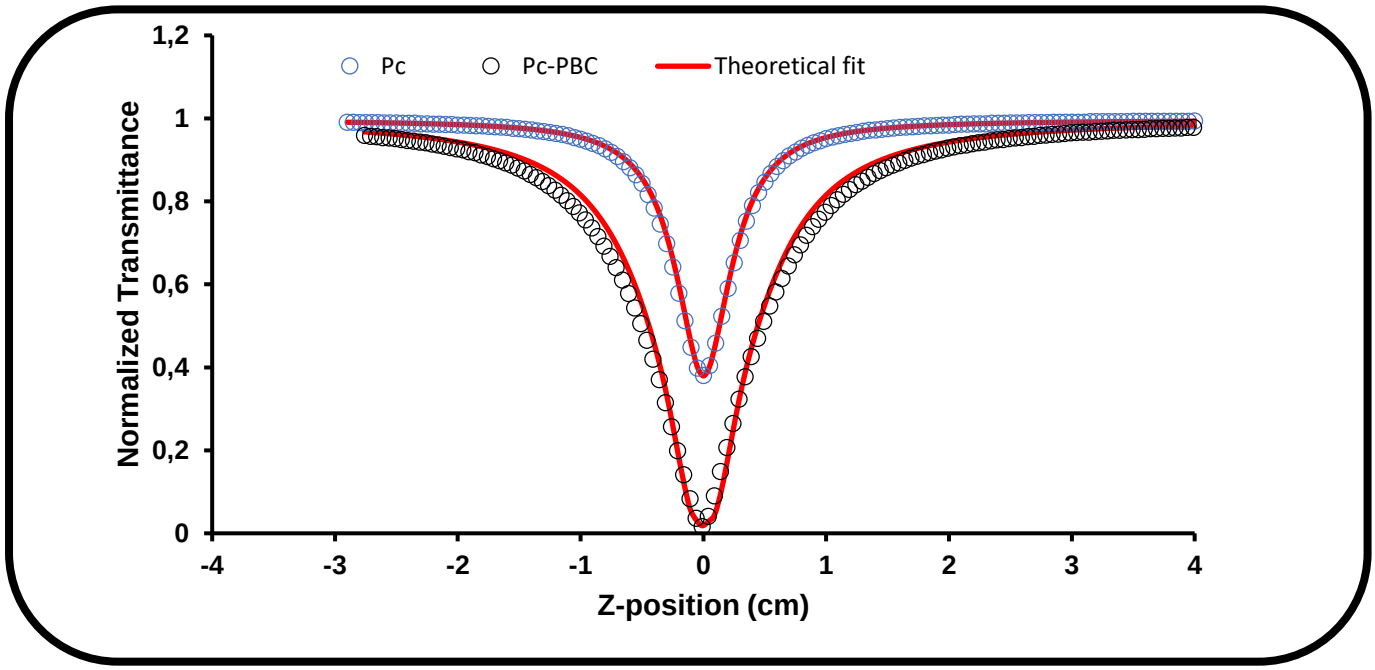

Figure 1.10: Typical open aperture Z-scan curves [Unpublished work].

Summary of aims of this thesis are:

- ✓ The Synthesis of symmetrical and asymmetrical porphyrins and covalently linking them to Pluronic silica nanoparticles/encapsulating them into Pluronic micelles.
- ✓ The photophysical (singlet oxygen quantum yield, fluorescence quantum yield and life-time) studies of the porphyrins alone or in the presence of Pluronic micelles.
- ✓ The fluorescence quenching to determine the relative location of porphyrins and interaction within the micelles
- ✓ The cytotoxicity and photodynamic effects of porphyrin derivatives alone or in the presence of Pluronic silica nanoparticles or Pluronic micelles.
- ✓ Synthesis and nonlinear behaviour of phthalocyanines in solution and thin films.

Chapter 2

Experimental

This chapter provides the materials, instrumentation, synthetic procedure of all porphyrins and phthalocyanines synthesized in this work. The cytotoxity and photodynamic therapy methods will be provided.

2.1. Materials.

2.1.1. General reagents and solvents

Tetraethyl orthosilicate (TEOS), dimethylformamide (DMF), isopropanol, deuterated dimethyl sulfoxide (DMSO-d_6), acetone-d_6, deuterated chloroform ($CDCl_3$), D_2O, petroleum ether, dichloromethane (DCM), poly(bisphenol A carbonate) (PBC), Zinc tetraphenyl porphyrin (ZnTPP) and tetra sulfophenyl porphyrin (H_2TSP) were purchased from Sigma-Aldrich. Tetrahydrofuran (THF) was purchased from MERCK. Methanol (MeOH), trifluoroacetic acid, chloroform, ethanol, ethylacetate, hexane and propionic acid were purchased from Saarchem. Hydrochloric acid was purchased from MINENA. Ultra-pure water was obtained from a Milli-Q Water System (Millipore Corp., Bedford, MA, USA).

2.1.2. Reagents for the synthesis of porphyrin and incorporation into Pluronic micelles and Photophysical/Chemical parameters

Benzaldehyde, sodium acetate, sodium azide, oxalic acid, anthracene-9,10-bis-methylmalonate (ADMA), 4-(4-formylphenoxy) acetic acid), folic acid (FA), 1-ethyl-3-(3-dimethylaminopropyl) carbodiimide (EDC), propionic acid, N-hydroxysuccinimide (NHS), N,N dicyclohexylcarbodiimide (DCC), anhydrous potassium carbonate, anhydrous sodium sulphate, pyrrole, silicon tetrachloride, zinc acetate, gallium chloride, trimethylamine (NEt_3), N,N,N′,N′-tetramethyl-O-(1H-benzotriazol-1-yl)uranium hexafluorophosphate (HBTU), Pluronic F127 (MW ~ 12,600 g/mol), Pluronic P123 (MW ~ 5800 g/mol), and potassium iodide were purchased from Sigma-Aldrich. The synthesis of metal free derivatives, 5-(4-carboxyphenyl)- 10,15,20-tris(phenyl) (**1-H_2**) [**29]**,

5,10,15,20-tetra(4-nitrophenyl) (**3-H_2**) [**30**], 5,10,15,20-tetra(4-sulfophenyl) (**4-H_2**) [**31**], 5, 10, 15, 20-tetra(4-bromophenyl) (**5-H_2**) **[32]**, 5,10,15,20-tetra[4-(benzyloxy) phenyl] porphyrin (**6-H_2**) **[33]** and 5,10,15,20-tetra(1-pyrenyl) porphyrin (**8-H_2**) as well as **8**-Zn have been reported as well **[34]**. The synthesis of ethyl ester δ-aminolevulinic acid (ethyl ester ALA) has been reported **[111]**.

2.1.3. Reagent and solvents for the synthesis of phthalocyanines

Isoamyl alcohol (*i*-AmOH), trichlorobenzene (TCB), gallium ($Ga(acac)_3$ and indium acetylacetonates ($In(acac)_3$) were purchased from Sigma Aldrich. Isoamyl alcohol was distilled over sodium under argon. The rest of the reagents were employed as received.

2.1.4. Reagents for cell work

MCF-7 breast cancer cells were obtained from Cellonex. Dulbecco's phosphate-buffered saline (DPBS), Dulbecco's modified Eagle's medium (DMEM), trypsin, trypan blue and neutral red were obtained from Lonza, 10% (v/v) heat-inactivated fetal calf serum (FCS) and 100 mg/mL-penicillin–100 unit/mL-streptomycin–amphotericin B mixture) were obtained from Biowest®. Cell proliferation reagent, WST-1, was acquired from Roche, South Africa.

2.2. Equipment

a). **Ground state electronic absorption spectra** of the complexes were performed on a Shimadzu UV-2550 spectrophotometer. Quartz cells with 1 cm path-length were used.

b). **Fluorescence emission spectra** were recorded on a Varian Eclipse fluorescence spectrofluorometer.

c). **Fluorescence lifetimes** were measured using a time correlated single photon counting setup (TCSPC), Fluo Time 200, Picoquant GMbH, with a diode laser as excitation source (LDH-P-670 driven by PDL 800-B, 670 nm, 20 MHz repetition rate). Fluorescence was detected under the magic angle with a peltier cooled photomultiplier tube (PMT) (PMA-C 192-N-M, Picoquant GmbH) and integrated electronics (PicoHarp 300E, Picoquant GmbH). A monochromator with a spectral width of about 4 nm was used to select the required measured emission wavelength. The response function of the system, which was measured with a scattering Ludox solution (DuPont), had a full width at half-maximum (FWHM) of about 300 ns. The ratio of stop to start pulses was kept low (below 0.05) to ensure good statistics. All luminescence decay curves were measured at the maxima of the emission peak. The data were analysed with the program FluoFit (Picoquant GmbH). The support plane approach was used to estimate the errors of the decay times

d). **Dynamic light scattering** (DLS) experiments were done on a Malvern Zetasizer nanoseries, Nano-ZS90 with standard 633 nm laser.

e). **Elemental analyses** for CHNS were done using a Vario-Elementar Microcube ELIII Series.

f). **Mass spectral** data were collected with a Bruker AutoFLEX III Smartbeam TOF/TOF Mass spectrometer. The instrument was operated in positive ion mode using a m/z range of 400 – 3000 amu. The voltage of the ion sources was set at 19 and 16.7 kV for ion sources 1 and 2 respectively, while the lens

was set at 8.50 kV. The reflector 1 and 2 voltages were set at 21 and 9.7 kV respectively. The spectra were acquired using α-cyano-4-hydroxycinnamic acid as the MALDI matrix and a 354 nm nitrogen laser as the ionizing source.

g). **Nitrogen adsorption/desorption isotherms** were measured at 77 K using a Micrometrics ASAP 2020 Surface Area and Porosity Analyzer. Prior to each measurement, degasing was carried at 900 ^{0}C for four days. The Brunauer–Emmett–Teller (BET) method was employed to determine surface area and porosity. The BET surface area and total pore volume were calculated from the isotherms obtained.

h). **^{1}H-nuclear magnetic resonance spectra** (^{1}H-NMR) were recorded in deuterated solvents (DMSO-d_6, acetone-d_6, $CDCl_3$-d_6, D_2O) using Bruker AMX 600 MHz spectrometer.

i). **Infrared** (IR) spectra were recorded on a Perkin–Elmer Spectrum 100 ATR FT-IR spectrometer

j). **The $^1O_2$ generation determination** was quantified using the singlet oxygen luminescence method (SOLM) and chemical method, in DMF and water respectively. For the SOLM method quantification was carried out in the absence and presence of sodium azide (NaN_3), a physical quencher of singlet oxygen, using an ultrasensitive Germanium detector (Edinburgh Instruments, EI-P) combined with a 1000 nm long pass filter (Omega, 3RD 1000 CP) and a 1270 nm band pass filter (Omega, C1275, BP50) to detect the intensity of the phosphorescence band at 1270 nm. The detection direction was perpendicular to that of a 421nm excitation beam from the optical parametric oscillator (OPO) unit of an Ekspla NT 342B-20-AW laser (0.5 mJ/7

ns, 10 Hz), which ran through a 1 cm quartz fluorescence cell holding the sample solution. The signal was averaged over 128 measurement pulses with a digital oscilloscope (Tektronix TDS 3032C) to obtain the dynamic decay curve for $^1O_2$ formation. The lifetime of the $^1O_2$ was calculated by decay curve fitting using the approach described by Wöehrle and co-workers **[112]**, and the quantum yield for $^1O_2$ formation (Φ_Δ) was determined. The data obtained was analysed using ORIGIN Pro 8 software.

The chemical method was employed in water due to the low singlet oxygen phosphorescence signal. The two methods have been compared and found to give similar results [**112**]. The singlet oxygen quantification in water was carried out using General Electric Quartz lamp (300 W) as irradiation source. Water filters were used to filter off ultra-violet and far infrared radiations, respectively **Fig. 2.1**. The intensity of the light reaching the reaction vessel, was measured with a power meter (POWER MAX 5100, Molectron Detector Inc).

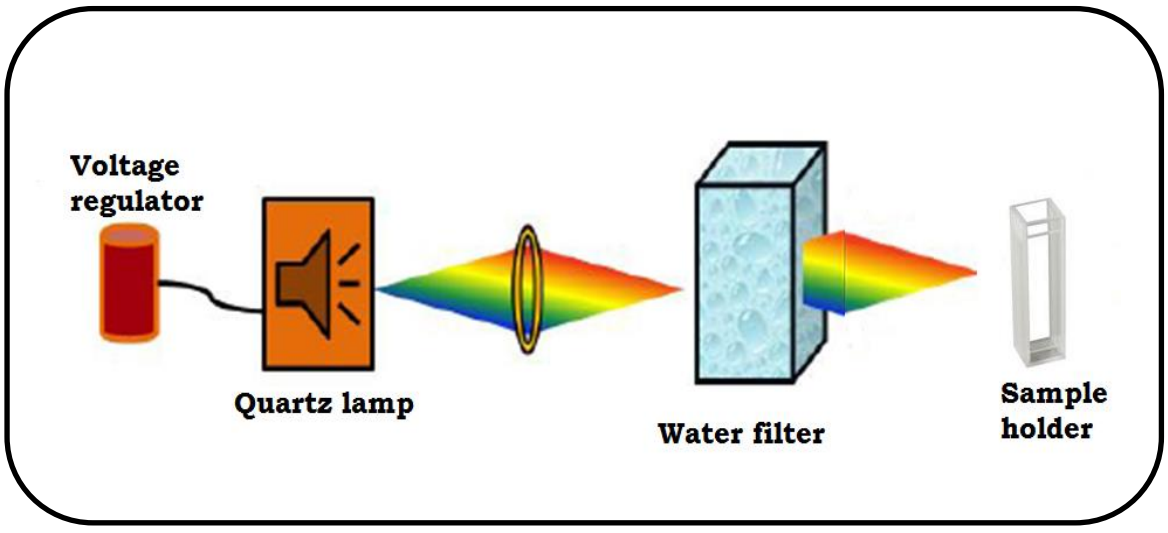

Figure 2.1: Schematic diagram of a photochemical setup.

k). **Scanning electron microscope** (SEM) images of Pluronic micelles were obtained using a JOEL JSM 840 scanning electron microscope.

l). **Energy dispersive spectroscopy** (EDS) was done on an INCA PENTA FET coupled to the VAGA TESCAM using 20 kV accelerating voltage.

m). **X-ray powder diffraction (XRD)** patterns were recorded on a Bruker D8 Discover equipped with a Lynx Eye Detector, using Cu-Kα radiation (λ= 1.5405 Å, nickel filter). Data was collected at various 2θ ranges (5-100^{o}) scanning at 1° min^{-1} with a filter time constant of 2.5 s per step and a slit width of 6.0 mm. Samples were placed on a zero background silicon wafer slide. The X-ray diffraction (XRD) data were treated using Eva (evaluation curve fitting) software. Baseline correction was performed on each diffraction pattern by subtracting a spline fitted to the curved background.

n). **Time-of-Flight Secondary Ion Mass Spectrometer** (TOF-SIMS) data were recorded with ION TOF GmbH TOF SIMS 5-100 run in micro-raster mode. The raster area was 3000 µm x 3000 µm, and the sample was run in both positive and negative ion modes. The analyzer was set to a standard operating mode with a cycle time of 100 µs, whilst the primary beam was a Bi_3 ion cluster gun with a current of 0.4 pA and an energy of 3000 eV (also termed as spectrometry mode). The Bi_3 cluster and electron flood gun was used to get a better ion signal from the sample. Charge compensation was used to account for the electron flood gun. The raw data was processed using the SurfaceLab 6.5 software provided by ION TOF.

o). **Biological photo-irradiation** is indicated in **Fig. 2.2.** The biological samples are placed at the base of a box which can be closed, above which a

beaker of water is placed to prevent infrared radiation from reaching the samples. Enclosing the samples in a box is to ensure that no unwanted ambient light can reach the samples, thus invalidating the results observed. At the very top, a 420 nm mounted light-emitting diode (LED) (M420L3 purchased from Thorlabs) is shone into the box through a hole. The LED is connected to a T-cube LED driver (LEDD1B purchased from Thorlabs), which is used to regulate the current it receives. The purpose of this setup is to allow the samples to be irradiated at a specific wavelength of light for specific time intervals, followed by examination of any changes that may have occurred due to this procedure. The power of light was 93 mW/cm^2 while the irradiation time was 300 s to result in irradiation doses (fluence) of 28 J/cm^2. In this case what is being examined the how quickly the biological material is being destroyed by the synthesized molecules.

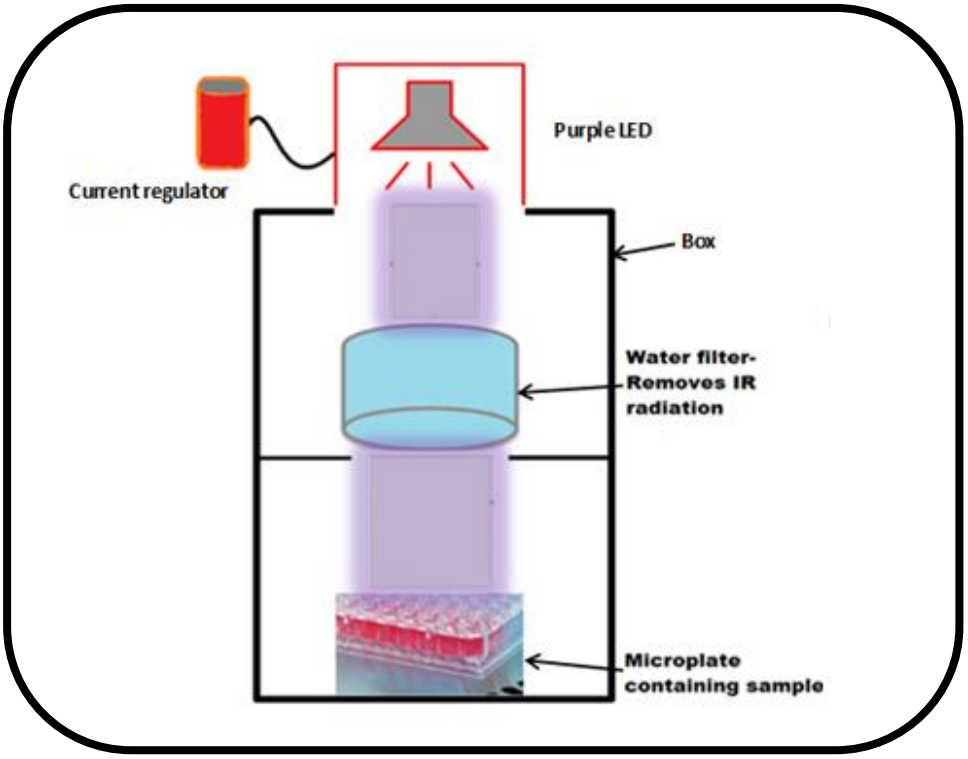

Figure 2.2: Schematic diagram of a photochemical setup in a box for biological photo-irradiation

p). **All plate readings** (Optical density) for the antimicrobial studies were obtained using the LEDETECT 96 for in vitro diagnostic from LABXIM PRODUCTS

q). **Laser flash photolysis experiments** were performed to determine the triplet decay kinetics. The excitation pulses were produced by a tunable laser system consisting of a Nd:YAG laser (355 nm, 135 mJ/4–6 ns) pumping an optical parametric oscillator (OPO, 30 mJ/3–5 ns) with a wavelength range of 420–2300 nm (NT-342B, Ekspla). Solutions for triplet state studies were de-aerated with argon for 20 min before measurement. The absorbance of the solution at the Q-band was 1.5 for these studies. Triplet lifetimes were

determined by exponential fitting of the kinetic curves using Origin Pro 8 software.

r). **Z-scan analyses** were performed using a frequency-doubled Nd:YAG laser (Quanta- Ray, 1.5 J/10 ns fwhm pulse duration) as the excitation source. The laser was operated in a near-Gaussian transverse mode at 532 nm (second harmonic), with a pulse repetition rate of 10 Hz and energy range of 0.1 μJ–0.1 mJ, as limited by the energy detectors (Coherent J5-09). The low repetition rate of the laser prevents cumulative thermal nonlinearities. The beam was spatially filtered to remove the higher order modes and tightly focused with a 15 cm focal length lens. The Z-scan system size (l × w × h) used was 600 mm × 300 mm × 350 mm (excluding the computer, energy meter, translation stage driver, and laser system). The liquid samples were placed in a cuvette (internal dimensions: 2 mm × 10 mm × 55 mm, 0.7 mL) and a path length of 2 mm (Starna 21-G-2). 2.3.

2.3. *In vitro* cell studies

MCF-7 cancer cell lines were cultivated as monolayer in T75 cm^2 culture flasks in DMEM supplemented with 10% heat-inactivated fetal calf serum (FCS), 1% amphotericin B and 1% penicillin-streptomycin mixture. Cells were incubated at 37 ^oC in a 5% CO_2 humidified incubator.

2.3.1. Cell culture preparations

After reaching 70-80% confluence, cells were detached from the flask using trypsin. The activity of trypsin was quenched by adding fresh supplemented DMEM, and the cells were centrifuged for 2 min at 2000 rpm. Viable cells were counted with the neubauber hemocytometer cell counter, using trypan

blue exclusion test of viability. A concentration of 10^4 cells was seeded and incubated with different concentrations 0, 4.2, 8.5, 17, 30 and 60 μg/ml of compounds for dark and phototoxicity studies. The complexes employed are **1**-H_2, **1**-ClGa, **2**-H_2, **2**-ClGa, **2**-Zn, **2**-Cl_2Si, **2**-H_2 (Linked Plus NPs), **2**-ClGa (Linked Plus NPs), **2**-Zn (Linked Plus NPs), **2**-Cl_2Si (Linked Plus NPs), **2**-H_2+F127, **2**-ClGa+F127, **2**-Zn+F127, **2**-Cl_2Si+F127, **7**-ClGa, **8**-H_2+F127, **8**-ClGa+F127, and **8**-Zn+F127. Cellular viability was conducted by incubating cells with neutral red, or with tetrazolium reagents WST-1. Unless stated otherwise, data obtained represents the mean values from three independent experiments. Error bars are standard deviations.

2.3.2. Dark cytotoxicity

Cells were incubated for 24 h with different concentrations of porphyrins as stated above. The media containing the photosensitizer was removed and cells were washed with DPBS. Fresh media was added, and cells were further incubated for 24 h. Assays outlined above were used to quantify cellular viability; results are given in percentage survival relative to the untreated control (cells with no photosensitizer added).

2.3.3. Photodynamic therapy (PDT) studies

Cells were incubated for 24 h with different concentrations of porphyrins as stated above. Wells were washed twice with DPBS and the culture media was replaced with the fresh media (with no phenol red). The wells containing cells were illuminated, and after irradiation, the culture media (without phenol red) was replaced with the fresh media containing phenol red. Cells were

incubated for 24 h at 37 ^{o}C in 5% CO_2, the cellular viability was expressed in percentage.

2.3.4. Statistical analysis

The data obtained from the three independent (n=3) triplicate experiments were analysed with a 3-way factorial ANOVA (analysis of variance) to determine the statistical differences between the *in vitro* cytotoxicity and photodynamic effect of the photosensitizers on MCF-7 cancer cells. TukeyHSD posthoc test was used to determine the mean differences in vitro photodynamic effect of the photosensitizers on MCF-7 cancer cells. p-value of <0.05 was considered significant

2.4. Synthesis

2.4.1. Synthesis of 5-(4-carboxyphenyl)-10,15,20-tris(phenyl) porphyrin ClGa [1-ClGa]. Scheme 3.1

In a two necked flask, DMF was brought to reflux temperature while stirring and then, **1**-H_2 (2 g, 2.6 mmol) was added and temperature brought to 100 ^{o}C. Then, gallium chloride (1 g, 5.6 mmol), was added and heating continued for 15 min. The completion of the reaction was checked using UV/Vis spectrophotometer. The reaction vessel was then allowed to cool in ice water. The ice cold MeOH (500 mL) was added onto the resulting partially crystalline precipitate, which was then filtered off and washed with water then air dried. The product was purified by column chromatography using DCM and THF ratio of 1:1 as a mobile phase and silica as a stationary phase.

Yield: (50%). IR (KBr, cm^{-1}): 3306 (O-H), 1556(C=C), 1343(CH_2), 962(C-O), 791(C-H). ^{1}H NMR (600 MHz, $CDCl_3$) δ (ppm) 8.93-8.87 (m, 6H, Ar-H), 8.60

(m, 4H, Ar-H), 8.25-8.23 (d, 10H, Ar-H), 7.79-7.77 (m, 8H, Ar-H). UV/Vis (DMF) λ_{max} nm (log ε): 425 (4.23), 557 (3.87), 598 (3.35). calc. for $C_{45}H_{28}N_4O_2GaCl.2H_2O$: C = 67.73, H = 4.04, N = 7.02, Found: C = 67.04, H= 4.81, N= 7.87 MALDI-TOF-MS m/z calc: 762.91. Found: 762.0 $(M-H)^-$

2.4.2. Linking of 1-ClGa to δ- aminolevulinic acid [7-ClGa], Scheme 3.2

1-ClGa (0.025 g, 0.032 mmol) was stirred for 5 min with NEt_3 (1.2 ml) in DMF (5 ml). HBTU (0.4 g) was added to the reaction mixture with further stirring for 5 min, followed by addition of ethyl ester ALA (0.0042 g, 4.26 mmol). The reaction was left to stir for 24 h at room temperature. After reaction completion, the resulting crude product was dissolved in ethyl acetate (10 ml), washed with water (3 ×10 ml), brine (10 ml), then dried in $MgSO_4$ to obtain the conjugate **7**-ClGa

Yield: (48%). IR (KBr, cm^{-1}): 2912 (C-H), 1718 (C=O) 1557 (N-H), 1483 (C=C), 1395(CH_2), 1182 (C-H), 951 (C-O), 837(C-H). ^{1}H NMR 600 MHz, DMSO- d_6) δ (ppm) 12.31 (s, H, NH), 8.82-8.79 (m, 5H, Ar-H), 8.26-8.00 (m, 13H, Ar-H), 7.85 (m, 5H, Ar-H), 7.24-7.22 (d, 4H, Phenyl-H), 3.95(s, 2H, CH_2) 3.36 (t, 2H, CH_2), 2.76-2.73 (t, 4H, CH_2), 2.49 (t, 3H, CH_3) UV/Vis (DMF) λ_{max} nm (log ε): 425 (4.91), 557 (4.36), 559 (3.97). calc. for $C_{51}H_{39}N_5O_3ClGa$ C = 70.00, H = 4.49, N = 8.00, Found: C= 69.95, H= 4.44, N= 7.87. MALDI-TOF-MS m/z calc: 875.0 Found: 875.0

2.4.3. Synthesis of 5-(4-(4-carboxy phenoxy) phenyl)-10,15,20-tris (phenyl) porphyrin [2-H_2], [2-ClGa], [2-Zn] and [2-Cl_2Si], Scheme 3.3

The synthesis of **2**-H_2 was as follows: Benzaldehyde (3.98 g, 0.024 mol) and 4-(4-formylphenoxy) acetic acid (1.8 g, 0.0074 mol) were dissolved in 250 ml

propionic acid and refluxed at 140 ^{o}C while vigorously stirring. Then pyrrole (3.25 ml) was added drop wise through an additional funnel. This mixture was then refluxed for 30 min and then allowed to cool down to room temperature overnight. MeOH was then added and the solid left to precipitate. The porphyrin mixtures were then filtered. Column chromatography was carried out to purify the product using petroleum ether and hexane.

Yield: (72%). IR (KBr, cm^{-1}): 3278 (O-H), 1531(C=C), 1374(CH_2), 1006(C-O), 770(C-H). ^{1}H NMR (600 MHz, $CDCl_3$) δ (ppm) 8.86 (m,5H) 8.25-8.23 (d, J=12,6H) 8.11-8.10 (d, J=6, 4H) 7.82-7.76 (m, 14H) 7.25-7.23 (d, J=12,2H) (OH was not observed). UV/Vis (DMF) λ_{max} nm (log ε): 416 (4.99), 512 (4.27), 548 (3.89), 643 (3.22). calc. for $C_{51}H_{34}N_4O_3.H_2O$ = 79.96, H = 4.55, N = 7.28, Found: C=80.52, H=4.41 N =7.21 MALDI-TOF-MS m/z calc: 750.84. Found: 750.0 $(M-H)^-$

The metalation of **2**-H_2 to form **2**-ClGa**,** **2**-Zn and **2**-Cl_2Si was the same as for metalation of **1**-H_2 to form **1**-ClGa, except **2**-H_2 (3 g, 3.9 mmol) was employed and then gallium chloride (1 g, 5.6 mmol), silicon tetrachloride (1.48 g, 8.7 mmol) or zinc acetate (1 g, 5.5 mmol) were added. The other reagents, as well as reaction conditions were kept the same.

2-ClGa

Yield: (48%). IR (KBr, cm^{-1}): 3306 (O-H), 1556(C=C), 1343(CH_2), 962(C-O), 791(C-H). ^{1}H NMR (600 MHz, $CDCl_3$) δ (ppm) 8.88 (m,5H) 8.26-8.24 (d, J=12,6H) 8.13-8.11 (d, J=6, 4H) 7.85-7.77 (m, 14H) 7.28-7.22 (d, J=12,2H)

(OH was not observed). UV/Vis (DMF) λ_{max} nm (log ε): 425 (4.23), 552 (3.87), 591 (3.35). calc. for $C_{51}H_{32}N_4O_3GaCl.H_2O$: C = 70.17, H = 3.78, N = 6.42, Found: C 70.59, H= 3.68, N= 6.47 MALDI-TOF-MS m/z calc: 854.0. Found: 854.0

2-Zn

Yield: (67%). IR (KBr, cm^{-1}): 3306 (O-H), 1556(C=C), 1343(CH_2), 962(C-O), 791(C-H). ^{1}H NMR (600 MHz, $CDCl_3$) δ (ppm) 8.85 (m,5H) 8.26-8.22 (d, J=12,6H) 8.13-8.10 (d, J=6, 4H) 7.84-7.77 (m, 14H) 7.26-7.24 (d, J=12,2H) (OH was not observed). UV/Vis (DMF) λ_{max} nm (log ε): 429 (4.21), 559 (3.90), 599 (3.39). calc. for $C_{51}H_{32}N_4O_3ZnCl.H_2O$: C = 70.60, H= 3.95, N=6.46, Found: C=70.68, H=3.42, N=6.21 MALDI-TOF-MS m/z calc: 814.21. Found: 814.0

2-Cl_2Si

Yield: (52%). IR (KBr, cm^{-1}): 3306 (O-H), 1556(C=C), 1343(CH_2), 962(C-O), 791(C-H). ^{1}H NMR (600 MHz, $CDCl_3$) δ (ppm) 8.89 (m,5H) 8.24-8.2 (d, J=12,6H) 8.11-8.10 (d, J=6, 4H) 7.82-7.76 (m, 14H) 7.25-7.22 (d, J=12,2H) (OH was not observed). UV/Vis (DMF) λ_{max} nm (log ε): 446(4.33), 662 (3.75) calc. for $C_{51}H_{32}N_4O_3Cl_2Si.2H_2O$: C = 69.30, H= 3.80, N=6.61, Found: C = 73.16, H=3.56, N=6.24. MALDI-TOF-MS m/z calc: 847.82. Found: 812.36 $(M-Cl)^+$

2.4.4 Synthesis of complexes 3-6. Scheme 3.4

The metalation of **3**-H_2 (1.5 g, 1.9 mmol), **4**-H_2 (0.1 g, 0.096 mmol), **5**-H_2 (1.5 g, 1.6 mmol), **6**-H_2 (0.1 g, 0.096 mmol) to form **3**-ClGa, **4**-ClGa, **5**-ClGa and

6-Zn was outlined above for the metalation of **1**-H_2 to form **1**-ClGa, except for difference in amounts of porphyrins but same amounts of metal salts.

3-ClGa

Yield: (37%) UV/Vis (DMF) λ_{max} nm (log ε): 419 (4.10), 572 (3.77), 512 (3.42). ^{1}H NMR (300 MHz, Acetone-d_6) δ 9.23 (d, J = 4.9 Hz, 2H), 9.16–9.10 (m, 4H), 8.97 (d, 2H), 8.32–8.20 (m, 6H), 8.08 (d, J = 7.9 Hz, 2H), 7.87 (dd, J = 5.6, 1.5 Hz, 6H), 7.33 (d, J = 8.6 Hz, 2H). calc. for $C_{44}H_{24}N_8O_8Ga{\cdot}4H_2O$: C = 56.55, H = 3.45, N = 11.99, Found: C 55.68, H = 3.14, N = 10.98 MALDI-TOF-MS m/z calc: 897.89, Found: 862 $(M-Cl)^+$

4-ClGa

Yield: (25%) UV/Vis (H_2O) λ_{max} nm (log ε): 428 (4.58), 557 (3.92), 596 (3.77). ^{1}H NMR (600 MHz, D_2O) δ 8.82 (s, 7H, Ar-H), 8.21 (d, J = 35.0 Hz, 9H, Ar-H), 8.02 (d, J = 6.9 Hz, 7H, Ar-H), 7.76 (s, 1H, Ar-H), 3.54 (s, 4H, sulponated-H). calc. for $C_{44}H_{28}N_4O_{12}GaClS_4$: C = 50.91, H = 2.72, N = 5.40, Found: C = 49.20, H = 3.00, N = 5.22 MALDI-TOF-MS m/z calc: 1038.15 Found: 1002.03 $(M-Cl)^+$

5-ClGa

Yield: (29%) UV/Vis (DMF) λmax nm (log ε): 427 (4.59), 559 (3.81), 598 (3.57) ^{1}H NMR (600 MHz, $CDCl_3$) δ 8.87 (s, 8H), 8.09 (d, J = 8.1 Hz, 8H), 7.93 (d, J = 8.1 Hz, 8H). calc. for $C_{44}H_{24}N_4Ga$: C = 52.95, H = 2.42, N = 5.61, Found: C 51.23, H = 2.39, N = 5.53 MALDI-TOFMS m/z calc: 1214.45. Found: 1179.0 $(M-Cl)^+$

6-Zn

Yield: (48%). IR (KBr, cm^{1}): 2914 (CH), 1598(C¼C), 1379 (CH2), 1224(CO), 795(CH). ^{1}H NMR 600 MHz, $CDCl_3$) d (ppm) 8.89 (s, 1H, Ar-H), 8.54 (d, J = 8.5 Hz, 8H, Ar-H), 8.50 (s, 6H, Ar-H), 8.16 (d, J = 8.5 Hz, 1H, Ar-H), 7.68 (s, 8H, Ar-H), 7.63 (d, J = 15.8 Hz, 6H, Ar-H), 7.56 (s, 8H, Ar-H), 7.50 (s, 5H, Ar-H), 7.40 (d, J = 8.4 Hz,1H, Ar-H), 5.44 (s, 8H, CH_2-H). UV/vis (DMF) λ_{max} nm (log e): 429 (4.58), 558 (3.92), 600 (3.56). Calc. for $C_{72}H_{52}N_4O_4$. $2H_2O$ = 75.95, H = 4.96, N = 4.92, Found: C = 75.37, H = 4.67 N = 4.81 MALDI-TOFMS m/z calc: 1102.60. Found: 1102.08.

2.4.5. Synthesis of 5,10,15,20-tetra(1-pyrenyl) porphyrin [8-ClGa], Scheme 3.5

In a 25 ml reaction flask, the **8**-H_2 (0.047 g, 0.042 mmol) was dissolved in 15 ml toluene and sodium acetate (0.31g, 3.78 mmol), anhydrous K_2CO_3 (0.31g, 2.23 mmol) and $GaCl_3$ (0.19 g, 1.07 mmol) were added. The reaction mixture was refluxed under Ar for 24 h, after which it was allowed to cool to room temperature, neutralized with acetic acid and washed with water. The organic layer was separated and dried under anhydrous Na_2SO_4. The solvent was removed in vacuo, and the crude product was purified with silica gel using DCM as the eluent.

Yield: (78%). ^{1}H NMR (600 MHz, $CDCl_3$) δ (ppm) 8.90-8.83 (m, 4H) 8.38-8.32 (m, 12H) 8.31-8.12 (m, 12H) 8.05-7.78 (m, 8H) 7.77-7.62 (m 4H), 7.60-7.28 (m, 4H). UV/Vis (DMF) λ_{max} nm (log ε): 440 (4.01), 563 (3.74), 603 (3.24). calc. for $C_{84}H_{44}N_4GaCl$.: C = 85.57, H = 3.76, N = 4.75, Found: C 85.28, H= 3.39, N= 4.39 MALDI-TOF-MS m/z calc: 1214.45 Found: 1179.0 $(M\text{-}Cl)^{+}$

2.4.6. Linking Pluronic polymer to Folic acid (F127-FA), Scheme 3.6.

The linking of FA to Pluronic F127 has been reported in the literature [**113,114**], however the current work employed a different method where oxalic acid was linked to Pluronic F127 before conjugating to FA. First, the esterification of Pluronic 127 was carried out as follows: oxalic acid (1.5 g, 0.017 mol), EDC (4.0 g, 0.026 mol) and NHS (4.0 g, 0.035 mol) were dispersed in 16.0 mL of DCM and stirred at room temperature for 24 h. After this time, a solution of Pluronic 127 (3.0 g) in DCM (8 mL) was added drop-wise to the reaction mixture and the reaction was allowed to continue at room temperature for 48 h under inert environment, followed by evaporation the bulk of the solvent (DCM).

The product was precipitated out of solution using diethyl ether. The product was filtered off and washed with diethyl ether several times by centrifugation. The pure product (represented as Oxalic-F127 in **Scheme 3.6A**) was then air dried. The linking of Oxalic-F127 to FA was carried out as follows: Oxalic-F127 (2.0 g), EDC (3.0 g, 0.020 mol) and NHS (2.5 g, 0.022 mol) were dispersed in 10.0 mL of DCM and stirred at room temperature for 24 h. After this time, a solution of folic acid (4.5 g, 0.010 mol) in DCM (10.0 mL) was added to the reaction mixture and allowed to react at room temperature for 48 h. After 48 h the product (represented as F127-FA in **Scheme 3.6B**) was collected and purified as described above for Oxalic-F127. The discussion regarding characterization is in Chapter 3.

2.4.7. Incorporation of porphyrins into Pluronic polymer micelles, Schemes 3.7 and 3.8.

The formation of micelles in the presence of porphyrins was carried out using the solid dispersion method which has been previous described in literature [**48**]. This method involves cosolubilization of copolymer with the porphyrin which is then followed by rotative evaporation, **Scheme 3.7**. The porphyrins at ~10^{-4} M in all cases, and Pluronic F127 was 20% w/V (1.5×10^{-2} M) were added in 10 mL DCM except for **complex 4** which was dissolved in methanol. The mixtures were sonicated for 15 min at room temperature. The solvent was then removed using the rotary evaporator. The achieved solid products were left in a vacuum desiccator for 12 h and then hydrated and vigorously stirred (Dubnoff metabolic shaking) at 70 ^{o}C for 4 h. The solutions were transferred onto test tubes and left for 24 h undisturbed for precipitation of porphyrins which were not bound onto the polymer, which were then filtered and the required product was dried. The porphyrins when loaded into Pluronic F127 are represented as **1**-H_2+F127, **1**-ClGa+F127 etc. for all porphyrins (where F127 represents Pluronic F127). **5**-H_2 and **5**-ClGa were also embedded into F127-FA represented as **5**-H_2+F127-FA and **5**-ClGa+F127-FA respectively.

Scheme 3.8

Complexes 6-H_2 and **6**-Zn were embedded into Pluronic binary mixtures of F127/P123. The mixed micelles were prepared according to literature methods [**47**] with slight modification. Weight-average molecular weight describes the molar mass of a polymer and was calculated using **Equation 2.1** [**115**].

$$M_w = \frac{\sum N_i M^2}{\sum N_i M} \quad (2.1)$$

where N_i is the number of moles of polymer, M is the molecular weight of polymer. The Pluronic mixture was composed of P123 and F127 (1:1, w/w). The polymer masses used were 1 g, 1.1 g, 1.2 g, 1.3 g, 1.4 g, 1.5 g dissolved in 10 ml. Hence the concentration of the F127/P123 binary mixture was determined.

6-H_2 or **6**-Zn (4 mg each), and 270 mg of Pluronic mixture composed of F127 and P123 (1:1, w/w) were dissolved in 10 ml dichloromethane. The solvent was evaporated by rotary evaporation at 35 ^oC to obtain solid **6**-H_2 or **6**-Zn/copolymer matrixes. The matrixes were then placed under vacuum overnight at room temperature. The product was hydrated with 4 ml water at 60 ^oC for 30 min to obtain a micelle solution, which was then filtrated through 0.2 mm filter membrane to remove the unincorporated **6**-H_2 or **6**-Zn followed by drying. The porphyrins when loaded into Pluronic F127/P123 binary mixture are represented as **6**-H_2+F127/P123, **6**-Zn +F127/P123.

2.4.8. Synthesis of Pluronic Silica nanoparticles and linking to complex 2, Scheme 3.9.

The nanoparticles were synthesised according to literature **[116]** with slight modification as follows: Pluronic 127 (2 g) was dissolved in a mixture of H_2O (15 ml) and 2 M HCl (60 ml) and then TEOS (4.25 g) was added and the mixture was vigorously stirred at 45 ^oC for 20 h. The mixture was then further

heated to 100 °C in an oven for 12 h and then cooled to room temperature. The resulting product was filtered and vacuum dried at room temperature. The product was then calcinated at 550 °C for 12 h.

The conjugation of **2**-ClGa**, 2**-Zn and **2**-Cl_2Si to PluS NPs was carried out as follows: **2**-ClGa**, 2**-Zn and **2**-Cl_2Si (0.02 g, 0.023 to 0.025 mmol) were firstly dissolved in DMF (10 mL), then DCC (0.03 g, 0.145 mmol) was added to convert the carboxylic group (-COOH) of the porphyrin into an active carbodiimide ester group. This mixture was stirred at room temperature for 24 h. After this time 0.04 g of PluS NPs were added and the mixture was allowed to stir for further 24 h. The conjugate was separated from the un-conjugated nanoparticles using Bio-Beads S-X1 from Bio-Rad

2.4.9. Synthesis of Pcs, Scheme 7.1

The synthesis of **9**-OHGa was as follows: Under inert atmosphere **9**-H_2 (0.03 mg, 0.026 mmol), $Ga(acac)_3$ (0.047 g, 0.128 mmol), phenol (0.07 g, 0.74 mmol) and 1.5 ml *i*-AmOH were dissolved in 5 mL TCB and refluxed at 215 °C. In this synthesis phenol was used because it has been previously shown that for direct and high metalation of Pcs with $Ga(acac)_3$, a mixture of solvents (*i*-AmOH and TCB) is needed **[117]**. The completion of the reaction was checked using UV/Vis spectra. The crude product was purified using column chromatography with hexane and chloroform 3:7 as elutes and remaining product on the column was eluted with methanol and chloroform.

9-OHGa

Yield: (82.6%). IR (KBr, cm^{1}): 3394(O-H), 2929 (C–H), 1718 (C-O), 1600 (C=C) 1463 (C-H), 1379 (N-H), 1272 (C-H), 1198 (C-O), 1047 (C–O), 734 (=C-H). UV–Vis (DMSO) λ_{max} (log ε): 693 (4.89), 436 (4.70), 359 (4.51). ^{1}H NMR (600 MHz, $CDCl_3$+CD_3OD) δ 8.41-8.35 (m, 8H, H_{Pc}), 4.76-4.24 (br m, 20H, OCH_2^{Bu} + α,β-OCH_2^{DEG}), 3.86 (s, 8H, γ,δ-OCH_2^{DEG}), 2.16 (br m, 12H, 2-CH_2^{Bu}), 1.81 (br m, 12H, 3-CH_2^{Bu}), 1.19 (t, J = 7.2 Hz, 18H, CH_3). Calc. for $C_{64}H_{81}N_8O_{13}Ga$: C 61.99; H, 6.58; N, 9.04. Found: C, 60.63; H, 6.46; N, 8.45 %. MALDI-TOF-MS m/z calc: 1240.10. Found $(M+H)^+$ 1241.33.

Synthesis of **9**-OAcIn was as follows: **9**-H_2 (0.03 g, 0.026 mmol) and $In(acac)_3$ (0.079 g, 0.189 mmol) were dissolved in 3 mL 1-chloronaphthalene under inert atmosphere. The reaction mixture was heated to 300 ^{o}C and the completion of the reaction was checked every 10 min using UV/Vis spectra. The mixture was allowed to cool to room temperature and column chromatography was carried out for purification using methanol and chloroform as eluting solvents. Finally acetic acid was used to collect the desired product **9**-OAcIn.

9-OAcIn

Yield: (97.4%). IR (KBr, cm^{-1}): 3397(O-H), 2944 (C–H), 1718 (C-O), 1594 (C=C) 1453 (C-H), 1373 (N-H), 1274 (C-H), 1202 (C-H), 1021 (C–O), 731 (=C-H). UV–Vis (DMF) λ_{max} nm (log ε): 699 (4.92), 630 (4.82), 356 (4.61). ^{1}H NMR (600 MHz, DMSO, 80 °C) 8.94-8.88 (m, 8H, H_{Pc}), 4.74-3.91 (br m, 20H, OCH_2^{Bu} + α-δ-OCH_2^{DEG}), 2.05-1.99 (m, 12H, 2-CH_2^{Bu}), 1.77-1.70 (br m, 12H, 3-CH_2^{Bu}), 1.14 (t, J = 7.4 Hz, 18H, CH_3). MALDI-TOF-MS m/z calc. for $C_{66}H_{85}InN_8O_{15}$:

1344.5; found 1344.5 $(M+H_3O)^+$; calc. for $C_{73}H_{90}InN_8NaO_{18}$: 1504.5, found 1504.6 $(M+Na)^+$.

2.4.10. Preparation of polymer thin films

Thin films were prepared according to literature methods [**108,118**]. Poly(bisphenol A carbonate) (110 mg) and 0.1 mg of **complexes 9**-OAcIn and **9**-OHGa were respectively dissolved in dichloromethane (1.5 mL) and sonicated for 30 min until a homogeneous mixture of Pc-polymer solutions was obtained. The Pc-polymer solutions were dropped on glass substrates then placed in a Petri dish and the solvent was allowed to evaporate at room temperature, forming **9**-OAcIn-TF and **9**-OHGa-TF where TF stands for thin films.

PUBLICATIONS

The results presented in the following chapters have either been published or submitted for publication. These articles are not referenced in this thesis

1. **M. Managa**, S. Mkhize, J. Britton, E. Prinsloo, T. Nyokong. Synthesis and dark toxicity of GaCl 5-(4-carboxyphenyl)-10,15,20-tris(phenyl)-porphyrin when conjugated to δ-aminolevulinic acid, J. Coord Chem 69 (20) (2016) 3035-3042.

2. **M. Managa**, J. Britton, E. Prinsloo, T. Nyokong, Effects of Pluronic silica nanoparticles on the photophysical and photodynamic therapy behavior of triphenyl-p-phenoxy benzoic acid metalloporphyrins, J. Coord Chem 69 (23) (2016) 3491 – 3506.

3. **M. Managa**, J. Britton, E. K. Amuhaya, T. Nyokong, Photophysical properties of GaCl 5,10,15,20-Tetra(1-pyrenyl)porphyrin incorporated in Pluronic F127, J. Luminescence, 185 (2017) 34-41

4. **M. Managa**, B. P. Ngoy, T. Nyokong, The photophysical studies of Pluronic F127/P123 micelle mixture system loaded with H2 and Zn5,10,15,20-Tetrakis[4-(benzyloxy) phenyl]porphyrin, J. Photochem. Photobiol. A: 339 (2017) 49-58.

5. **M. Managa**, B. P. Ngoy, D. Mafukidze, J. Britton, T. Nyokong, Photophysical studies of meso-tetrakis(4-nitrophenyl) and meso-Tetrakis(4-sulfophenyl) gallium porphyrins incorporated into Pluronic F127 polymeric micelles, J. Photochem. Photobiol. A, 348 (2017) 179–187.

6. **M. Managa**, T. Nyokong. Photophysical studies of asymmetrically substituted porphyrins containing carboxy substituents when encapsulated into Pluronic F 127. Macroheterocycles 10 (2017)467-473

7. **M. Managa**, B. P. Ngoy, D. Mafukidze, T. Nyokong, Incorporation of H_2 and Ga 5,10,15,20-Tetrakis(4'-bromophenyl) porphyrin into Pluronic F127-Folic acid micelle, Journal of Luminescence 194 (2018) 739–746

8. **M. Managa**, O. J. Achadu, T. Nyokong. Photophysical studies of graphene quantum dots - Pyrene-derivatized porphyrins conjugates when encapsulated within Pluronic F127 micelles. Dyes and Pigments 148 (2018) 405-416

9. **M. Managa**, S. Khene, J. Britton, A. Martynov, Y. Gorbunova, T. Nyokong, Nonlinear optical properties of Gallium and Indium 2,3-bis[2'-(2"-hydroxyethoxy)ethoxy]-9,10,16,17,23,24-hexa-n-butoxyphthalocyanine when embedded in poly(bisphenol A carbonate) as thin films, Journal of Porphyrins and Phthalocyanines 22 (2018)137–148

10. **M. Managa**, J. Britton, E. Prinsloo, T. Nyokong. Effects of Pluronic F127 micelles as delivering agents on the vitro dark viability and photodynamic therapy activity of carboxy and pyrene substituted porphyrins. Submitted to Polyhedron

Side Publications

1. M. Managa. J. Mack, L. D. Gonzalez. S. R. Buenamanana. C. Tshangana. A. N Cammidge. T. Nyokong. Photophysical properties of tetraphenyl

porphyrin subphthalocyanine conjugates. Journal of Porphyrins and Phthalocyanines 20 (2016) 204-212

2. A. J. Ojodomo. **M. Managa**, T. Nyokong. Fluorescence behaviour of supramolecular hybrids containing graphene quantum dots and pyrene-derivatized phthalocyanines and porphyrins. J. Photochem. Photobiol A: Chemistry 333 (2017)174-185.

Results and Discussion

Chapter 3

Synthesis and characterization of porphyrins

This chapter provides all the characterization for unmetalled and metallated porphyrins alone or when embedded into Pluronic polymer micelles and linked to PluS NPs.

3.1. Synthesis and characterization of porphyrins

3.1.1. Complexes 1-ClGa and 1-ClGa+ALA (7-ClGa)

Complex 1-H_2 was converted to **complex 1**-ClGa by heating the former in DMF at reflux temperature in the presence of gallium chloride (**Scheme 3.1**). ^{1}H NMR, IR and mass spectroscopies as well as elemental analysis techniques were employed for the characterization of all the porphyrins and gave satisfactory results. The aromatic protons of the outer phenyl rings were observed between 8.93-8.23 integrated to give a total number of 20 protons while the inner pyrrole ring protons was observed between 7.79-7.77 ppm integrated into 8 protons as expected. The carboxylic acid proton was not observed due to deshielding effect [**119**]. The C, H and N elemental analysis data of complexes are in agreement with their structure.

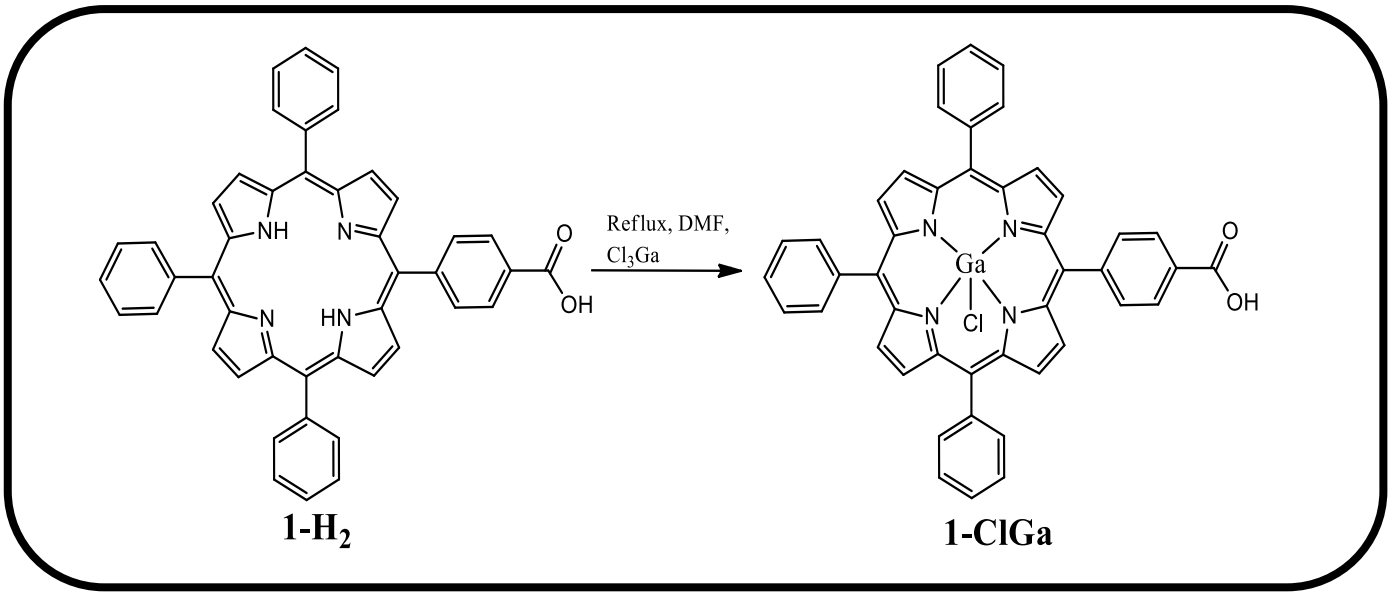

Scheme 3.1: Synthetic pathway for 1-ClGa

Conjugation of **1**-ClGa to ethyl ester ALA was achieved by using HBTU in the presence of trimethylamine as activating agents (**Scheme 3.2**).

In the ^{1}H NMR for **complex 7**, the amide proton was observed at 12.31 ppm integrated to 1 proton. The aromatic protons of the outer phenyl rings were observed between 8.82-7.22 integrated to give a total number of 27 protons. The CH_2 protons of the ethyl ester ALA was observed between 3.95-2.73 while the CH_3 was observed at 2.49 as expected.

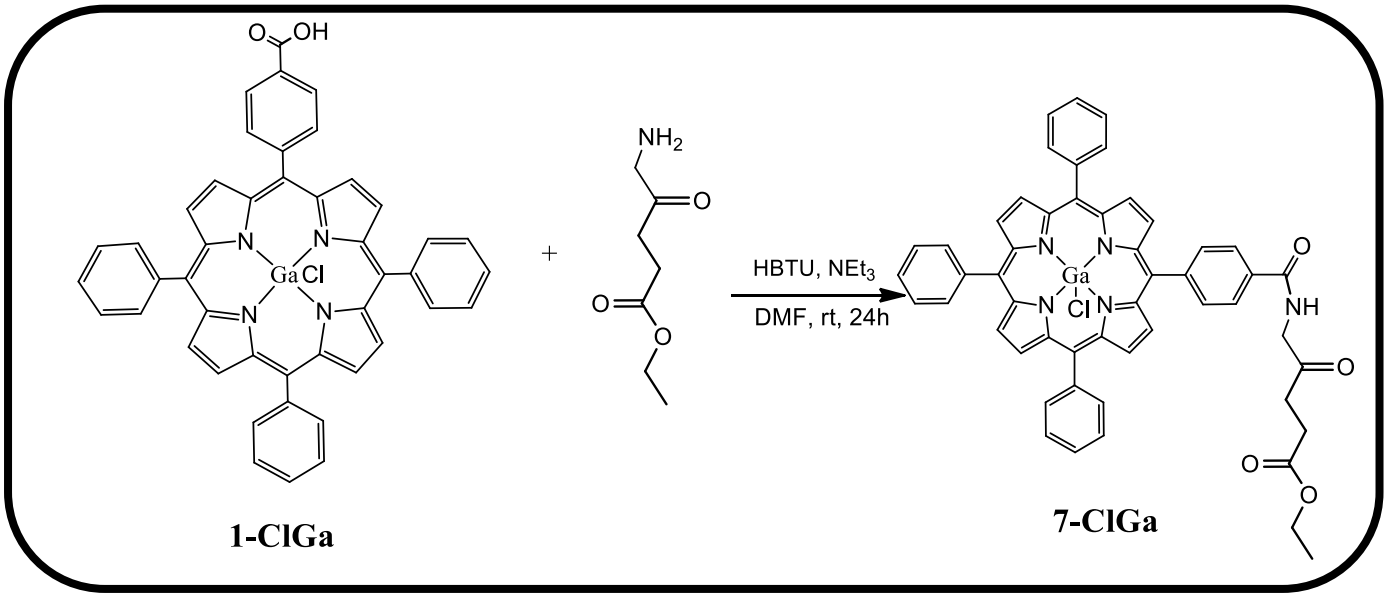

Scheme 3.2: Covalent linkage of ALA ester to 1-ClGa to form 7-ClGa

The traditional approach using coupling agents such as 1-ethyl-3-(3-dimethylaminopropyl)-carbodiimide/N-hydroxysuccinimide or *N,N'*-dicyclohexylcarbodiimide gave low yields **[120]**. It is suggested that this is due to racemization and/or formation of side products, which was done by employment of N,N,N′,N′-tetramethyl-O-(1H-benzotriazol-1-yl)uranium hexa-fluorophosphate (HBTU) achieving a moderate yield of 48%, for the formation

of an amide bond between the COOH of **complex 1**-ClGa and the NH_2 of ethyl ester ALA.

The linkage of the porphyrins to the ALA ester using an amide bond was confirmed using FT-IR spectra. The amide bond (N-H bending) can be observed at 1557 cm $^{-1}$ (**Fig. 3.1**) for **complex 7**-ClGa confirming the conjugation. The α and β unsaturated carbonyl (ester bond) can be observed for both ethyl ester ALA and **complex 7**-ClGa at 1720 cm $^{-1}$ and 1718 cm $^{-1}$ respectively, where a slight shift was observed. An aliphatic C-H stretch is seen at 2912 cm $^{-1}$ for **complex 7**-ClGa.

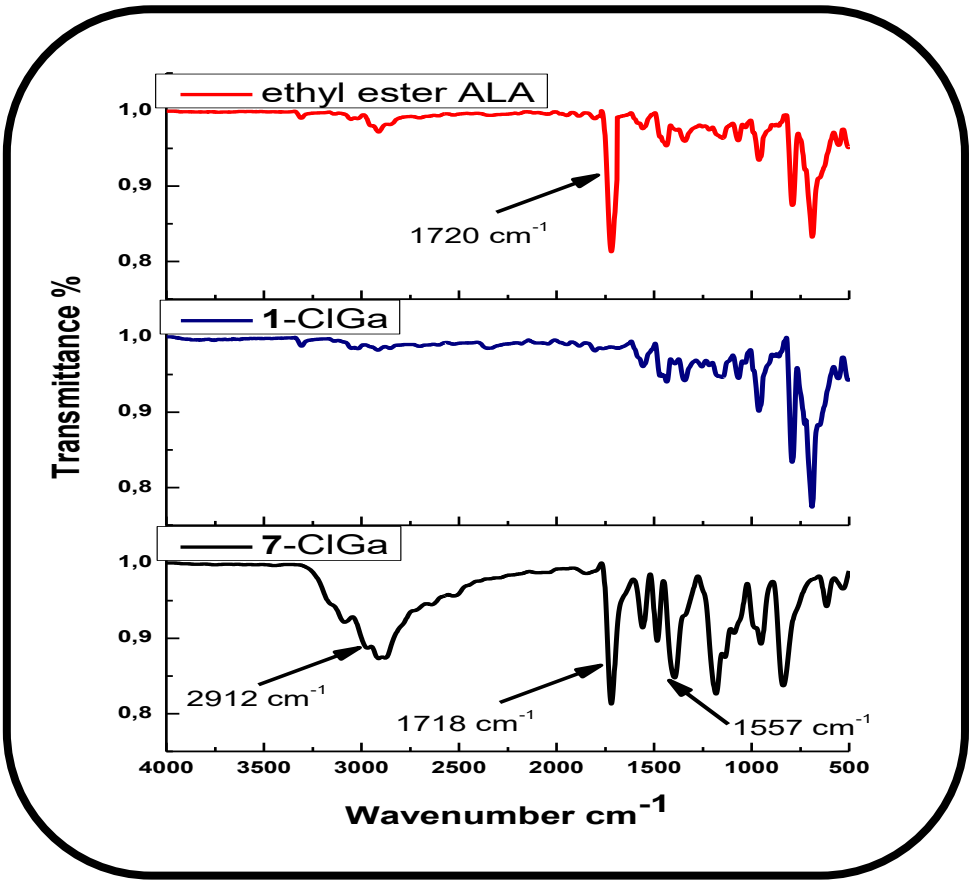

Figure 3.1: FT-IR spectra of ethyl ester ALA, complex 1-ClGa and complex 7-ClGa

Porphyrins are characterized by an intense band that is called the Soret or B band that is observed around 400 nm and other weak bands known as the Q bands which are observed between 500-600 nm. On metalation of **1**-H_2 to **1**-ClGa a red shift in the Soret band was observed (**Table 3.1**). Introduction of heavy metal such as gallium could result in degree of perturbation and electron delocalisation within the porphyrin macrocycle **[121]**, resulting in red shifts in absorption spectra.

Fig. 3.2 shows the spectra of **complexes 1**-ClGa and **7**-ClGa. The Soret band is observed at 425 nm while the Q bands are observed at 557 and 598 nm for both complexes and this also indicates that there was no spectral change upon conjugation.

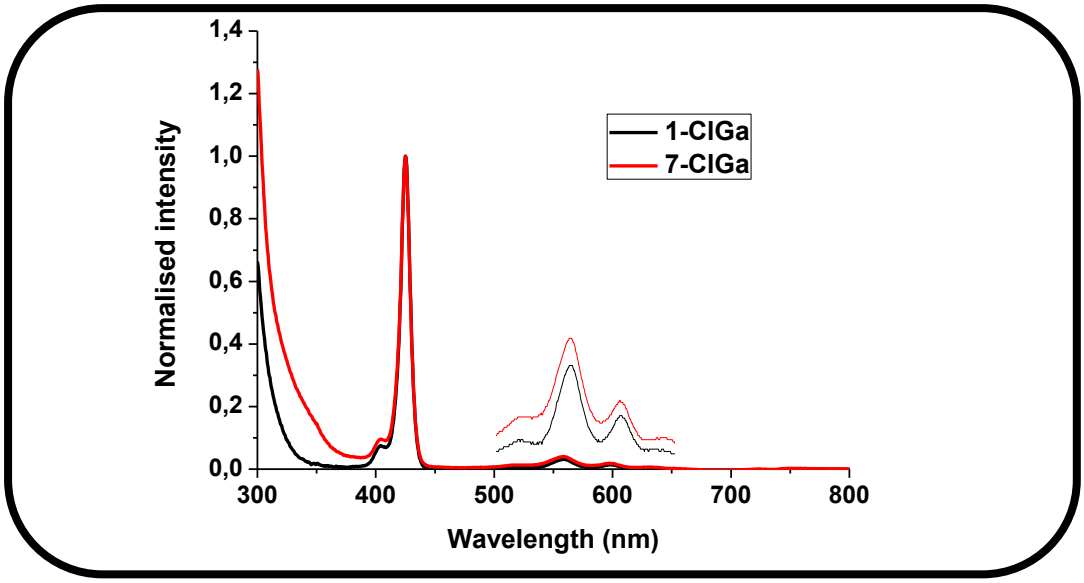

Figure 3.2: Absorption spectra of complex 1-ClGa and complex 7-ClGa.

Fig. 3.3 shows the emission spectra of **complexes 1**-ClGa and **7**-ClGa, which are typical **[122]** of a metallated porphyrin with two bands differing in

intensity at 607 nm and 655 nm for **complex 1**-ClGa, and 610 nm and 657 nm for **complex 7**-ClGa, **Table 3.1**.

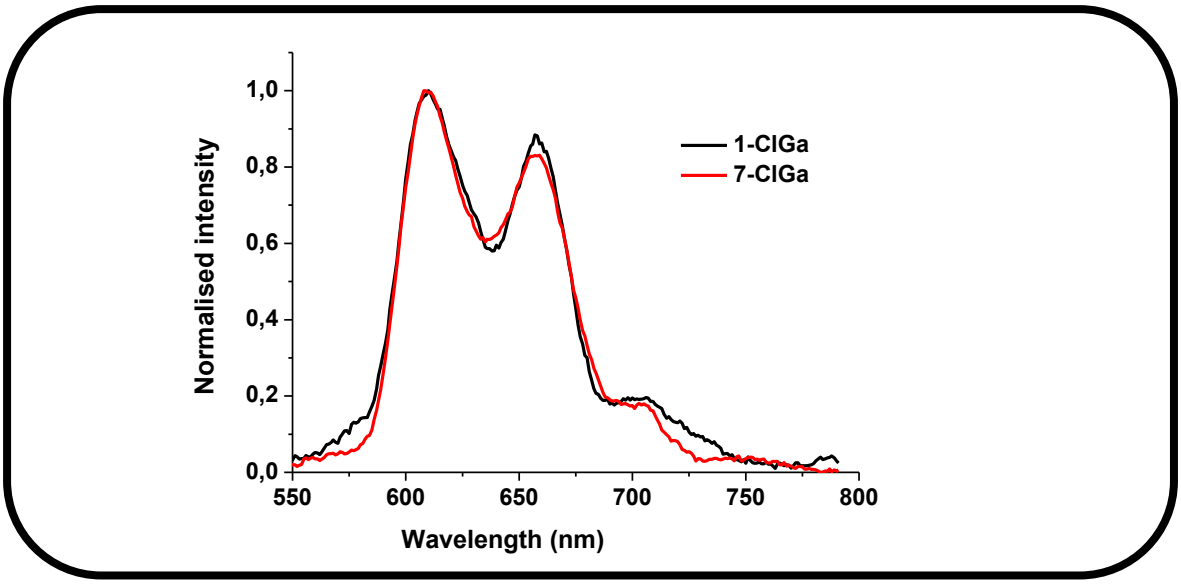

Figure 3.3: Fluorescence emission spectrum of complexes 1-H_2 and 7-ClGa.

3.1.2. Complexes 2

Complexes 2 were synthesized as shown in **Scheme 3.3**.

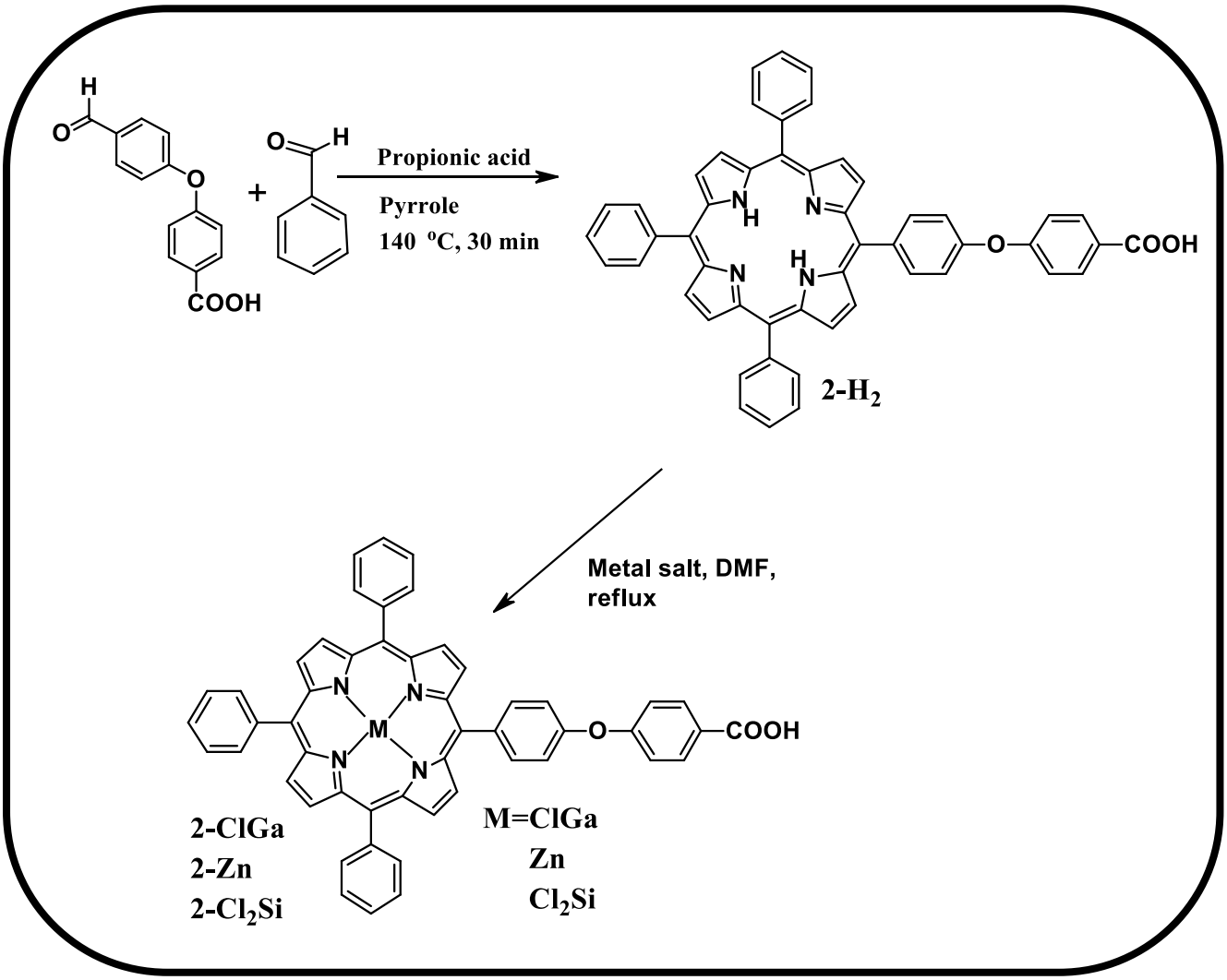

Scheme 3.3: Synthetic pathway of metal free 2-H_2 and its metal derivatives 2-ClGa, 2-Zn and 2-Cl_2Si

The metallated and unmetallated complexes showed the aromatic ring protons between 8.89-7.23 integrated to give anticipated number of protons. The inner porphyrin protons for **2**-H_2 was not observed due to induced ring current that results in shielding of such protons [**119**].

Fig. 3.4 shows the spectra of **2**-Zn, **2**-ClGa and **2**-Cl_2Si. The Soret band of **2**-Zn is at 427 nm while the Q bands are at 563 and 604 nm. The Soret bands of **2**-ClGa and **2**-Cl_2Si are observed at 425 nm and 446 nm, respectively (**Table 3.1**). Thus the Soret band of **2**-Cl_2Si is highly red-shifted compared to **2**-Zn and **2**-Ga. The red-shift of Soret bands are often observed for distorted porphyrins **[121]**. A very prominent and intense Q band is observed at 669 nm for **2**-Cl_2Si with a weaker second component (**Fig. 3.4**). Metallated porphyrins contain two Q bands called α (high energy band) and β (low energy band) **[122]**. The relative intensities of these bands have been associated with the stability of the metal complex. When α > β as is the case for **2**-ClGa and **2**-Zn, the metal forms a stable square-planar porphyrin complex **[122]**. For **2**-Cl_2Si β > α, implying an unstable complex where the central metal can easily be displaced.

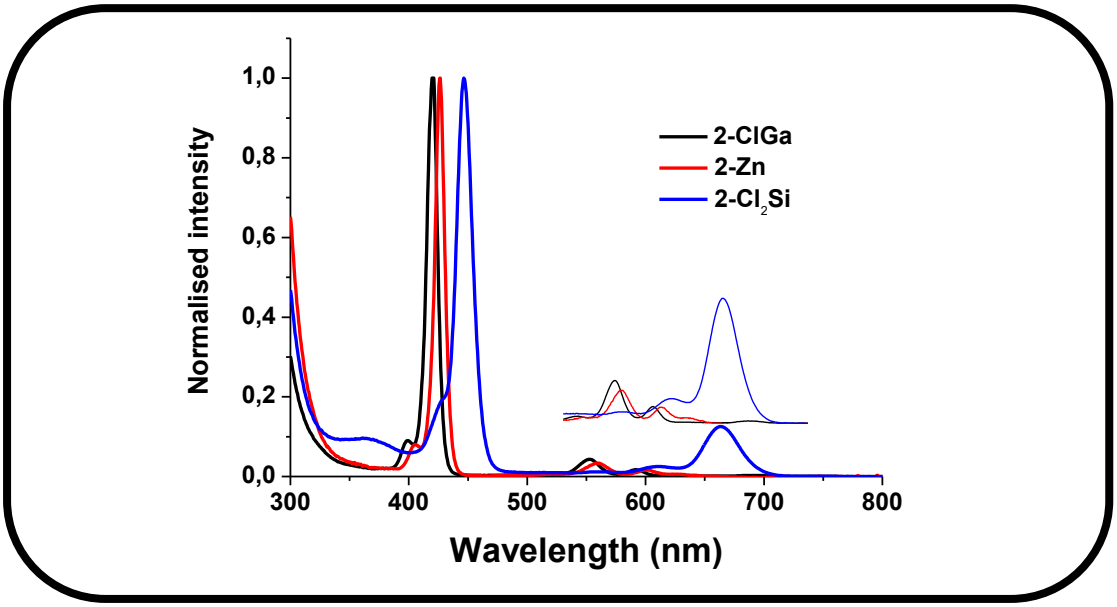

Figure 3.4: Absorption spectra of 2-ClGa, 2-Zn and 2-Cl_2Si with insert of expanded Q band region

Fig. 3.5 shows the emission spectra of **2**-ClGa and **2**-Zn, which are typical **[121]** of a metallated porphyrin with two bands differing in intensity at 605 nm and 652 nm for **2**-Zn, and 604 nm and 648 nm for **2**-ClGa. However, **2**-Cl_2Si gave an emission spectrum which is not typical metallated porphyrins, corresponding to the absorption spectra above. Comparing **1**-H_2 and **2**-H_2, the Soret bands are the same value showing no substituent effect as shown in **Table 3.1**, this applies to **1**-ClGa and **2**-ClGa

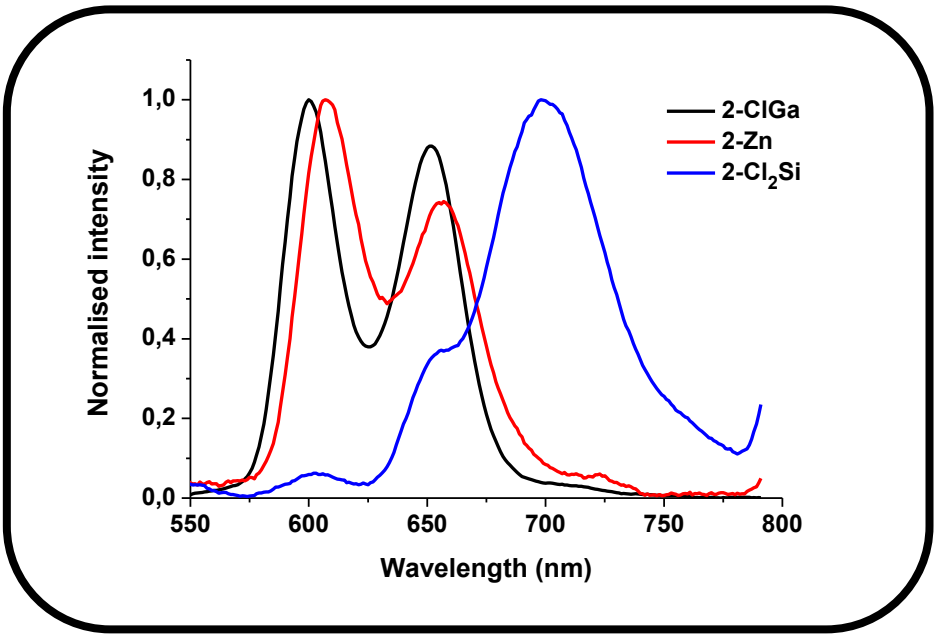

Figure 3.5: Fluorescence emission spectrum 2-ClGa, 2-Zn and 2-Cl_2Si

3.1.3. Complexes 3-6

In the ^1H NMR for **complex 3**, the aromatic protons were observed between 9.23-7.33 ppm integrated to give a total number of 24 protons as expected.

3-ClGa, **4**-ClGa, **5**-ClGa and **6**-Zn (**Scheme 3.4**) were synthesized by metalation the metal free derivative (**3**-H_2 – **6**-H_2) at DMF reflux temperature in the presence of gallium chloride for **complexes 3-5** and zinc chloride for **complex 6**. In the ^{1}H NMR for **complex 4**, the aromatic protons of the outer phenyl rings were observed between 8.82-7.76 ppm integrated into 24 protons as expected. The sulphonated protons resonates at 3.54 ppm integrated to give 4 protons. For **complex 5**, the ^{1}H NMR showed the aromatic ring between 8.87-7.93 integrated to give 24 protons.

For **complex 6**, the ^{1}H NMR showed the aromatic ring between 8.89-7.40 integrated to give 44 protons. The singlet peak of CH_2 protons was observed at 5.44 ppm integrated into 8 protons confirming the proposed structure.

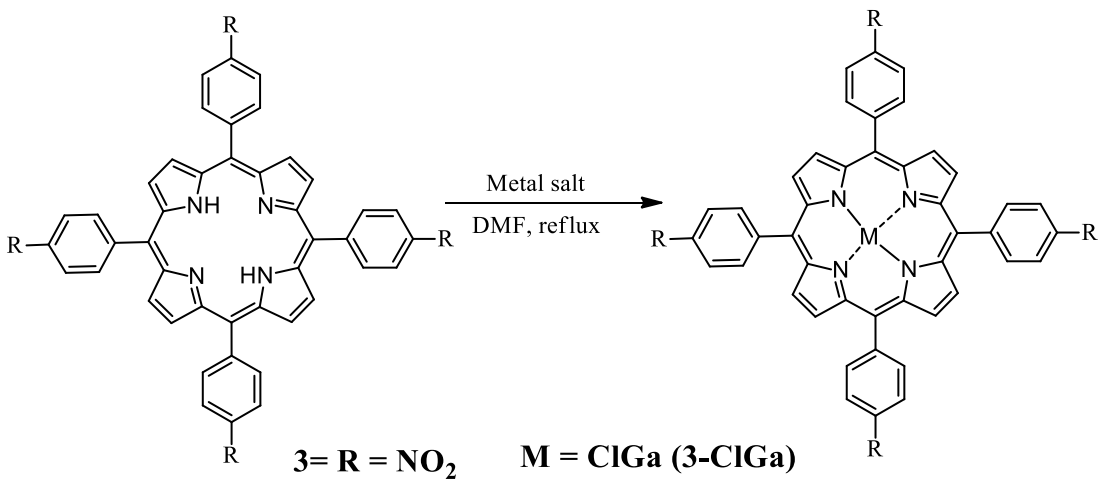

Scheme 3.4: Metal insertion for complexes 3-6

The Soret band of **3**-H_2 was observed at 417 nm while the Q bands were observed at 510, 543, 583 and 641 nm. The Soret band of **3**-ClGa was observed at 419 nm (**Table 3.1**) while the Q bands are observed at 573 and 611, respectively, **Fig. 3.6**. using **3**-H_2 and **3**-ClGa examples. **Table 3.1** shows that there was a red shift of the Soret band for metallated derivatives when compared to H_2 complexes. All complexes gave emission spectra which is typical of porphyrins with maxima listed in **Table 3.1**, except for **5**-ClGa which gave a very weak emission spectra due to the heavy atom effect of Br.

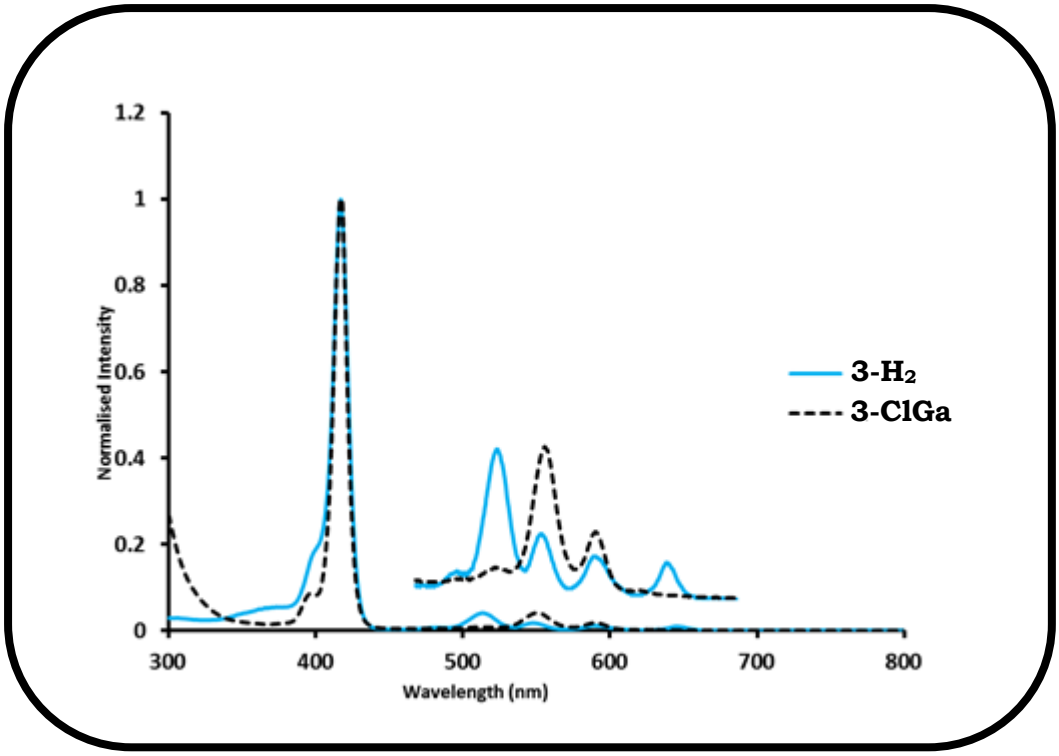

Figure 3.6: Electronic absorption spectra of 3-H_2 and 3-ClGa

Comparing the Soret band maxima for **3**-ClGa (419 nm), **4**-ClGa (428 nm) and **5**-ClGa (427 nm) differing in ring substituent but same central metal, **3**-ClGa at 419 nm is blue shifted compared to **4**-ClGa at 428 nm and **5**-ClGa at 427 nm. However, for the unmetalled **complexes 4**-H_2 and **5**-H_2 there is no shift. **6-**H_2 is red shifted compared to **3**-H_2, **4**-H_2 and **5** H_2 due to added π electrons from benzyloxy group (**Table 3.1**). Comparing **6**-Zn with **2**-Zn a slight blue shift is observed, for the latter.

Table 3.1: Spectroscopic characterisation of porphyrins all in DMF

Complex	**λ (Soret)/nm[a]**	**λ_{Em} (nm)**
1-H_2	417	651, 713
1-ClGa	425	607, 655
2-H_2	418 (418)	650, 714
2-Zn	427 (427)	605, 652
2-ClGa	425 (425)	604, 648
2-Cl_2Si	446 (446)	730
3-H_2	417	650, 714
3-ClGa	419	605, 655
4-H_2	419	648, 708
4-ClGa	428	551, 596
5-H_2	419	615, 715
5-ClGa	427	[b]
6-H_2	421	658, 720
6-Zn	429	616, 658
7-ClGa	425	610, 657
8-H_2	431	659, 718
8-ClGa	439	615, 660
8-Zn	440	615, 661

[a]Values in brackets are for PluS linked. [b]Weak emission was observed

3.1.4. Complex 8

Scheme 3.5 shows the metalation of **8**-H_2 to form **8**-ClaGa and **8**-Zn

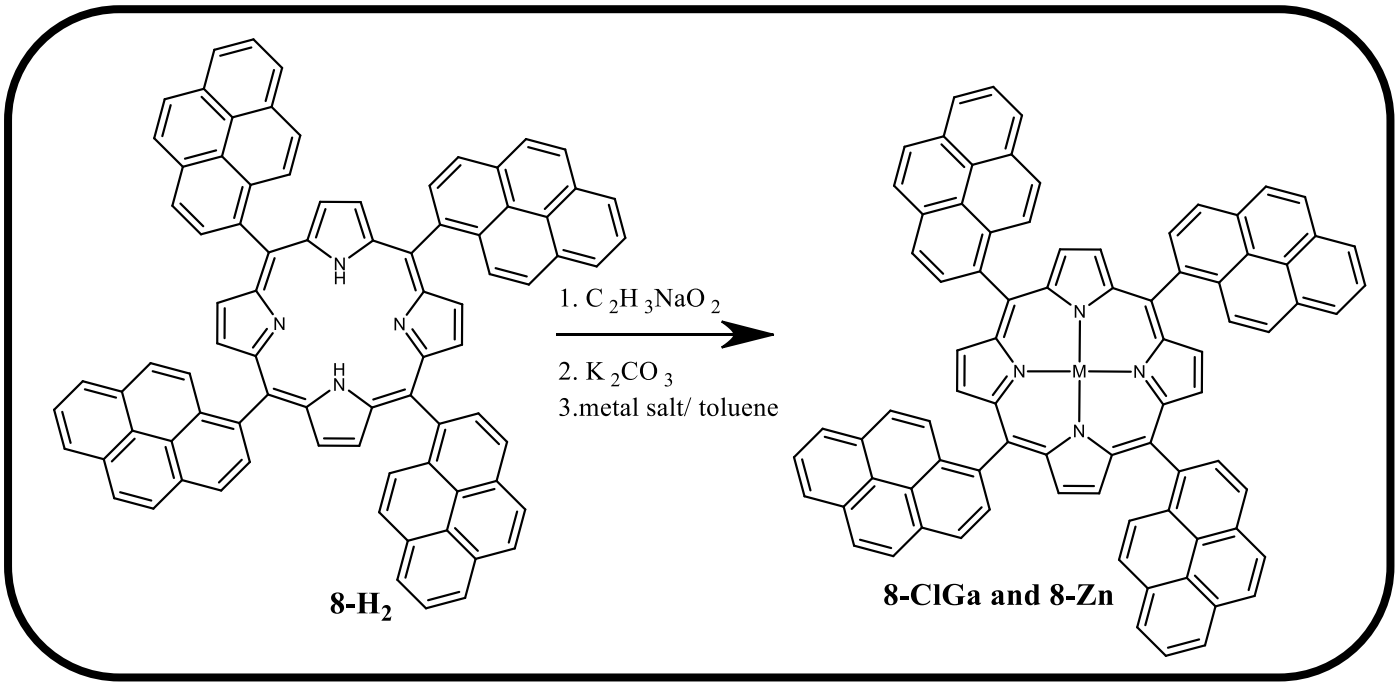

Scheme 3.5: Metal insertion of 8-H_2 to form 8-ClGa and 8-Zn

The ^{1}H NMR for **complex 8**, the pyrene protons were observed between 8.90-7.28 ppm integrated into 44 protons as expected. The Q bands **8**-H_2 are observed at 518, 553, 594 and 650 nm, while the two Q bands are observed at 563 and 603 nm for **8**-ClGa and at 564 and 605 nm for **8**-Zn. The Soret band can be observed at 431 nm for **8**-H_2 and 439 nm **8**-GaCl and 440 for **8**-Zn, **Table 3.1**. Absorption peaks below 350 nm are due to 1-pyrenyl absorption [**122**]. **Fig. 3.7** (**Table 3.1**) shows that there is a slight red shift for the **8**-GaCl and **8**-Zn compared to **8**-H_2. As discussed above this slight red shift of **8**-GaCl is a result of the insertion of the central metal. Comparing **6**-H_2, **6**-Zn (421 and 429 nm, respectively) with **8**-H_2, **8**-Zn (431 and 440 nm,

respectively), there is a slight red shift for the metallated derivatives **Table 3.1**. The porphyrins that have been metallated with gallium, **1**-GaCl (425 nm), **2**-GaCl (425 nm), **3**-GaCl (419 nm), **4**-GaCl (428 nm), **5**-GaCl (427 nm) and **8**-GaCl (439 nm), **complex 8** shows a huge red shift due to the π conjugation of pyrene.

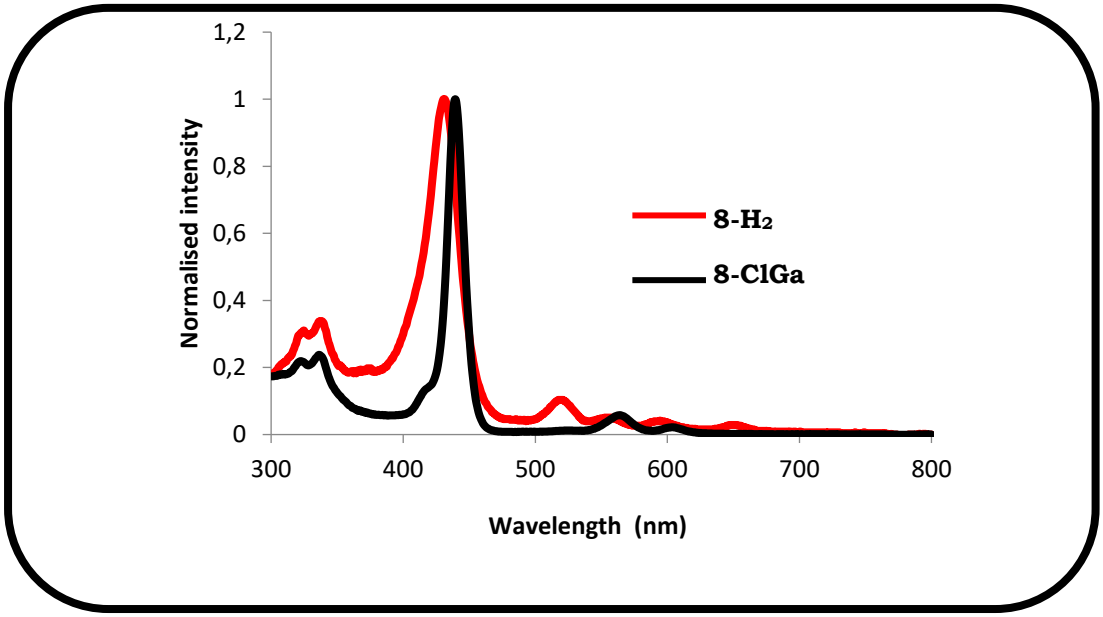

Figure 3.7: Electronic absorption spectra of 8-H_2 (Red) and 8-ClGa (Black).

Fig. 3.8 showed the emission spectra of **8**-H_2 and **8**-GaCl porphyrins, which are typical as stated above **[34]** of a metallated porphyrin with two bands differing in intensity at 659 nm and 718 nm for **8**-H_2, and 615 nm and 660 nm **8**-GaCl, 615 and 661 nm for **8**-Zn. The emission of spectra of 1-pyrenyl alone shows the main emission peak at 425 nm (See **Fig. 3.8B**).

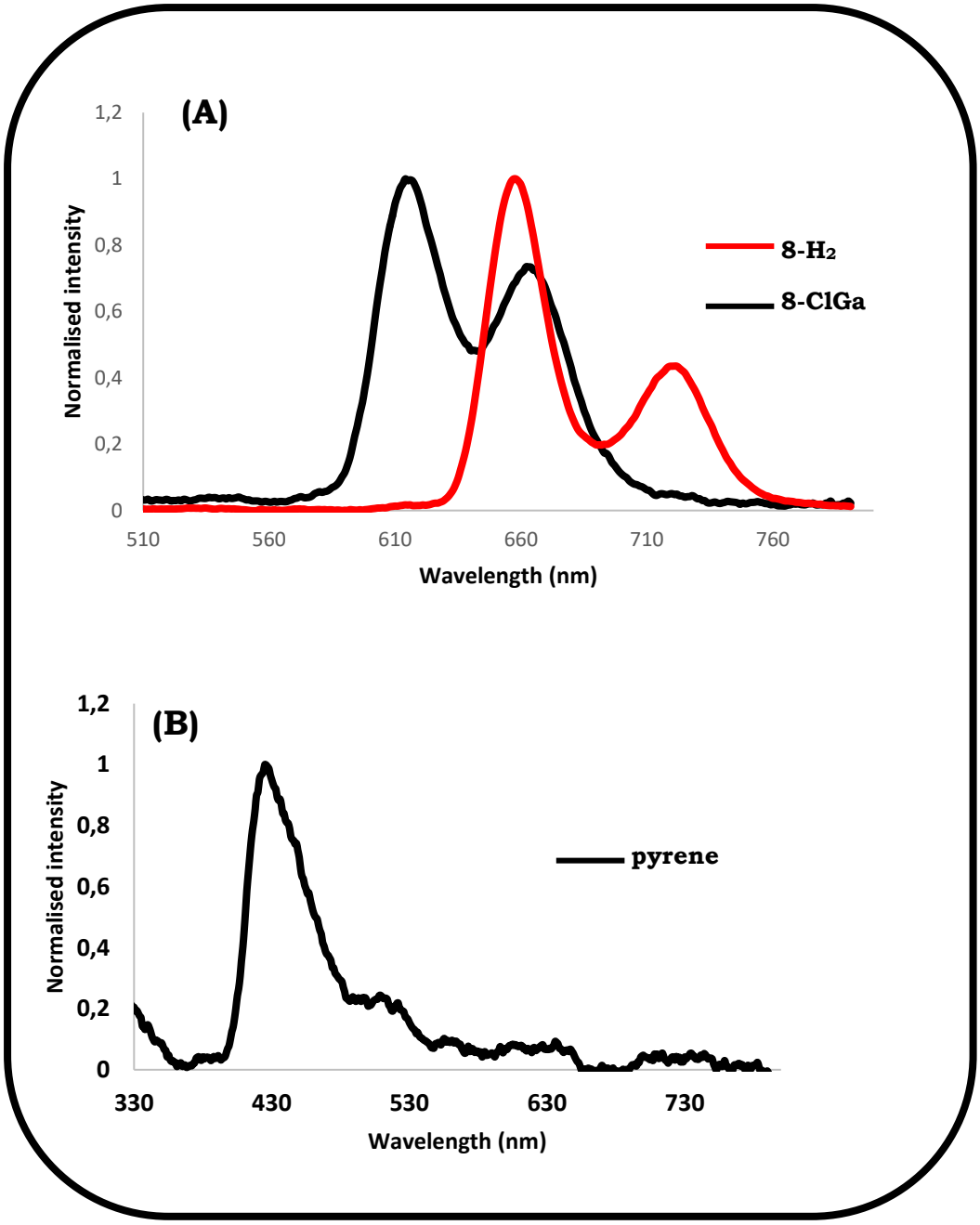

Figure 3.8: Fluorescence emission spectrum of 8-H_2 and 8-ClGa (A) and1-pyrenyl (B). The porphyrins were excited at 490 nm and 520 nm respectively. The 1-pyrenyl was excited at 330 nm.

3.2. Pluronic-FA synthesis

The synthesis of Pluronic-FA was done for embedding of **complex 5** as an example, since FA is selectively recognized and internalized by cancer cells

that over-express FA receptors [**76, 77**]. This in turn will enhance the potency of the embedded drug. The synthesis of Pluronic-FA was as follows: firstly, the Pluronic polymer OH groups were converted to COOH using oxalic acid then conjugated to FA (**Scheme 3.6**) which is abbreviated as F127-FA. The linking of Pluronic-FA could not be characterized by mass spectrometer. This was due to the fact that mass spectrometers equipped with electron impact (EI) or chemical ionization (CI) cannot give any information on the average molecular weigh of a polymer, because the polymeric chain breaks apart and it is no longer intact [**123]** and that the limit range of detection is 10 000 m/z

The ^{1}H NMR was used ascertain the successful linkage of F127 to FA. It is with relevance to note that the use of NMR in this case is to detect signals belonging to F127 as well as those belonging to folic acid rather than to assign number of protons. This is because the exact number of protons in F127 are not exact but dependent on polymeric extension during the polymerization reaction. The ^{1}H NMR of pluronic F127 prior to linkage showed the characteristic signal of this molecules between 3.25-3.80 ppm, which correspond to already reported chemical shift for F127 [**124, 125**]. upon the linkage of F127 to FA, two strong singlets between 2.55-2.85 ppm appear which is typical peak for CH_2 protons of FA [**126**]. The appearance of aromatic protons and NH_2 protons at 6.5 ppm and 5.5 ppm respectively are characteristic peak of FA [**126**] and these peaks were absent in the spectra of F127 prior to linkage, hence confirming successful linkage.

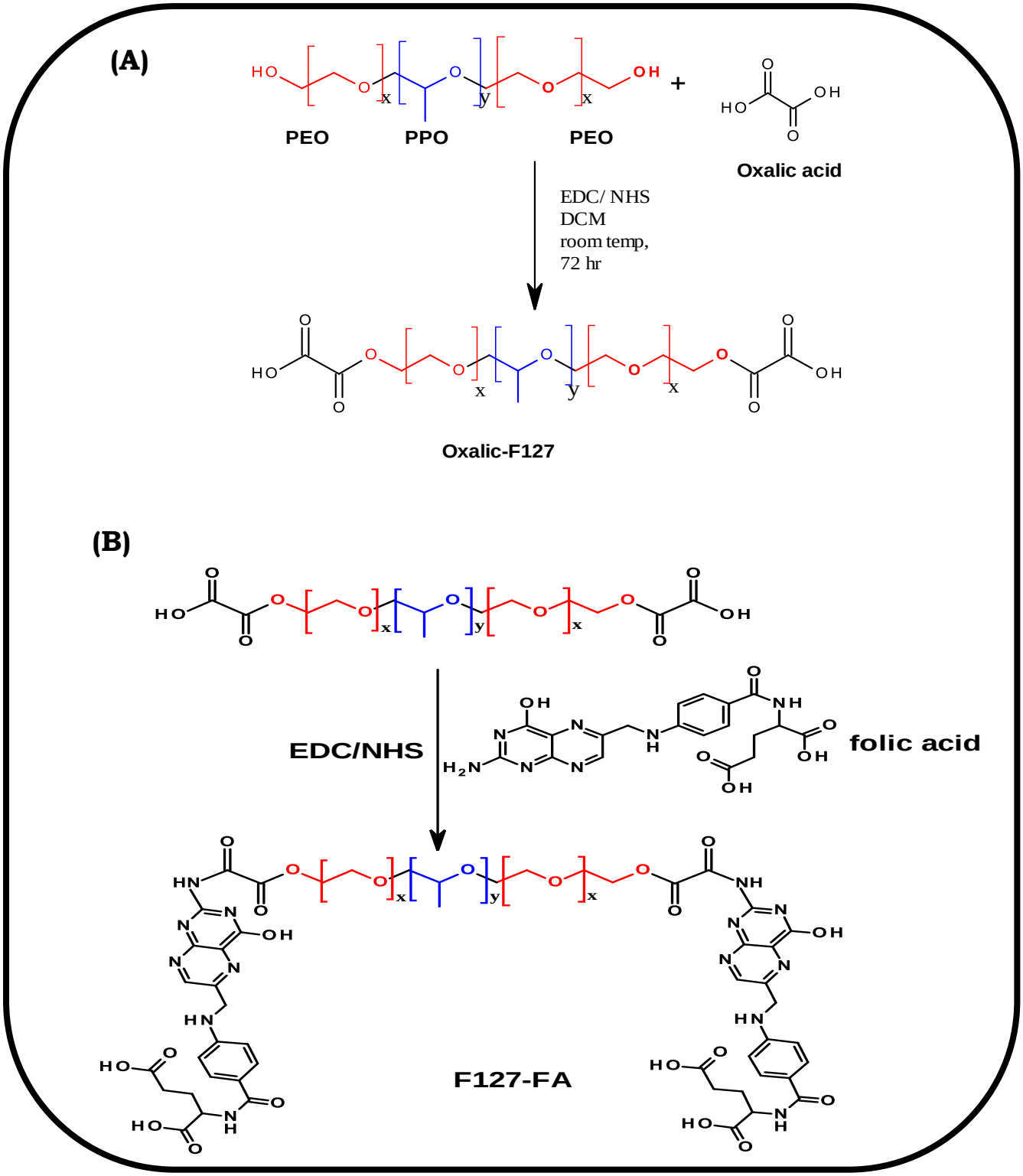

Scheme 3.6: Conjugation of (A) Pluronic F127 to oxalic acid to form Oxalic-F127 and (B) Oxalic-F127 to folic acid.

The formation of Oxalic-F127 was confirmed in FT-IR by the emergence of peaks at 1734 and 1778 cm^{-1} which are assigned to ester and carbonyl groups from the carboxylic respectively, **Fig. 3.9**. These bands are not present in the FT-IR spectra of oxalic acid or Pluronic F127. Anhydride bond formation was unexpected, but it turned out to be a positive result as it is more reactive compared to carboxylic acids. The ester peak (1734 cm^{-1}) is non-symmetrical and this can be attributed to the presence of a carboxylic carbonyl peak at a slight lower wavelength (1714 cm^{-1}). The emergence of a relatively broad peak at 3350 to 3390 cm^{-1} is ascribed to carboxylic -OH groups also confirmed the functionalization as indicated on the insert, hence this gives an indication that there will be free COOH groups to link to FA.

In the F127-FA spectrum, the decrease in the intensity of the peak at 1734 cm^{-1} in Oxalic-F127 to a broad shoulder (now at 1732 cm^{-1}) and the disappearance of the peak at 1778 were attributed to the conversion of the anhydride and carboxylic carbonyl groups to amide carbonyl groups at lower wavenumbers (around 1680 cm^{-1}). Success of conjugation was further confirmed where one of the amine peaks (3455 cm^{-1}) in FA disappears in the final F127-FA conjugate leaving that at 3408 cm^{-1} which was slightly shifted to 3404 cm^{-1}. The observation of only one characteristic amine peak is consistent with the presence of secondary amines such as amides.

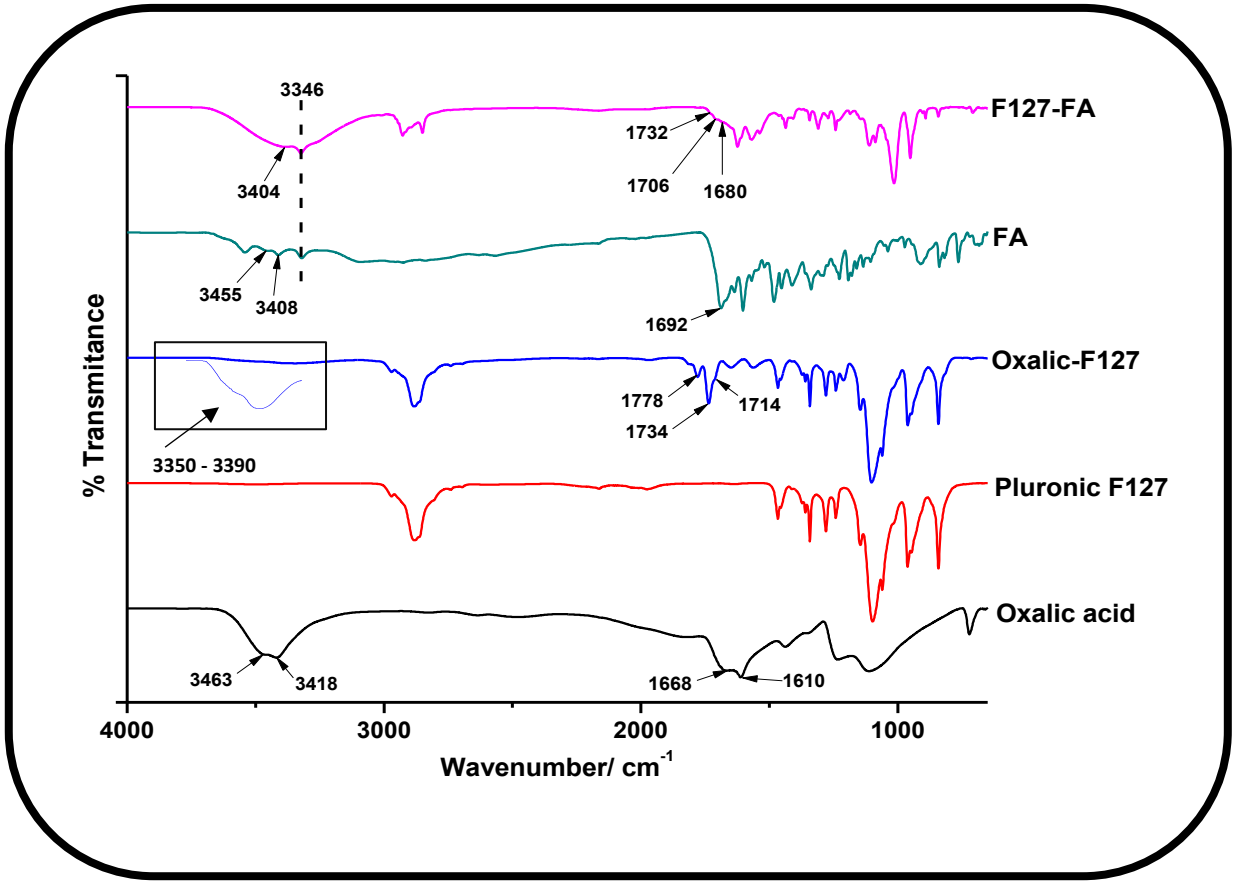

Figure 3.9: Fourier transform infrared spectroscopy (FTIR) of F127-FA, FA, Oxalic-F127 (with insert), Pluronic F127 and oxalic acid.

3.3. Incorporation of porphyrins into Pluronic polymer micelles.

3.3.1. Pluronic F127

Complexes 1-6 and **8** were further loaded into Pluronic F127 polymer. The incorporation of all porphyrins into micelles was carried out using the solid dispersion method (**Scheme 3.7**), which has been described in literature as stated in chapter 2. The porphyrins which were not water soluble, become water soluble after incorporation into Pluronic F127 micelles as also observed before [**127**], hence all the studies below are done in water. No comparison can be made between porphyrins alone dissolved in organic solvents and

when they are embedded in micelles since different solvents are used. **4**-H_2 and **4**-ClGa are water soluble before being embedded into micelles hence can be compared.

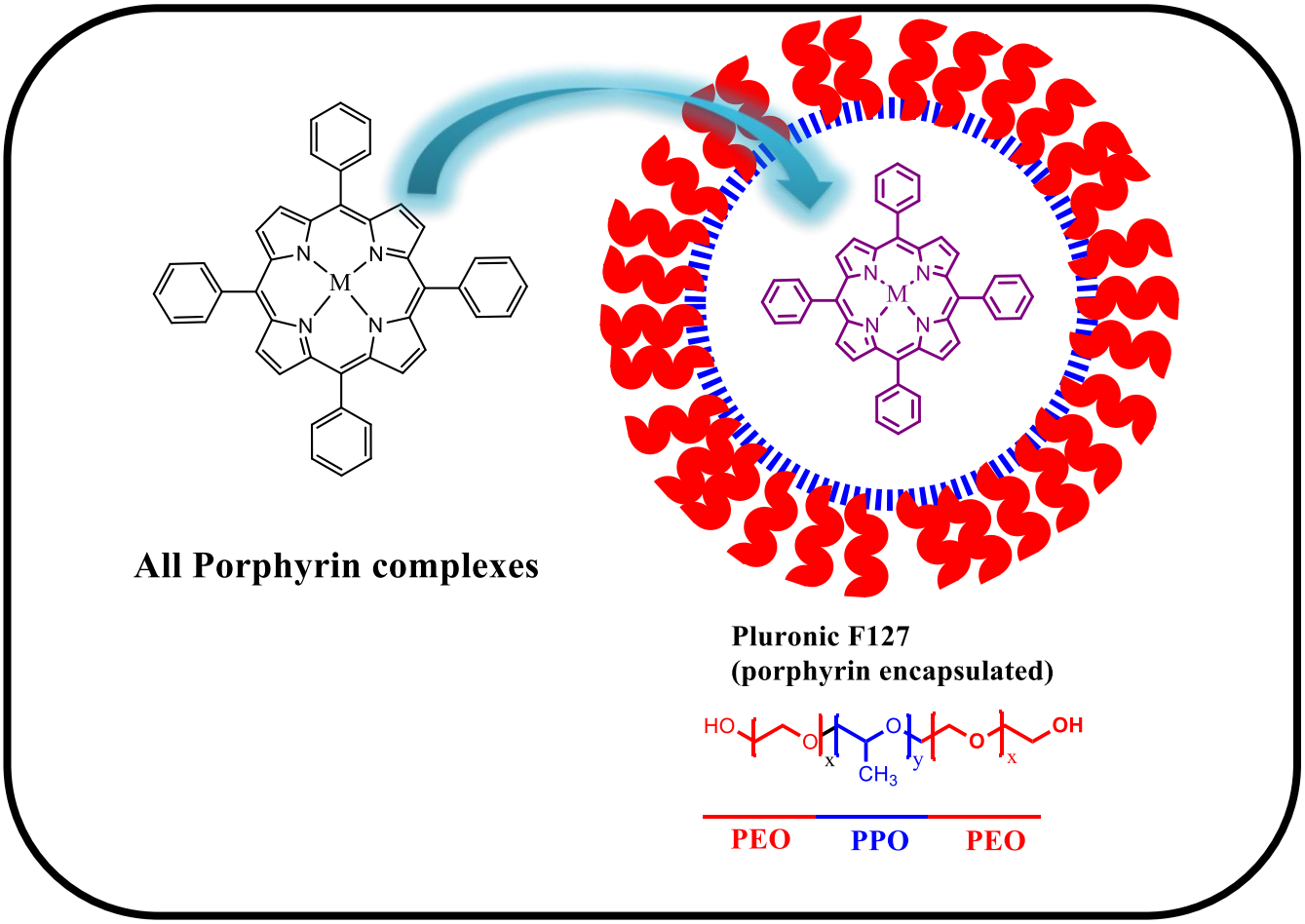

Scheme 3.7: Representation scheme of incorporation the porphyrins into Pluronic F127. Scheme not in scale in terms of size of porphyrin and Pluronic.

The porphyrins are referred to as **1**-H_2+F127, **1**-ClGa+F127, **2**-H_2+F127, **2**-ClGa+F127, **2**-Zn+F127, **2**-Cl_2Si+F127, **3**-ClGa+F127, **4**-H_2+F127, **4**-ClGa+F127, **5**-H_2+F127, **5**-ClGa+F127, **6**-H_2+F127, **6**-Zn+F127, **8**-H_2+F127, **8**-ClGa+F127 and **8**-Zn+F127.

Table 3.2: Spectroscopic characterisation of porphyrins loaded in Pluronic polymer as well as the DLS size and amount of porphyrin within the micelles in water.

Conjugates	DLS (nm)	Amount of porphyrin (mg)	λ_{Abs} Soret (nm)	λ_{Em} (nm)
1-H_2+F127	15.7	0.077	418	655, 719
1-ClGa+F127	30.9	0.071	423	615, 654
2-H_2+F127	16.4	0.075	419	657, 720
2-ClGa+F127	33.6	0.011	423	615, 657
2-Zn+F127	32.7	0.036	426	620, 655
2-Cl_2Si +F127	31.9	0.055	446	652, 699
3-H_2+F127	23.7	0.065	417	648, 703
3-ClGa+F127	31.4	0.045	421	601, 648
4-H_2+F127	28.6	0.076	419 (419)[a]	649, 709
4-ClGa+F127	39.6	0.032	428 (428)[a]	552, 598
5-H_2+F127	28.3	0.058	419	657, 719
5-ClGa+F127	30.7	0.049	427	-
5-H_2+F127-FA	30.5	-	419	558, 720
5-ClGa+F127-FA	33.2	-	427	-
6-H_2+F127	20.9	0.075	421	620, 661
6-Zn+F127	23.8	0.061	429	615, 662
6-H_2+F127/P123	22.0	0.092	422	621, 662
6-Zn+F127/P123	26.0	0.086	429	615, 663
8-H_2+F127	19.6	0.058	432	657, 720
8-ClGa+F127	28.6	0.067	439	616, 663
8-Zn+F127	28.0	0.070	439	618, 664

[a]For porphyrins alone.

The electronic absorptions spectral data are listed in **Table 3.2** and **Fig. 3.10** shows the spectra of **Complexes 1** and **2** as examples.

The Soret bands were observed at 418 nm, 423 nm for **1**-H_2+F127 and **1**-ClGa+F127 respectively. While the Soret bands of **2**-H_2+F127, **2**-ClGa+F127,

2-Zn+F127 and **2**-Cl_2Si +F127 were observed at 419 nm, 423 nm, 426 nm and 446 nm, respectively (**Table 3.2**).

The red shifts on metalation followed the same trend as previously discussed. For **4**-H_2+F127 and **4**-ClGa+F127 which are soluble in water, there were no spectral changes in the presence Pluronic F127 compared to the porphyrins alone, **Table 3.2.**

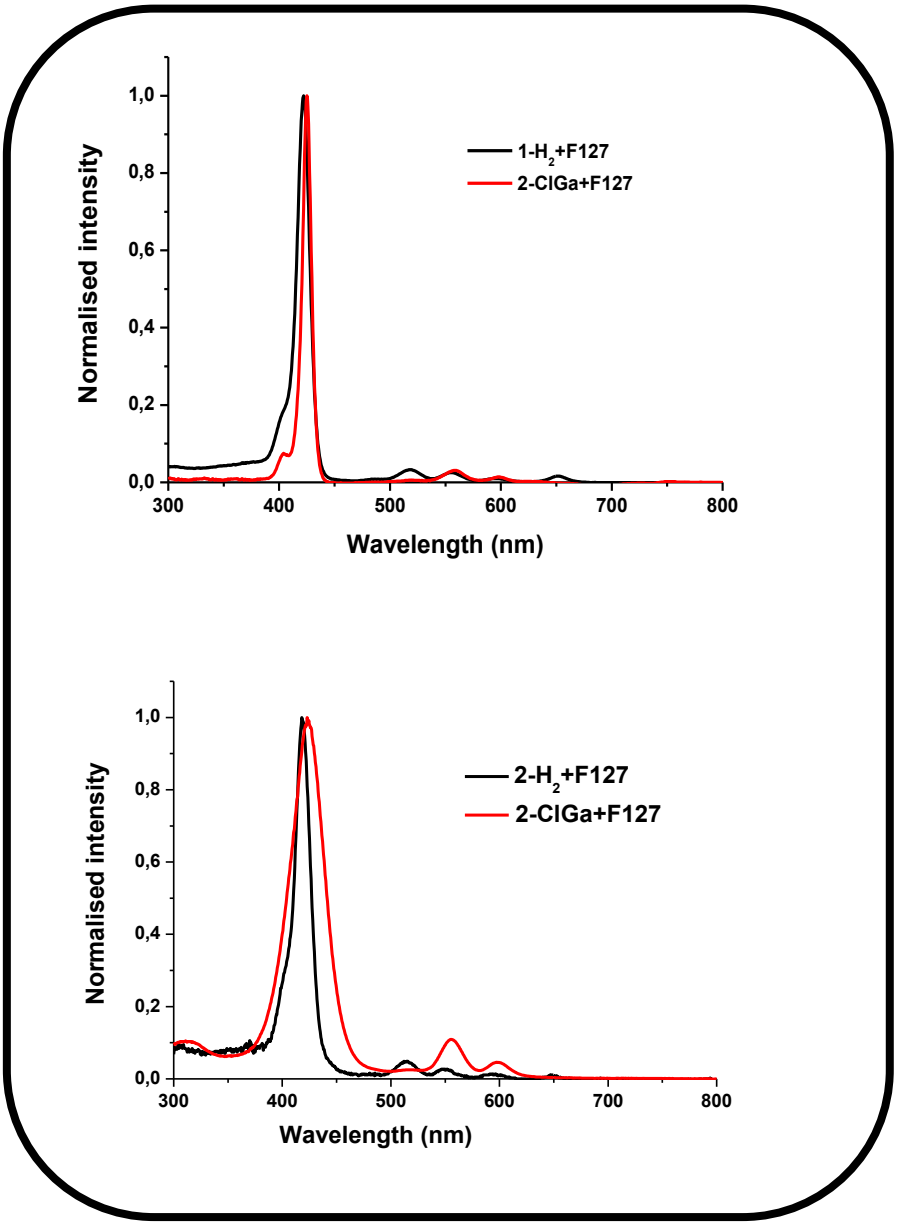

Figure 3.10: Normalised electronic absorption spectra of complexes 1 and 2 when loaded in Pluronic F127 in water.

In order to check the effect of the substituent on the spectra, **complexes 1**-ClGa+F127 and **2**-ClGa+F127 containing the same central metal and different substituents were compared, but there was no shift in the Soret peak maxima for these two complexes, showing no substituent effect as observed in the absence of Pluronic. The same applies when comparing **1**-H_2+F127 and **2**-

H_2+F127, both metal free but containing different substituents. However, when comparing **3**-ClGa+F127, **4**-ClGa+F127, **5**-ClGa+F127 and **8**-ClGa+F127 the shifts were similar to porphyrins without F127 for same reason stated above.

After the determination of the ε values of porphyrins in F127 aqueous solutions, the relationships between the photosensitizer incorporation capacity and the concentration were evaluated. The actual amounts of porphyrins embedded into micelles were determined from ε values using the Beer-Lambert law and maximum absorbance of the Soret bands following reported methods [**53**]. The amounts ranged from 0.011 to 0.092 mg, hence the highest loading was observed for complexes with carboxyphenyl ring.

3.3.2. Embedding in binary mixture of Pluronic F127/P123

The incorporation of **complex 6** was also carried using the same method as previously described for other complexes. The spectra in water are shown in **Fig. 3.11** for **6**-H_2+F127/P123 and **6**-Zn+F127/P123. There was a red shift in **6**-Zn+F127 compared with **6**-H_2+F127 (**Table 3.2**) as well as in binary mixture of **6**-Zn+F127/P123 as compared to **6**-H_2+F127/P123 in water, as was the case in the absence of Pluronic micelles for the reasons given above.

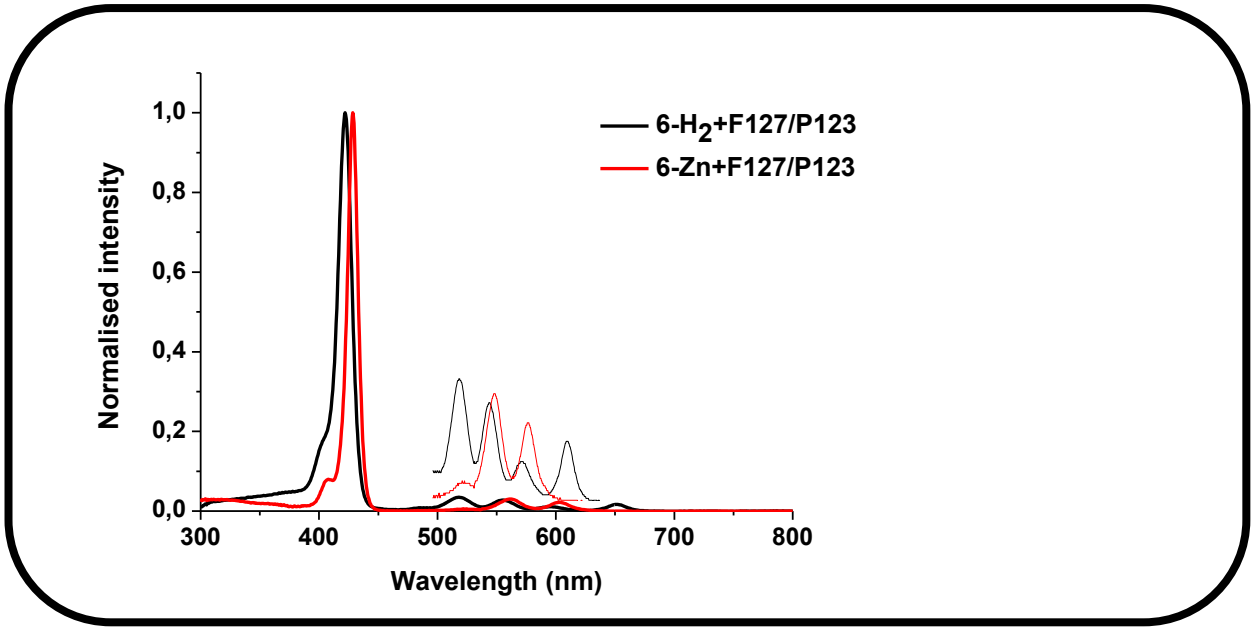

Figure 3.11: Electronic absorption spectra of 6-H_2+F127/P123 and 6-Zn+F127/P123 in H_2O. Insert is the expansion of the Q band region.

3.3.3. Pluronic-FA

Complex 5 was used as an example for incorporation into Pluronic micelles that has been modified with FA (**Scheme 3.8**). The spectra for **5**-H_2 and **5**-GaCl following incorporation into F127-FA show the peak due the FA at approximately 366 nm, **Fig. 3.12B**, which is absent in **Fig. 3.12A** (where there is no FA).

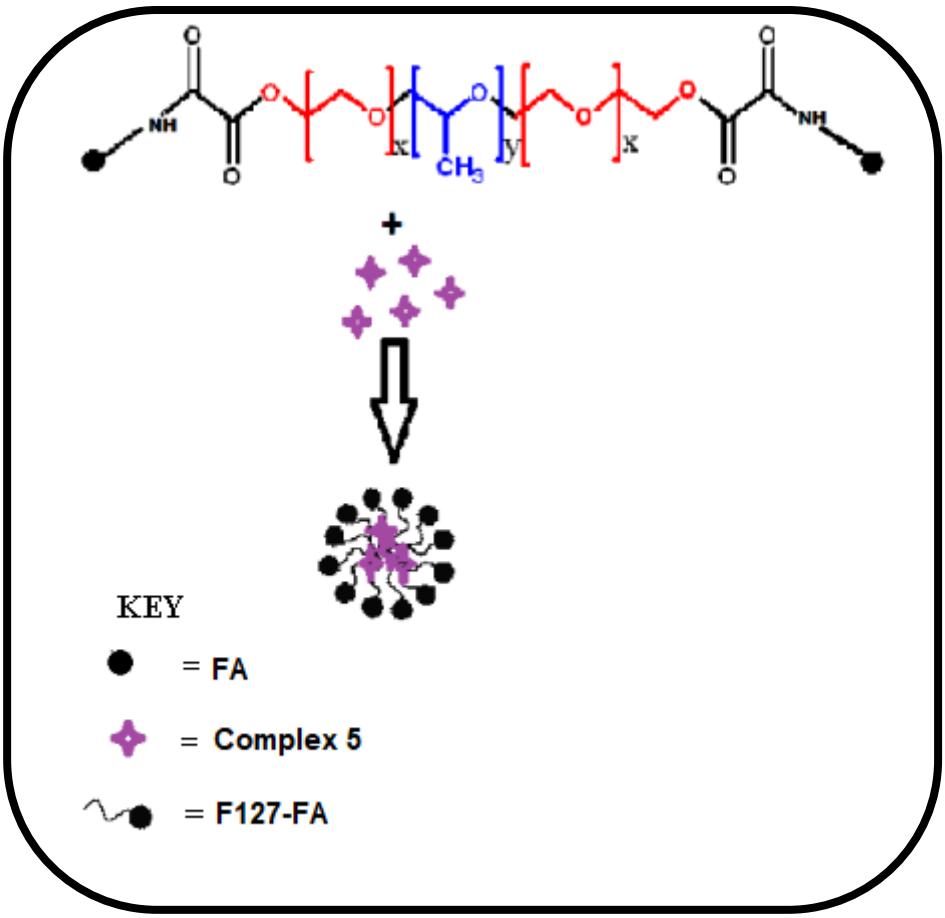

Scheme 3.8: Incorporation of the porphyrins into Pluronic F127-FA micelle.

The FA peak is assigned to the π–π* transition localized on the pterin ring. The F127-FA peak is blue shifted compared to FA alone, **Fig. 3.12B**. These spectral changes confirm the presence of both FA and porphyrins in the conjugate. The Soret bands were observed at 419 nm and 427 nm for **5**-H_2+F127-FA and **5**-GaCl+F127-FA, respectively, in water. The values were the same as for the corresponding **5**-H_2+F127 and **5**-GaCl+F127, **Table 3.2**. Since the spectra of the porphyrins alone was recorded in DMF due to lack of solubility in water, the two sets of spectra cannot be compared. The two spectra can not be compared because it was reported that micelles are not stable in DMF and that the micelle shape changes [**128**].

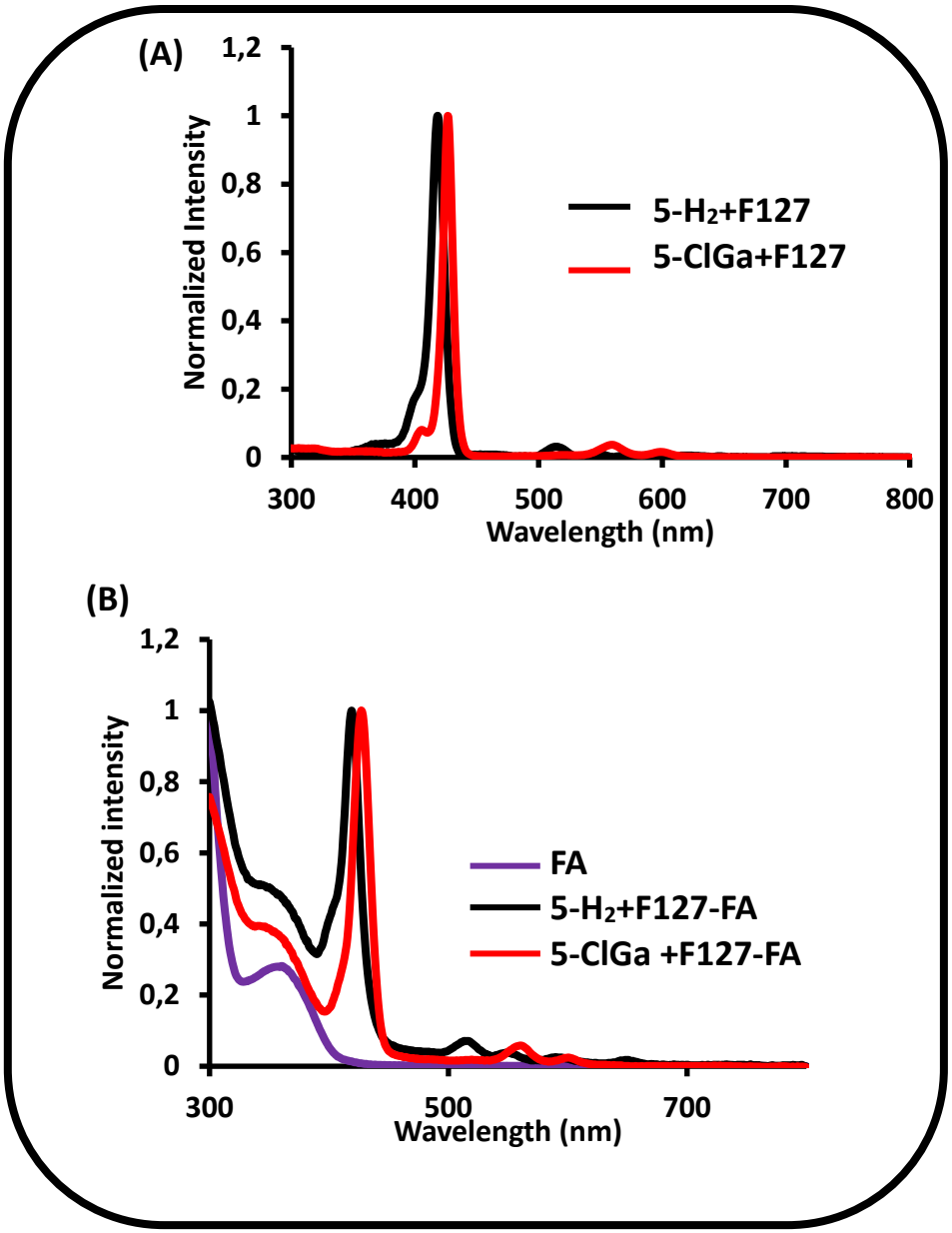

Figure 3.12: Electronic absorption spectra of (A) 5-H_2+F127 and 5-ClGa+F127 as well as (B) Folic acid (FA), 5-H_2+F127-FA and 5-ClGa+F127-FA in water.

3.3.4. Size determination by DLS

The micelle sizes were determined using dynamic light scattering (DLS). It has been reported that micelles should be small enough to evade detection and destruction by the reticular endothelial system therefore increasing the efficiency and circulation in blood of the encapsulated drug; hence the determination of micelle size is crucial for this work **[36].**

There was an increase in micellar size upon incorporation of the porphyrin into the F127 polymer micelles, F127-FA or binary mixture of F127/P123 micelles compared to Pluronic F127 alone 14.6 nm **Table 3.2**. A similar trend was observed in literature when ibuprofen, aspirin, and erythromycin were incorporated into Pluronic F127 **[41]**. The sizes of the porphyrin containing micelles were determined to be 15.7 nm, 30.9 nm, 16.4 nm, 33.6 nm, 32.7 nm and 31.9 nm for **1**-H_2+F127 and **1**-ClGa+F127, **2**-H_2+F127, **2**-ClGa+F127, **2**-Zn+F127 and **2**-Cl_2Si+F127 respectively, **Fig. 3.13** (as example). The sizes for the rest of the conjugates are listed in **Table 3.2**. In all cases (**Table 3.2** and **Fig. 3.13**), metal free conjugates have smaller sizes as compared to the corresponding metallated derivatives. It has been reported that micelles with diameters below 50 nm are able to deeply penetrate tumor tissue in spite of elevated interstitial pressure [**129**]. The micelles sizes that were obtained in this work are all below 50 nm.

It was found that the most metallated drugs increased the sizes of the micellar core and corona [**61**], hence the increase in size for micelles containing metallated porphyrins compared to metal free ones could be a result of change in hydrophobicity of the former, while small differences in sizes for the

micelles of metallated derivatives reflect small differences in hydrophobicity **[61]**. Comparing **1**-H_2+F127 with **2**-H_2+F127 both metal free, but containing different substituents shows that the latter gave slightly larger micelles. The same applies when comparing **1**-ClGa+F127 with **2**-ClGa+F127, both containing the same Ga central metal but different substituents. It seems the presence of phenoxy benzoic acid which is a bulkier substituent result in larger micelles. Comparing **2**-ClGa+F127, **2**-Zn+F127 and **2**-Cl_2Si+F127, containing the same substituent but different central metals, shows no direct correlation with the size of the central metal ion. Comparing **1**-ClGa+F127, **2**-ClGa+F127, **3**-ClGa+F127, **4**-ClGa+F127, **5**-ClGa+F127 and **8**-ClGa+F127 as well as the unmetallated derivatives, it shows that larger micelle size is that of **complex 4** which is negatively charged. Comparing **2**-Zn+F127, **6**-Zn+F127 and **8**-Zn+F127 all containing Zn but different substituent; the micelles size is larger for **2**-Zn+F127 followed by **8**-Zn+F127 and this could be due to the presence of bulky substituent.

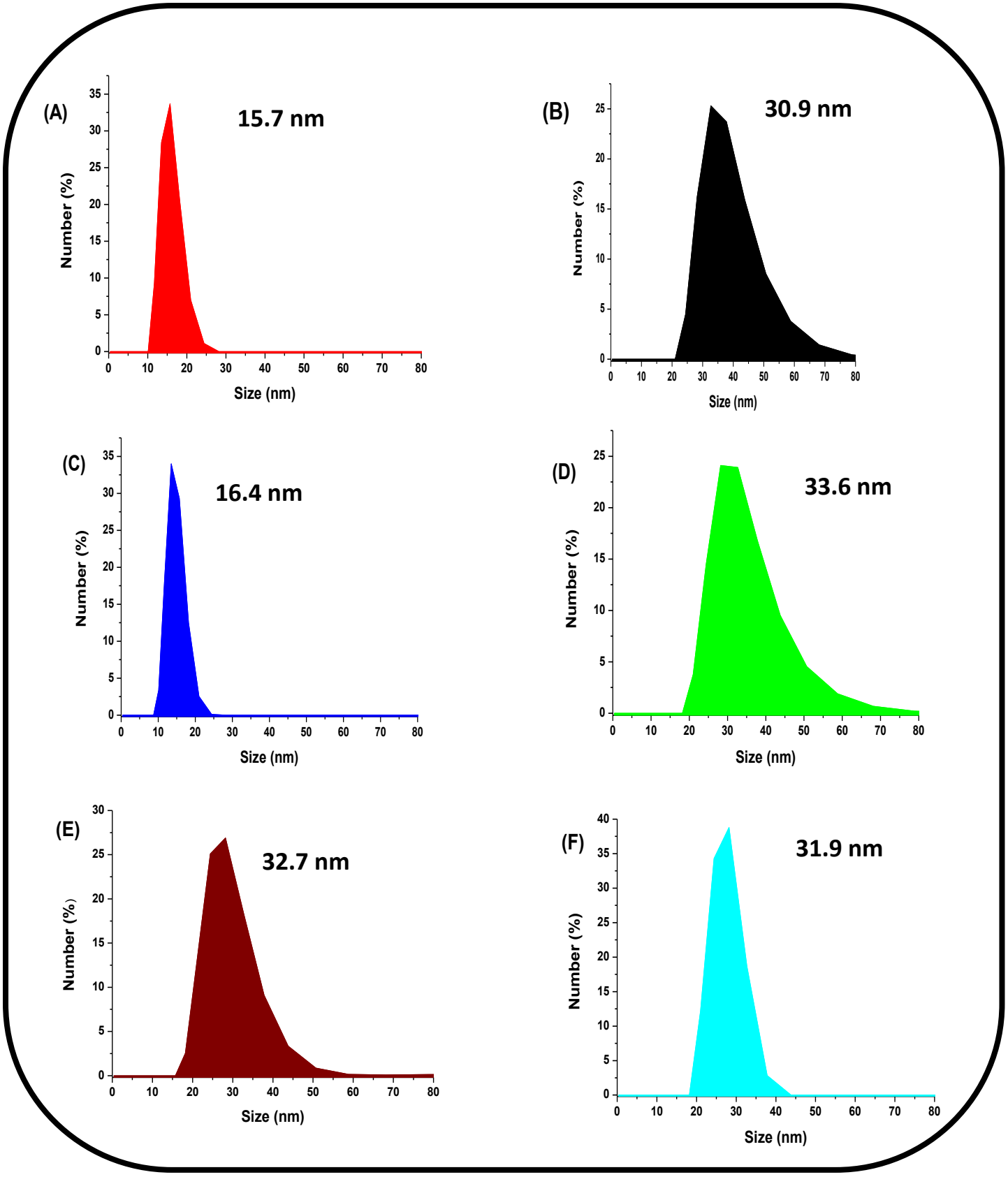

Figure 3.13: Dynamic light scattering of 1-H_2+F127 (A) and 1-ClGa+F127 (B), 2-H_2+F127 (C), 2-ClGa+F127 (D), 2-Zn+F127 (E) and 2-Cl2Si+F127 (F)

Chaibundit *et.al* **[130]** observed that binary mixtures of Pluronics®, which have the same hydrophobic block length, formed stable comicelles in diluted aqueous solution. These mixtures also showed a single narrow distribution and small particles at room temperature **[130, 131]**. This behaviour was observed for the mixtures of Pluronic F127 and P123 used for solubilizing the drug Paclitaxel [**132**] with DLS sizes ranging from 20.0 to 30.0 nm.

Pluronic F127/P123 also formed stable comicelles in this work as previously reported **[130, 131].** The size determined for **6**-H_2+F127/P123 was 22.0 nm while that of **6**-Zn+F127/P123 was 26.0 nm, **Table 3.2**, which is within the range obtained by the previous researchers **[132]**. For the same ratio of Pluronic P123/F127 micelles in the absence of the porphyrin, the DLS size was 14 nm. The size for **6**-H_2+F127/P123 and **6**-Zn+F127/P123 are slightly larger than **6**-H_2+F127 and **6**-Zn+F127 probably due to the micellization of the two polymers.

3.3.5 TOF-SIMS spectral characterization

The principle of TOF-SIMS is that a pulsed primary ion beam is incident on the sample surface and time-of-flight (TOF) secondary ion mass analysis is performed on the ejected positive or negative secondary ions **[133]**. With the use of multi-stop timing electronics, TOF mass analysis enables the entire mass spectrum to be derived from each pulse to be collected.

The elemental compositions of the nanoconjugates of **3**-ClGa+F127 and **8**-ClGa+F127 as examples were characterized by TOF-SIMS. **Fig. 3.14** shows

the TOF SIMS image of **3**-ClGa+F127. The presence of CH_2-C-CH_3 is as a result of the F127 hydrophobic chain, -CN- is a segment from **complex 3** and OH-CH_2CH_2 is a segment of the F127 hydrophilic chain. The images on the right show an overlay of the segments.

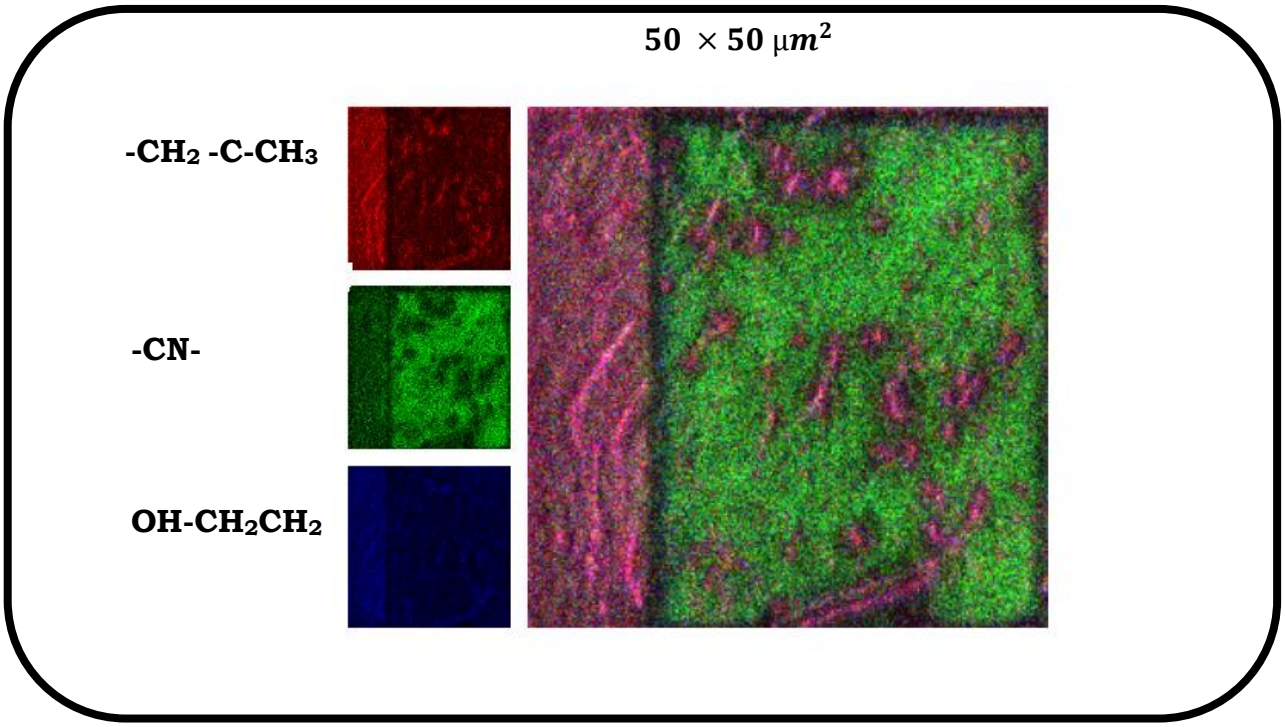

Figure 3.14: TOF-SIMS images of 3-ClGa+F127

The mass spectrum for **8**-ClGa+F127 showed the surface elemental compositions mostly to be $–C_2H_3O$, -OH, CH_2, -O and Ga in **Fig. 3.15A** and **B**, and further showed -OH both in the positive and negative mode. The oxygen is from the Pluronic F127 encapsulating polymer.

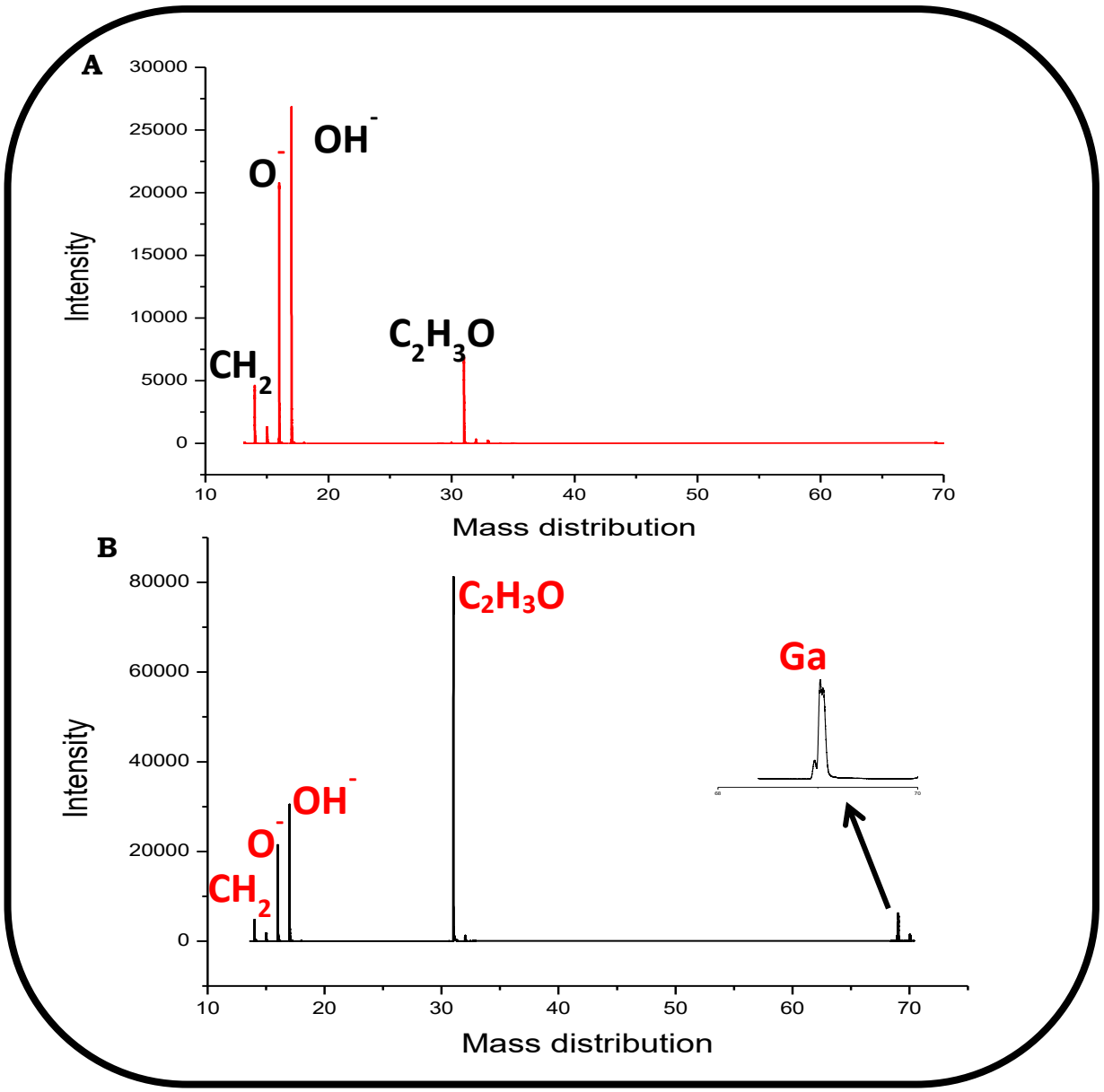

Figure 3.15: Secondary ion mass spectrum of 8-H_2+F127 (A) and 8-ClGa+F127 (B).

In **Fig. 3.16**, the images for **8**-ClGa+F127 are shown, the bar on the side in μm (left side and bottom) shows the total area of the sample where the data was obtained from while the legend on the right shows the intensity of the ions. **Fig. 3.16A** (i and ii) where **8**-ClGa+F127 was used as an example shows a high concentration for Ga as indicated by the bright yellow sections on the

image. In comparison **Fig. 3.16B** (i and ii) shows even higher concentration of the organics, due to the presence of porphyrins and Pluronic F127

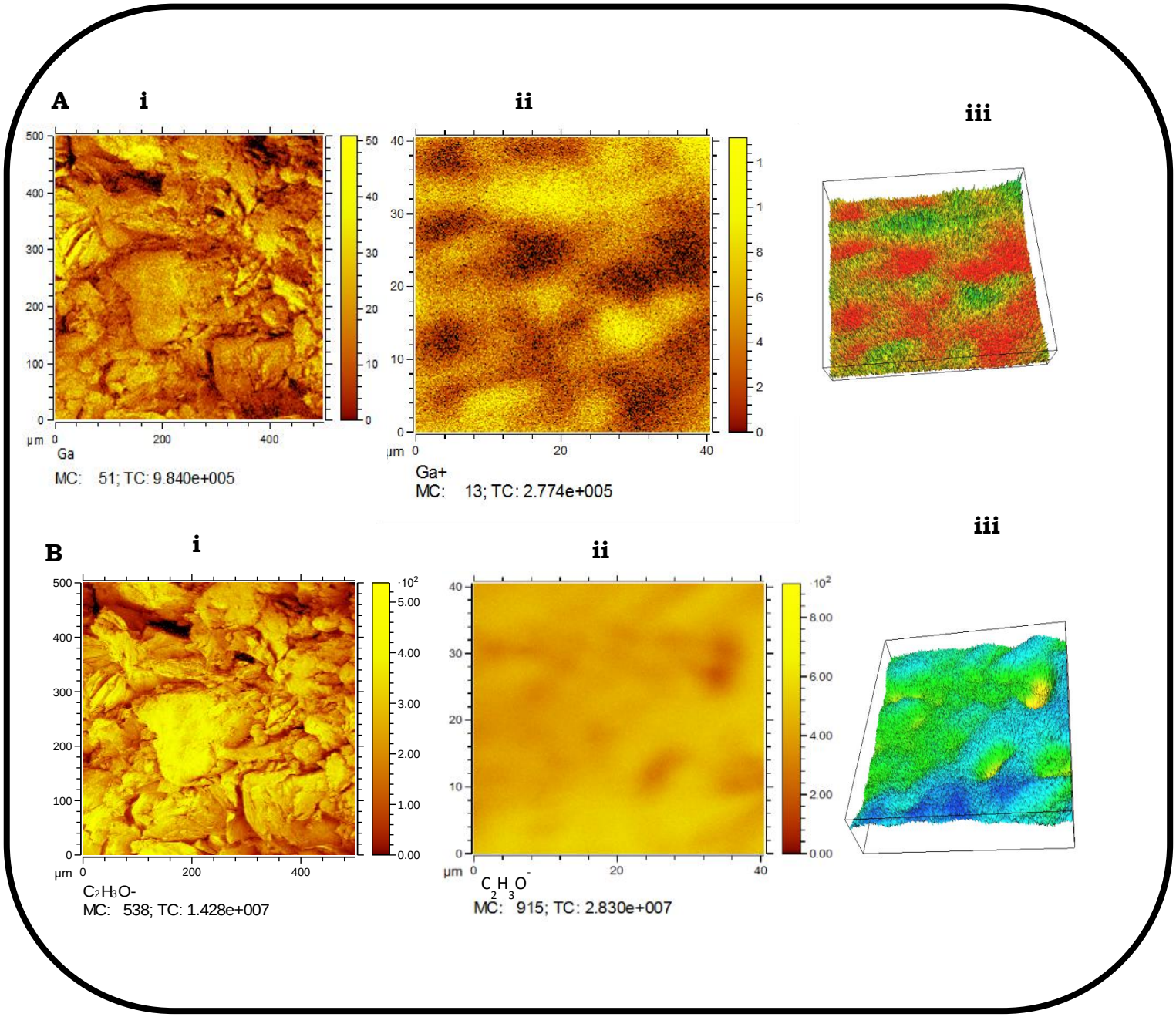

Figure 3.16: TOF-SIMS images ((i) 500 x 500 µm and (ii) 40 x 40 µm) and the carpet plots (iii) of 8-ClGa+F127. (A) Ga region and (B) organic region (Pluronic F127).

The carpet plots are a 3D representative of the TOF-SIMS images. A carpet plot is a means of displaying data that is dependent upon two variables in a format that allows interpolation and interpretation that is much easier than when normal multiple curve plots are used. Hence this allows one to have an idea on how the porphyrin is interacting with the polymer and the location of the porphyrin with the polymer. The interaction of the polymer and the porphyrin is shown on the carpet plots (plots iii) as well as the zoomed in images (plots ii). On the carpet plots, the location of the porphyrin is seen where the colour is green on the Ga carpet plot (**Fig. 3.16A** (iii)) corresponding to the bright yellow (high counts) in **Fig. 3.16A** (i and ii). For the organics, the carpet plot (**Fig. 3.16B** (iii)), shows the dominance of green corresponding to yellow in **Fig. 3.16B** (i and ii). The high intensity in **Fig. 3.16B** indicates the high organic content resulting from a porphyrin/polymer micelle mixture.

3.3.6. SEM images

Fig. 3.17 shows the SEM micrographs of F127, **8**-H_2+F127 and **8**-ClGa+F127, respectively, as examples. Triblock copolymers such as Pluronic F127 reduce the self-aggregation and increase solubility of porphyrins. The triblock copolymer core of the micelles consists of the hydrophobic PPO blocks that are separated from the aqueous exterior by the shell of hydrated hydrophilic PEO chains. By itself the core represents a “cargo hold” for incorporation therapeutic or diagnostic drugs. SEM has been used to investigate the morphological changes of the polymeric micelles [**134, 135**].

The SEM image of the Pluronic F127 polymer, **Fig. 3.17A** shows the presence of the “cargo hold”. However after encapsulation of the porphyrin, **Fig. 3.17B**

and **C** the "cargo hold" are no longer observed which is an indication that the porphyrin have been loaded.

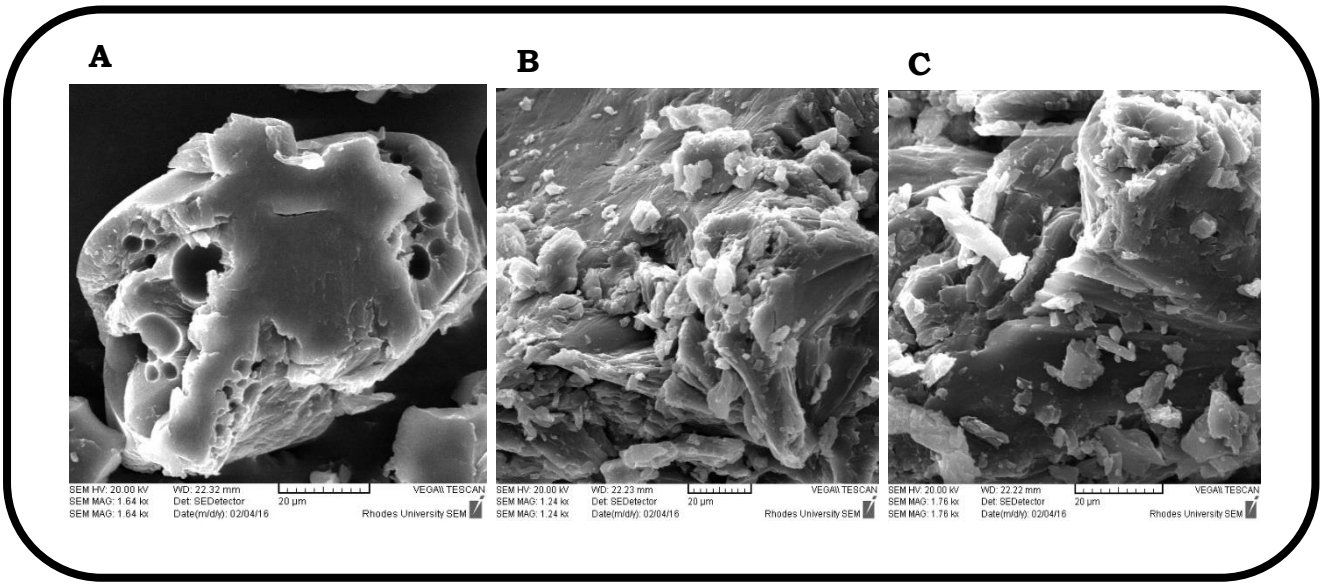

Figure 3.17: SEM micrographs of F127 (A), 8-H_2+F127 (B) and 8-ClGa+F127 (C)

3.4. Complex 2 linked to PluS NPS

Complexes 2-H_2, **2**-Zn, **2**-ClGa and **2**-Cl2Si were linked into PluS NPs (**Scheme 3.9**). The linking of these NPs does not form micelles [**116**]. There was no change in spectra following conjugation of the **2**-Zn, **2**-ClGa and **2**-Cl_2Si to PluS NPs (**Table 3.1**), **Fig. 3.18** (**2**-Zn showed as an example). The PluS NPs showed no absorption in the visible region.

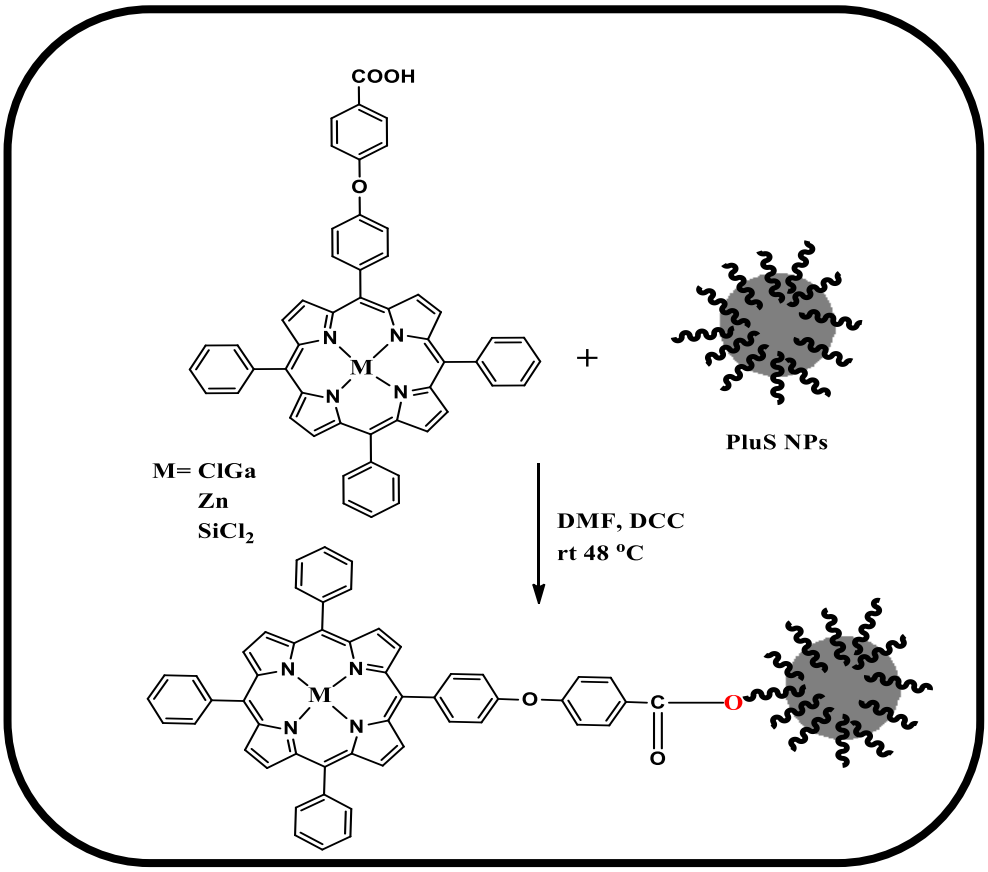

Scheme 3.9: Covalent attached of PluS NPs to complex 2

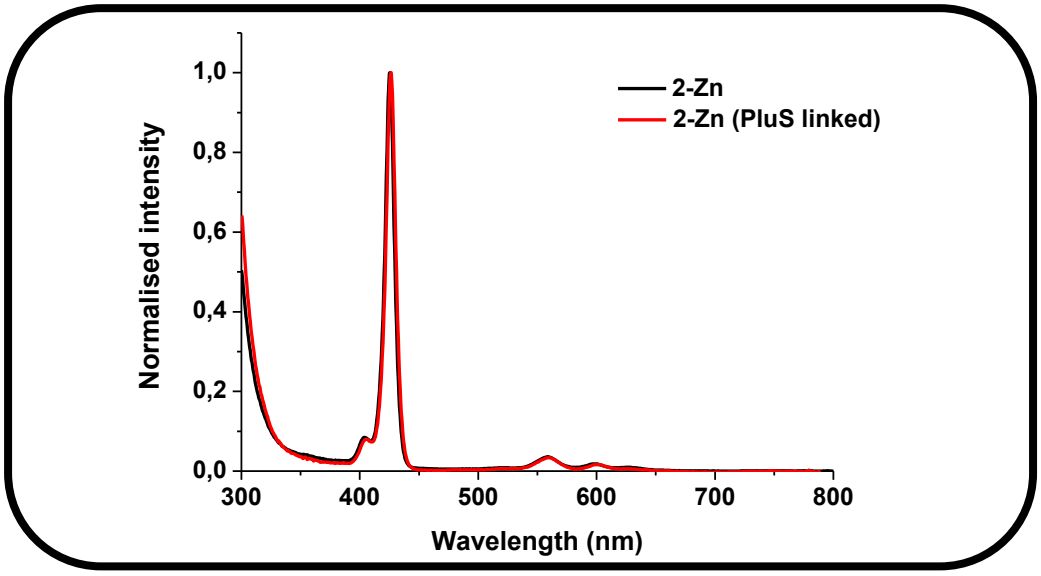

Figure 3.18: Absorption spectra of 2-Zn (PluS linked) in DMF

The linking of the porphyrins to the PluS NPs using an ester bond was confirmed using FT-IR spectra. The ester bond can be observed at 1651 cm^{-1} (**Fig. 3.19**) for **2**-Zn (PluS linked), confirming conjugation via an ester bond. An aliphatic C-H vibrations can be seen at 2929 cm^{-1} while OH vibration is at 3473 cm^{-1}. The FT-IR of PluS NPs shows Si-O-Si peak at 1054 cm^{-1}, Si-O peak at 794 cm^{-1} and the OH peak is observed at 3340 cm^{-1}. The Si-O-Si peak and Si-O peak have been reported at 1050 and 800 cm^{-1} respectively [**136**].

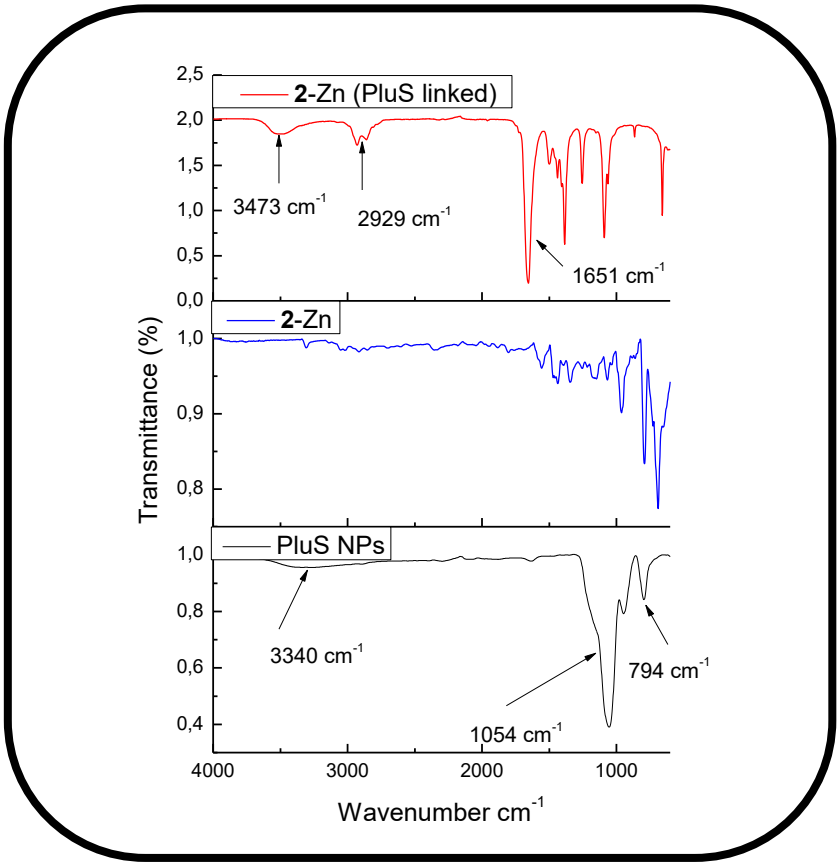

Figure 3.19: FTIR spectra of 2-Zn (PluS linked) PluS NPs and 2-Zn alone.

The PluS NPs were further characterised by TEM, EDS, XRD, TOF-SIMS and BET. **Fig. 3.20A** shows TEM images of PluS NPs. The particles are mono

dispersed with an average size of 163 nm (see accompanied histogram, **Fig. 3.20B**). The PluS NPs particles are spherical. The F127 allows the NPs to have a well ordered mesostructured [**137**]. Upon conjugation the PluS NPs to **2**-Zn (**Fig. 3.20C**) aggregation was observed. It was difficult to obtain the overall average size for all the **2**-Zn (PluS linked) due to aggregation.

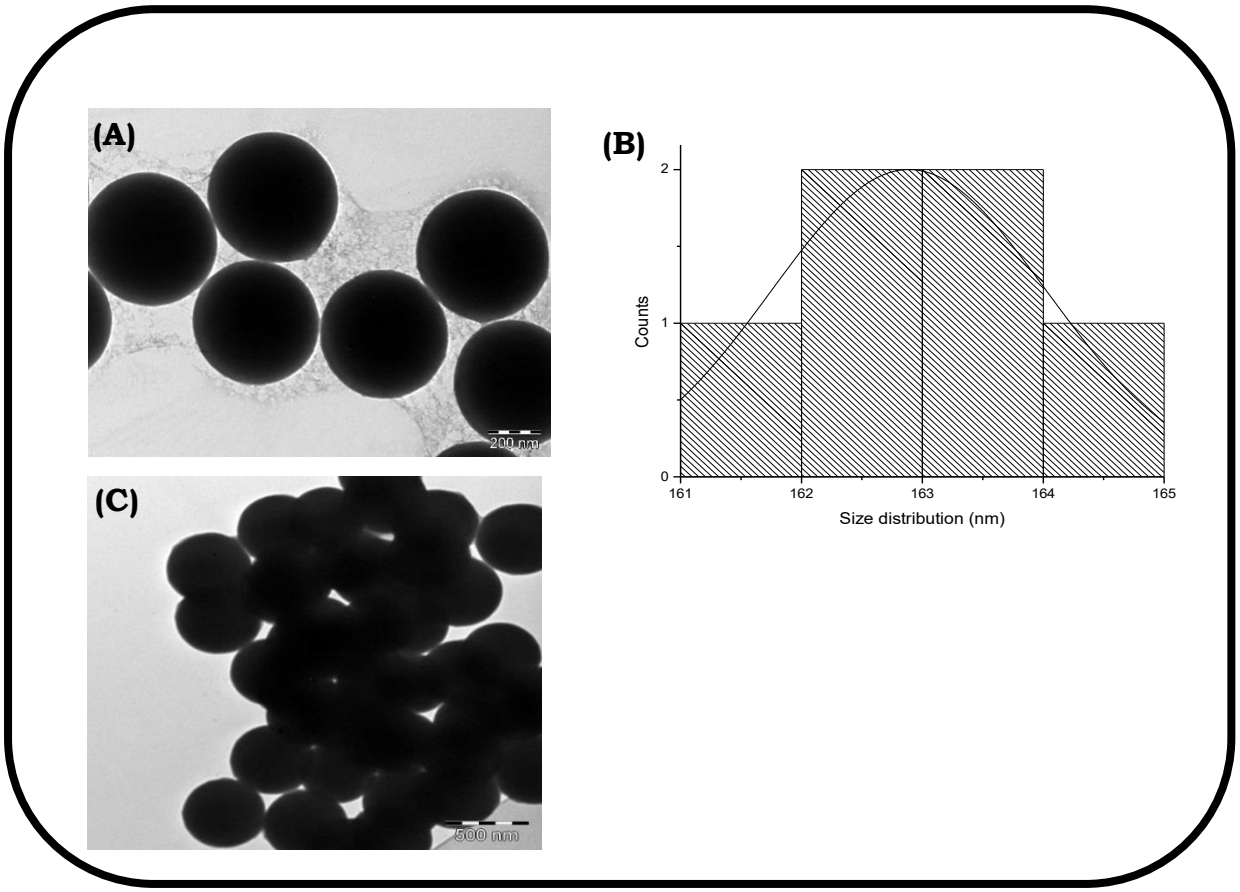

Figure 3.20: TEM micrographs (A), accompanied histogram (B) of PluS NPs and (C) 2-Zn (PluS linked) conjugate as an example.

Energy dispersive spectra (EDS) was carried out in order to determine the elemental composition of the PluS NPs and it was found that Si and O (from the Si NPs core) were the major elements and carbon was observed from the

Pluronic 127 as it can be seen in **Fig. 3.21** no other peaks were observed rather than the reference peak 0 keV.

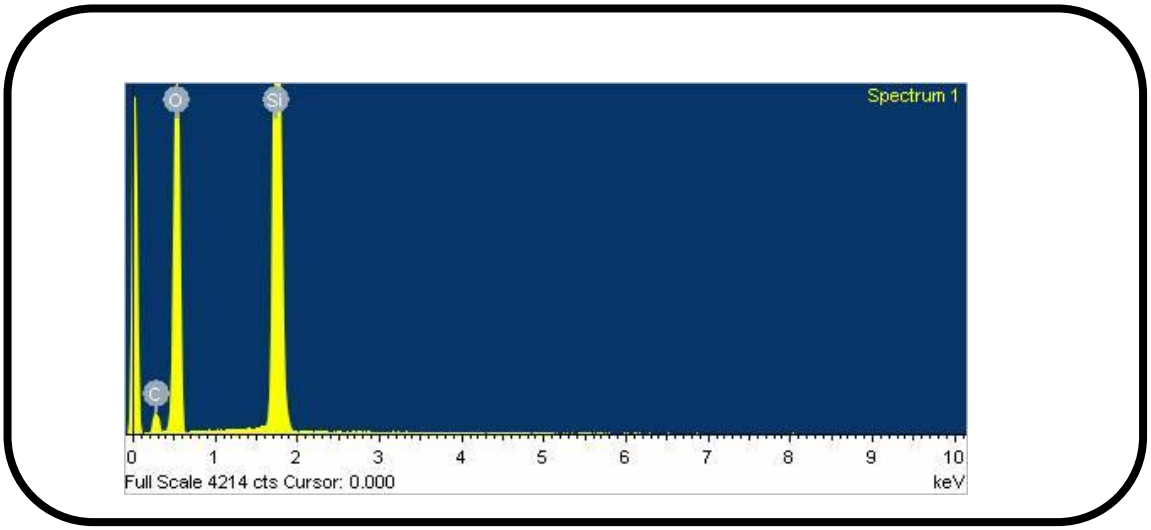

Figure 3.21: Energy dispersive spectra (EDS) of PluS NPs.

The X-ray diffraction (XRD) pattern for the PluS NPs, **Fig. 3.22**, shows a broad band between 2θ = 20° to 40°. The broadness of the band confirms the amorphous nature (as a result of the surfactant) of the nanoparticles. The amorphous nature continues following conjugation to porphyrins (**Fig. 3.22**). XRD was employed for crystalline size determination using (**Fig. 3.22**) and the Debye Scherrer **Equation 3.1 [138]**:

$$L = \frac{k\lambda}{\beta Cos\theta} \qquad (3.1)$$

where k is an empirical constant equal to 0.9, λ is the wavelength of the X-ray source, (1.5405 Å), β is the full width at half maximum of the diffraction peak, and θ is the angular position of the peak.

The average particle size was determined to 161 nm which is similar to that obtained by TEM. The size following conjugation does not change much due to the large size of the PluS NPs compared to the size of the porphyrins (~1 nm).

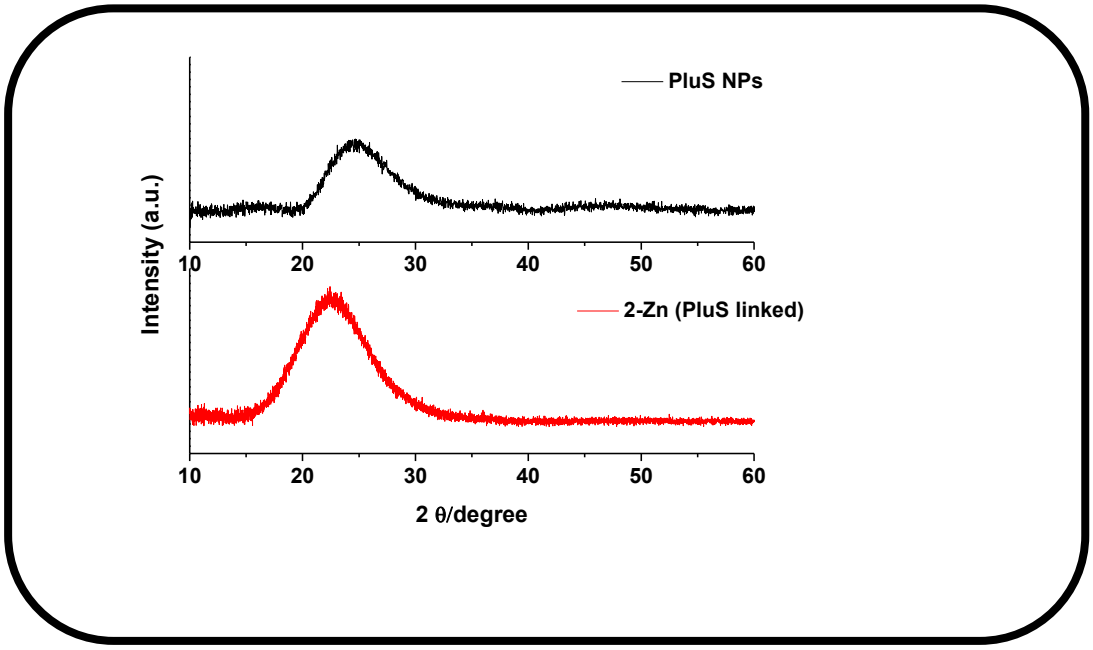

Figure 3.22: X-ray powder diffraction (XRD) of PluS NPs and 2-Zn (PluS linked).

The PluS NPs composition was further confirmed using TOF-SIMS, **Fig. 3.23**. The mass distribution spectra together with the images showed the surface elemental compositions mostly to be –C, -OH, O^- and Si (**Fig. 3.23B**) and further showed -OH both in the positive and negative mode as indicated by the bright yellow colour. **Fig. 3.23A(a)** shows a high concentration of Si from the silica core indicated by red to bright yellow in colour. **Fig. 3.23A(b)**, shows an even higher content of OH^- and O^- from Pluronic F127 which contains poly(ethylene oxide)–poly(propylene oxide)–poly(ethylene oxide) units as described above**. Fig. 3.23A(c)** shows the C^- content from Pluronic F127.

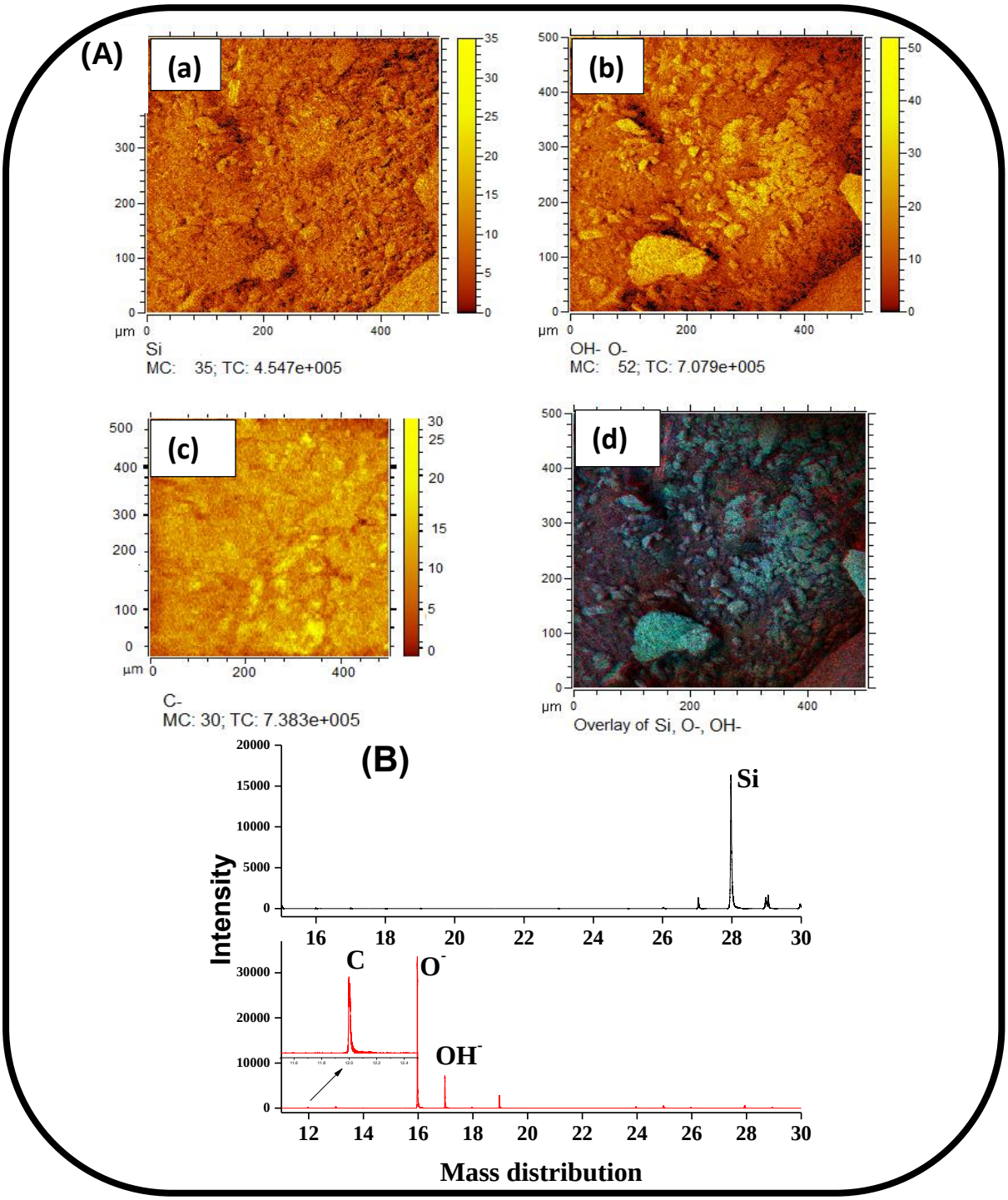

Figure 3.23: (A) TOF-SIMS images (a) Si, (b) OH-, O-, (c) C- and (d) over lay of (a), (b) and (c) and B spectra of the mass distribution of PluS NPs.

Brunauer–Emmett–Teller (BET) was performed in order to determine the pore size and surface area of the PluS NPs before and after linking to porphyrin. The isotherm of the nanoparticles was shown to be type 4 **Fig. 3.24A**. Type

4 BET isotherm indicates an indefinite multi-layer formation after completion of the monolayer and is found in adsorbents with a wide distribution of pore sizes. The BET isotherm of **2**-Zn (PluS linked) was used as an example, **Fig. 3.24B**, as similar trends were observed for the other conjugates. **Fig. 3.24B** shows that the isotherm for the **2**-Zn (PluS linked) is type 1. The pore size of the PluS NPs was determined to be 18.9 nm and the surface area was 330 m^2/g. The isotherm describes the partitioning between gas phase and adsorbed species as a function of applied pressure. The pore size decreased from 18.9 nm for PluS NPs to 2.4 nm for **2**-Zn (PluS linked). The surface area for the conjugate is 192.5 m^2/g, a decrease from 330 m^2/g for PluS NPs alone. Therefore, both pore size and surface area decreased for PluS NPs on conjugation to porphyrins. It has been documented that a rough surface results in larger surface area than a smooth one **[139]**. Thus, the observed decrease in surface area in the presence of the porphyrin, suggests decreased roughness. The decrease in pore size in the presence of porphyrins may suggest that the porphyrins might have been entrapped in the pore of the PluS NPs, causing a reduction in the pore size.

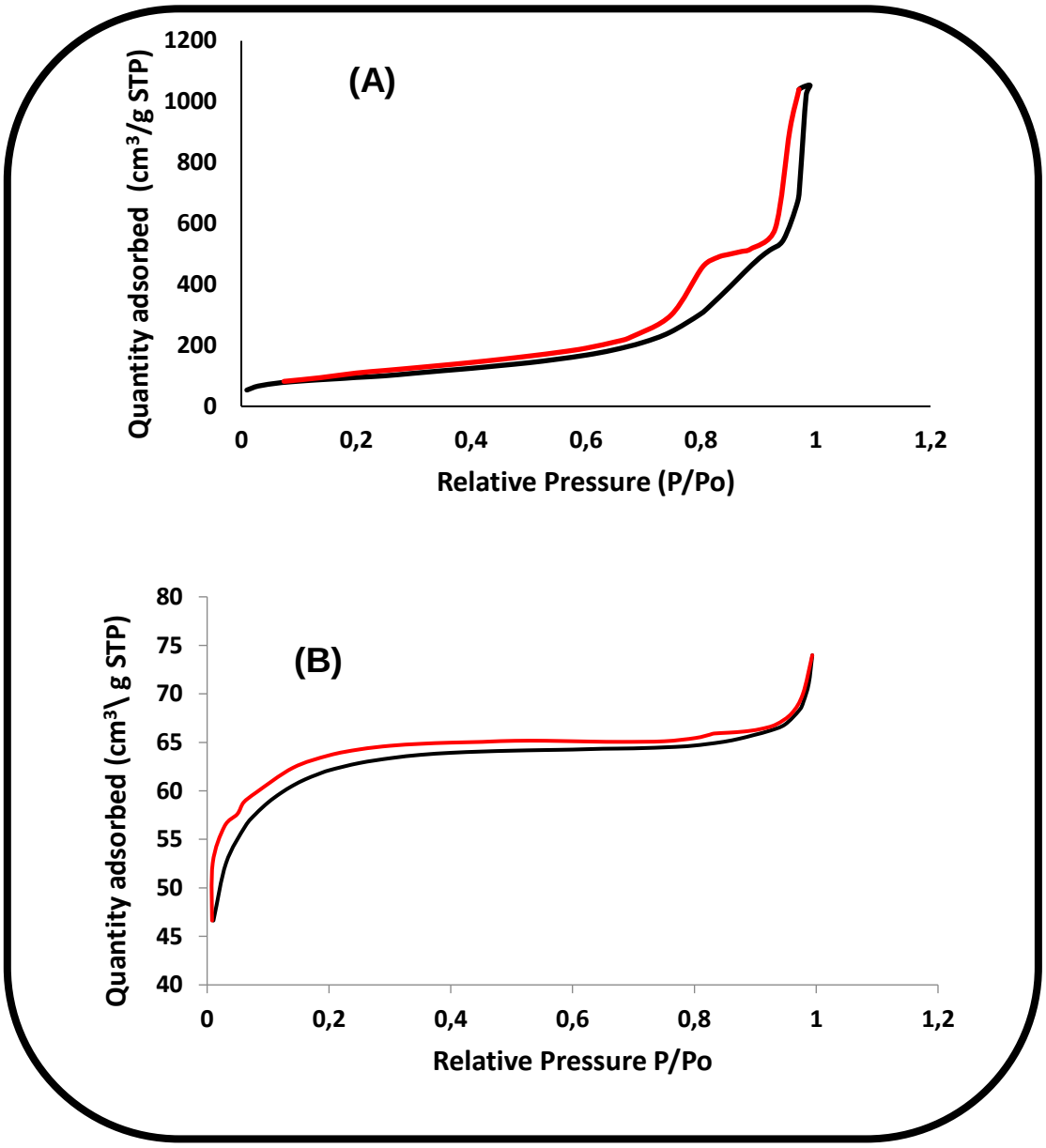

Figure 3.24: Nitrogen adsorption-desorption isotherm of (A) PluS NPs and (B) 2-Zn (PluS linked). The red line denotes the absorption while the black lines are desorption of the sample.

3.5. Conclusion for the chapter

Complexes 1-8 were successfully synthesised and fully characterized using ^{1}H NMR, IR and mass spectroscopies as well as elemental analysis. These complexes were embedded into Pluronic micelles and further characterized

using UV/Vis, DLS, TOF-SIMS, TEM, SEM ect. **Complex 2** was linked with PluS NPs. The Pluronic micelles used to embed **complex 5** was modified with FA to enhance selectivity. **Complex 6** was the only one that was imbedded into binary mixture micelles of F127/P123. These results showed promising trend to be potential drug candidates for PDT.

Chapter 4
Polymer-Porphyrin interactions

This chapter provides the characterization of the interaction between the polymer and porphyrins. The relative location of the porphyrins within the micelles, the binding constant and number of binding sites are also discussed.

4.1. Relative location of porphyrins using fluorescence quenching.

4.1.1. Pluronic F127

In this work, fluorescence quenching was used to assess the relative locations of porphyrins in Pluronic micellar system as well as the interaction of porphyrin-Pluronic polymer. Fluorescence quenching refers to any process that can decrease the fluorescence intensity of a given fluorophore **[140, 141]**. In general, fluorescence quenching processes, even though they are widely used, are known to be affected by pH, concentration, solvents and temperature **[142]**. A variety of processes can result in quenching. These include excited state reactions, energy transfer, complex formation, and collisional quenching **[140]**.

There are many different quenchers of fluorescence, for example molecular oxygen or halogenated compounds **[141]**. In this work iodine and Pluronic polymer were used. Quenching by iodine may be a result of intersystem crossing to an excited triplet state which is promoted by spin-orbit coupling in the presence of heavy atom I^- in this case **[140, 141]**.

This work will concentrate on quenching resulting from collisional encounter between the fluorophore and quencher which is called collisional or dynamic quenching. Dynamic quenching requires molecular contact between the fluorophore and quencher **[143, 144]**. For this quenching, the quencher must diffuse to the fluorophore during the lifetime of the excited state. Upon contact, the fluorophore returns to the ground state, without emission of a photon. In the case of static quenching, a complex is formed between the fluorophore and the quencher, and this complex is non-fluorescent **[140, 141,**

143]. It is not in all cases that the fluorophore is fully in contact with the quencher. Fluorescence quenching for these studies were carried out as follows: stock solutions (1.0 x 10^{-6} M based on the Soret band absorption peak of the porphyrin within the micelles) of porphyrin-micelles were prepared. Solution of I^- with different concentrations of 0 M to 0.6 M in water were also prepared. For the quenching experiments 2.5 mL of the porphyrin-micelles and 500 µL of different concentrations of I^- were mixed (a total volume of 3 mL each time) and allowed to equilibrate for 5 min before fluorescence measurement were taken. Thus, the concentration of the porphyrin-micelles were kept constant while that of I^- was varied. The actual concentration of I^- in the mixture is employed for the calculations of the Stern-Volmer constant. The relative locations of porphyrins in Pluronic micellar system were determined by Stern-Volmer constants (K_{SV}) using **Equation 4.1**.

$$\frac{F_o}{F} = 1 + K_{SV}[Q] \qquad (4.1)$$

where F_o and F are the fluorescence intensities in the absence and in the presence of the quencher, respectively, [Q] is the concentration of the quencher. In an ideal situation, Stern–Volmer plots (derived from spectra in **Fig 4.1A**) are supposed to show a linear relationship**,** however nonlinear relationships were observed in **Fig. 4.1B**. The plots in are a characteristic feature of two fluorophore population, but with some fluorophores being less accessible than others **[141]**.

The deviation from linearity in the Stern–Volmer plots is accommodated by treating the data using a modified Stern–Volmer equation by Sam Lehrer **Equation 4.2** which considers situations where two populations of fluorophores exist, with one being accessible to quencher and the other being buried and not accessible **[145]**.

$$\frac{F_0}{\Delta F} = \frac{1}{([Q]f_a K_{sv})} + \frac{1}{f_a} \qquad (4.2)$$

where F_0 is the fluorescence intensity in the absence of quencher, ΔF is the observed decrease in the fluorescence and K_{sv} is the Stern–Volmer quenching constant of the accessible fluorophore. f_a is the fluorescence of the fluorophore which is accessible to the quenchers (Q). Plots of $\frac{F_0}{\Delta F}$ versus $1/[Q]$ with a Y-axis intercept of $1/f_a$ are shown in **Fig. 4.1C**.

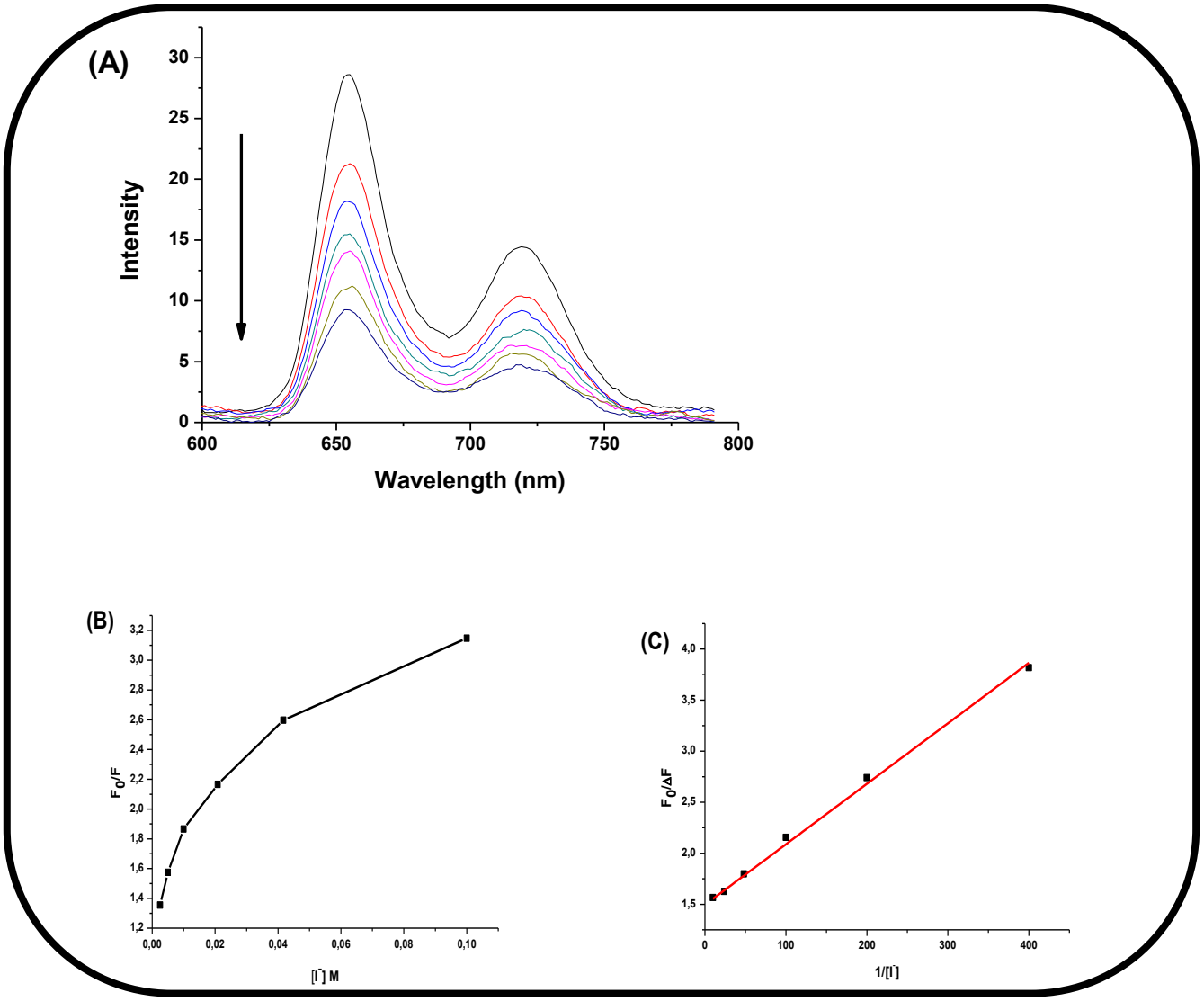

Figure 4.1: Fluorescence emission spectra of (A) 2-H_2+F127 (as an example), (B) characteristic plot which feature two fluorophore populations using Stern–Volmer equation 4.1 and (C) characteristic plot using modified Stern–Volmer equation 4.2 by Sam Lehrer in the presence of 0 M to 0.1 M of KI. Excitation wavelength = 490 nm.

The values of K_{sv} were determined from **Fig 4.1C** and are listed in **Table 4.1**. These values may be used to indicate relative location of the porphyrin on the polymer according to literature **[61]**. A low K_{SV} indicates that dyes are located

in the micelle core, resulting in less encounter between incorporated photosensitizer and iodine **[141, 142]**.

When comparing **1**-H_2+F127 with **2**-H_2+F127 and **1**-ClGa+F127 with **2**-ClGa+F127, it shows that **complex 2** has larger K_{sv} than **complex 1**. The K_{sv} **2**-H_2+F127, **2**-ClGa+F127, **2**-Zn+F127 and **2**-Cl_2Si +F127 were determined to be 0.35, 2.18, 2.27 and 1.91 (**Table 4.1**). Thus, **2**-Zn+F127 is located more on the hydrophilic outer area (and can interact with the quencher more) than the corresponding **2**-H_2+F127, **2**-ClGa+F127, and **2**-Cl_2Si +F127 since the former has a larger K_{sv} values. Comparing **2**-ClGa+F127, **2**-Zn+F127 and **2**-Cl_2Si +F127 differing only in the central metal, the Si derivative is located more in the hydrophobic inner core (smaller K_{sv} value) probably due to the smaller size.

Metal free derivatives **1**-H_2+F127 and **2**-H_2+F127 are located more in the hydrophobic inner core since they have the lower K_{SV} values compared to the corresponding metallated derivatives. Metal free derivatives have been reported to have stronger interaction with the micelles [**146**]. Generally metals in the centre of porphyrins changes the hydrophobicity of the molecule therefore resulting in the different locations for the porphyrins. Comparing **3**-H_2+F127, **4**-H_2+F127, **6**-H_2+F127 and **8**-H_2+F127 the largest K_{sv} value is that of **8**-H_2+F127.

The K_{sv} values for **complex 5** could not be calculated due to very weak emission obtained. Comparing the ClGa derivatives **2**-ClGa+F127 has the largest K_{sv} and **4**-ClGa+F127 is the lowest. **Complex 4** is water soluble as previously mentioned. **Complex 4** is not encapsulated within the micelles but

rather it has been reported [**147**] that the four sulfonate groups of the porphyrin impart appreciable hydrophilicity while the complexing capability of the central macrocycle (**4**-H_2) provides strong attractive interactions with the triblock copolymer. Comparing **6**-Zn+F127 and **8**-Zn+F127 there is not much difference.

Table 4.1: Properties of the porphyrins embedded in Pluronic polymer in water.

Conjugates	**K_{sv}**	**K_b ($\times 10^3$ M^{-1})**	**n**	**K_p**
1-H_2+F127	0.26	67.3	2.97	-
1-ClGa+F127	1.76	106.6	3.16	-
2-H_2+F127	0.35	88.8	3.19	106
2-ClGa+F127	2.18	131.4	3.27	116
2-Zn+F127	2.27	150.9	3.48	126
2-Cl_2Si +F127	1.91	124.3	3.13	-
3-H_2+F127	0.20	100	3.39	-
3-ClGa+F127	1.25	156	3.22	-
4-H_2+F127	0.19	70	3.68	-
4-ClGa+F127	0.59	98	2.57	-
5-H_2+F127	-	1.52	-	105
5-ClGa+F127	-	2.68	-	129
5-H_2+F127-FA	-	108	-	117
5-ClGa+F127-FA	-	251	-	165
6-H_2+F127	0.29	92.3	1.05	-
6-Zn+F127	1.16	115	0.64	-
6-H_2+F127/P123	0.33	102	1.75	-
6-Zn+F127/P123	1.63	158	0.87	-
8-H_2+F127	0.58	63.7	2.13	110
8-ClGa+F127	0.79	95.8	3.18	130
8-Zn+F127	1.17	75.0	3.32	121

4.1.2. Binary mixture of Pluronic F127/P123

Complexes 6-H_2 and **6**-Zn were loaded into binary mixture, as examples. The relative location of porphyrins in F127/P123 micellar system was carried out by fluorescence quenching. **Fig. 4.2A** shows the decrease in the intensity of fluorescence emission of **6**-H_2+F127/P123 (as an example) with increase in the iodide concentration. The K_{sv} values obtained using **Equation 4.2.** for **6**-H_2+F127/P123 was 0.33 M^{-1} and for **6**-ClGa+F127/P123 was 1.63 M^{-1}. Hence porphyrins embedded in binary mixtures are more on the surface of the micelles as compared to porphyrins embedded on mono micelles, **Table 4.1** as judged by the larger values for the former.

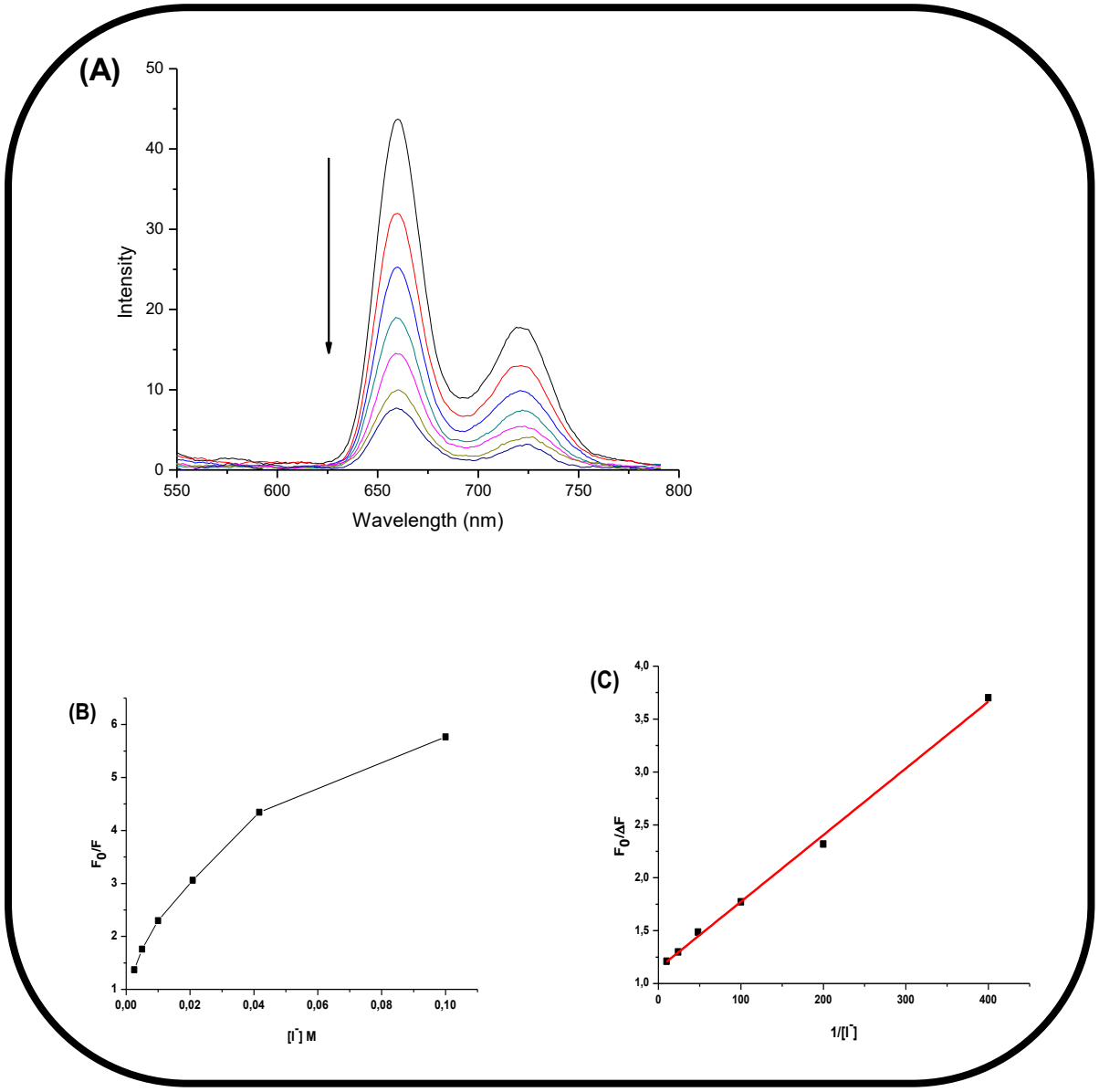

Figure 4.2: Fluorescence emission spectra of (A) 6-H_2+F127/P123 (as an example), (B) characteristic plot which feature two fluorophore populations using Stern–Volmer equation 4.1 and (C) characteristic plot using modified Stern–Volmer equation 4.2 by Sam Lehrer in the presence of 0 M to 0.1 M of KI in water. The porphyrins were excited at 490 nm.

4.2. Binding of porphyrins to micelles

Drug interactions with heterogeneous media (micelles, lipid bilayer vesicles, biomembranes) can result in changes of some physicochemical properties of the drugs (porphyrins) which include solubility, spectroscopic and acid–base properties **[145,148]**. By monitoring these changes, it is possible to quantify the degree of drug/micelle interaction which is normally expressed as drug/micelle binding constant, K_b and micelle/water partition coefficient, K_p. The elucidation of these constants is important for the understanding of interactions with biomembranes **[149]**.

Binding studies were done using fluorescence for **complexes 1-4, 6** and **8** which were fluorescent using Scatchard **Equation 4.3**; for **complex 5** which is not fluorescent absorption spectra was used with **Equation 4.4**.

$$\text{Log}\,\frac{[F_o - F]}{[F - F_\infty]} = \log K_b + n\log[F127] \qquad (4.3)$$

where F_0 and F denote the fluorescence intensities in the absence and presence of Pluronic F127 (represented as F127 in **Equation 4.3**), respectively. F_∞ denotes fluorescence intensity when the fluorophores are completely saturated with Pluronic F127, [F127] is the total concentration of Pluronic and n is the number of binding sites. The concentration of the fluorophore (porphyrin) was kept constant and that of the quencher (Pluronic F127) was varied **Fig. 4.3**. Plots of $\log\frac{[F_o - F]}{[F - F_\infty]}$ against log [F127] provided the values for n (from slope) and K_b (from intercept).

Stock solutions (1.0 x 10^{-6} M based on the Soret band absorption peak of the porphyrin within the micelles) of porphyrin-micelles were prepared. F-127 stock solutions of 21-31% were prepared separately in water and were added to the Stock solution of the porphyrin micelle stock. Absorbance spectra were recorded and excitation was at 490 nm.

For all conjugates except **complex 4** (which is water soluble) studies were done by already formed porphyrin+F127 micelles. The rest of the porphyrin are only soluble in water following the formation of micelles. In the case of **4**-H_2 and **4**-GaCl which are water soluble, the porphyrins alone were used as a starting material. The concentration of the fluorophore (porphyrin) was kept constant and that of the quencher (Pluronic F127) was varied.

As stated above that the absorbance (not fluorescence) was used for **complex 5**. In the first incidence for **complex 5** where absorbance was used, there was an increase in porphyrin absorbance with increase in the concentration of Pluronic F127 or F127-FA, **Fig. 4.4** until the critical micelle concentration (CMC) was obtained, then the absorbance decreased as shown in **Fig. 4.5**. **Equation 4.4** was then employed to determine the apparent binding constant K_b on F127 or F127-FA [**64**].

$$P = P_f \frac{P_0 - P_f}{\left(\frac{1}{K_b}([M] - CMC)^N + 1\right)} \qquad (4.4)$$

where P is the decreasing absorption intensity in **Fig. 4.5**, P_0 denote absorption intensities of porphyrins before formation of F127 or F127-FA micelles, i.e. the starting curves in **Fig. 4.4**, P_f is the absorption intensity of the bound porphyrin to the micelles, the first curve in **Fig. 4.5**, [M] is the

concentration (in mass %) of the F127-FA (Pluronic F127) and N is the number of porphyrin to micelle ratio. CMC is critical micelle concentration.

K_b values for **1**-H_2+F127 and **1**-ClGa+F127 were determined to be 67.3 $\times 10^3$ M^{-1}, 106.6 $\times 10^3$ M^{-1} respectively, while those for **2**-H_2+F127, **2**-ClGa+F127, **2**-Zn+F127 and **2**-Cl_2Si+F127 were determined to be 88.8 $\times 10^3$ M^{-1}, 131.4 $\times 10^3$ M^{-1}, 150.9 $\times 10^3$ M^{-1}, and 124.3 $\times 10^3$ M^{-1} respectively, the rest of the K_b values are listed in **Table 4.1**. When comparing all the ClGa derivatives, **3**-ClGa+F127 has the highest K_b value and **5**-ClGa+F127 has the smallest value in the absence of FA, suggesting Br substituent does not encourage binding. Comparing **6**-H_2+F127/P123 and **6**-Zn+F127/P123 with F127 micelles the former gives larger K_b showing the advantage of binary mixtures.

When comparing all the Zn derivatives, for F127 alone a higher K_b was observed for **2**-Zn+F127. The n values were determined and no trend between the metalled and unmetalled derivatives was observed but the highest n values were observed for complex **4**-H_2+F127.

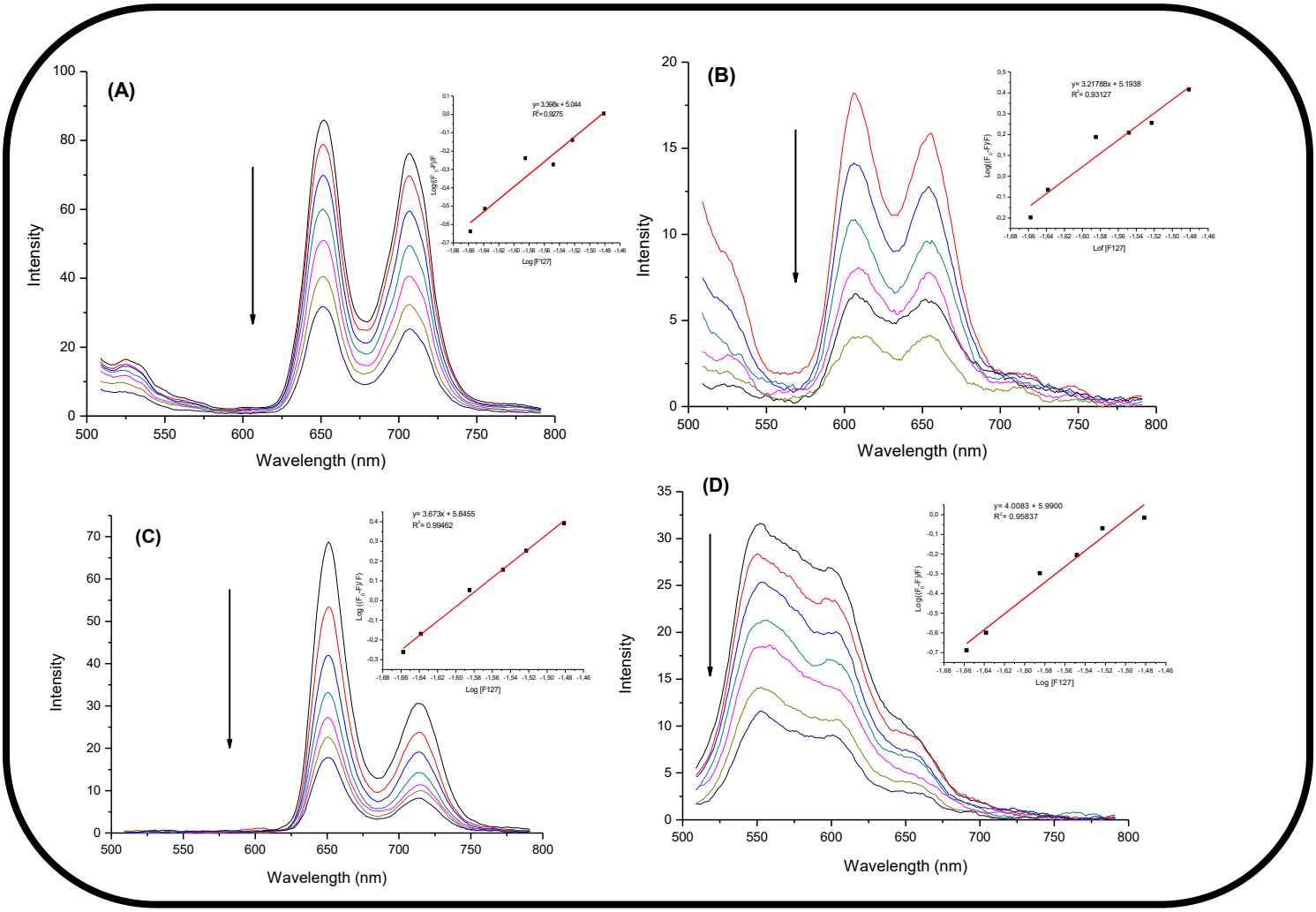

Figure 4.3: Fluorescence emission spectra of 3-H_2-F127 (A), 3-ClGa-F127 (B), 4-H_2-F127 (C) and 4-GaCl-F127 (D) in the presence of 0 M 0,022 to 0.033 M (20-30% w/v) of F127. The starting porphyrins already had Pluronic F127 for 3-H_2 and 3-ClGa as well as 4-H_2 and 4-ClGa.

When comparing F127-FA with F127, the former has larger K_b. This could be due to the interaction (electron or static) between the porphyrin macrocycle and the folic acid.

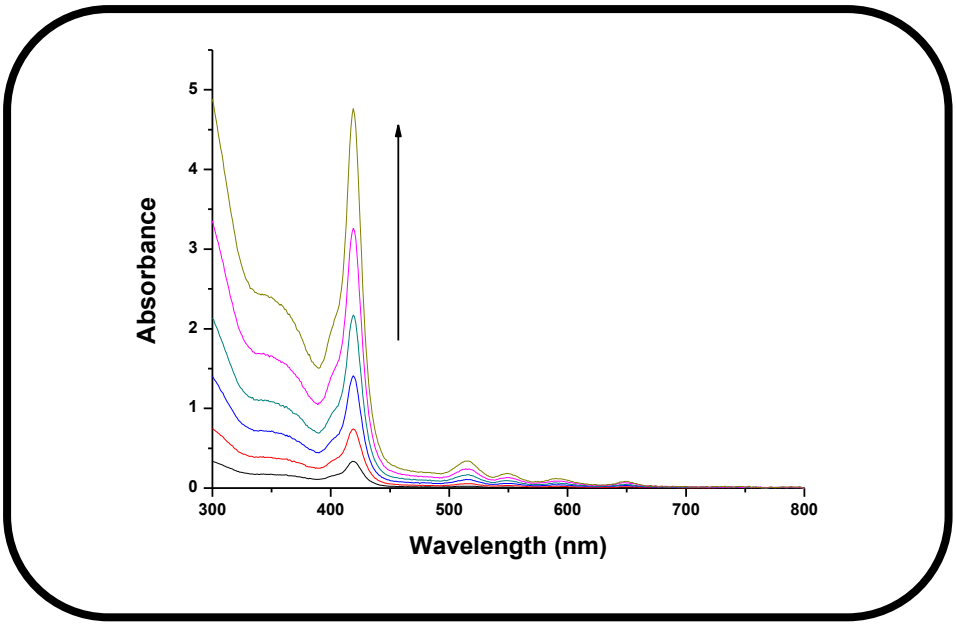

Figure 4.4: Absorption spectra of 5-H_2+F127-FA in the presence of 1 to 20% F127-FA. The starting porphyrins already had F127-FA (to allow for water solubility) hence 1 to 20% F127-FA refer to before (0 M) and after addition of more F127-FA.

The partition coefficient (K_p) was determined in biphasic octanol and water system as previously reported by **[61]**, **complexes 2, 5** and **8** were used according to as examples **Table 4.1**. The conjugates were added to a 50 % (v/v) mixture of octanol and water, which was vigorously stirred and left to rest in the dark for 48 h. The porphyrin concentration in the aqueous $[PS]_{water}$ and organic $[PS]_{octanol}$ phases were then determined using UV-vis spectra and the data fitted in **Equation 4.5**: **[61]**

$$K_p = [PS]_{octanol}/[PS]_{water} \quad (4.5)$$

The K_p values were determined to be 105, 129, 117 and 165 for **5**-H_2+F127, **5**-ClGa+F127, **5**-H_2+F127-FA and **5**-ClGa+F127-FA respectively. The rest for

complexes 2 and **8** are shown in **Table 4.1**. When comparing K_p values for **5**-ClGa+F127 and **8**-ClGa+F127, there is no difference, but both are higher than **2**-ClGa+F127. When comparing **5**-H_2+F127 and **2**-H_2+F127 there is no difference, but both are slightly lower than **8**-H_2+F127. According to literature **[61]** a higher log K_p value may demonstrate a preferential partition for organic phase. The highest K_p was observed for **5**-ClGa+F127-FA and this may demonstrate that the drug may not be released anywhere in the body but rather where the cancer cells are located.

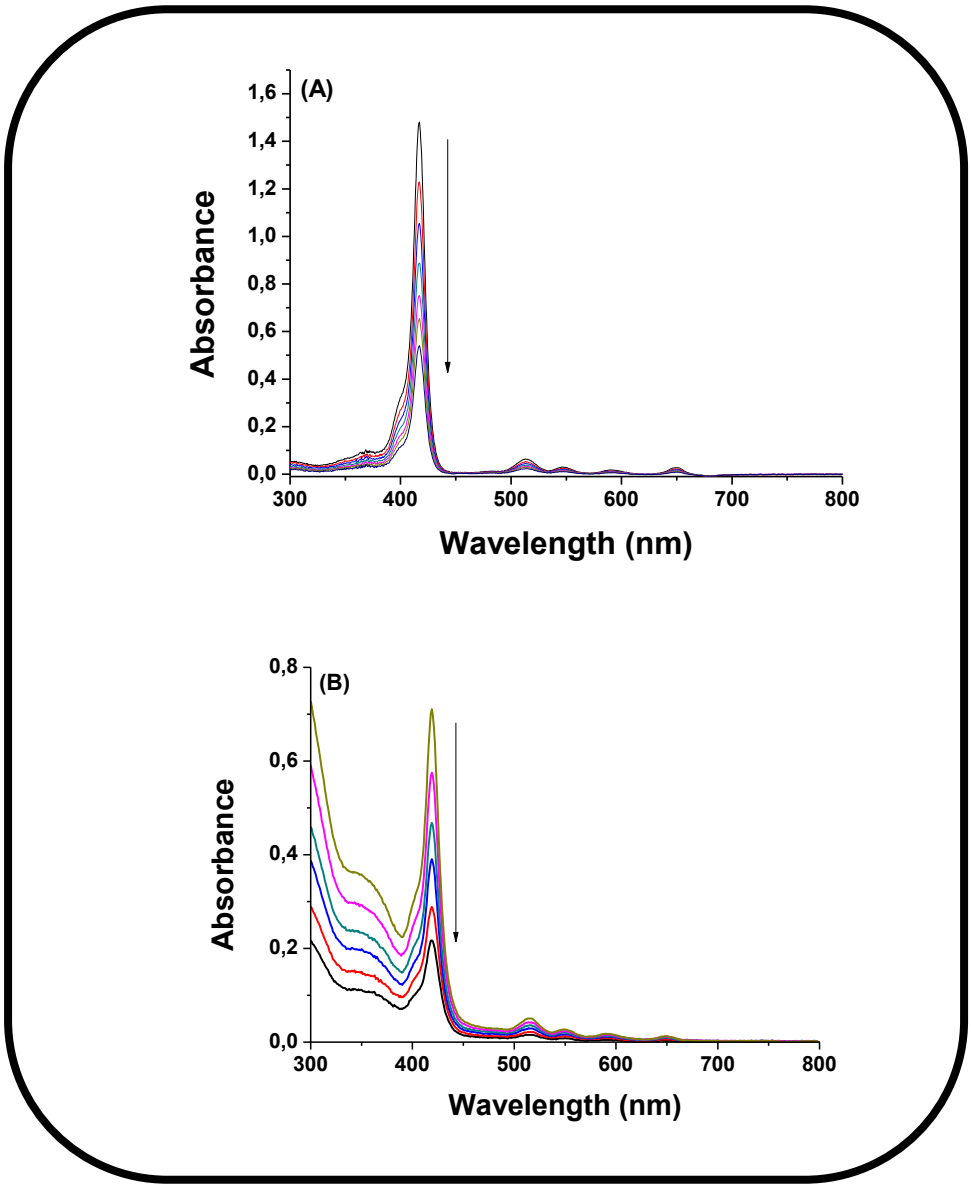

Figure 4.5: Absorption spectra of 5-H_2+F127 (A) and 5-H_2+F127-FA (B) in the presence of 21 to 31% F127 for A and F127-FA for B. Solvent= Water

4.3. Conclusion for the chapter

The interactions between the polymer and porphyrins were determined using fluorescence quenching as well as absorbance quenching. Relative location of the porphyrin within the micelles, the binding constant and number of

binding sites were determined. The highest K_{SV} value obtained was that of **2**-Zn+F127. Binding of porphyrins to micelles was determined by K_b which the highest was that of **6**-Zn+F127/P123. The lowest number of binding sites were determined for **complex 6**-Zn+F127/P123. High K_p values demonstrate a preferential partition for organic phase which was also observed in this work.

Chapter 5

Photophysical and Photochemical properties

This chapter explains the photophysical and photochemical properties; fluorescence quantum yields and life-times as well as the singlet oxygen quantum yields of all the porphyrin complexes synthesised in this work, when they are on their own or linked to PluS NPs or loaded into Pluronic polymers.

5.1. Fluorescence quantum yield (Φ_F) and lifetimes (τ_f).

The fluorescence efficiency of a chromophore (porphyrin) is defined by the fluorescence quantum yield and fluorescence lifetime **[150]**. The Φ_F values of all the complexes were determined using a comparative method **[151-155]**, where the emission spectrum of a sample is compared with that of standard ZnTPP in DMF (Φ_F^{Std}) = 0.033 **[156]** both being excited at the same wavelength. Φ_F was calculated according to **Equation 5.1**.

$$\Phi_F = \Phi_F^{Std} \frac{F\,A^{Std}\,n^2}{F^{Std}A\,(n^{Std})^2} \qquad (5.1)$$

where F and F^{Std} are the areas under the fluorescence curves for sample and standard, respectively. A and A^{Std} are the absorbances of the sample and reference at the excitation wavelength, respectively. n and n^{Std} are the refractive indices of the solvent used for the sample and standard, respectively.

The Φ_F values were determined for all porphyrins exciting at 490 nm. Values in the absence of micelles were done in DMF and those in the presence of micelles were done in water, apart from **complex 4** which is water soluble and all the Φ_F were done in water. Values without micelles as well as PluS NPs cannot be compared with those with micelles as they are not water soluble.

Fluorescence lifetime (τ_f) is defined as the average time a molecule spends in its excited state before returning to the ground state through fluorescence. There are several techniques that are available for the determination of fluorescence lifetimes, but time-correlated single-photon counting (TCSPC) is

the most popular and widely used technique [**157, 158**] and is employed in this work.

The Q-band absorbance of the studied complexes were kept between 0.05 and 0.1, this was done to ensure a low concentration for both Φ_F and τ_f determination. The complexes were excited at their emission maxima τ_f determination.

5.1.1. Asymmetrical complexes 1,2 and 7

There is a slight increase in fluorescence quantum yields for **complex 1**-H_2 compared to **1**-ClGa (**Table 5.1**). The Φ_F values are the higher for **complex 1**-H_2, due to the lack of the heavy central metal, resulting in fluorescence being favoured. There is a slight increase in fluorescence quantum yields of **complex 2** in the presence of PluS NPs as shown in **Table 5.1**.

It has been reported [**159**] that linking porphyrins with Pluronic NPs leads to the recovery of the fluorescence of the former. Thus, the increase in the fluorescence quantum yields of the porphyrin could be due to their protection by the PluS NPs. **1**-H_2 with **2**-H_2 have the same Φ_F values as well as **1**-ClGa with **2**-ClGa, which shows no effect of substituent. The values in the presence of ClGa and Zn and Cl_2Si are low due to the heavy atom effects of central metals and axial ligands, which results in intersystem crossing to the triplet state, reducing fluorescence. Typical decay curve is shown in **Fig. 5.1**. In the absence and presence of Pluronics, complexes follow the same trend (**Table 5.1** and **5.2**) for Φ_F and τ_f.

Table 5.1: Fluorescence quantum yields (Φ_F) and lifetimes (τ_f) of complex 1-8 on their own, complex 2 linked to PluS NPs in DMF

Complex	**(Φ_F) ± 0.01**	**τ_F(ns)**
1-H_2	0.19	5.98
1-ClGa	0.11	4.21
2-H_2	0.19 (0.25)[a]	5.23
2-ClGa	0.12 (0.17)[a]	3.96
2-Zn	0.09 (0.11)[a]	3.31
2-Cl_2Si	0.15 (0.22)[a]	4.21
3-H_2	0.22	16.36
3-ClGa	0.07	5.15
4-H_2	0.27 (0.013)[b]	15.01(9.78)[b]
4-ClGa	0.15 (<0.01)[b]	9.16 (7.32)[b]
5-H_2	0.11	5.08
5-ClGa	<0.01	3.24
6-H_2	0.034	15.14
6-Zn	0.023	9.94
7-ClGa	0.14	3.42
8-H_2	0.12	4.87
8-ClGa	0.09	3.89
8-Zn	0.10	3.26

[a]values in brackets are for **complex 2** linked to PluS NPs

[b]values in brackets are for **complex 4** in water

5.1.2. Symmetrical complexes 3-6 and 8

Of the H_2 derivatives, Φ_F in DMF, **4**-H_2 has the largest value while **6**-H_2 has the lowest which could be due to the extended bond of the phenoxy carboxy substituent. Comparing ClGa derivatives in DMF, **4**-ClGa has an Φ_F which is slightly larger than the rest as was the case for H_2 derivatives. Values in water for **4**-H_2 and **4**-ClGa were determined to be 0.013 and <0.01 respectively. Values in micelles followed the same trend as without micelles in that the decreases were observed following insertion of a central metal. FA has no significant effect on Φ_F comparing **5**-H_2+F127 and **5**-H_2+F127-FA as well as the ClGa derivatives.

Mono-exponential fluorescence decay profiles were obtained for porphyrin complexes, while biexponential decays were observed in the presence of F127-FA. The observation of two lifetimes in the latter could be due to different orientations of the porphyrins in the conjugate. Average lifetimes are given in **Tables 5.1** and **5.2**.

The τ_f values for decrease for all complexes upon metalation. The shortening is due to the heavy atom effect discussed above. **Complex 4** is water soluble hence values can be compared with and without Pluronic. The τ_f for **4**-H_2 is 9.78 ns (**Table 5.1**) and when incorporated into F127 it was 5.48 ns (**Table 5.2**), the τ_f values for **4**-ClGa was determined to be 7.32 ns (**Table 5.1**), when it is interacting with F127 it was 3.49 ns (**Table 5.2**). Thus, upon incorporation into the polymer, lifetimes were shortened compared to the

porphyrin alone, suggesting the quenching of the lifetimes of the porphyrin by the polymers [**64**].

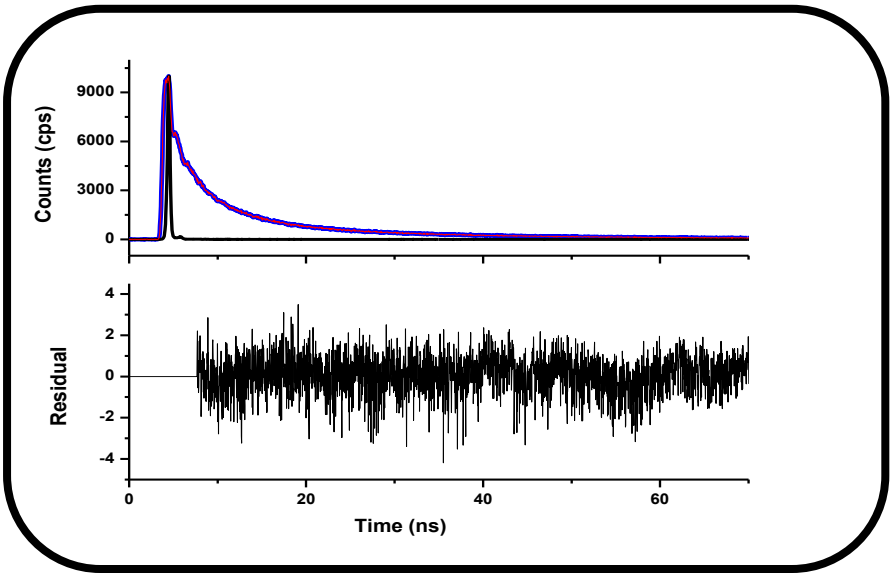

Figure 5.1: Fluorescence decay profile of 2-ClGa as an example in DMF.

Table 5.2: Fluorescence quantum yields (Φ_F) and lifetimes (τf) of complex 1-8 embedded into Pluronic polymer in water

Complex	**(Φ_F) ± 0.01**	**τ_F(ns)**
1-H_2+F127	0.10	4.63
1-ClGa+F127	<0.01	3.20
2-H_2+F127	0.11	4.06
2-ClGa+F127	<0.01	3.11
2-Zn+F127	<0.01	3.01
2-Cl2Si+F127	<0.01	3.32
3-H_2+F127	0.19	15.76
3-ClGa+F127	0.07	4.67
4-H_2+F127	<0.01	5.48
4-ClGa+F127	<0.01	3.49
5-H_2+F127	0.15	3.91
5-ClGa+F127	<0.01	2.84
5-H_2+F127-FA	0.17	4.33
5-ClGa+F127-FA	<0.01	3.11
6-H_2+F127	<0.01	2.78
6-Zn+F127	<0.01	2.24
6-H_2+F127/P123	<0.01	3.35
6-Zn+F127/P123	<0.01	3.03
8-H_2+F127	0.12	4.87
8-ClGa+F127	0.09	3.89
8-Zn+F127	0.10	3.26

5.2. Singlet oxygen quantum yield (Φ_Δ).

Singlet oxygen ($^1O_2$) is one of the most reactive intermediates involved in chemical and biochemical reactions. On populating the triplet state, the porphyrin can lose energy by phosphorescence or by energy transfer to the

ground state molecular oxygen ($^3O_2$), converting it to the highly reactive $^1O_2$ **[160]**.

Singlet oxygen quantum yield (Φ_Δ) is defined as the number of molecules of $^1O_2$ molecules generated for each photon absorbed by a photosensitizer. Experimentally, Φ_Δ of porphyrin is determined using optical or chemical methods **[161]**. Two methods have been compared **[112]** and found to give same results. The optical method involves the observation of a time-resolved phosphorescence decay of singlet oxygen at 1270 nm **[162].** The chemical method requires the use of singlet oxygen quenchers that react rapidly with the singlet oxygen generated by the sensitizer in a 1:1 ratio without the possibility of side reactions taking place. The decomposition products of the quencher should neither react nor interfere with the detection of singlet oxygen **[161]**. Both singlet oxygen luminescence method (SOLM) (organic solvents) and chemical (water) methods were employed in this thesis. The chemical method was used in water due to low singlet oxygen phosphorescence signal. In DMF, the SOLM was employed since the signal is strong. There are many different singlet oxygen quenchers **[162,163]**. In this work sodium azide (NaN_3) for SOLM method and anthracene- 9,10-bis-methylmalonate (ADMA) for chemical method were employed.

When using the SOLM method, singlet oxygen quantum yields can be determined using the comparative method in organic solvents using **Equation 5.2 [161, 162]**:

(5.2)

$$I(t) = B\frac{\tau_D}{\tau_T - \tau_D}[e^{-t/\tau_T} - e^{-t/\tau_D}]$$

where, I(t) is the phosphorescence intensity of $^1O_2$ at time t, τ_D is the lifetime of $^1O_2$ phosphorescence decay, τ_T is the triplet state lifetime of the standard or sample and B is a coefficient involved in sensitizer concentration and $^1O_2$ quantum yield. The singlet oxygen quantum yields, Φ_Δ of the complexes were then determined using **Equation 5.3**:

$$\Phi_\Delta = \Phi_\Delta^{Std} \cdot \frac{B.A^{Std}}{B^{Std}.A} \quad (5.3)$$

where Φ_Δ^{Std} is the singlet oxygen quantum yield for the standard ZnTPP (Φ_Δ^{Std} = 0.53 in DMF **[112]**), B and B^{Std} refer to coefficient involved in sensitizer concentration and $^1O_2$ quantum yield for the sample and standard, respectively; while A and A^{Std} refer to the absorbance of the sample and standard, respectively at the excitation wavelength.

The chemical method of singlet oxygen generation involves the spectroscopic monitoring of the absorption decay mixture of the photosensitizer and the singlet oxygen quencher over a period of time. Singlet oxygen quantum yield values in water were determined under ambient conditions using **Equation 5.4 [164]**.

$$\Phi_\Delta = \Phi_\Delta^{std} \frac{W.I_{abs}^{Std}}{W^{Std}.I_{abs}} \quad (5.4)$$

where Φ_Δ^{Std} is the singlet oxygen quantum yield for the standard (H_2TSPP) in water (Φ_Δ^{Std} = 0.51) **[165]**), W and W^{Std} are the ADMA photobleaching rates in

the presence of porphyrin derivatives under investigation and the standard, respectively. I_{abs} and I_{abs}^{Std} are the rates of light absorption by the porphyrin derivative and standard, respectively.

I_{abs} is determined by **Equation 5.5.**

$$I_{abs} = \frac{\alpha SI}{N_A} \qquad (5.5)$$

where α is the fraction of light absorbed, S is the cell area irradiated, N_A is Avogadro's constant and I the light intensity. The absorbances used for **Equation 5.5** are those of the porphyrins embedded in micelles. The light intensity measured refers to the light reaching the spectrophotometer cells and it is expected that some of the light may be scattered since the system is heterogeneous. In addition, the wavelength employed covers a wide range, hence the Φ_Δ values of the porphyrins in the micelles are estimates. Since the light used for singlet oxygen studies covered the range where ADMA absorbs, the effect of light on ADMA alone was investigated. There was no significant decrease in the absorbance of ADMA within the time scale used for singlet oxygen quantum yield studies.

5.2.1. Asymmetrical complexes 1,2 and 7

Fig. 5.2, using **2**-Zn (PluS linked) as an example shows the phosphorescence decay curve in DMF.

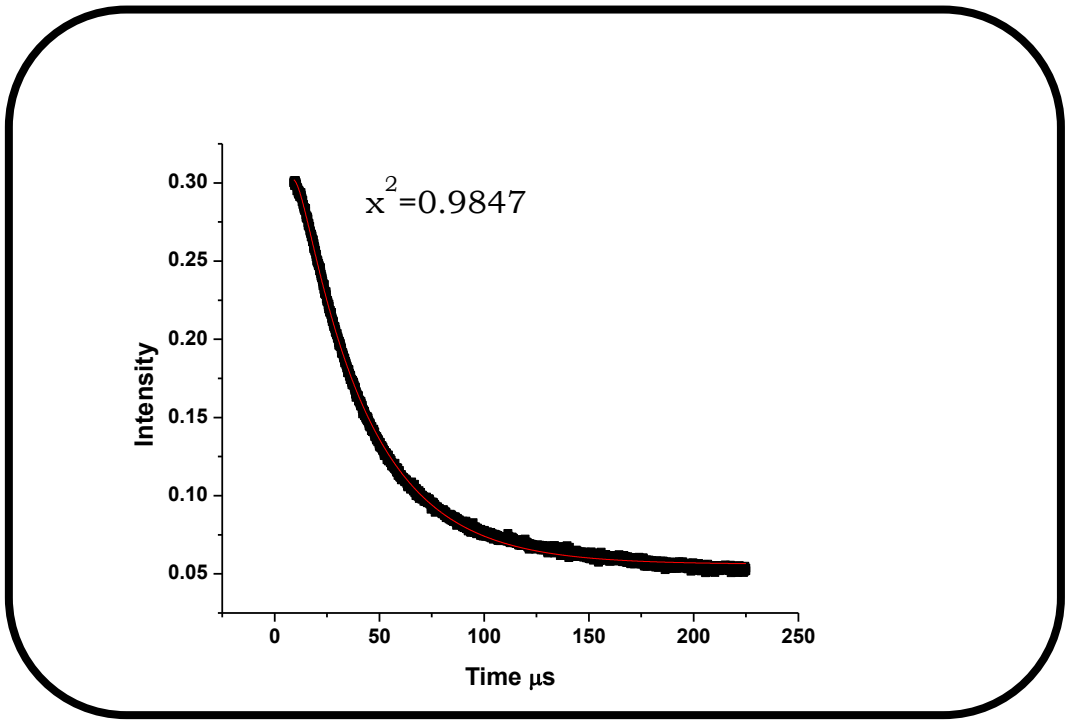

Figure 5.2: Singlet oxygen phosphorescence decay curve for 2-Zn (PluS linked). Solvent=DMF.

Φ_Δ was calculated to be 0.34 for **1**-H_2, 0.40 for **1**-ClGa and 0.42 for **7**-ClGa **Table 5.3**. There is a slight increase in the Φ_Δ values for **7**-ClGa conjugated to ethyl ester ALA when compared to **1**-ClGa porphyrin. There is an improvement for **complex 1**-ClGa compared to **1**-H_2 as a result of the heavy atom effect of Ga in the former which encourages intersystem crossing to the triplet state as discussed previously.

Table 5.3: Singlet oxygen quantum yields of complexes 1-8 on their own and complex 2 linked to PluS NPs in DMF while complex 4 is in water

Complex	**(Φ_Δ) ± 0.01**
1-H_2	0.34
1-ClGa	0.40
2-H_2	0.30 (0.27)
2-Zn	0.41 (0.33)
2-ClGa	0.38 (0.30)
2-Cl_2Si	0.35 (0.29)
3-H_2	0.30
3-ClGa	0.39
4-H_2	0.51
4-ClGa	0.54
5-H_2	0.50
5-ClGa	0.60
6H_2	0.54
6-Zn	0.68
7-ClGa	0.42
8-H_2	0.26
8-Zn	0.31
8-ClGa	0.32

Values in brackets are for complex **2** linked to PluS NPs

There is a general decrease in the Φ_Δ values for **complex 2** linked to PluS NPs compared to corresponding porphyrins alone. Such a decrease in Φ_Δ values was explained to be due to the fact silica nanoparticles can be singlet oxygen quenchers **[166].** It has also been reported that inclusion of photosensizers in nanocarriers result is less production of reactive oxygen species due to self-quenching of the excited states [**167**].

Comparing **1**-H_2 and **2**-H_2 with (**Table 5.4**) or without Pluronic in **Table 5.3**, shows that the latter has slightly lower Φ_Δ value. The same applies for **1**-ClGa and **2**-ClGa, however the difference are small. Comparing **2**-ClGa+F127, **2**-

Zn+F127 and **2**-Cl_2Si+F127 shows that **2**-Cl_2Si+F127 (containing the lighter Si central metal) gave the lowest Φ_Δ value, even though it contains Cl^- axial ligands which will encourage inter-system crossing due to the heavy atom effect.

5.2.2. Symmetrical complexes 3-6 and 8

The Φ_Δ values were determined to be 0.30 and 0.39 for **3**-H_2 and **3**-ClGa, respectively in DMF, the increase for ClGa is due to the heavy atom effect. The increase in the presence of metals applies to all the complexes with or without Pluronic as shown in **Tables 5.3** and **5.4**. Comparing **1**-ClGa, **2**-ClGa, **3**-ClGa, **5**-ClGa and **8**-ClGa in DMF the largest Φ_Δ value is for **5**-ClGa due to Br substituent which add heavy atom effect. The same applies for H_2 derivative. There is an increase in Φ_Δ for water soluble **complex 4** when in the presence of Pluronic F127 when compared to the porphyrins alone **Tables 5.3** and **5.4**. It has been reported in literature **[127]** that an increase in Φ_Δ values is expected when porphyrins are incorporated or interacting with Pluronic polymers. According to literature, **[168]** the PEO segment of the polymer may hinder collision of the porphyrin with surrounding molecules thus obstructing idle losses of the triplet state energy therefore increasing Φ_Δ. Φ_Δ values are lower in the presence of FA for **5**-H_2+F127-FA and **5**-ClGa+F127-FA when compared to the corresponding **5**-H_2+F127 and **5**-ClGa+F127. The low Φ_Δ values in the presence of FA could be due to the reported degradation of FA by the singlet oxygen generated by the porphyrin, hence reducing singlet oxygen quantum yields [**169**]. However, the Φ_Δ values in the presence of FA

are still adequate for PDT applications, since values as low as 0.11 are known for porphyrins in clinical trials such as Lutetium Texaphyrin [**84**].

Table 5.4: Singlet oxygen quantum yields of complexes 1-8 embedded into Pluronic polymer micelles. Solvent=Water.

Complex	**(Φ_Δ)**
1-H_2+F127	0.34
1-ClGa+F127	0.40
2-H_2+F127	0.30
2-Zn+F127	0.41
2-ClGa+F127	0.38
2-Cl_2Si+F127	0.32
3-H_2 +F127	0.25
3-ClGa+F127	0.30
4-H_2+F127	0.55 (0.51)[a]
4-ClGa +F127	0.59 (0.54)[a]
5-H_2+F127	0.41
5-ClGa +F127	0.47
5-H_2+F127-FA	0.37
5-ClGa +F127-FA	0.44
6-H_2+F127	0.14
6-Zn +F127	0.23
6-H_2+F127/P123	0.57
6-Zn +F127/P123	0.69
8-H_2 + F127	0.30
8-Zn +F127	0.39
8-ClGa +F127	0.38

[a]Porphyrin alone in water

The Φ_Δ were determined to be 0.57 and 0.69 for **6**-H_2+F127/P123 and **6**-Zn+F127/P123 respectively which were larger than when imbedded into F127 alone, showing the importance of binary mixture.

5.3. Conclusion for the chapter

Fluorescence quantum yield (Φ_F) and lifetimes (τ_f) of all these complexes were determined. Generally, upon metalation the Φ_F and τ_f of the complexes decreased. Binary mixture for **complex 6** had higher Φ_F and Φ_Δ, as expected since binary mixtures increases photophysical properties. An increase in Φ_Δ for **complex 4** in water when in the presence of Pluronic F127 when compared to the porphyrins alone was observed.

Chapter 6

Photodynamic therapy of cancer

This chapter describes the cytotoxicity and photodynamic therapy activities of porphyrins alone, linked to PLuS NPs, encapsulated into Pluronic polymer micelles on MCF-7 breast cancer cells.

6.1. Dark cytotoxicity effect on MCF-7 breast cancer cells

In *vitro* dark viability is undesirable for photosensitizers aimed for use in PDT. The *in vitro* cytotoxicity studies for all porphyrins were done in the absence of micelles for asymmetric **complexes 1,2** and **7** (as examples) and in micelles for **complexes 2** and **8** as examples. The studies were done on human breast cancer (MCF7) using WST-1 assay. The stock concentrations 0, 4.2, 8.5, 17, 30 and 60 μg/ml of **1**-H_2, **1-**ClGa, Plus NPs, **2**-H_2**, 2**-ClGa**, 2**-Zn, **2**-H_2 (PluS linked)**, 2**-ClGa (PluS linked), **2**-Zn (PluS linked) and **7**-ClGa were prepared by dissolving them in DMSO and making the volume up with supplemented media. It has reported before that 0.8% (v/v) DMSO had negligible effect on the cells **[170]**, and this was also observed in this work.

The percent cell viability was determined using **Equation 6.1**:

$$\%\ \text{cell viability} = \frac{\text{Absorbance sample at 450 nm}}{\text{Absorbance control at 450 nm}} \times 100 \qquad (6.1)$$

where, the absorbance of sample is the cells containing drugs while absorbance of control were the placebo cells containing only supplemented DMEM with phenol red. After 5 h incubation with supplemented DMEM with phenol red, cell proliferation neutral red reagent (WST-1) was used to quantify the surviving cells. The WST-1 assay was used to assess the toxicity and cell proliferation as per manufacturer's instructions (Roche) using a Spectramax M5 multimode microplate reader (Molecular Devices) at a wavelength of 450 nm.

There was very minimal dark toxicity for all the complexes as the values were above 90% cell survival, examples are shown in **Figs. 6.1** to **6.4** in the absence

and presence of micelles. The control cells were incubated without DMSO in supplemented media. P > 0.05 indicated that there is no significant difference within the concentrations. The dark cell viabilities of water which was used as the stock diluents was found to be similar with what was obtained in the control (supplemented DMEM alone).

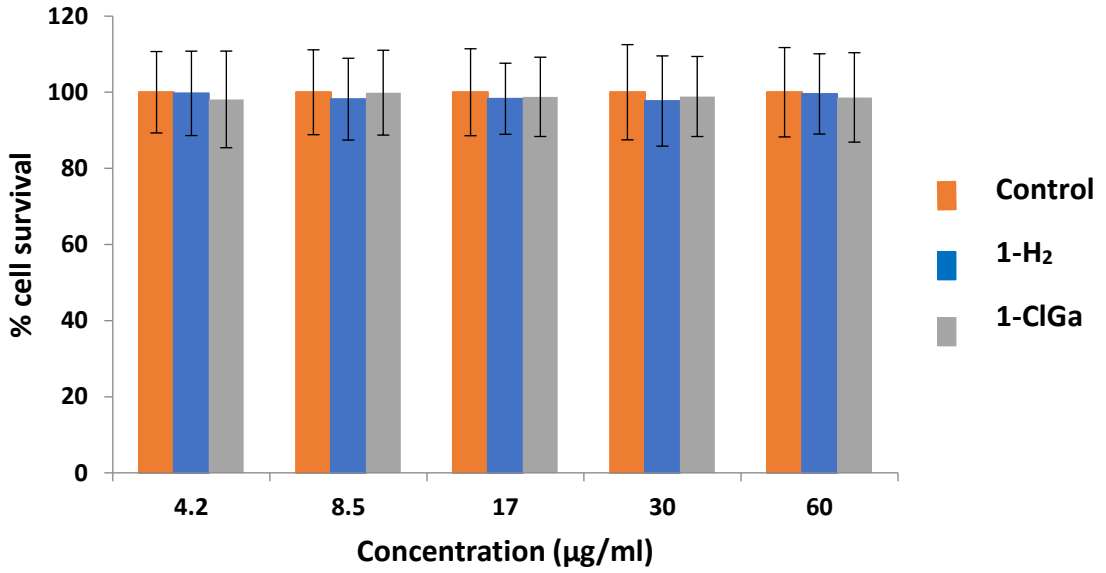

Figure 6.1: Dark toxicity plot of Complex 1-H_2 and 1-ClGa with concentrations from 4.2-60 µg/ml. Solvent =DMSO

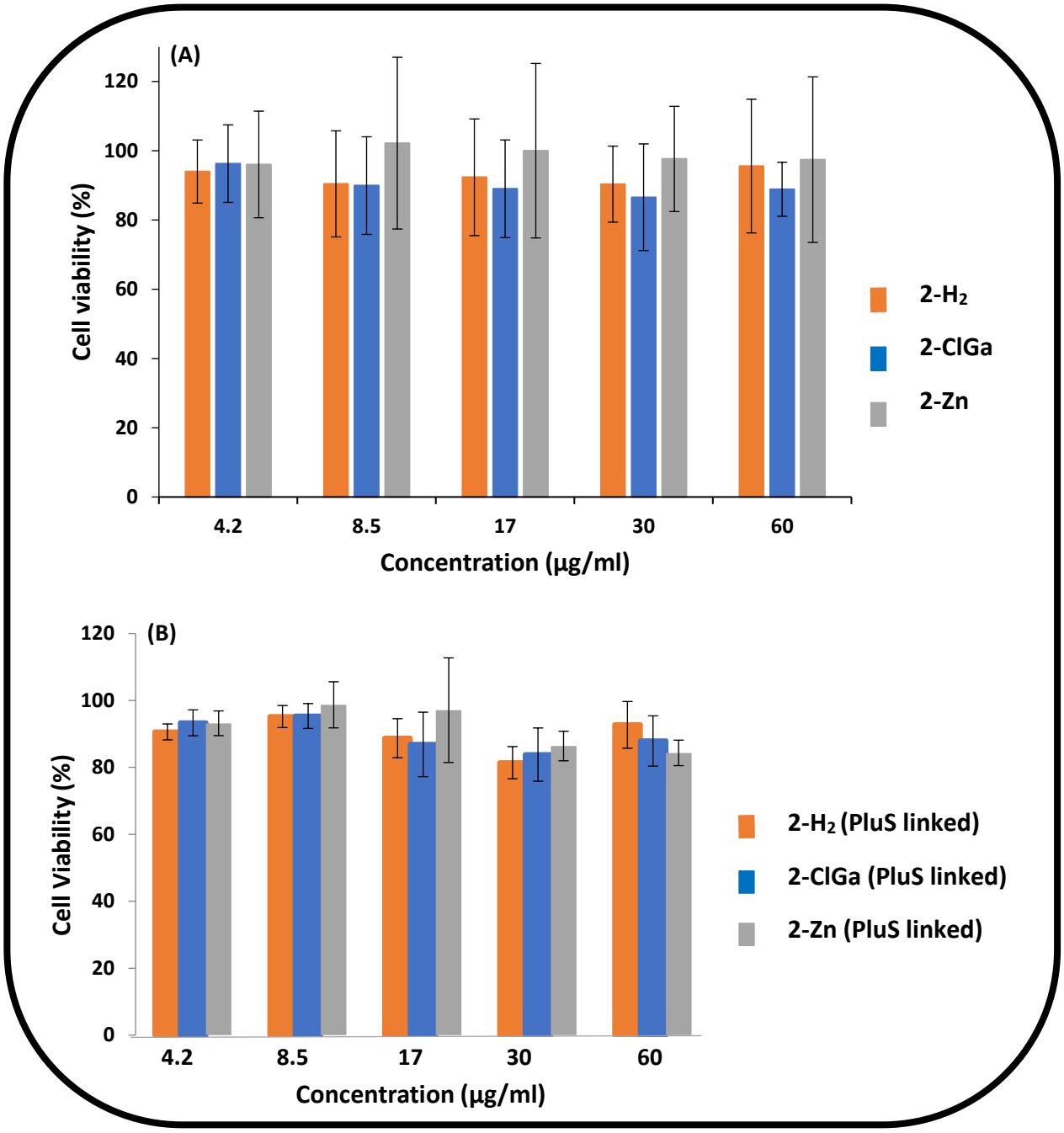

Figure 6.2: Dark toxicity (A) 2-H_2, 2-ClGa and 2-Zn and (B) 2-H_2 (PluS linked), 2-ClGa (PluS linked) and 2-Zn (PluS linked).

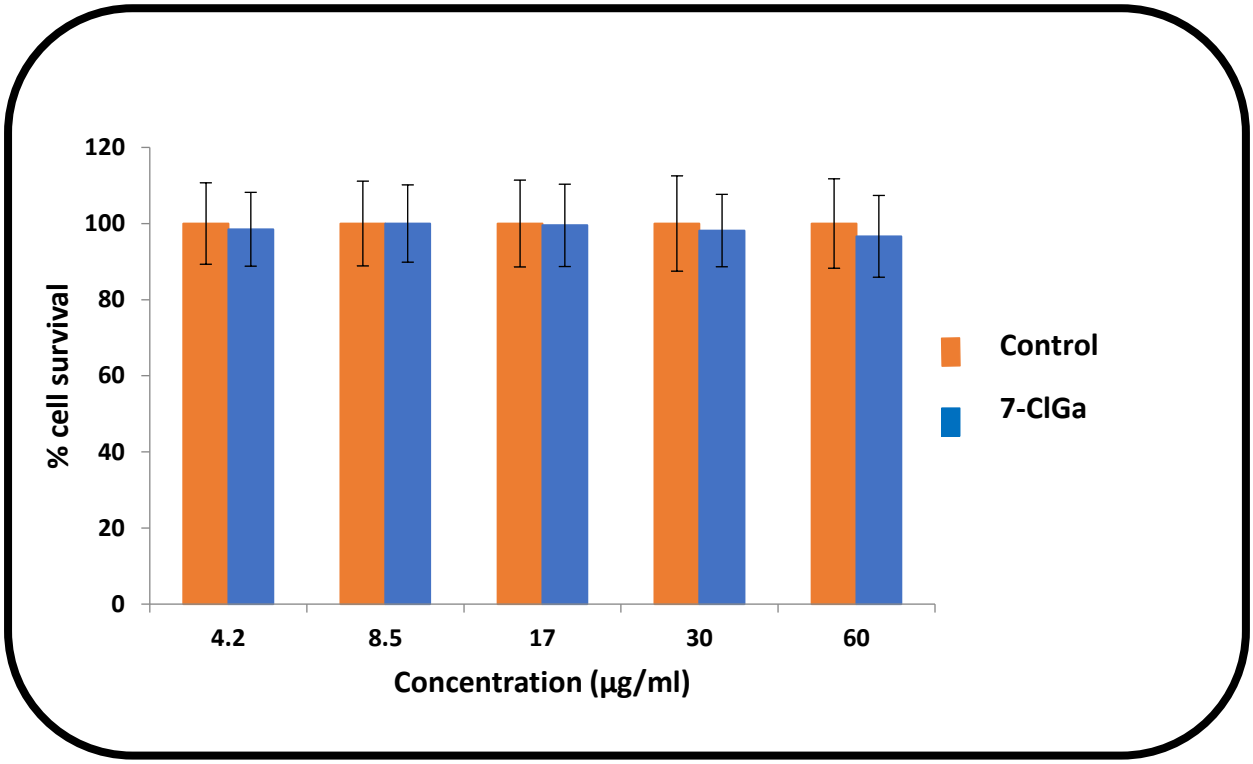

Figure 6.3: Dark toxicity 7-ClGa

Dark toxicity has been reported for ALA at high concentrations using PAM212 keratinocyte cells [**171**], hence in this work the examination of dark toxicity when ALA is linked to a porphyrin is studied. Hexyl ester ALA has also been reported to show dark toxicity [**171**]. There was minimal cytotoxic response when **7**-ClGa was introduced to the cell as the % cell viability was above 90% and $P > 0.05$ indicated that there is no significant difference within the concentrations employed (**Fig. 6.3**). Thus, in this study it was observed that there was no dark toxicity when ALA is linked to the porphyrin.

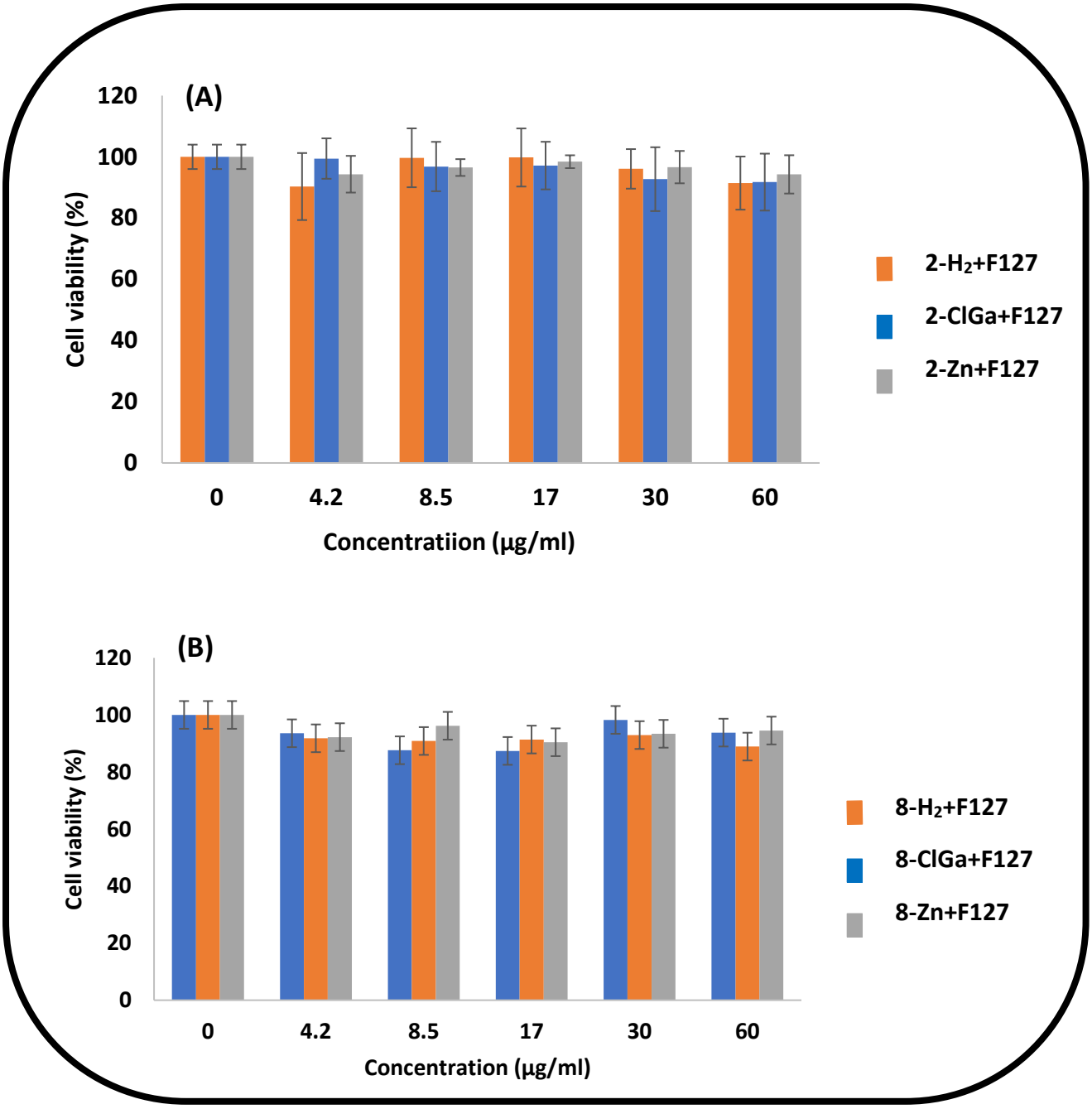

Figure 6.4: Dark toxicity plots for (A) 2-H_2+F127, 2-ClGa+F127, 2-Zn +F127 and (B) 8-H_2+F127, 8-ClGa +F127, 8-Zn +F127, all at 0, 4.2, 8.5, 17, 30 and 60 µg/ml

The PluS NPs also on their own were tested for dark toxicity with all showing the cell viability were above 90%. High percentage cell viability represents low dark toxicity **Fig. 6.5**.

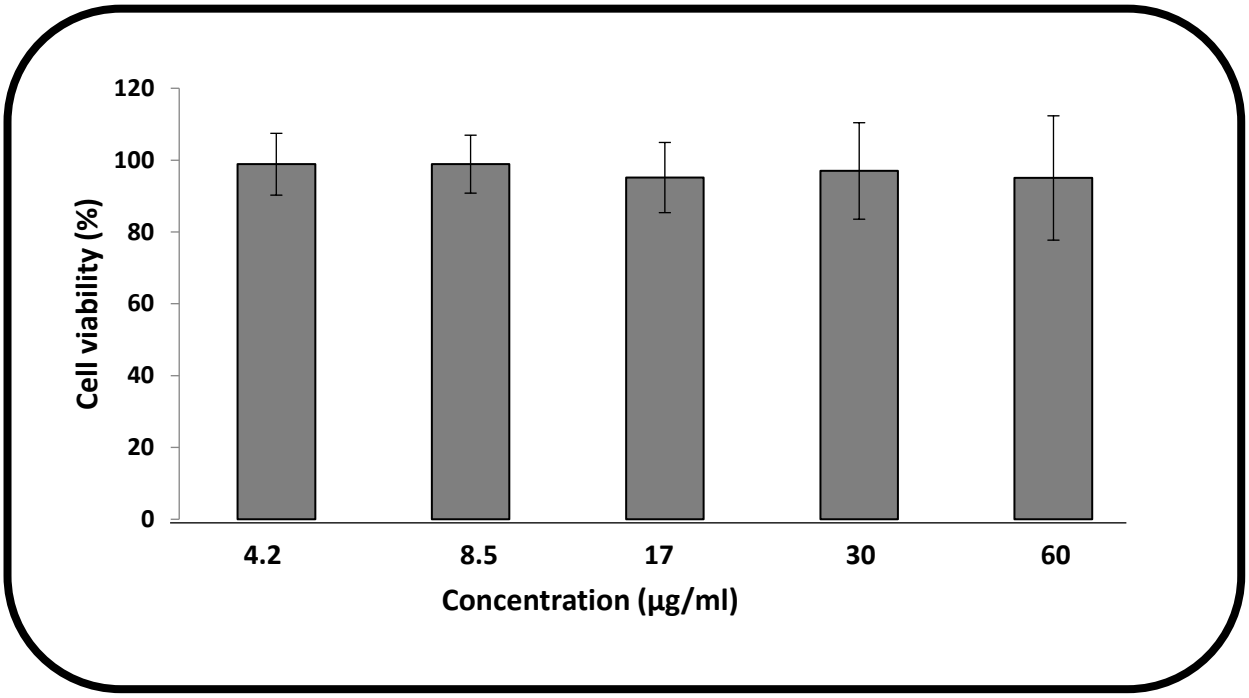

Figure 6.5: Dark toxicity plot of PluS NPs

6.2. Photodynamic therapy effect on MCF-7 breast cancer cells

Photodynamic therapy (PDT) has continued to gain attention as an effective treatment approach for some cancers as stated in the introduction. PDT involves administration of a tumor localizing photosensitizing agent, followed by activation of the photosensitizer by light of a specific wavelength **[82, 83]**.

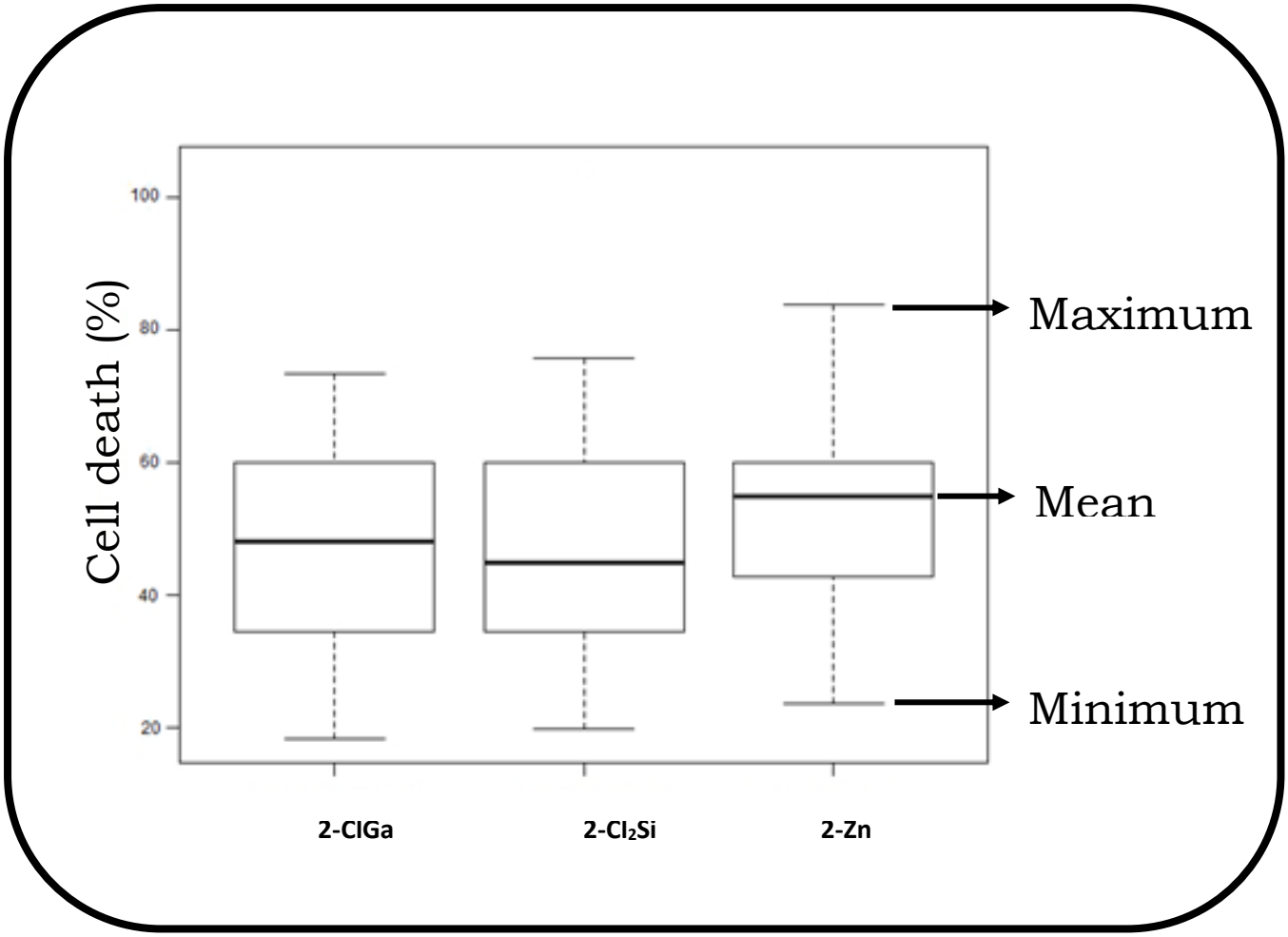

Figure 6.6: Distribution of the 2-ClGa, 2-Cl_2Si, 2-Zn at 60 µg/ml. Statistically, there is significant difference between phototoxicity effects of 2-Zn and other porphyrin complexes as P < 0.05. Irradiation for 5 min for PDT activity and vehicle control was carried out

Fig. 6.6 shows a box plot of **2**-ClGa, **2**-Cl_2Si, **2**-Zn at 60 µg/ml alone in the absence of PluS NPs. It is observed from the boxplot that **2**-Zn has a higher average of about 55% meaning that it kills about 55% of cells on average followed by **2**-CIGa with an average of about 51% then **2**-Cl_2Si with an average of about 45%. This can be further supported by the lower and upper percentiles as shown from the boxplot with **2**-Zn having the higher percentiles. Looking at the maximum and minimum percentages of the

effectiveness of all the three molecules, still **2**-Zn proves to be the most effective with maximum of almost 90%.

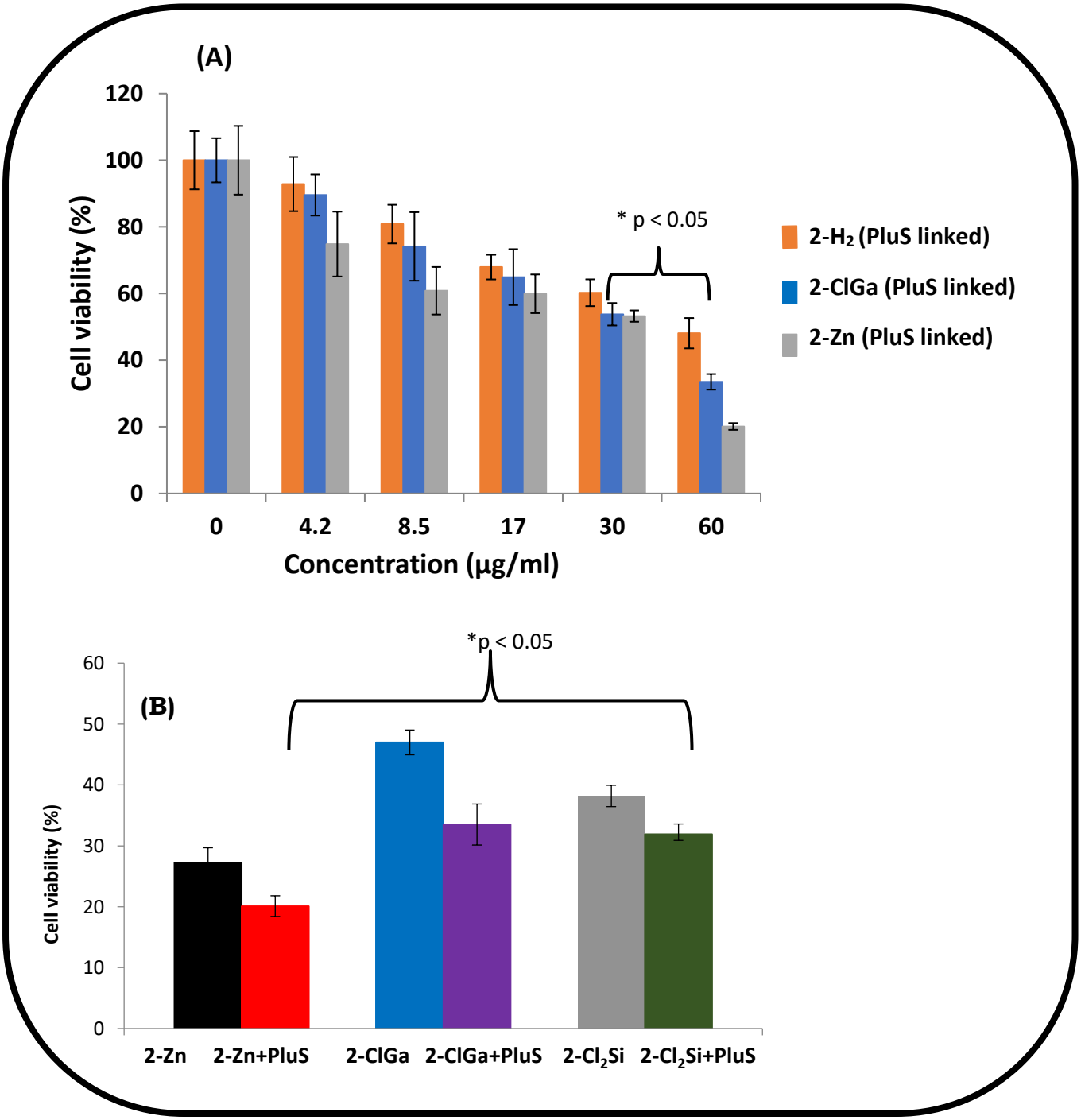

Figure 6.7: (A) PDT activity of 2-H_2 (PluS linked), 2-ClGa (PluS linked) and 2-Zn (PluS linked; (B) comparison of PDT activities of the porphyrins alone at 60 µg/ml.

The phototoxicity of porphyrin molecules increased with increase in concentration, **Fig. 6.7A**. **2**-Zn (PluS linked) at 4.2 µg/ml showed 82.8 ± 4.5 % cell viability but at 60 µg/ml there was a decrease to 27.5 ± 3.4%. **2**-Zn has the highest PDT effect followed by **2**-Cl_2Si and then **2**-ClGa, **Fig. 6.7B**. **2**-Zn gave the largest singlet oxygen quantum yield **2**-ClGa and **2**-Cl_2Si **Table 5.3**, hence the increased PDT activity. As stated in the introduction, singlet oxygen is the cytotoxic species for PDT, hence the larger the singlet oxygen the better the PDT activity. It was observed that the percent cell viability decreased more for the conjugates of porphyrins with PluS NPs when compared to the porphyrins alone (**Fig. 6.7B**).

The increase in PDT activity of the porphyrins in the presence of PluS NPs may be due to the fact that the latter act as the delivering agents and increase solubility of the compounds. The highest PDT effect was achieved for **2**-Zn (PluS linked) at 60 µg/ml which showed 20 ± 1.6% cell viability, followed by **2**-Cl_2Si (PluS linked) at 33 ± 3.3%, and **2**-ClGa (PluS linked) at 38 ± 3.7% cell viability. The $p > 0.05$ indicated that **2**-Zn (PluS linked) is significantly different compared to the other porphyrins.

Complexes 2 and **8** were loaded into Pluronic polymer micelles (F127) as stated above. The phototoxicity of porphyrin molecules increased with increase in concentration as observed above without F127 **Fig. 6.8**. **8**-Zn+F127 showed better activities as compared to **8**-H_2+F127, **8**-ClGa+F127 as well as **2**-H_2+F127, **2**-ClGa+F127, **2**-Zn+F127. *In vitro* and *In vivo* studies were carried out in literature [**64, 172**] with benzoporphyrin derivatives regioisomers encapsulated in micelles [**64 172**] It was found that the micellar

regioisomers derivatives localized in mitochondria [**64**] as well as in KLN205 and LM8 mouse tumor models [**172**] and that they reached their maximum cellular uptake after 4 h. This can serve as an indication that the complexes encapsulated in polymer micelle maybe be stable enough to localise in cancerous cells.

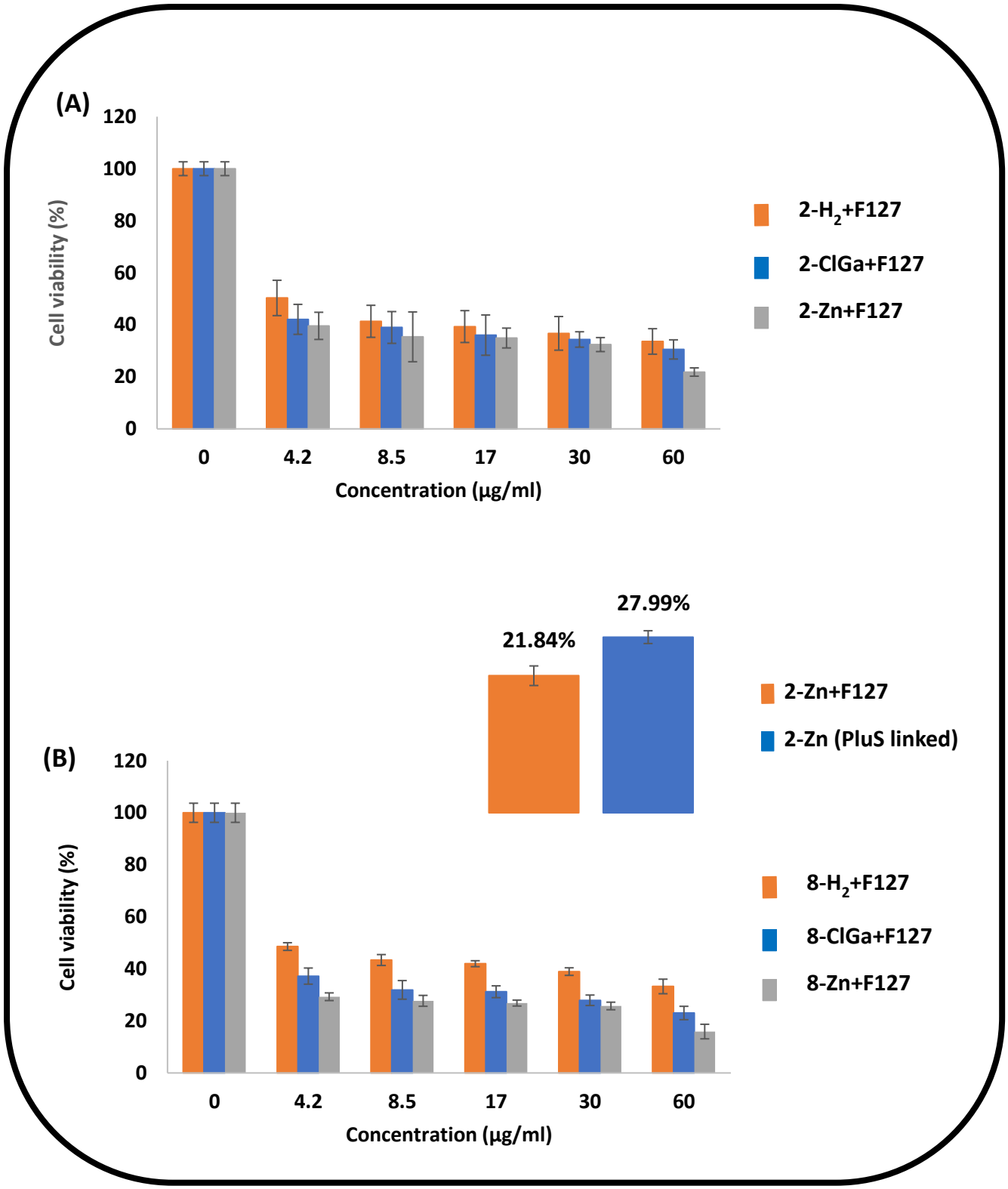

Figure 6.8: PDT plots for (A) 2-H_2+F127, 2-ClGa+F127, 2-Zn+F127, (B) 8-H_2+F127, 8-ClGa+F127, 8-Zn+F127 at 0, 4.2, 8.5, 17, 30 and 60 µg/ml. with insert of 2-Zn+F127 and 2-Zn+F127 (PluS linked) at 60 µg/ml. Statistically, there is significant difference between phototoxicity effects of 8-Zn+F127 and other porphyrin complexes as $p<0.05$

It was found that **2**-Zn+F127 showed better activities (less cell viability) compared to **2**-H_2+F127, **2**-ClGa +F127, **Fig. 6.8A** as also observed for PluS NPs above.

PDT activities are expected to follow the same trend as the singlet oxygen quantum yields. However, the PDT activity when embedded in Pluronics, does not follow the trend in singlet oxygen quantum yield, where **2**-ClGa+F127 (Φ_Δ= 0.38) and **2**-Zn+F127 (Φ_Δ=0.41) (**Table 5.4**) have about the same singlet oxygen quantum yield values but significantly different PDT activities with 21.84% of the cells viable at 60 μg/ml for **2**-Zn+F127 **Fig. 6.8A**. and 30.53% for **2**-ClGa.

Comparison between loading or linking to micelles, showed that at 60 μg/ml, 21.84% of the cells were viable for **2**-Zn+F127 and 27.99% for **2**-Zn (PluS linked) as shown in **Fig. 6.8** (insert), showing the importance of loading of porphyrins into Pluronic F127 as a drug delivering agent rather than linking. The bioavailability of a drug is influenced by a number of factors which include the route of drug administration, tissue distribution, extent of drug metabolism, and drug clearance **[173]**. Such factors may directly affect the response of a cell and the difference in drug concentration at the tumor site is expected to create differences in antitumor effects.

*P < 0.05 is considered to be statistically significant difference. Statistically significant difference was observed as the concentration increases. There was a significant difference between the dark cytotoxicity and PDT data of all complexes.

6.3. Conclusion for the chapter

Asymmetric **complexes 2** and **8** were embedded in micelles while **complex 2** was both embedded in micelles and linked to PluS NPs and their dark toxicity and PDT activity successfully studied on MCF-7 breast cancer cells. Photodynamic studies confirmed that the loading of porphyrins to carrier molecules (F127) improves *in vitro* PDT efficiency. The low dark toxicity of the porphyrins in cells is very promising for PDT applications.

Chapter 7

Synthesis and characterization of Pcs

This chapter provides the synthetic route and characterization of phthalocyanines (Pc) as well as their nonlinear optical (NLO) properties.

7.1. Synthesis and characterisation of complexes 9-OHGa and 9-OAcIn

9-OHGa complex was formed by metalation of **9**-H_2 with $Ga(acac)_3$ in the refluxing mixture of *i*-AmOH and TCB (**Scheme 7.1**). Upon the elution of complex from alumina with the mixture of chloroform and methanol, the exchange of axially coordinated acetylacetonate counterion to OH^- group occurred. **9**-OAcIn complex was also prepared by reaction of **9**-H_2 with $In(acac)_3$ in refluxing 1-chloronaphthalene [**174**]. Elution of complex from alumina was performed using the mixture of chloroform, methanol and acetic acid which resulted in the exchange of axially coordinated acetylacetonate counterion to acetoxy (OAc)-group which was then confirmed by MALDI TOF mass-spectrometry (**Fig. 7.1**).

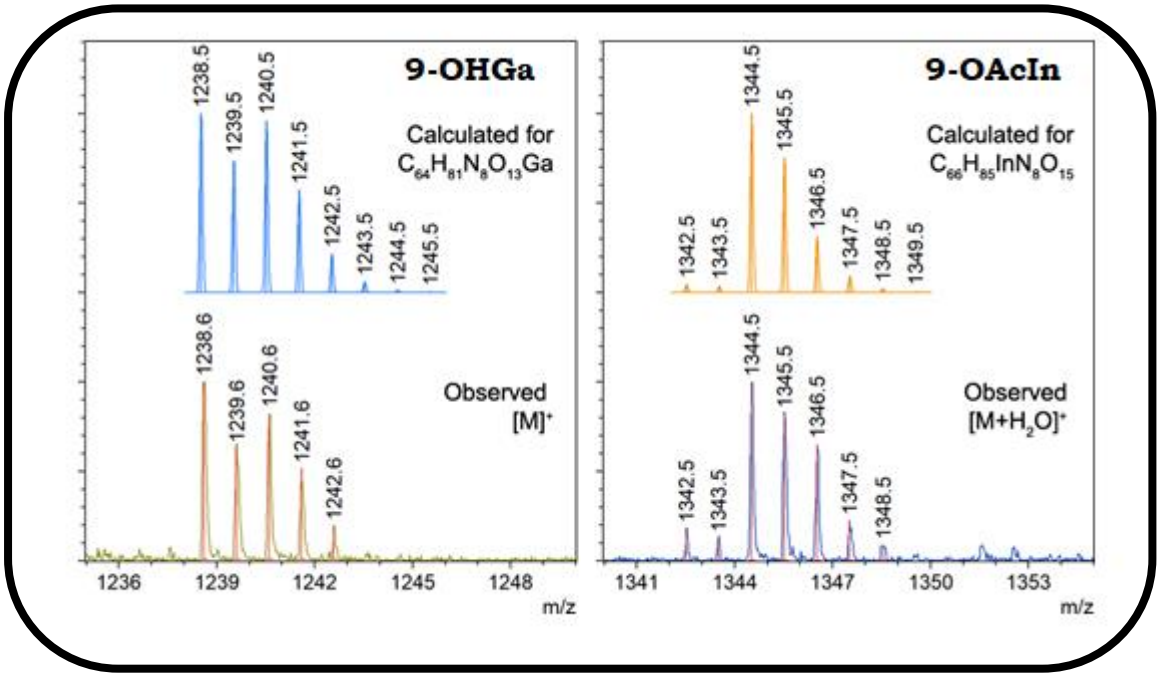

Figure. 7.1. Isotopic distributions of molecular ions in MALDI TOF mass-spectra of complexes 9-GaOH and 9-OAcIn.

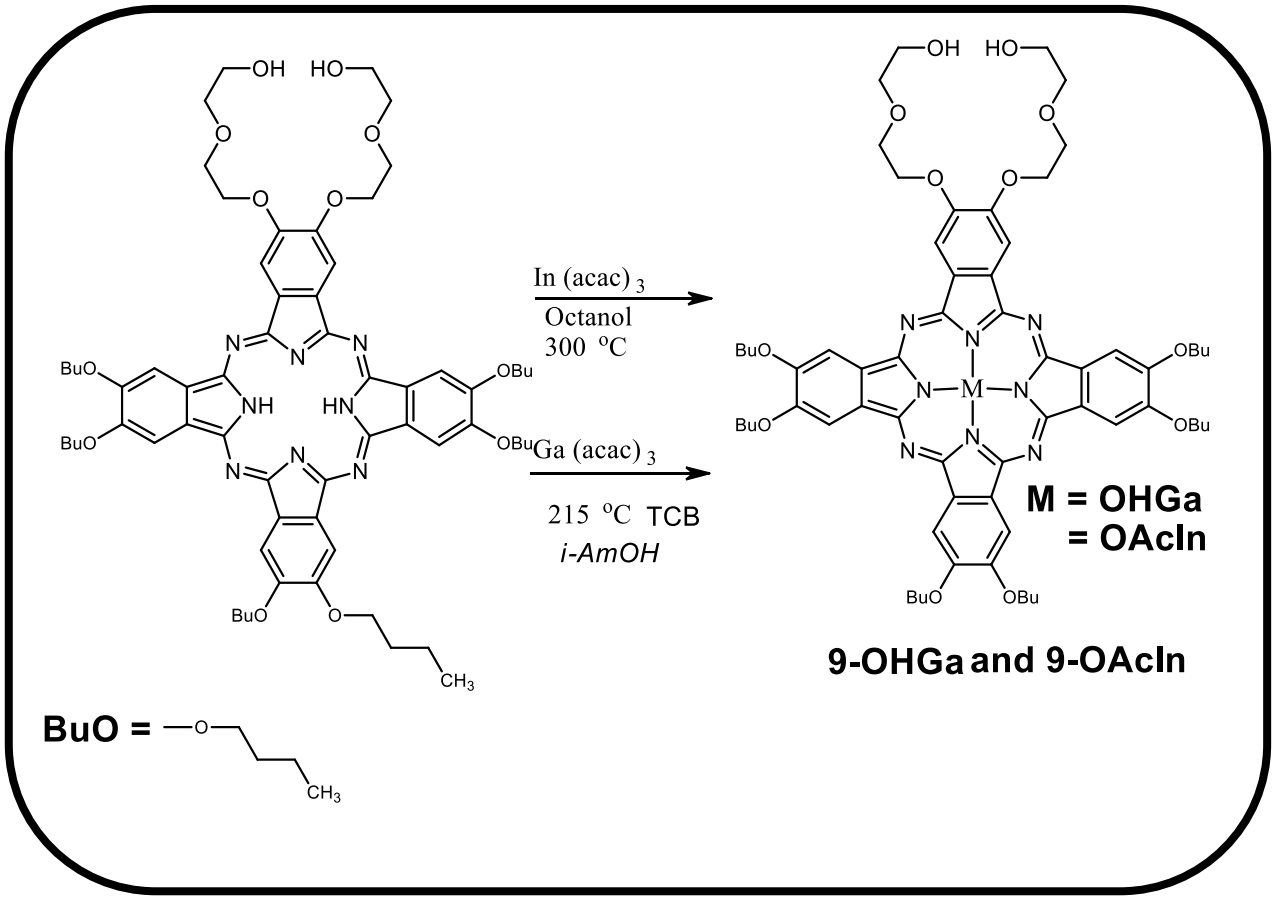

Scheme 7.1: Synthesis of 9-OAcIn and 9-OHGa

Fig. 7.2 shows the electronic absorption spectra of **complexes 9**-OHGa and **9**-OAcIn in DMSO. The Q band for **complex 9**-OHGa is slightly blue shifted at 693 nm with respect to the Q band of **complex 9**-OAcIn observed at 695 nm (**Table 7.1**) as Ga is smaller than In, large metals shift the Q band to the red region [**175**]. The absorption band between 400 and 500 nm, observed in both complexes, is attributed to charge transfer transition.

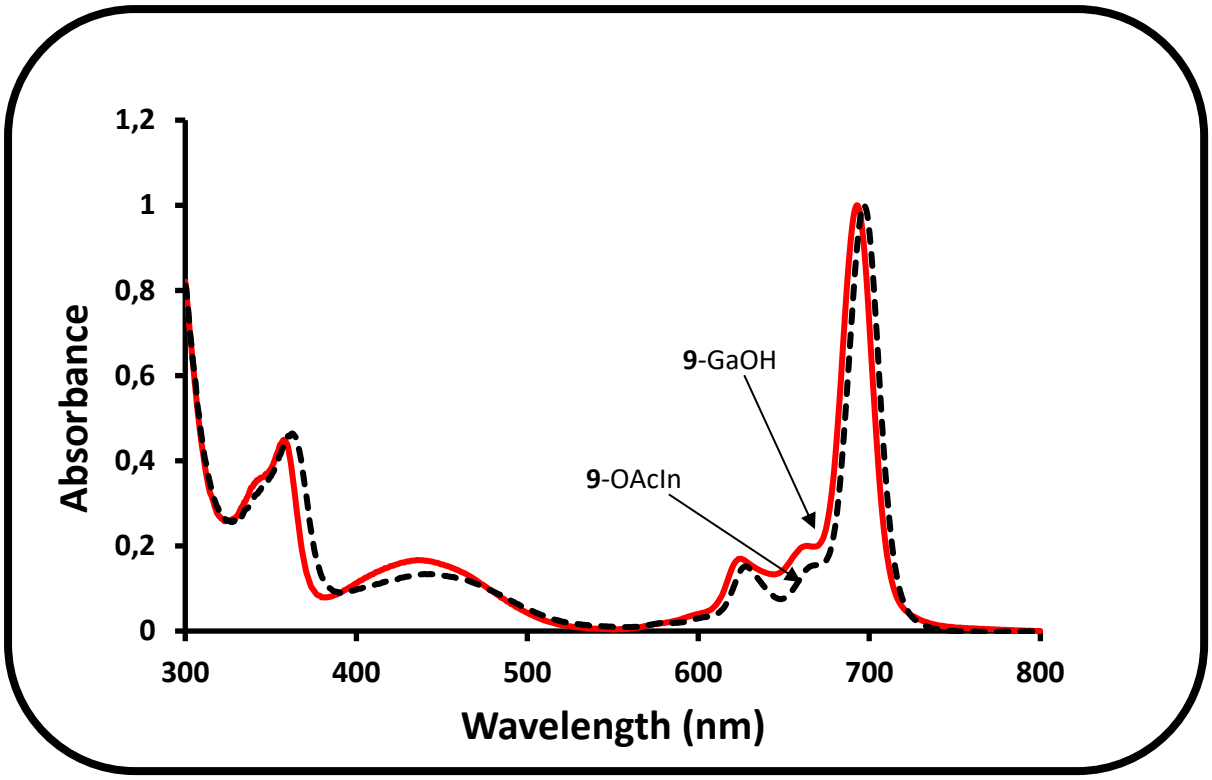

Figure 7.2: Electronic absorption spectra of complexes 9-OHGa and 9-OAcIn in DMSO.

7.2. Photophysical photochemical parameters

7.2.1. Fluorescence quantum yield (Φ_F) and life times (τ_F)

Fig. 7.3 shows the absorbance, excitation and emission spectra of **complexes 9**-OAcIn and **9**-OHGa in DMSO. The Q band maxima of the absorption and excitation spectra were similar and mirror image of the emission spectra for both complexes. The above observation suggest that the nuclear configurations of the ground and excited states are similar and not affected by excitation in DMSO.

Fluorescence (Φ_F) quantum was determined by comparative methods **Equation 5.1** using the fluorescence quantum yield ZnPc in DMSO as a

standard (Φ_F) = 0.20 [**151**]. Φ_F values of **complexes 9**-OAcIn and **9**-OHGa were determined using a time correlated single photon count (TCSPC) method, following excitation at the emission maxima **Fig. 7.4**. (**Table 7.1**). A mono-exponential decay profile was obtained for both compounds. The τ_F values were determined to be 3.1 ns for both compounds. The fluorescence life-time values are typical for Pcs [**176**].

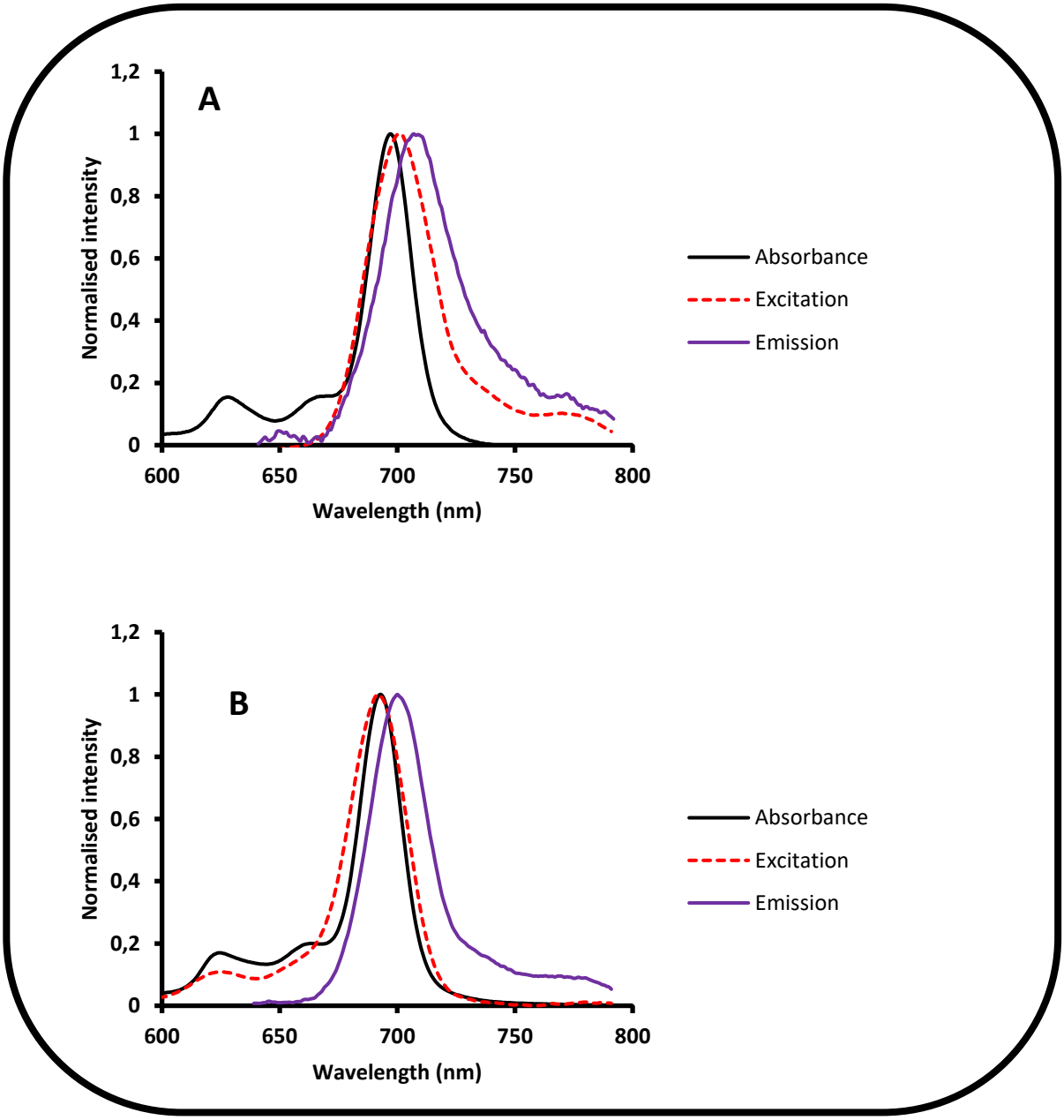

Figure 7.3: Absorption (black), excitation (dotted red) and emission (purple) spectra of complexes 9-OAcIn (A) and 9-OHGa (B). Solvent = DMSO

The florescence quantum yield (Φ_F) for **complex 9**-OHGa was determined to be 0.052 which is higher than that of **complex 9**-OAcIn at 0.014 (**Table 7.1**). **Complex 9**-OAcIn contains indium which is a heaver metal than gallium in

complex 9-OHGa, resulting in increased intersystem crossing for the former, resulting in reduced fluorescence.

7.2.2. Triplet quantum yields (Φ_T) and life times (τ_T)

The triplet quantum yields (Φ_T) were determined by comparative methods, using ZnPc in DMSO as a Φ_T^{std} = 0.65 [**177**]). Using **Eq 7.1**

$$\phi_T^{sample} = \phi_T^{std} \frac{\Delta A_T^{sample}}{\Delta A_T^{std}} \frac{\varepsilon_T^{std}}{\varepsilon_T^{sample}} \qquad (7.1)$$

where A_T^{Sample} and A_T^{Std} are the changes in the triplet state absorbance of the sample and the standard, respectively. ε_T^{Sample} and ε_T^{Std} are the triplet state extinction coefficients for the sample and standard, respectively. $\phi_T^{std}$is the triplet state quantum yield for the standard.

The triplet decay (τ_T) is measured using laser flash photolysis and the data is analysed using OriginPro 8.0 software.

Table 7.1: Photophysical parameters of 9-OAcIn and 9-OHGa in DMSO

Compound	λ_{abs} (nm)	λ_{Em} (nm)	Φ_T	τ_T (µs)	Φ_F	τ_F (ns) ±0.01
9-OAcIn	695	703	0.35	48	0.014	3.1
9-OHGa	693	697	0.27	48	0.052	3.1

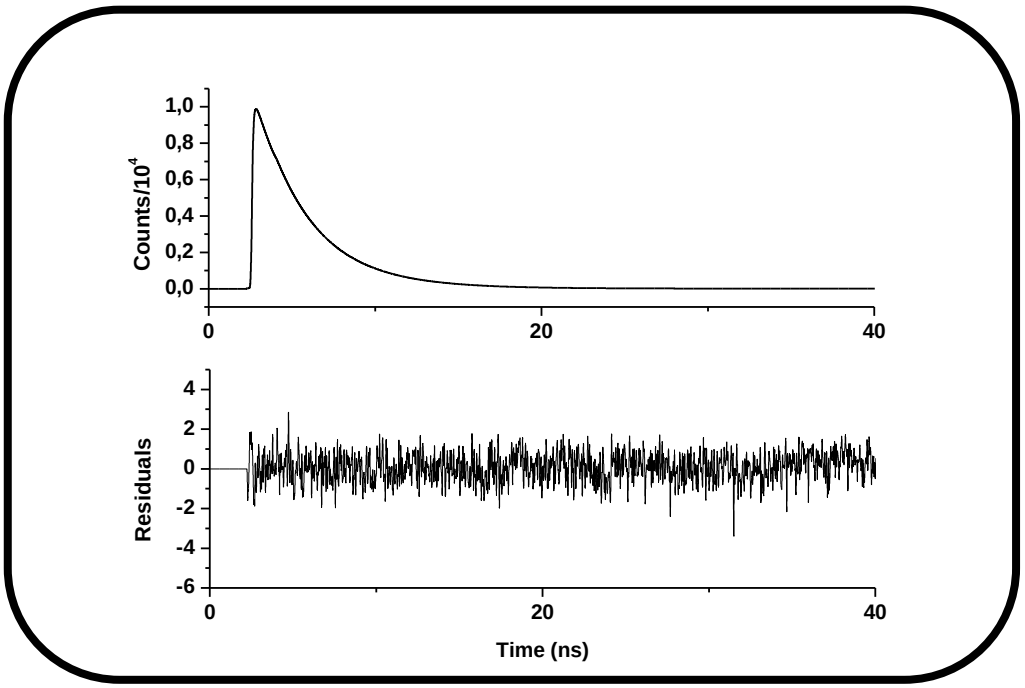

Figure 7.4: Fluorescence decay profile of complex 9-OHGa in DMSO.

The transient absorption spectra of **complexes 9**-OAcIn and **9**-OHGa are shown in **Fig. 7.5**. The spectra were recorded in argon-degassed DMSO solution, by exciting the complexes at 680 nm and recording the spectra from 400 to 800 nm. The transient absorption spectra for **complex 9**-OHGa shows a singlet depletion peak and a very weak triplet-triplet absorption peak around 500 nm as compared to **complex 9**-OAcIn which shows a strong triplet-triplet absorption peak.

The τ_T for **complexes 9**-OAcIn and **9**-OHGa were determined to be 48 μs (**Table 7.1**), while the Φ_T were 0.35 and 0.27 for **complexes 9**-OAcIn and **9**-OHGa, respectively. The Φ_T value for **complex 9**-OAcIn is larger than for **9**-OHGa due to the presence of a heavier In central metal in the former, which

results in improved population of the triplet state as a result of the heavy atom effect discussed above.

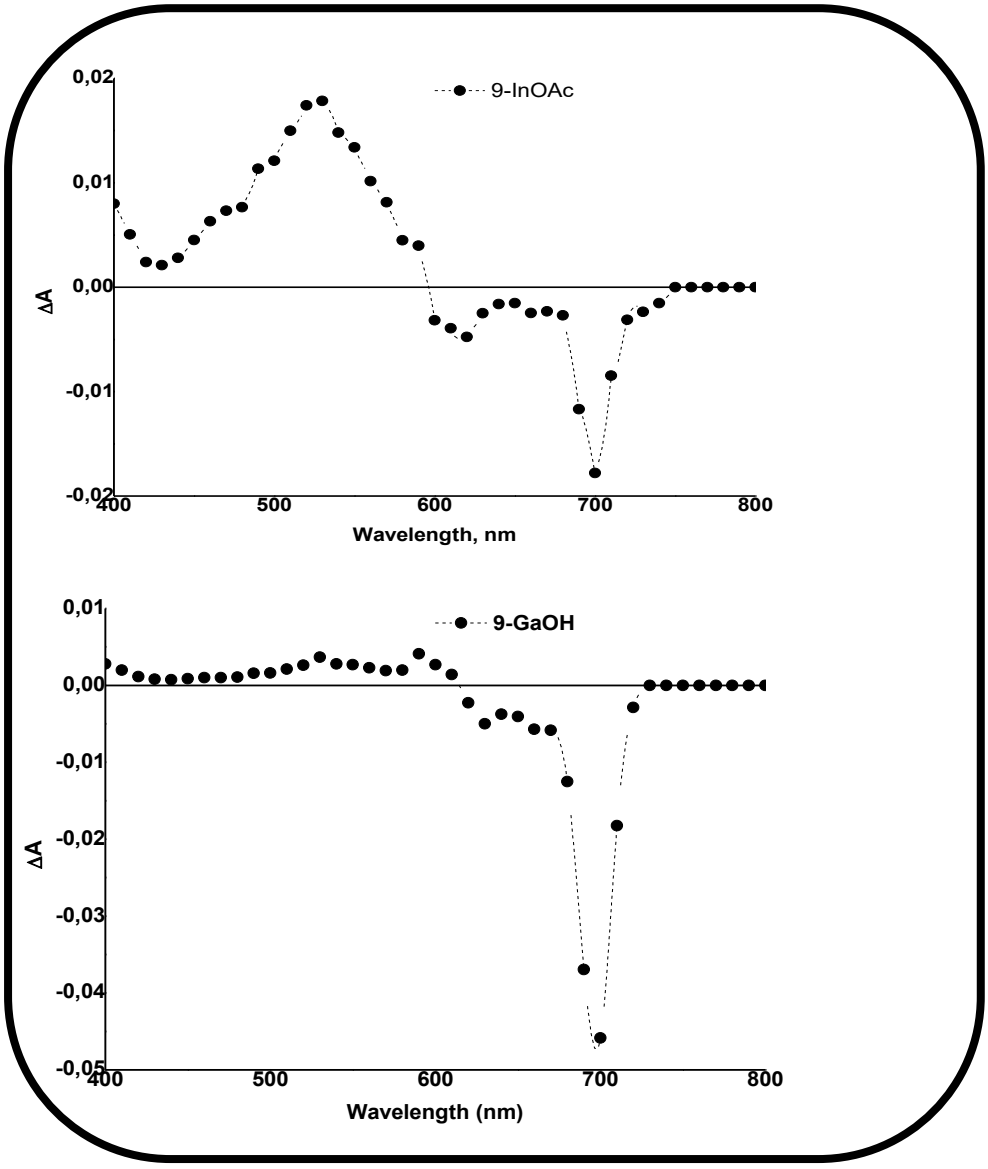

Figure 7.5: Transient differential spectra of complexes 9-OAcIn (A) and 9-OHGa (B) in DMSO. Insert in (A) is triplet decay curve of complex 9-OHGa as an example.

7.3. Nonlinear optical (NLO)

7.3.1. Equations employed

The nonlinear optical properties of phthalocyanines were evaluated using the Z-scan technique that has been previously described **[178, 179]**. All Z-scan calculations and plots were done on Origin 7 and Microsoft excel 2016. Z-scan technique relies on the total transmittance passing through the molecule as a result of the incident laser pulses. The normalised transmittance is given by **Equation 7.2** [**179, 180**]:

$$T_n(z_s) = \frac{1}{Aq_0(Z_s)} \int_{-\infty}^{+\infty} \ln[1 + q_0(z_s) f(\tau)] d\tau \qquad (7.2)$$

where $f(\tau)$ is a function of time (t) describing the temporal profile of the pulse for Gaussian pulses and has the form $f(\tau) = e^{(-\tau^2)}$. A is a normalization constant equal to $\int_{-\infty}^{+\infty} f(\tau) d\tau$ and $q_0(z_s)$ is a parameter characterizing the strength of the nonlinearity. Given by q_0 is represented by **Equation 7.3** [**180**]:

$$q_0(z_s) = \frac{2\beta P_0 L_{eff}}{\pi w^2(z_s)} \qquad (7.3)$$

where β is the nonlinear absorption coefficient of the material, P_0 is the peak power of the pulses and the L_{eff} the effective propagation length in the material, given by **Equation 7.4**:

$$L_{eff} = \frac{1 - e^{-(\alpha L)}}{\alpha} \qquad (7.4)$$

where L is the sample length (or the thickness of the sample) and α is the linear absorption coefficient. α is be determined using **Equation 7.5:**

$$\alpha = \frac{hv}{N}\beta \tag{7.5}$$

where N corresponds the number of active species per unit volume, h is Planck's constant and v the frequency of a laser excitation. The parameter $w(z_s)$ (in **Equation 7.3**) is the beam width at the sample defined as the distance from the beam centre to the point where the intensity reduces to $1/e^2$ of its axis value. $w(z_s)$ is defined by **Equation 7.6** [**180**]:

$$w(z_s) = w_0\sqrt{1 + \left(\frac{z_s - z_0}{z_R}\right)^2} \tag{7.6}$$

where w_0 is the beam width at the focus and z_0 is the location of the beam focus. The parameter z_R is the Rayleigh length, defined by **Equation 7.7:**

$$z_R = \frac{\pi w_0^2}{\lambda} \tag{7.7}$$

where λ is the bean wavelength. **Equations (7.2) - (7.7)** are used to determine the nonlinear absorption coefficient (β) from experimentally measured transmittance. Tsigaridas et al. [**180**] have produced an analytical formula given by **Equation 7:8:**

$$q_0(z_s) = \begin{cases} a_0 + a_1 T_n(z_s) + a_2 T_n^2(z_s) + a_3 T_n^3(z_s) \;\; for \;\; T_n(z_s) \leq 0.75 \\ c_0 + c_1[T_n(z_s)]^{c_2} \; for \; T_n(z_s) \geq 0.75 \end{cases} \tag{7.8}$$

where the coefficients $a_0, a_1, a_2, a_3, c_0, c_1, c_2$ for Gaussian pulses are given as 15.66, -37.45, 30.76, -8.97, -2.301, 2.156, -1.563 respectively [**180**]. **Equation 7.8** provides values of $q_0(z_s)$ directly from the normalized transmittance $T_n(z_s)$. The method developed by Tsigaridas et al. allows straight forward determination of β and is very robust to noise [**180**].

Absorption coefficient (β), as well as the beam parameters z_0 and Z_R can be determined from $q_0(z_s)$ values obtained from **Equation (7.8)**. Substituting **Equation 7.6** into **Equation 7.3**, $q_0(z_s)$ is then defined by **Equation 7.9**:

$$q_0(z_s) = \frac{Q_0}{1+(z_s-z_0)^2/z_R^2} \tag{7.9}$$

where

$$Q_0 = \frac{2\beta P_0 L_{eff}}{\pi w_0^2} = \frac{2\beta P_0 L_{eff}}{\lambda z_R} \tag{7.10}$$

Equation 7.11 is then used to calculate the nonlinear absorption coefficient (β).

$$\beta = \frac{\lambda z_R Q_0}{2P_0 L_{eff}} \tag{7.11}$$

The imaginary component of the third order optical susceptibility Im[$x^{(3)}$] is directly proportional to β via **Equation 7.12** [**181**]:

$$\mathrm{Im}[\chi^{(3)}] = \frac{(n^2 \varepsilon_0 c \lambda \beta)}{(2\pi)} \tag{7.12}$$

in which c and n, respectively, are the speed of light in a vacuum and the linear refractive index of the system. ε_0 is the permittivity of free space and λ is the wavelength of the laser light. At a molecular level, there is a direct correlation of Im[$x^{(3)}$] with the hyperpolarizability, γ, which provides the nonlinear absorption per mole of the sample via the relationship shown by **Equation 7.13** [**182**]:

$$\gamma = \frac{\mathrm{Im}[\chi^{(3)}]}{N^* f^4} \tag{7.13}$$

where N* = $C_{mol}N_A$ (with C_{mol} being the concentration in mol) and f represents Lorenz local field factor and is given by **Equation 7.14**:

$$f = \frac{n^2 + 2}{3} \qquad (7.14)$$

Practical procedure followed for data analysis

Equation 7.8 provides values of $q_0(z_s)$ directly from the normalized transmittance ($T_n(z_s)$) data (following Tsigaridas [**180**]), see **Scheme 7.2**. Excel was used to convert ($T_n(z_s)$) to $q_0(z_s)$. **Equation 7.9** is used to nonlinearly fit the $q_0(z_s)$ data in order to obtain Q_0 (full width at half maximum, FWHM) and z_R (Ray leigh length) values. These values are then used to calculate β using **Equation 7.11**. The fitting is carried out using Nonlinear fitting from Origin program. The β values were then used to calculate third order optical susceptibility Im[$x^{(3)}$] using **Equation 7.12**. The Im[$x^{(3)}$] values were converted to esu units using the conversion value 1,39556 x 10^{-08} esu.

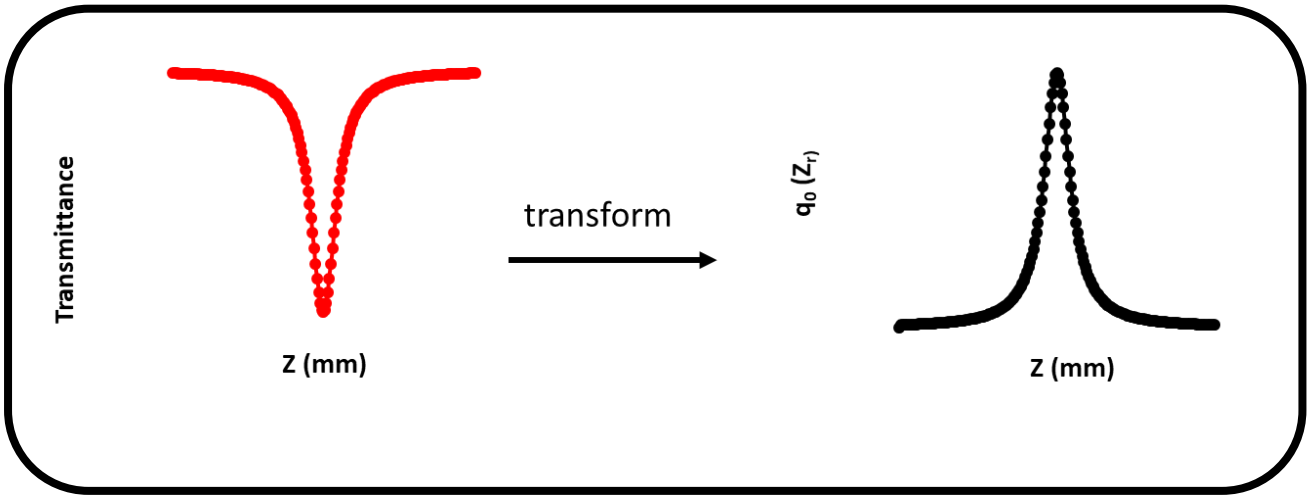

Scheme 7.2: Transformation of experimental transmittance ($T_n(z_s)$) data to $q_0(z_s)$ values.

7.3.2. Z scan data

The concentration of the **complexes 9**-OAcIn and **9**-OHGa used for NLO were determined to the order of 10^{-5}M. The thickness of the films were determined to be 53 and 58 μm for **complexes 9**-OAcIn-TF and **9**-OHGa-TF shown in **Table 7.2**, respectively using SEM. The Z-scan plots for **complexes 9**-OAcIn and **9**-OHGa in solution and as films are shown in **Fig. 7.6.** The Z-scan plots show a typical nonlinear absorption behaviour, with reverse saturable absorption (RSA) profiles.

The experimental β values for **complexes 9**-OAcIn and **9**-OHGa in DMSO were found to be $7.2 \times 10^{-9} m.W^{-1}$ and $6.0 \times 10^{-9} m.W^{-1}$, respectively (**Table 7.2**). The results suggest that **complex 9**-OAcIn has a better β values compared to **complex 9**-OHGa. The above results are consistent with the calculated triplet state quantum yield, which shows a greater triplet state population for **9**-OAcIn with respect to **9**-OHGa. The magnitude of the β values are within range or better than β values of monomeric Pcs reported in literature [**106, 183**].

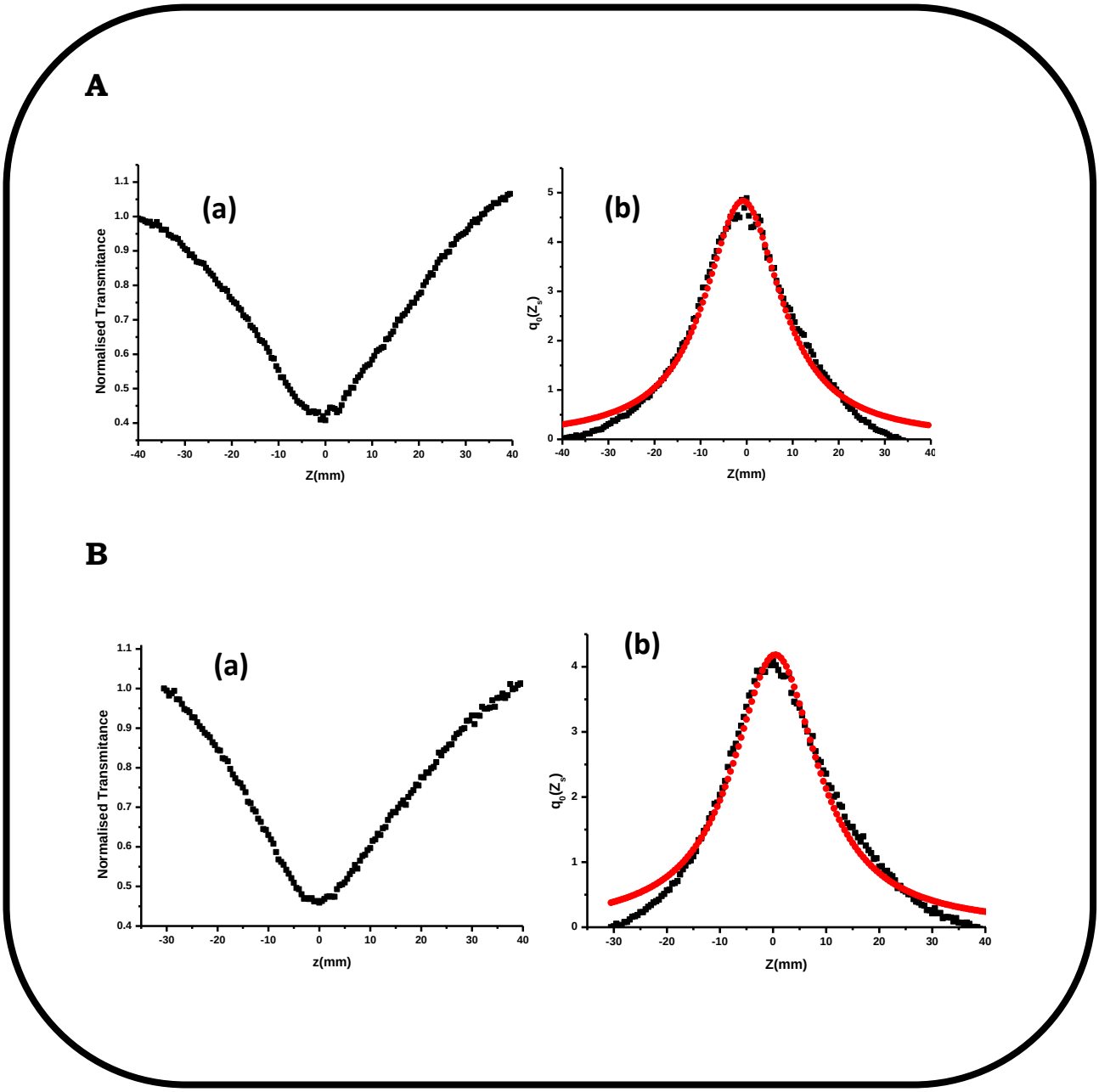

Figure 7.6: Z-scans (a) and nonlinear fit (b) curves (q0(Zs)) for complexes (A) 9-AOcIn and (B) 9-OHGa in DMSO solution.

The two complexes were imbedded in a PBC polymer and supported on glass subtrate for Z-scan measurements and their β values measured. Z scans of the films are shown in **Fig. 7.7. Complex 9**-OAcIn when imbedded in PBC gave a higher β value of $6.0 \times 10^{-10} m.W^{-1}$ compared to **complex 9**-OHGa

with a β value of 4.77 $\times 10^{-10} m.W^{-1}$. Thus, similar to solutions, **complex 9**-OAcIn gives better β values compared to **complex 9**-OHGa. The β values obtained for **complexes 9**-OAcIn-TF and **9**-OHGa-TF were found to be less than the values determine in solution surprisingly, since this was not expected, **Table 7.2**.

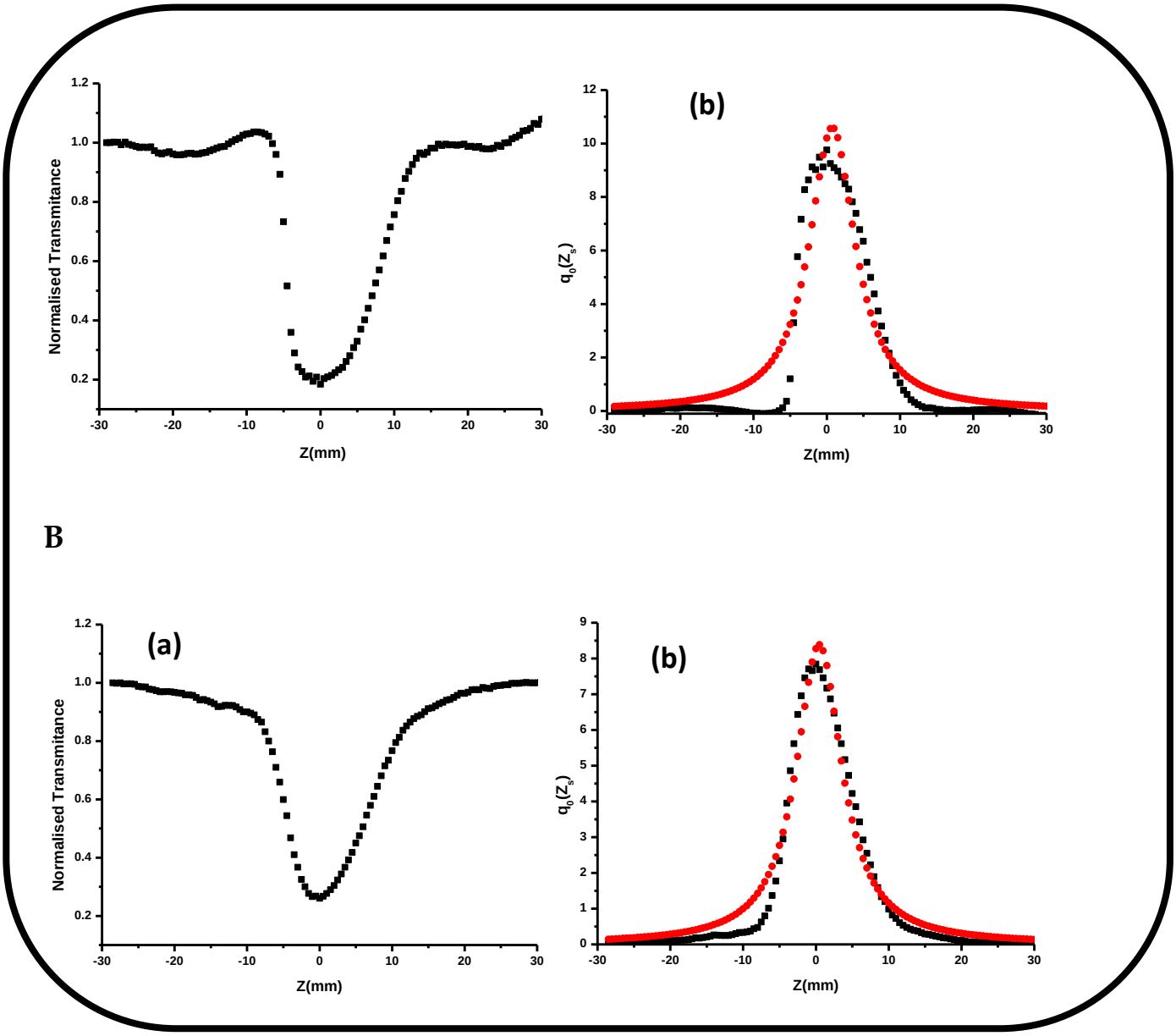

Figure 7.7: Z-scans (a) and nonlinear fit (q0(Zs)) curves (b) for complexes (A) 9-OAcIn-TF and (B) 9-OHGa-TF on films.

Table 7.2 summarizes the $Im[\chi^{(3)}]$ and γ values of **complexes 9**-OAcIn and **9**-OHGa in solution. $Im[\chi^{(3)}]$ and γ values are larger for **complex 9**-OAcIn compared **9**-OHGa, due to heavy atom effect of the former. The ground state absorption cross sections (σ_{01}) of the samples at 532 nm were calculated using **Equation 7.15 [141]**.

$$\sigma_{01} = \frac{\ln(10)10^3\alpha}{N_A} \qquad (7.15)$$

where α and N_A are the linear absorption coefficient at 532 nm and concentration in the excited state, repectively. **Table 7.2** shows the determined absorption cross section value for **complexes 9**-OAcIn and **9**-OHGa as 4.95×10^{-18} and 1.67×10^{-18} cm^2 repectively, which are in range to reported for ZnPc deravitives [**184**]. The optical limiting properties (I_{lim}), which is a threshold limit intensity or fluence at which the transmittance is 50% of the linear transmittance [**185**], were calculated using **Equation 7.16**:

$$I_{lim} = \frac{h\upsilon}{2\pi\sigma_{01}\tau_T} \qquad (7.16)$$

where σ_{01} and τ_T are the single absorptipon cross section and triplet life times respectively. υ is the frequency of the laser and h is the Planck's constant. The I_{lim} value can be used to classify material which are ideal for optical limiting application, such as nonlinear material developed for the protection of human eyes from an intense laser beam. **Table 7.2** shows the I_{lim} values of **complexes 9**-OAcIn and **9**-OHGa to be 2.51×10^{-6} and 7.43×10^{-6} J/cm^2 repectively. The lower the I_{lim} value the more ideal the material is as an optical

limiter [**185**]. In this case I_{lim} values suggest that **complex 9**-OAcIn is better nonlinear optical limiter compared to **complex 9**-OHGa.

The above conclusion is affirmed by the β values determined for these complexes, whereby **complex 9**-OAcIn gave a larger β value compared to **complex 9**-OHGa. The I_{lim} could not be calculated for the films using the above solution based calculation, hence as a rough estimate using logarithmic plot of output vs input intensity was used for comparison. **Fig. 7.8** shows the logarithmic plot of output vs input intensity of **complexes 9**-OAcIn and **9**-OHGa in DMSO and as films.

Table 7.2: Nonlinear optical complexes 9-OAcIn and 9-OHGa in DMSO and thin films.

Complex	**[C]**$\times 10^{-5}M$)	$Im[\chi^{(3)}]$ $(\times 10^{-10}\ esu)$	$\beta\left(\frac{m}{W}\right)$ $\times 10^{-10}$	γ $(\times\ 10^{-30}\ esu)$	$\sigma_{01} \times 10^{-18}cm^2$	I_{lim} $(\mu J.cm^{-2})$	I_{out}% $at\ 50\%\ I_{in}$
9-OAcIn	1.12	2.36	7.2	10.82	4.95	2.51	53
9-OHGa	1.21	1.97	6.0	8.30	1.67	7.43	51
9-OAcIn-TF	53[a]	1.97	6.0	-	-	-	54
9-OHGa-TF	58[a]	1.56	4.77	-	-	-	68

[a]**Film-Thickness** (μm)

Table 7.2 records the I_{out} percentage at 50% of the I_{in} percentage. The I_{out} percentage values suggest that **complex 9**-OAcIn and **9**-OHGa in DMSO response (53% and 51% respectively) to the incident laser beam are nearly identical. However as a film **complex 9**-OAcIn shows a better response of 54% compared to **complex 9**-OHGa (68%) embeded in a film.

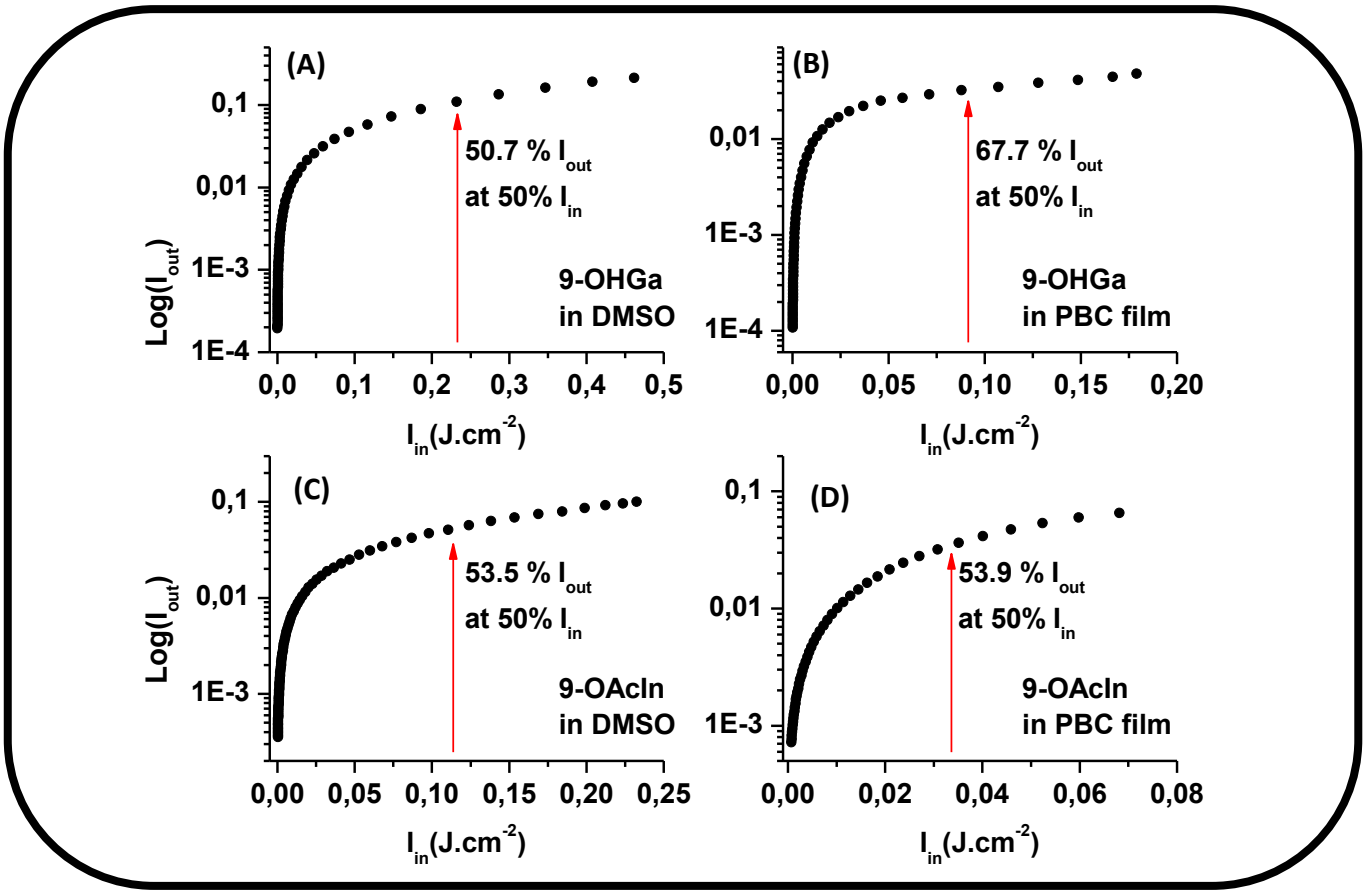

Figure 7.8: Plot of log of I_{out} versus I_{in} for complex 9-OAcIn in (A) DMSO and (B) as thin films and for complex 9-OHGa in (C) DMSO and (D) as thin films.

7.4. Conclusion for the chapter

Photophysical measurements showed that Φ_T values were higher and Φ_F values lower for **9**-OAcIn. The NLO properties of these complexes were studied in solution and when embedded in poly(bisphenol A carbonate) films. The $Im\left[\chi^{(3)}\right]$ and γ values were measured, they were found to be higher for **complex 9**-OAcIn in solution as compared to **complex 9**-OHGa. I_{lim} values and I_{out} vs I_{in} plots suggested that **complex 9**-OAcIn is a better nonlinear optical limiter compared to **complex 9**-OHGa in DMSO

Chapter 8

Conclusions and Future prospects

8.1. Conclusions

This work presents the successful synthesis and characterization of new mono and tetra substituted porphyrins and asymmetrical phthalocyanine. The prepared porphyrins and phthalocyanines showed improved solubility in common organic solvents and were found to exhibit monomeric behaviour in solution. The porphyrins were successfully embedded/incorporated into Pluronic polymer and they became water soluble. The τ_f values for metalled derivatives are shorter than metal free derivatives. The shortening is due to the heavy atom effect. The τ_f values upon incorporation into the polymer were shortened compared to the porphyrin alone for **complex 4** which is water soluble, suggesting the quenching of the lifetimes of the porphyrin by the polymers.

The PDT activity generally followed the same trend as the singlet oxygen quantum yields. However, the PDT activity for **2**-ClGa+F127 and **2**-Zn+F127, does not follow the trend in singlet oxygen quantum yield as their singlet oxygen quantum yields were very close but PDT activities differed. The PDT activities of **complexes 2** and **8** was examined as examples when loaded into Pluronic polymer micelles (F127). The phototoxicity of porphyrin molecules increased upon irradiation and increased with increase in concentration.

The Φ_T value of the phthalocyanines were higher for **9**-OAcIn. The NLO properties of these complexes were studied in solution and when embedded on films. The $Im[\chi^{(3)}]$ and γ values are higher for **9**-OAcIn in solution as compared to **complex 9**-OHGa. I_{lim} values and I_{out} vs I_{in} plots suggested that

complex 9-OAcIn is better nonlinear optical limiter compared to **complex 9**-OHGa in DMSO and as films.

8.2. Future prospects

Binary mixture of Pluronic polymers overcomes the drawbacks of mono system and it could be of high interest to have explored ternary mixtures. The modification of F127 and linking to FA showed very interesting results in PDT, it could be of interest to have linked the F127 with other biological molecules that enhance cancer cells selectivity. Detailed in *vitro* and in *vivo* experiments of these complexes on different cancer cell lines will be required to advance ongoing research on the treatment of cancer.

References

[1]. L. R. Milgrom, in The colours of life: in An introduction to the chemistry of porphyrines and related compounds, Oxford University press. (1997).

[2]. A.P. Castano, T.N. Demidova, M.R. Hamblin, Photodiagn. Photodyn. Ther. 1 (2004) 279.

[3]. A. Pfitzner, B.W. Sigusch, V. Albrecht, E. Glockmann. J. Periodontol. 75 (2004) 1343

[4]. A.S. Garcez, M.S. Ribeiro, G.P. Tegos, S.C. Nunez, A.O. Jorge, M.R. Hamblin. Lasers Surg. Med. 39 (2007) 59.

[5]. M. Ethirajan, Y. Chen, P. Joshi, R. K. Pandey, Chem. Soc. Rev. 40 (2011) 340.

[6]. S. Ishihara, J. Labuta, W. Van Rossom, D. Ishikawa, K. Minami, J. P. Hill and K. Ariga, Phys. Chem. Chem. Phys. 16 (2014) 9713.

[7]. A. K. Burrell, M. R. Wasielewski, J. Porphyr. Phthalocya. 4 (2000) 401.

[8]. Z.W. Küster, Physiol. Chem. 82 (1912) 463.

[9]. H. Fischer, K. Zeile, Ann. Chem. 468 (1929) 98.

[10]. M. R. Moore, An historical introduction to porphyrin and chlorophyll synthesis. In: M. J. Warren, A. G. Smith, M. R. Moore (eds) Tetrapyrroles, their birth, life and death. Molecular Biology Intelligence Unit. Springer, New York, pp 1–28 (2009)

[11]. Y. Li, T. M. Pritchett, J. Huang, M. Ke, P. Shao, W. Sun, J. Phys. Chem. A 112 (2008) 7200.

[12]. M. O. Liu, C. H. Tai, A. T. Hu, T. H. Wei, J. Organomet. Chem., 689 (2004) 2138.

[13]. P. J. Rothemund, Am. Chem. Soc. 57 (1936) 2010.

[14]. E. B. Fleischer, Acc. Chem. Res. 3 (1970)105

[15]. A.D. Alder, F.R. Longo, F. Kampas, J. Kin, J. Inorg. Nucl. Chem. 32 (1970) 2449.

[16]. J.S. Lindsey, I.C. Schreiman, H. C. Hsu, P.C. Kearney, A. M. Marguerettaz, J. Org. Cherm. 52 (1987) 836.

[17]. M.S. Rodriguez-Morgade, G. de la Torre, T. Torres, in The Porphyrin Handbook, K.M. Kadish, K.M. Smith, R. Guilard (Eds.), Academic Press, Elsevier Science, 15 (2003) 99.

[18]. Y. Liu, D. Zhu, T. Wada, A. Yamada, H. Sasabe, Heterocyclic Chem., 31 (1994) 1017.

[19] C.F. van Nostrum, R.J.M. Nolte, Chem. Comm., (1996) 2385.

[20] N. Kobayashi, R. Kondo, S.I. Nakajima, T. Osa, J. Am. Chem. Soc., 112 (1990) 9640.

[21]. M. Gouterman, in The Porphyrins, Part A. Physical Chemistry, D. Dolphin (Ed) Academic Press, New York, Vol. 3 (1978).

[22]. K. M. Smith, in Porphyrins and Metalloporphyrins, Elsevier, Amsterdam, (1975).

[23]. P. J. Spellane, M. Gouterman, A. Antipas, S. Kim, Y. C. Liu, Inorg. Chem. 19 (1980) 391.

[24]. M. Gouterman, J. Mol. Spectrosc. 6 (1961) 138.

[25]. M.E. Milanesio, M. Gervaldo, L. A. Otero, L. Sereno, J. J. Silber, E. N. Durantini, J. Phys.Org.Chem 15 (2002) 844.

[26]. V. Goedken, G. Dessy, C. Ercolana, V. Fares, L. Gastaldi, Inorg. Chem. 24 (1985) 991.

[27]. J. Mack, M. Stillman, Coord. Chem. Rev., 219 (2001) 993.

[28]. E.G. Azenha, A. C. Serra, M. Pineiro, M. M. Pereira, J. S. de Melo, L. G. Arnaut, S. J. Formosinhoa A.M.d'A. R. Gonsalves. J. Chem. Phys 280 (2002) 177.

[29]. E. Fagadar-Cosma, D. Vlascici, M. Birdeanu, G. Fagadar-Cosma, Arabian Journal of Chemistry.

[30]. T. Kangwanwong, W. Pluempanupat, W. Parasuk, H.E. Keenan, A. Songsasen, Science Asia 38 (2012) 278.

[31]. C.A. Busby, R. K. Dinello, D. Dolphin, J. Chem. 53 (1975) 1554.

[32]. M.M. Pereira, G. Muller, J. I. Ordinas, M. E. Azenhaa, L.G. Arnaut, J. Chem. Soc. Perkin Trans. 2 (2002) 1583.

[33]. N.D. Gupta, D. Malakar, L. Rice, S. Rivers, J. Heterocycl. Chem. 24 (1987) 629.

[34]. T. Zoltan, F. Vargas, C. Rivas, V. Lopez, J. Perez, A. Biasutto, Sci. Pharm. 78 (2010) 767.

[35]. Britton J, Martynov AG, Oluwole DO, Gorbunova YG, Tsivadze AY and Nyokong T. J. Porphyrins Phthalocyanines 20 (2016) 1296.

[36]. K. S. Oh, J. Y. Song, S. H. Cho, B. S. Lee, S. Y. Kim, K. Kim, H. Jeon, I. C. Kwon, S. H. Yuk. J. Contr. Release. 148 (2010) 344.

[37]. A. V. Kabanov, E. V. Batrakova. Curr Pharm Des. 10 (2004) 1355.

[38]. U. Kedar, P. Phutane, S. Shidhaye, V. Kadam, Nanomed Nanotech Biol Med 6 (2010) 714

[39]. S. R. Croy, G. S. Kwon. Polymeric micelles for drug delivery. Curr Pharm Des. 12 (2006) 4669.

[40]. G. S. Kwon and K. Kataoka, Adv. Drug Deliv. Rev 16 (1995) 295

[41]. D. Missirlis, N. Tirelli, and J. A. Hubbell, Langmuir 21 (2005) 2605

[42]. H. S. Yoo and T. G. Park, J. Control. Release, 96 (2004) 273.

[43]. A. V. Kabanova. E. V. Batrakovaa, V. Y. Alakhovb. J. Control. Release 82 (2002) 189.

[44]. R. Nagarajan, Colloids Surfaces B Biointerfaces 16 (1999) 55.

[45]. A. Venne, S. Li, R. Mandeville, A. V. A. Kabanov. Cancer Res. 56 (1996) 3626.

[46]. D. Sutton, N. Nasongkla, E. Blanco, J. Gao. Pharmaceutical Research. 24 (2007) 1029

[47]. G. S. Kwon, Critical Rev 20 (2003) 357

[48]. V. Alakhov, E. Klinski, S. Li, G. Pietrzynski, A. Venne, E. V. Batrakova, T. Bronitch, A. V. Kabanov Colloids Surf B: Biointerfaces 16 (1999)113.

[49]. W. Zhang, Y. Shi, Y. Chen, J. Ye, X. Sha, X. Fang. Biomaterials 32 (2011) 2894.

[50]. M. Yokoyama, P. Opanasopit, T. Okano, K. Kawano, Y. Maitani. J. Drug Target., 12 (2004) 384

[51]. Z. Sezgin, N. Yuksel, T. Baykara. Int. J. Pharm. 332 (2007) 161.

[52]. Liu L, Yong KT, Roy I, Law WC, Ye L, Liu J, Liu J, Kumar R, Zhang X, Prasad PN. Theranostics 7 (2012) 705.

[53]. B. H. Vilsinski, J. L. Aparicio, P. C. de Souza Pereira, S. L. Fávaro, K. S. S. Campanholi, A. P. Gerola, A. L. Tessaro, N. Hioka, W. Caetano, Quim. Nova, 37 (2014) 1650.

[54]. A. B. Solovieva, N. S. Melik-Nubaro, T. M. Zhiyentayev, P. I. Tolstih, I. I. Kuleshov, N. A. Aksenova, E. A. Litmanovich, N. N. Glagolev, V. A. Timofeeva, A. V. Ivanov, Laser physics 19 (2009) 81.

[55]. T. M. Zhientaeva, N. S. Melik-Nubarova, E. A. Litmanovicha, N. A. Aksenovab, N. N. Glagolevb, A. B. Solov'evab. Polymer science Series A 51 (2009) 502.

[56]. Y. T. Yang, C. T. Chen, T. Tsai, Dyes Pigm 96 (2013) 763.

[57]. H. Park, K. Na, Biomaterials 34 (2013) 6992.

[58]. Z. Sezgin, N. Yu¨ ksel, T. Baykara. Eur. J. Pharm. Biopharm. 64 (2006) 261

[59]. J. Sobczyński, S. Kristensena, K. Berga. Photochem. Photobiol. Sci. 13 (2014) 8.

[60]. B. H. Vilsinski, A. P. Gerola, J. A. Enumo, K. da Silva Souza Campanholi, P. C. de Souza Pereira, G. Braga, N. Hiok, E. Kimura, A. L. Tessaro, W. Caetano, Photochem. Photobiol. 91 (2015) 518.

[61]. A. C. Wenceslau, G. L. Q. C. Ferreira, N. Hioka, W. Caetano J. Porphyr Phthalocyanines 19 (2015) 1168.

[62]. J. P. F. Mota, A. E. da Costa Júnior, V. G. P. Ribeiro, S. G. Sampaio, N. M. A. Lima, F. L. F. da Silva, C. S. Clemente, G. Mele, D. Lomonacoa, S. E. Mazzetto, J. Braz. Chem. Soc. 28 (2017) 1063.

[63]. E. S. Lee, Y.T. Oh, Y.S. Youn, M. Nam, B. Park, J. Yun, J.H. Kim, H.T. Song, K.T. Oh, Colloids Surf. B: Biointerfaces 82 (2011) 190.

[64]. D. S. Pellosi, A. L. Tessaro, F. Moret, E. Gaio, E. Reddi, W. Caetano, F. Quaglia, N. Hioka. J. Photochem. Photobiol A: Chemistry 314 (2016) 143.

[65]. F. Moret, E. Redd. J. Porphyrins Phthalocyanines 21 (2017) 239.

[66]. L. Lamch, U. Bazyli´nska, J. Kulback, J. Pietkiewicz, K. Bie˙zu´nska-Kusiak, K.A. Wilk. Photodiagnosis Photodyn Ther. 11 (2014) 570.

[67]. B. Sarkar, V. Venugopal, M. Tsianou, P. Alexandridis, Colloids Surf A Physicochem Eng Asp 422 (2013) 155

[68]. F. Figueira, J. A.S. Cavaleiro, J.P.C. Tomé, J. Porphyr. Phthalocya. 15 (2011) 517.

[69]. C. Mauriello-Jimenez, J. Croissant, M. Maynadier, X. Cattoën, M. W. C. Man, J. Vergnaud, V. Chaleix, V. Sol, M. Garcia, M. Gary- Bobo, L. Raehm, Jean-Olivier Durand, J. Mater. Chem. B, 3 (2015) 3681.

[70]. E. Secret, M. Maynadier, A. Gallud, M. Gary-Bobo,A. Chaix, E. Belamie, P. Maillard, M. J. Sailor, M. Garcia, J. Durand, F. Cunin, Chem. Comm. 49 (2013) 4202.

[71]. N. A. Aksenovaa, V. V. Kardumyana, N. N. Glagoleva, V. T. Shashkovaa, I. A. Matveeva, P. S. Timashev, and A. B. Solov'eva, Russian J. Phys. Chem. A, 89 (2015) 1486.

[72]. A. Sundblom, A. E. C. Palmqvist, K. Holmberg. Langmuir 26 (2010) 1983.

[73]. B. Lee, Z. Ma, Z. Zhang, C. Park, S. Dai. Microporous and Mesoporous Materials 122 (2009) 160.

[74]. D. H. Nguyen, J. W. Bae, J. H. Choi, J. S. Lee, K. D. Park. J Bioact Compat Polym 28 (2013) 34.

[75]. P.S Low, W.A. Henne, D.D. Doorneweerd, Acc Chem Res 41 (2008) 120.

[76]. N. Li, X. Yang, G. Zhai, L. Li, J. Colloid Interface Sci. 350 (2010) 117.

[77]. Y. Li, Y. Bi, Y. Xi, L. Li, J. Drug Target. 21 (2013) 188.

[78]. F. Yamamoto, Y. Ohgari, N. Yamaki, S. Kitajima,O. Shimokawa, H. Matsui, S. Taketani, Biochem. Biophys. Res. Commun. 353 (20017) 541.

[79]. C. Perotti, H. Fukuda, G. DiVenosa, A. J. MacRobert, A. Batlle, A. Casas, Br. J. Cancer. 90 (2004) 1660.

[80]. D. He, S. Behar, N. Nomura, S. Sassa, H.W. Lim, Photochem Photobiol. 61 (1995) 656.

[81]. M. Wachowska, A. Muchowicz, M. Firczuk, M. Gabrysiak, M. Winiarska, M. Wańczyk, K. Bojarczuk and J. Golab, Molecules 16 (2011) 4140.

[82]. T.J. Dougherty, C.J. Gomer, B.W. Henderson, G. Jori, D. Kessel, M. Korbelik, J. Moan, Q. Peng, R. J. Natl. Cancer Inst. 90 (1998) 889.

[83]. R. K. Pandey, G. Zheng. In The Porphyrin Handbook, K.M. Kadish, K.M. Smith, R. Guilard (Eds), Vol. 6, Academic Press (2000).

[84]. R. Bonnett. In Chemical Aspects of Photodynamic Therapy, Gordon and Breach Science Publishers, Amsterdam (2000).

[85]. K. Kano, K. Fukuda, H. Wakami, R. Nishiyabu, R.F. Pasternack, J. Am. Chem. Soc. 122 (2000) 7494.

[86]. G. M. Whitesides, J. P. Mathias, C. T. Seto, Science, 254 (1991) 1312.

[87]. J.R. Tozoni, N.M. Barbosa Neto, C.A. Ribeiro, W.M. Pazin, A.S. Ito, I.E. Borissevitch, A. Marletta, Polymer 102 (2016) 136.

[88]. U. Sigge, U. Bindig, C Endisch, T. Komatsu, E. Tsuchida, J. Voigt, J.H. Fuhrhop, Ber. Bunsenges. Phys. Chem, 100 (2010) 2070.

[89]. A. B. Solov'eva, N. S. Melik-Nubaro, N. A. Aksenova, N. N. Glagolev, V. G. Vstovskii, V. S. Bugrin, V. N. Luzgina, V. A. Ol'shevskaya, G. V. Belkova. Russian J. Phys Chem 80 (2006) 124.

[90]. R. R. Allison, G. H. Downie, R. Cuenca, X. H. Hu, C. J. H. Childs, C. H. Sibata, Photodiagnosis Photodyn Ther. 1 (2004) 27

[91]. L R.W. Boyd, Nonlinear Optics; Academic Press: San Diego, CA, (1992).

[92] J. Zyss, Ed. Molecular Nonlinear Optics: Materials, Physics and Devices; Academic Press: New York, (1994).

[93] B.E.A. Saleh, M.C. Teich, Fundamentals of Photonics; Wiley: New York, (2012).

[94]. G. de la Torre, P. Vázquez, F. Agulló-López, T. Torres, Chem. Rev. 104 (2004) 3723

[95] H.S. Nalwa, S. Miyata (Eds.), Nonlinear Optics of Organic Molecules and Polymers, CRC Press, Boca Raton, p. 813. (1997)

[96] G. de la Torre, T. Torres, F. Agullo-Lopez, Adv. Mater. 9 (1997) 265.

[97] H. S. Nalwa, J. S. Shirk, in: C.C. Leznoff, A.B.P. Lever (Eds.), Phthalocyanines. Properties and Applications, VCH, Cambridge, p. 79. (1996)

[98]. K. Sakamoto, E. Okumura, R. Hirohashi, In: Phthalocyanine as Functional Dyes, IPC, Tokyo, Japan, (2004).

[99]. N.B. McKeown, In: Phthalocyanine Materials-Synthesis, Structure and Function, Cambridge University Press, (1998).

[100] D. Dini, M. Barthel, M. Hannack, Eur. J. Org. 20 (2001) 3759.

[101] G. de la Torre, P. Vazquez, F. Agullo-Lopez, T. Torres. Chem. Rev. 104 (2004) 3723.

[102] V. Rao, P. T. Anusha, T. S. Prashant, D. Swain, S. P. Tewari, Mater. Sci. Appl. 2 (2011) 299.

[103]. R.C. Hollins, Curr. Opin. Solid State Mater. Sci. 4 (1999) 189.

[104] M.D. Hecimovich, Sport. Chiropr. Rehabil. 55912 (2000) 24.

[105] T. Kololuoma, J.A.I. Oksanen, P. Raerinne, J.T. Rantala, J. Mater. Res. 16 (2011) 2186.

[106] A. Sarkar, P.R. Dvornic, J.P. Godschalx, Polymeric Dye for Optical Power

[107]. O. M. Bankole, T Nyokong, J Coord Chem 68 (2015) 3727

[108]. C. Mkhize, J. Britton, T. Nyokong. Polyhedron 81 (2014) 607

[109]. S.J. Mathews, S. Chaitanya Kumar, L. Giribabu, S. Venugopal Rao Optics Communications 280 (2007) 206

[110]. R.L. Sutherland, Handbook of Nonlinear Optics, Marcel Dekker, New York, NY, 2nd ed., 2003.

[111]. X. Qiu, T. Kosobe, N. Kawashima, Chemical Research in Chinese Universities 26 (2010), 66.

[112]. W. Spiller, H. Kliesch, D. Woehrle, S. Hackbarth, B. Roeder, G. Schnurpfeil, J. Porphyr. Phthalocya. 2 (1998) 158.

[113] W. Zhang, Y. Shi, Y. Chen, J. Ye, X. Sha, X. Fang, Biomaterials 32 (2011) 2894.

[114] J.J. Lin, J.-S. Chen, S.J. Huang, J.H. Ko, Y.-M. Wang, T.-L. Chen, L.-F. Wang, Biomaterials 30 (2009) 5114

[115]. J.U. Izunobi, C.L. Higginbotham, J. Chem. Educ. 88 (2011) 1098.

[116]. B. Lee, Z. Ma, Z. Zhang, C. Park, S. Dai. Microporous Mesoporous Materials 122 (2009) 167

[117]. V. Vannikov, A. D. Grishina, Y. G. Gorbunova, T. V. Krivenko, A. S. Laryushkin, L.A. Lapkina, V. Savelyev, A. Y. Tsivadze, Polym. Sci. A 2011, 53, 1069.

[118] K.E. Sekhosana, E. Amuhaya, T. Nyokong. Polyhedron 85 (2015) 347.

[119]. J. E. Falk, Edited by K. M. Smith, In porphyrins and metalloporphyrins (1975) New York, Elsevier.

[120]. A. El-Faham, F, Albericio, Chem. Rev. 111 (2011) 6557

[121]. R. Giovannetti in: Macro To Nano Spectroscopy (Ed:J. Uddin) (2012). Intech, Open science

[122]. M. Uttamlal, A.S. Holmes-Smith, Chem. Phys. Lett. 454 (2008) 223

[123]. M. S. Montaudo, Mass Spectrometry Reviews 21 (2002) 108– 144.

[124]. E. Rampazzo, R. Voltan, L. Petrizza, N. Zaccheroni, L. Prodi, F. Casciano, G. Zauli, P. Secchiero. Nanoscale, 5 (2013) 7905

[125]. G. Gyulai, A. Magyar, J. Rohonczy, J. Orosz, M. Yamasaki, Sz. Bosze, É. Kiss, eXPRESS Polymer Letters.10 (2016) 226

[126]. T. Chakraborty, M. J. Bucknum, E. A. Castro. In: Computational and Experimental Chemistry: Developments and Applications. CRC press. 2013

[127] S.L. Kotova, V.A. Timofeeva, G.V. Belkova, N.A. Aksenova, A.B. Solovieva, Micron. 43 (2012) 445.

[128]. H. Aizawa, Open Chem Phys J. 3 (2011) 9

[129]. A. T. Press, A. Ramoji, M. vd Lühe, A. C Rinkenauer, J. Hoff, M. Butans, C. Rössel, C. Pietsch, U. Neugebauer, F. H Schacher, M. Bauer. NPG Asia Materials, 9 (2017) 13.

[130]. Chaibundit C, Ricardo NMPS, Costa FMLL, Yeates SG, Booth C Langmuir 23 (2007) 9229

[131]. P. Alexandridis, J. F. Holzwarth, T. A. Hatton, Macromolecules 27 (1994) 2414

[132]. Wei Z, Hao J, Yuan S, Li Y, Juan W, Sha X, Fang X. Int. J. Pharm. 376 (2009)176.

[133]. C. A. Prestidge, T. J. Barnes, W. Skinner. J. Pharm. Pharmaco. 59 (2007) 251.

[134]. Z. Jianzheng, J. Wei, Z. Xiuwen, W. Yundong, Tsinghua Sci Technol. 12 (2007) 496

[135]. J. Liu, D. Liu, Y. Yokoyama, S-ichi Yusa, K. Nakashima, Langmuir 25 (2009) 743

[136]. M. J. L. Portole´s, F. R. Nieto, D. B. Soria, J. I. Amalvy, P. J. Peruzzo, D. O. Ma´rtire, M. Kotler, O. Holub, M. C. Gonzalez, J. Phys. Chem. C 113 (2009) 13702.

[137]. K. Suzuki, K. Ikari, H. Imai, J. Am. Chem. Soc. 126 (2004) 463

[138]. S. Sapra, D. Sarma, Pramana – J. Phys. 65 (2005) 565.

[139]. S. Xu, S. Hartvickson, J.X. Zhao, ACS Appl. Mater. Interfaces 3 (2011) 1865.

[140]. D. M. Jameson. Introduction to fluorescence, CRC Press, Taylor & Francis Group, United State, 2014.

[141]. J. R. Lakowicz, Principles of Fluorescence Spectroscopy (3rd edition), New York: Springer, (2006).

[142]. Y. Zhang, T-H. Wang, Theranostics 7 (2012) 631

[143]. J. R. Albani. In: Principles and Applications of Fluorescence Spectroscopy. New York. Wiley, 2008

[144]. Z. Gu, W. Lei, W. Shi, Q. Hao, W. Si, X. Xia, F. Wang. Spectrochim. Acta A 132 (2014) 316.

[145]. B. Castro, P. Gameiro, J. L. Lima, C. Matos, S. Reis. Mater. Sci. Eng. C 18 (2001) 71.

[146]. M. Vermathen, E. A. Louie, A. B. Chodosh, S. Ried, U. Simonis. Langmuir 16 (2000) 221.

[147]. C. A. Steinbeck, N. Hedin, B. F. Chmelka, Langmuir 20 (2004)10412

[148]. A. Tanaka, K. Nakamura, I. Nakanishi, H. Fujiwara. J. Med. Chem. 37 (1994) 4563.

[149]. M. J. Ruiz-Angel, R. D. Caballero, E. F. Simo-Alfonso, M. C. Garcia-Alvarez- Coque. J. Chromatogr. A. 947 (2002) 31.

[150]. A. Harriman, M.C. Richoux, J Chem Soc Faraday Trans II 76 (1980) 1618.

[151]. A. Ogunsipe, J-Y. Chen, T. Nyokong, New. J. Chem. 28 (2004) 822.

[152]. J. Fu, X.Y. Li, D.K.P. Ng, C. Wu, Langmuir 18 (2002) 3843.

[153]. T.W.J. Gadella Jr, R.M. Clegg, T.M. Jovin, Biomaging 2 (1994) 139.

[154]. S. Fery-Forgues, D. Lavabre, J. Chem. Edu. 76 (1999) 1260.

[155]. A. M. Brouwer. Pure App. Chem 83 (2011) 2213.

[156]. R. L. Brookfield, H. Ellul, A. Harriman, G. Porter, J. Chem. Soc. Faraday Trans. 82 (1986) 219.

[157]. H.C. Gerritsen, R. Sanders, A. Draaijer, Proc. SPI 2329 (1994) 260.

[158]. A.G. Ryder, S. Power, T.J. Glynn, J.J. Morrison, Proc. SPI 4529 (2001) 102.

[159]. C. Mauriello-Jimenez, J. Croissant, M. Maynadier, X. Cattoën, M.W.C. Man, J. Vergnaud, V. Chaleix, V. Sol, M. Garcia, M. Gary-Bobo, L. Raehm, J.-O. Durand. J. Mater. Chem. B, 3 (2015) 3681.

[160]. C.S. Foote, in Singlet Oxygen, Waserman H.H., Murray R.W. (Eds). Academic Press, New York, San Francisco, London, 1979: 139-171

[161]. M. Niedre, M.S. Patterson, B.C. Wilson, J Photochem Photobiol 75 (2003) 382.

[162]. M.S. Patterson, S.J. Madsen, R. Wilson, J Photochem Photobiol B: Bio 5 (1990) 69.

[163]. H. Li, T.F. Guarr, J. Chem. Soc. Chem. Commun. (1989) 832.

[164]. C. Tanielian, C. Wolff, M. Esch. J Phys Chem 100 (1996) 6555.

[165]. N. Masiera, J. Buczyńska, G. Orzanowska, H. Piwoński, J. Waluk, Methods Appl. Fluoresc. 2 (2014) 024003 (7pp).

[166]. C.R. Lillo, J. J. Romero, M. L. Portolés, R. P. Diez, P. C. Caregnato, M. C. Gonzalez, Nano Research 8 (2015) 2047.

[167]. Nishiyama N, Morimoto Y, Jang W-D, Kataoka K. Adv Drug Deliv Rev 61 (20

[168] A. B. Solovieva, N. A. Aksenova. In Additives In Polymer: Analysis and Application, A. A. Berlin, S. Z. Rogovina, G. E. Zaikov (Eds), Apple Academic Press (2016)09) 327.

[169] K. Hirakawa, Shu Morimoto, J. Photochem Photobio A: Chemistry 318 (2016) 1.

[170]. R.O. Ogbodu, J. L. Limson, E. Prinsloo, T. Nyokong, Synthetic Met. 204 (2015) 122.

[171]. L. Bourré, F. Giuntini, I. M. Eggleston, M. Wilson, A.J. MacRobert, Mol Cancer Ther 7, 1720 (2008)

[172]. T. Osaki, S. Takagi, Y. Hoshino, M. Okumura, T. Fujinaga, Cancer Lett. 243 (2006) 292.

[173]. N. Nombona, K. Maduray, E. Antunes, A. Karsten, T. Nyokong. J. Photochem. Photobio B: Biol 107 (2012) 35.

[174]. L. A. Lapkina, Y. G. Gorbunova, D.O. Gil, V. K. Ivanov, N. Y. Konstantinov, A. Y. Tsivadze. J. Porphy. Phthalocya. 17 (2013) 564

[175]. T. Nyokong, H. Isago J. Porphyrins Phthalocyanines 8 (2004)1083

[176]. K. Ishii, N. Kobayashi. In: Kadish KM, Smith KM, Guilard R (eds) The Porphyrin Handbook. New York: Academic Press, 2003, pp. 1–42.

[177]. T. H. Tran-Thi, C. Desforge , C. Thiec, S. J. Gaspard, Phys Chem. 93 (1989) 1226.

[178]. M. Sheik-bahae, A.A. Said, E.W. Van Stryland. High-sensitivity, single-beam n2 measurements. Opt. Lett. 14 (1989) 955.

[179]. M. Sheik-Bahae, A.A. Said, T. Wei, D.J. Hagan, E.W. Van Stryland. IEEE J. Quantum Electron. 26 (1990) 760.

[180] G. Tsigaridas, I. Polyzos, P. Persephonis, and V. Giannetas, Opt. Commun. 26 (2006) 284.

[181]. E. M. García, S. M. O'Flaherty, E. M. Maya, G. de la Torre, W. Blau, P. Vázqueza and T. Torres, J. Mater. Chem., 13 (2003) 749.

[182]. J. Simon, C. Sirlin. Pure Appl. Chem. 61 (1989)1625.

[183]. D. Dini and M. Hanack. In the Porphyrin Handbook: Physical Properties of Phthalocyane-based Materials, Vol K. M. Kadish, K. M. Smith and R. Guilard (Eds.) Academic Press: USA, 2003, vol.17, pp. 22-31.

[184]. L. De Boni, E. Piovesan, L. Gaffo, C.R. Mendonça, J. Phys. Chem. A. 112 (2008) 6803.

[185]. Y. Chen, L. Gao, M. Feng, L. Gu, N. He, J. Wang, Y. Araki, W.J. Blau, O. Ito, Mini-Rev. Org. Chem. 6 (2009) 55.